ABSTRACT

PALMER, JEREMY ANDREW. Development of Millimeter Scale Motors For Miniature Direct Drive Robots. (Under the direction of Dr. Edward Grant, and Dr. Jeffrey W. Eischen)

The twentieth century marked a period of rapid expansion of technology associated with miniaturization of engineering systems. A recent theme in this trend is the development of miniature, distributed robots that mimic insect behavior and locomotion. This research addresses the need for millimeter-scale, direct drive, high force/torque motors to support these platforms. Among the technologies currently available, scalable motors based on piezoelectric transducers are the focus. The specific contributions of this work are as follows. (1.) The design, analysis, and characterization of a macro-scale linear piezomotor constructed with a parallel arrangement of stressed unimorph piezoelectric transducers are presented. The prototype demonstrates a novel application of passive mechanical latches to produce inchworm motion while eliminating the need for multiple control signals. (2.) A dimensional analysis is conducted to reveal scale factors that govern the relationship between stressed unimorph performance parameters and size. The results support a millimeter-scale version of the linear piezomotor that incorporates transducers with alternative annular geometry for improved stiffness. (3.) The development of a miniature mode conversion rotary ultrasonic motor based on a piezoelectric stack transducer is reported. Results of a dynamic analysis lead to scale factors for static torque and rotor velocity. Lastly, the linear and rotary piezomotor systems are compared in the context of scalability to determine the most effective system for miniature direct drive robotics.

Blocked force performance of the miniature linear piezomotor was limited to 0.25 N by back slip in the passive latches, and transducer displacement losses leading to greater compliance in the assembly. Since displacement of the annular stressed unimorph transducer decreases with the square of the outside radius, precision engineering is required to avoid these losses. The rotary ultrasonic motor proved to be a more effective choice for driving the robotic locomotion system. Dimensional analysis results indicate that static torque scales with the square of the rotor contact radius. Using alternative designs, a static torque density of 0.37 Nm/kg was measured in the prototype.

DEVELOPMENT OF MILLIMETER SCALE MOTORS FOR MINIATURE DIRECT DRIVE ROBOTS

JEREMY ANDREW PALMER

A dissertation submitted to the Graduate Faculty of
North Carolina State University
in partial fulfillment of the requirements for the Degree of
Doctor of Philosophy

MECHANICAL AND ELECTRICAL ENGINEERING

Raleigh
2002

APPROVED BY:

_____   _____
Co-Chair of Advisory Committee   Co-Chair of Advisory Committee

_____   _____

_____   _____

DEDICATION

This dissertation is dedicated to Holly, my loving wife who has supported me selflessly through this period. It's dedicated to God, who gives us the gifts of intellect and curiosity, and to my family and friends who help nurture them. Lastly, it's for a little kid who dreams really big.

BIOGRAPHY

JEREMY PALMER received his Bachelor of Science degree in Mechanical Engineering from the University of Connecticut in 1994. After a three-year tenure as a mechanical engineer with the General Electric Company, he received a Master of Science degree in Mechanical Engineering from North Carolina State University in 1999. He is currently a Ph. D. candidate in Mechanical and Electrical Engineering, conducting research in miniature mechatronic systems at the North Carolina State University Center for Robotics and Intelligent Machines (CRIM).

ACKNOWLEDGEMENTS

TABLE OF CONTENTS

TABLE OF CONTENTS (CONTINUED)

TABLE OF CONTENTS (CONTINUED)

LIST OF TABLES

LIST OF FIGURES

LIST OF FIGURES (CONTINUED)

LIST OF FIGURES (CONTINUED)

Chapter 1

Introduction

1.0 Introduction

The latter half of the twentieth century has marked a period of rapid expansion of technology associated with miniaturization of engineering systems. Fueled by the microelectronics revolution, some of the outstanding miniature products heralded by Feynman and Drexler in the 1960's and 1980's have come to fruition in the consumer, defense, and biomedical industries (Gilbert) [32], (Feynman) [27], (Drexler) [22]. A recent area of interest is the development of miniature, distributed robots with energy and power actuation systems that mimic insect architecture and locomotion. The U. S. Defense Advanced Research Projects Agency (DARPA) is currently sponsoring joint industrial and academic research into robotic insect "swarms" for reconnaissance, and search and rescue operations. The research presented in this dissertation is part of that effort.

1.1 Program Objectives

The North Carolina State University (N. C. State) *Planar Processed Robots* research program had the following objective: to construct an autonomous robot less than 5 cm^3 in volume that demonstrates controlled jumping locomotion, with an average jump height of 1 meter. A long-term strategy for miniaturizing the robot platform and its subsystems includes fabricating critical components from planar microfabrication processes, such as micro electromechanical systems (MEMS), LIGA, photochemical machining (PCM), or 3-D printing (Kovacs) [50]. Processing of parts using these manufacturing technologies is not addressed here.

1.2 Robotic Platform Design

Nature offers many examples of effective jumping mechanisms (Chapman and Joern) [13], (McMahon and Bonner) [56] (Okubo, Nakano, and Handa) [66]. To master the physical principle, the biology of several species of insects and amphibians was reviewed, including frogs, fleas, and locusts [13]. These animals share a common system whereby muscles stretch or compress a flexible tendon or protein to store elastic energy in a manner similar to a catapult [13]. A skeletal element serves as a latch which, when triggered, instantly releases the energy to a folding leg linkage that launches the animal's body upward [13]. The N. C. State robotic jumping platform shown in Figure 1.1 mimics the major components of such a biological system. Referring to Figure 1.1 (a), elastic energy is stored in sets of parallel coil springs. Actuation and triggering are accomplished by a motor and drive mechanism mounted to the upper platform. The storage springs are charged by
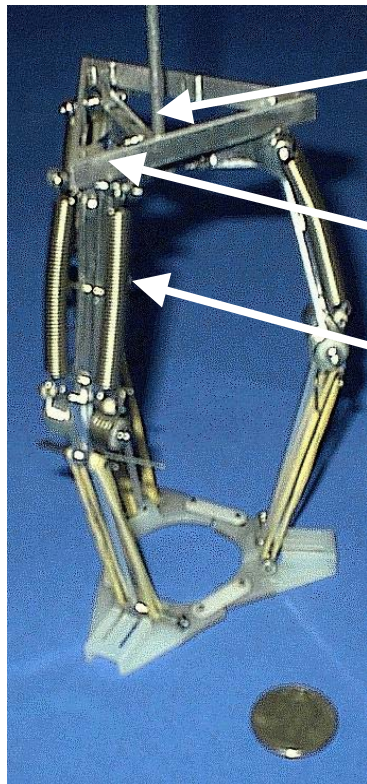
Rod and yoke assembly

Platform

Storage springs
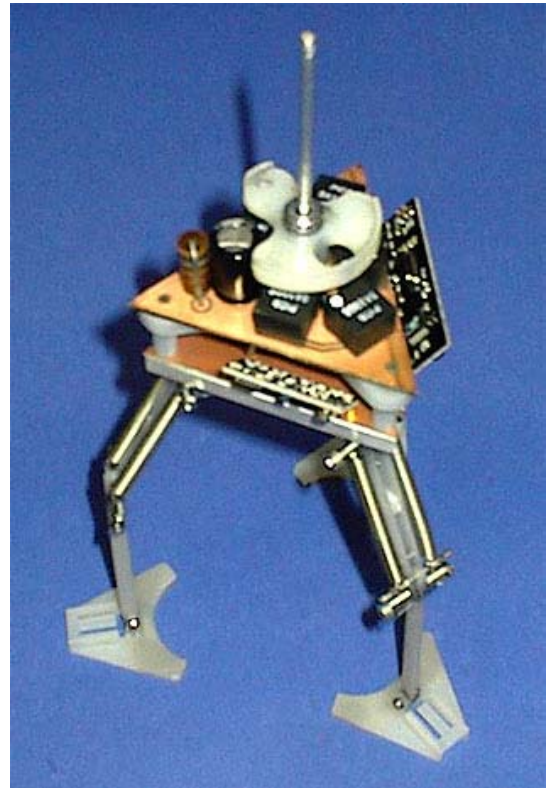
(a)   (b)

Figure 1.1. **N. C. State robotic jumping platform: (a.) Isometric view, (b.) Drive electronics installed**

displacing the rod and yoke assembly shown. In the linear configuration, the rod is driven by a linear motor with an integral passive latch acting as the trigger. A modified version used a rotary motor connected to a cam-follower mechanism, with the geometry of the cam governing the triggering action. Since the height of the jump is dependent on the mass of the platform, it was necessary to make the drive mechanism as simple and compact as possible. Consequently, motors with dimensions less than one inch in length and diameter were created. They were intended for directly driving the folding leg linkage without mechanical force/torque amplification (Figure 1.1). For these reasons and others discussed in the next chapter, motor designs based on piezoelectric transducers were pursued.

1.3 Dissertation Objectives

This dissertation presents the results of research and development of novel linear and rotary piezoelectric motor concepts to be used for driving miniature robotic platforms. Miniaturization is the central theme throughout, and in accordance with this theme, analysis is conducted to determine the *scalability* of performance metrics for these motors. In other words, the focus is to determine how motor performance varies with reductions in size. With the advent of microfabrication technologies, understanding scalability has increased in importance. Forces and energy conversion mechanisms (such as electrostatic attraction) that are insignificant at the macro scale take on greater importance when implemented in a micro system [22, 27].

1.4 Outline

The next chapter reviews the prior art in miniaturization of mechatronic systems, with an emphasis on electromagnetic and piezoelectric motors. The chapter includes the use of Dimensional Analysis, and the principles of Similarity as tools for evaluating scalability (Baker) [4], (Langhaar) [53], (Skoglund) [79]. Chapter 3 introduces a linear piezoelectric motor developed in this program, and an analysis that quantifies its performance. These performance metrics become the foundation for subsequent designs. A miniature version of the linear piezoelectric motor is presented in Chapter 4. Expressions are derived that are used to quantify the scalability of its performance. Chapter 5 presents the design and characterization of the rotary piezoelectric motor. Scalability of this device is discussed in Chapter 6, which also compares the performance of the piezoelectric motor concepts to each other, and to commercial products in the context of the robotic drive system requirements.

Chapter 2

Prior Art

2.0 Prior Art

This chapter documents the prior art in technologies that have created miniature engineering systems. The investigation surveys developments in the latter part of the twentieth century that have influenced the fields of Miniature, Micro-miniature, and Nanorobotics. Also described is the background of research into piezoelectric motors. The last century also witnessed the evolution of theories leading to predictions of the nature of scale, and what happens to physical systems as they are scaled geometrically. The following chapter summarizes important contributions over the past fifty years.

2.1 Trends in Miniaturization Technology

The post World War II period saw dramatic advances in technology. Amidst the rapid expansion in aerospace and military electronics in the 1950's and 60's, a 1961 book entitled *Miniaturization* was published. It chronicled the engineering community's desire to reduce size, and hence the weight and cost of countless components that were considered mission-critical (Gilbert) [32]. Some examples include portable radios, missile guidance systems, and of course, the computer. Richard Feynman heralded the age of micro and nanotechnology in the late 1950's with his article *There's Plenty of Room At The Bottom* [27]. In it, he establishes the technical feasibility of such feats as inscribing encyclopedia volumes on the head of a pin. Moreover, he launched a contest with a sizeable cash prize to the group who could develop working motors or similar devices on a scale smaller than the world had yet seen [32]. Miniaturization was boosted further by the

microelectronics revolution of the 1970's and 1980's. Novel microfabrication processes developed by government, academic, and industrial researchers, such as bulk and surface micromachining, LIGA (Lithography Electroplating and Forming), laser micromachining, Stereolithography, and 3-D printing, all led to the advent of Microelectromechanical Systems (MEMS). Most recently, federal research initiatives into Nanotechnology have pushed technology to an unprecedented scale (Drexler) [22]. These technologies, characterized by lithographic techniques, create micron and sub-micron-scale mechanical structures that are utilized to produce products such as advanced sensors for the automotive and biomedical industries [22]. Drexler [22] explores potential products resulting from these manufacturing advances in his 1986 book *Engines of Creation*. In it, he envisions microrobots as medical cell repair machines, and inexpensive planetary explorers, among others.

2.2 Miniaturization in Mechatronics

2.2.1 Miniature Robotics

Khatib, Craig, and Lozano-Perez describe the field of Microrobotics as the fusion of Microtechnology with Robotics (Khatib, Craig, and Lozano-Perez) [46]. They classify microrobots in three ways [46]. (1.) The miniature or "macro-scale" robot is essentially the size of an insect, 1 to 3 cm^3 in volume. Manufactured with modern precision machining techniques, miniature robots are powered by conventional DC motors, and carry their own on-board sensor array, microcomputer system, and power supply [46]. Recent examples include prototypes produced by Sandia National Laboratories (Baumgartner) [6], and MIT's GNAT robot [46]. To date, most research has been limited to this class of robot. The miniature robot is a current objective of the DARPA MTO Division Distributed Robotics program. This program supports the research presented in this dissertation. (2.) Microrobots, are 1-3 μm^3 in volume, and are characterized by direct-drive electrostatic motors that, as Trimmer and Jebens illustrate, do not scale advantageously to the macro domain (Trimmer and Jebens) [84], [46]. Constructed from a MEMS wafer, these robots may possibly manipulate individual cells in biomedical applications. A disadvantage of their construction is that their workspace is limited to a microscopic area. In cases where they are intended to operate in a fluid medium, their mobility systems must generate enough work to overcome viscosity [46]. (3.) The final frontier of miniature robotics is defined by the nanorobot. Hundreds of nanometers in size, these machines are intended to interact with cells and individual

molecules using an electrochemical tool kit [46]. At the dawn of the 21st century, nature provides the only examples of nanorobots, in the form of single-cell organisms.

2.2.2 Motors

Electric, hydraulic, and pneumatic motors are the products of mature technologies that are used widely in practical engineering systems. As engineers consider motors for application on the millimeter and micro scale, specific challenges arise. The task of building ultra-small motor windings and hydraulic fluid handling systems is particularly daunting. Among others, piezoelectric actuators and ultrasonic motors based on simple, scalable designs, often with no moving parts, have been identified as promising candidates for powering miniature robots [46]. The following paragraphs provide justification for selecting linear (non-ultrasonic piezomotors), and rotary ultrasonic piezomotors to address scalability issues, and document progress made in their development.

2.2.2.1 Linear Piezomotors

Linear motors constructed from piezoelectric transducers may be distinguished as ultrasonic, or non-ultrasonic. The non-ultrasonic variety reviewed in this segment is referred to as the linear piezomotor. Rather than employ vibration coupled with frictional traction to drive a moving output member, linear piezomotors embody architecture similar to that of a stepper motor to directly harness the transducer displacements. Several linear piezomotor designs have been successfully commercialized as precision positioning devices, exploiting the micron-scale strains that are characteristic of laminated-crystal, or stack-type, piezoelectric transducers. Each of the piezoceramic lead zirconate titanate (PZT) material layers within a stack transducer undergoes an axial strain when an electric field is applied (Uchino) [88]. The amount of strain is proportional to the magnitude of the field as determined by a piezoelectric strain coefficient d_{ij} specific to the polarization of the material [88]. Stacking PZT layers in series amplifies the individual strains to yield a total transducer displacement on the order of tens of microns [88]. Previous work by Burleigh Instruments (Bizzigotti) [9], and researchers including Zhang and Zhu [104]; and Xu and King [100]; have attempted to harness the high forces generated by these transducers. Some designs attached mechanical systems to amplify piezomotor displacement. To remove the need for external amplification, other classes of piezoelectric transducers, stressed unimorphs, have been developed (Hyder, Horner, and Clark), [40].

A device designated a thin layer composite unimorph ferroelectric driver and sensor (THUNDER™) was recently developed at the NASA Langley Research Center (Mossi, Selby, and Bryant) [59], and is marketed by the FACE Corporation. A THUNDER™ unimorph is created by bonding a piezoceramic and aluminum laminate to a spring steel substrate using a polyimide adhesive (Wise) [97]. The adhesive curing process introduces residual stresses into the composite structure. The complete transducer has a curved substrate that mechanically amplifies piezoelectric deflection. Accordingly, THUNDER™ transducers exhibit a flexural displacement many times that of stack transducers by virtue of their construction. Figure 2.1 shows both types of transducer, THUNDER™ and piezoelectric stack. A THUNDER™ is a *compliant* structure. When a voltage
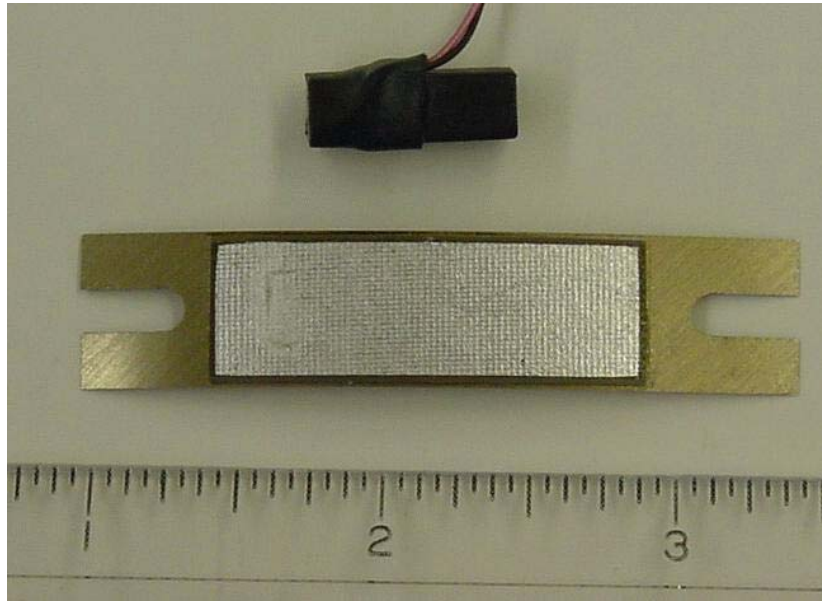
Figure 2.1. **THUNDER™ model 8R pre-stressed unimorph (bottom) with stack-type transducer (top)**
FACE International, Inc., www.face-int.com/thunder/prod/tprod.htm

is applied, bi-axial deformation occurs in the piezoceramic layer that reduces the radius of curvature of the substrate. Mechanical work is performed on the removal of the voltage from the transducer by harnessing the energy transferred during the period that the compliant substrate returns the transducer to its equilibrium position. The amount of work that can be produced by the THUNDER™ depends upon the stiffness of the substrate and the end conditions of its mounting (Mulling, Usher, Dessent, Palmer, Franzon, Grant, and Kingon)

[61]. An actuator system may be constructed by arranging THUNDERS in parallel. This arrangement increases the system stiffness, and impacts the amount of work that can be achieved.

Other researchers have engineered linear piezomotors based on unimorph and THUNDER™ technology. Hyder, Horner, and Clark document a prototype in which a series of THUNDERS are patterned on a continuous S-shaped steel strip [40]. A linear piezomotor is formed when two such strips are pressed against a rod or rail [40]. Actuating the THUNDERS in a pre-determined sequence generates a peristaltic, or wave-like traction on the output member [40]. Glumac and Robbins [34] demonstrate a linear actuator structure exhibiting displacement amplification through a series arrangement of bar-shaped unimorphs. Likewise, Bryant, Evans, Long, and Fox [12] report a "clam-shell" linear piezomotor for instrument deployment in satellite systems. This device also contains a series configuration of THUNDERS that are coupled at the middle, and hinged at the edges. The series arrangement causes the deflections of the individual devices to be accumulative.

The aforementioned stepper motor architecture consists of a set of clamps, coupled with the transducer acting as an extender. Figure 2.2 illustrates how the clamps alternately lock the device, thereby allowing the

(a)	(b)
(b)	(d)
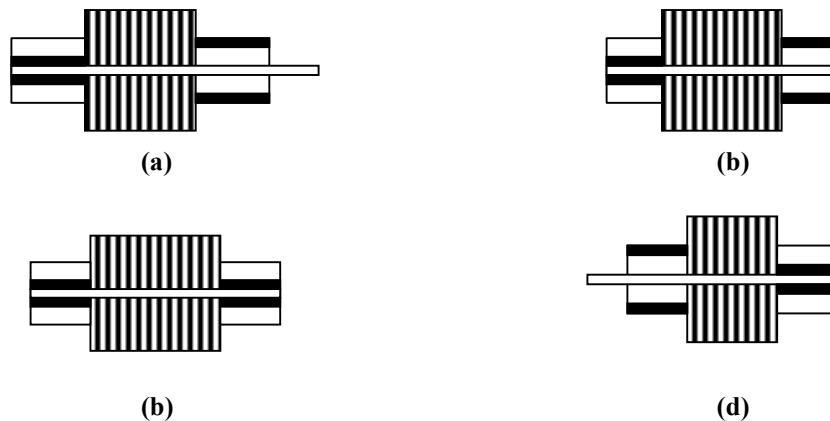
Figure 2.2. **Inchworm linear actuation sequence: a.) Rear clamp activation, b.) Extension, c.) Forward clamp activation, d.) Rear clamp release and relaxation causing rear clamp forward motion**

extender forces in one segment to move relative to the other. The result is an inchworm motion along a rod or fixed guide. Many groups have produced prototype inchworm piezomotors using a range of controlled clamping mechanisms. Recent research by Chen, Yao, Kim, and Carman [15] is significant in relation to the

miniaturization of linear piezomotors. This research integrates a unique micromachined rack structure with an interlocking active clamp [15].   Clamp mechanisms are necessary to harness the microscopic strains generated by piezoelectric transducers, and are a necessary component of linear piezomotors. The scale of these strains must be matched by the tolerances of the engineered structures housing the transducers. This condition places a high demand on the precision engineering used to produce linear piezomotors. The THUNDERWORM and miniature Milliworm prototypes described in subsequent chapters are THUNDER™-based linear piezomotors with latches that are *passive* in operation because they require no direct control. The latches are "mechanical diodes," permitting motion of the linear piezomotor in one direction only.   The style of the latch used was patented by inventors such as Drake [21] and Goul [35], and has been commercially available for decades. Recent commercial products using this latch include the so-called Bar Clamp or Fast C-clamp [21, 35].

A review of pertinent literature indicates the THUNDERWORM and related prototypes developed in this program are a unique integration of linear piezomotor design and THUNDER™ unimorph technology. There is no apparent precedent for a THUNDER™-based linear piezomotor with passive mechanical latches. Furthermore, no formal quasi-static analysis has been discovered in a literature search that attempts to quantify so-called back slip loss mechanisms in latches of this type. Studies that track the performance of THUNDER™ stressed unimorphs as a function of size appears to be a novelty. As the following section relates, such scale investigations are more prevalent in the study of electromagnetic and rotary ultrasonic motors.

2.2.2.2 Rotary Ultrasonic Motors

Rotary ultrasonic motors (USM's) also referred to as rotary vibromotors, use piezoelectric transducers to convert electric signals into resonant acoustic waves at kilohertz levels. A USM converts linear acoustic energy to useful rotary motion and torque. Uchino credits the early 1970's development of the first operational rotary USM's to Barth at IBM in the United States, and internationally to Soviet groups led by Lavrinenko and Vasiliev in the 1960's (Uchino) [89]. In the decades that followed, industrial USM research was most active in Japan, where they were applied in semiconductor devices, sports watches, and camera products that required inexpensive, compact, silent motors that did not produce magnetic interference [89].   Sashida led commercialization of the rotary USM in Japan in the early 1980's [89].

The principal components of a rotary USM include a resonant drive circuit, a resonator, a rotor, and an appropriate base or housing. The drive circuit, producing one or more harmonic signals at ultrasonic frequency

levels, provides electric input to the piezoelectric transducers. The transducer(s), as will be shown later, may be a discrete stack type, or a MEMS structure of varying geometry. There are two classes of resonators depending on the type of sound wave they produce, i.e. a traveling wave or a standing wave [89]. The components of a rotary USM with a standing wave resonator are illustrated in Figure 2.3. Standing wave resonator construction is sub-divided into two categories: (1) single transducer type or, (2) multi-transducer type. Category 1, multi-transducer type resonators, uses transducers that are orthogonal to each other (Nakamura and Ueha) [65]. When the output displacements generated by these two transducers are combined, an elliptical waveform results. It is this elliptical displacement waveform that is used to generate rotation of the output member [65]. In contrast, Category 2 uses a single transducer to create the desired elliptical motion. Although their design is simpler than the multi-transducer type, standing wave resonators that use a single-phase drive signal suffer from comparatively poor directional control [65]. Uchino [88, 89] describes a single transducer "mode conversion"
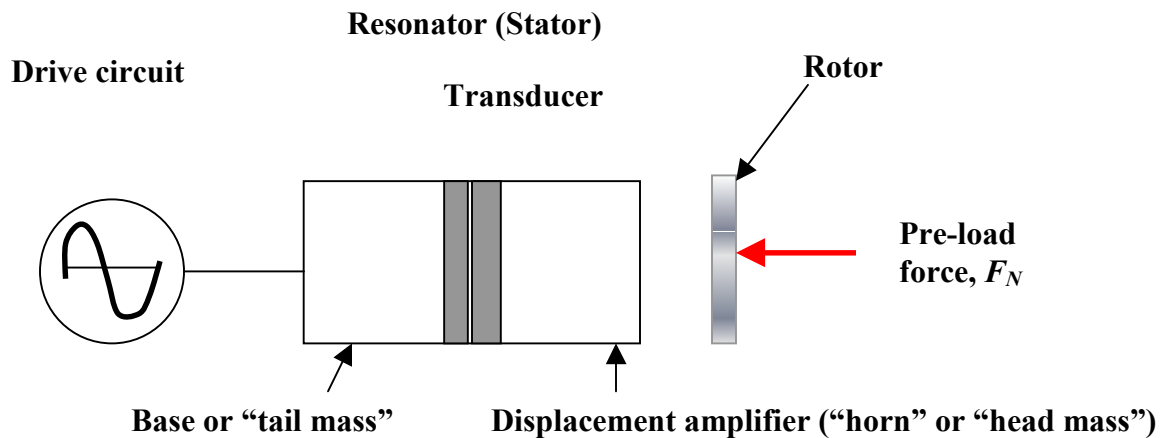
Figure 2.3. **Components of a rotary USM with a standing wave resonator**

system as being composed of an axially resonating transducer and a torsional coupler (see Figure 2.3). The torsional coupler passively converts longitudinal vibration into the desired elliptical waveform at the points of contact with the rotor [88, 89]. The complete resonator assembly is formed when the transducers are coupled to a base plate, and a displacement- amplifying member commonly referred to as a "horn" [89]. The standing wave resonator designs described here originated from the acoustic transducers patented by Paul Langevin in 1921 (Groves) [37]. In Langevin's "steel-quartz-steel" resonator construction, Stansfield [80] refers to the horn

and the base pieces as the head (or piston) and tail masses, respectively. He demonstrates that it is often desirable to select a tail mass larger than the head mass in order to direct acoustic energy towards the horn, i.e. higher to lower structural inertia [80]. This design heuristic was used for the USM constructed for the N.C. State research program. When the horn and the resonator are kept in contact by the application of a pre-load force F_N, an elliptical waveform produces a frictional moment on the face of the rotor. The applied elliptical waveform must be amplified by the horn to achieve the desired action. Lastly, the rotor's output rotation may be joined to an external load to perform useful work. Ueha and Uchino [87, 88] developed analytical expressions that describe USM torque and speed. These are discussed in this segment (Nakamura) [64, 89].

The following details standing and traveling wave USM prototypes. Ultrasonic motors can be classified into three size ranges. These ranges are assigned by the author to be consistent with those proposed by Khatib, Craig, and Lozano-Perez for robots. They are summarized in Table 2.1, below. Manufacturers like Piezosystems, and Panasonic offer conventional-sized USM's with outside diameters of 3 cm or more. In contrast, miniature or *mesoscale* USM's (largely experimental) span the range between 1 and 3 cm in diameter. Lastly, micro-scale USM's feature resonators based on MEMS transducers that can be hundreds of microns

Table 2.1 **Ultrasonic Motor Dimensional Classes**

Class	Stator Maximum Outside Diameter	Examples
Conventional	>3 cm	Piezosystems RU30-001 (Glenn and Hagood) [33]
Miniature (meso scale)	1–3 cm	(Kumada) [52]
Micro scale	1 um – 1 cm	Seiko (Chow and Thackery) [16], (Flynn, Tavrow, Bart, Brooks, Ehrlich, Udayakumar, and Cross) [17]

wide.

Examples of commercially produced conventional scale rotary USM's include the Shinsei USR60 disk type, and the Piezosystems RU30-001 (Glenn and Hagood) [33]. Unlike the standing wave resonator design described earlier, these motors generate torque using the frictional traction produced by a traveling wave. One or more ring-shaped transducers mounted to a toothed, disk-shaped, stator (shown below) induce the wave

(Kawai, Asai, Naito, Fukui, Adachi, Handa, Ikeda, and Tsuda) [45]. The transducers shown in Figure 2.4, are divided in sectors, the width of which corresponds to a fraction of the length of the corresponding standing wave, with adjacent sectors poled oppositely. When a pair of harmonic signals is applied to the poled sectors, the resulting standing waves undergo a relative shift with respect to wavelength *and* time [88]. The resulting tooth displacement is elliptical. This pattern of tooth displacement propagates around the rotor as a traveling wave. The toothed shape is unique, in that it amplifies the tip displacements [33]. The miniature mode
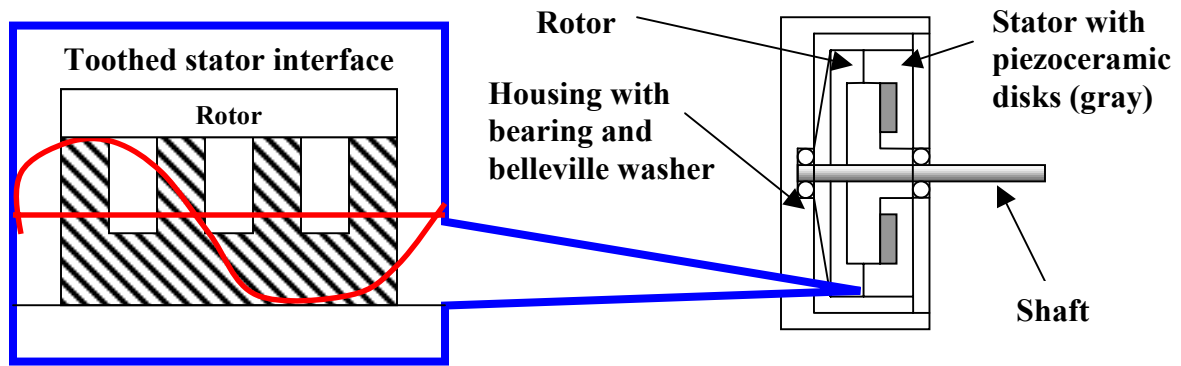
Figure 2.4. **Conventional scale disk type traveling wave rotary USM [45]**

conversion standing wave rotary USM fashioned like the one designed and patented by Kumada [52] is studied in this research program. It is illustrated in Figure 2.5. Although classified as a miniature device, the design in the 1987 patent is 6 cm in length. A so-called L/T coupler (longitudinal/ torsional coupler) bonded to the resonator assembly contacts the top surface of the horn at the outer perimeter.   The beam/spine on the upper portion of the L/T coupler (see Figure 2.6) is symmetrically offset from the vertical plane by an angle of twenty-six degrees [52]. This unique geometry converts the longitudinal vibration of the transducer to elliptical displacement. The outlying edges on the top face of the beam/spine are where contact with the rotor occurs. An exaggerated view of the deformed L/T coupler is depicted in Figure 2.6. The L/T coupler produces elliptical motion when the resonator assembly is loaded in compression. This motion ultimately drives the output shaft. Kumada's motor is bi-directional depending on frequency [52].
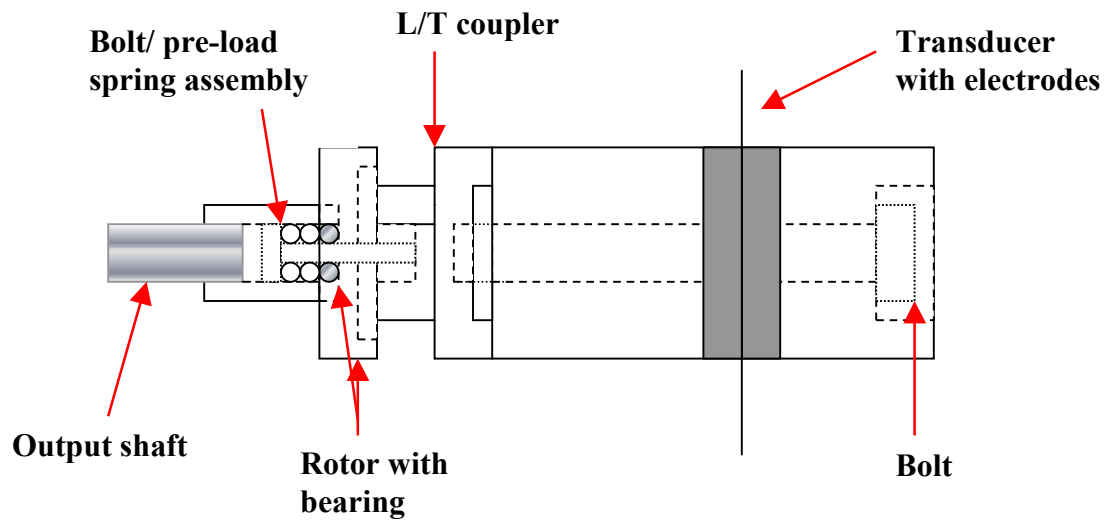
Figure 2.5. **Kumada rotary ultrasonic motor cross-section view [52]**
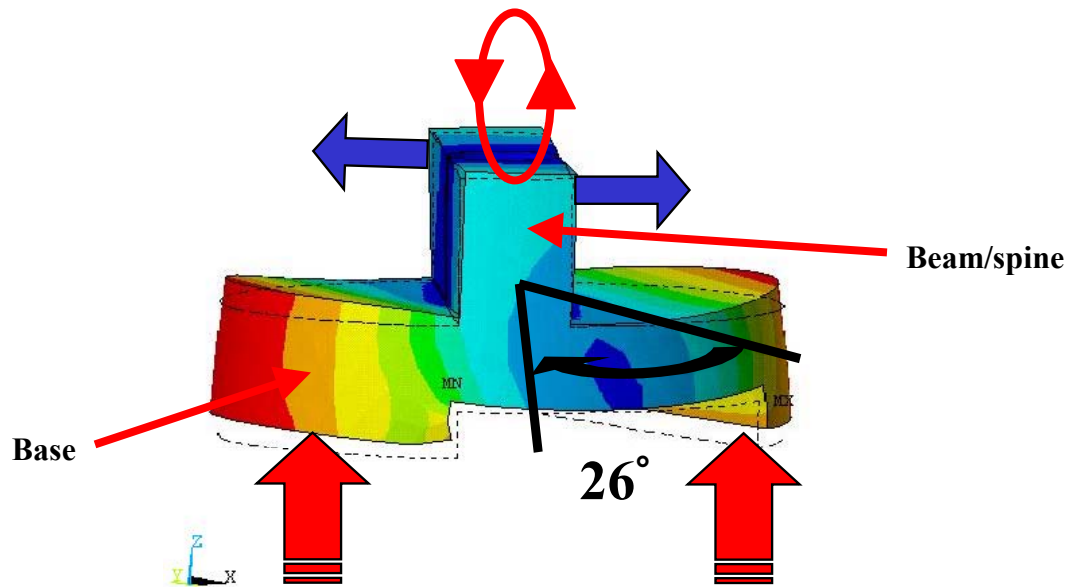
Figure 2.6. **L/T coupler deformed view**

Seiko Instruments introduced a remarkable second-generation commercial micro-scale USM in its 1998 line of Perpetual Calendar® sport watches (Chow and Thackery) [16] (see Figure 2.7). Its resonator is 4.5 mm in diameter, and 2.5 mm in thickness [16]. According to Chow and Thackery, Seiko modified the resonator of this microscopic USM so that it operates with a standing wave rather than a traveling wave to minimize the

Figure 2.7. **Seiko Instruments micro-scale rotary USM [16]**

complexity of the drive circuit [16]. Further miniaturization of traveling wave resonators is realized using thin film deposition and surface micromachined piezoceramics. Flynn et al. at the Massachusetts Institute of Technology developed prototype traveling wave rotary USM's with MEMS resonators (Flynn, Tavrow, Bart, Brooks, Ehrlich, Udayakumar, and Cross) [29]. Micro-scale versions of USM's based on Kumada's work have been prototyped by the Uchino group at the Pennsylvania State University (Yao, Koc, and Uchino) [101], (Uchino) [90].

Many of the performance metrics associated with electromagnetic motors also apply to rotary USM's. Considering motor performance, the primary interests of users include angular velocity, and torque. Torque may be characterized as static (stalled rotor), and continuous (steady state). These basic measures are divided by the mass of the device to yield torque, energy, and output power density. Table 2.2 lists motor metrics in SI units. The motor constant K_M listed in Table 2.2 is widely used by electric motor manufacturers. It is the constant of proportionality between the square of the continuous torque and the power consumed. It implies that the static and continuous torque, and hence the motor constant, increases with increasing motor size and mass (Wallace and Selig) [95]. The system selected to measure torque and angular velocity of motors depends upon budget, and the desired levels of resolution, accuracy, and precision. Modern commercial torque sensors utilize the dynamic signals from strain gauges mounted to a rotating shaft coupled to the motor's output. Other less sophisticated methods include simple braking mechanisms, and raising weights with a pulley. Similarly,

14

Table 2.2 **Motor Performance Metrics**

Metric	Symbol	SI Units
Angular Velocity, Frequency	ω	rad/sec
Static Torque	τ_s	Nm
Continuous Torque	τ_c	Nm
Torque Density	ρ_T	Nm/kg
Energy Density	ρ_E	J/kg
Power Density	ρ_P	W/kg
Motor Constant [95]	K_M	$Nm/W^{1/2}$

velocity measurements may be realized with equipment ranging from a shaft-mounted optical encoder, to timing shaft revolutions with a watch. However, interfacing macroscale transducers with the micro-scale world is problematic. In this situation, the continuous torque is estimated by observing the time required for the rotor to accelerate to its steady state velocity. It follows that the continuous torque is the product of the rotor moment of inertia, and the transient angular acceleration. This method was recently applied by Flynn to estimate torque performance of MEMS micro-scale USM's [29]. Nakamura achieved greater accuracy and repeatability by using an optical encoder to generate a voltage signal history of the transient state (Nakamura, Kurosawa, Kurebayashi, and Ueha) [63]. Performance data for rotary USM's is well documented by research organizations and manufacturers, which allows a direct comparison to be made between different classes of USM's and their electromagnetic counterparts.

Glenn and Hagood offer compilations of USM performance data, while Wallace and Selig have published a study of the electromagnetic "motor universe" that tracks torque performance of EM motors versus size [33, 95]. Using these studies, a set of direct comparisons between piezomotors, electromagnetic motors, and other types of actuators was prepared by Mulling at N.C. State University (Mulling) [60]. An excerpt appears in Table 2.3, below [33]. Included in the table are some of the pros and cons of rotary USM's as given by Uchino [90]:

- Compared to DC motors, rotary USM's deliver high torque at low rotational velocities, making them well suited for application in direct drive robotics. In contrast, high torque DC motors typically require a gearbox, which adds weight and complexity to the system.

- USM's are controllable, exhibit quick response, and do not require braking because of the pre-loaded frictional contact between rotor and stator.

- Since USM's operate at ultrasonic frequencies, their operation is virtually silent.

- USM's do not generate, nor are they affected by, external magnetic fields or radiation.

- Its simple, lightweight design contains no expensive copper windings, making the USM well suited for miniaturization.

- On the negative side, the frictional contact between the rotor and stator of a USM is a significant source of efficiency and endurance losses due to heat and wear.

- Powering USM's is a separate design problem, as certain prototypes require a high-voltage, resonant circuit that operates at ultrasonic frequencies.

Figure 2.8 is a graphical representation of the performance characteristics of common commercial DC motors versus their volume. The plot suggests that as motor volume approaches the micro scale, electromagnetic motors generate power exclusively from high angular velocity (recall power is the product of torque and angular velocity). The performance of scaled electromagnetic motors is discussed in more detail in Section 2.3.2. Considering the potential benefits as listed above, a micro USM designed for an optimized maximum continuous torque at low angular velocity remains a novel candidate for filling the so-called "motor gap" in miniature direct-drive robotics applications. Many groups have constructed models for designing prototype USM's with specific torque and angular velocity specifications (see Section 2.2.2.3).

2.2.2.3 Operational Models For Mode Conversion Rotary Ultrasonic Motors

The analytical models that have been devised to derive performance parameters of USM's, e.g., torque and velocity, and factors effecting efficiency, also include material wear rate at the interface between rotor and stator. This segment reviews models that are relevant to single transducer, mode conversion (Kumada) style rotary USM's, and published guidelines for design of similar motor systems. The discussion begins by considering the analysis of the resonator assembly, as described by Figure 2.3, then moves on to consider the rotor/stator interface. Finally, the equations related to performance are referenced for use in Chapter 5.

Table 2.3 **Performance Data of Prototype and Commercial Rotary Ultrasonic Motors vs. Commercial DC Motors**[1]

Rotary USM	Mass (kg)	No-Load Angular velocity (rad/sec)	Static Torque (Nm) (Stalled Rotor)	Energy Density (J/kg) (Stalled Rotor)	Power Density (W/kg)
Piezosystems RU30-001	0.02	31.4	0.1	31	157 (peak)
Kumada [33]	0.150	12.6	1.33	55.7	~50
Shinsei USR60 Disk type [33]	0.230	11.0	0.62	17.0	16
Canon EF 300/2.8L Ring type [33]	0.045	4.2	0.16	22.4	~5
MIT Double-Sided Prototype [33]	0.330	4.2	1.7	10.7	7.3
TITECH 5-mm Hybrid Transducer Type [65]	0.004	94.2	40×10^{-5}	0.624	9.36 (peak)
Seiko Instruments 10-mm Perpetual Calendar® [89], [16]	1.1×10^{-3} (est.: Al cylinder, 10 mm dia x 5 mm thk.)	628.3	1×10^{-05}	0.015	1.5 (peak)
EM Motor	Mass (kg)	No-Load Angular Velocity (rad/sec)	Static Torque (Nm) (Stalled Rotor)	Energy Density (J/kg) (Stalled Rotor)	Power Density (W/kg)
Smoovy™ 3-mm SYH39001,02	0.000326	7615.2	3.45×10^{-5}	0.66	1340 (peak)
Micro-Mo 1319E003S DC motor [33]	0.0112	1413.7	0.0033	1.85	104
Mabuchi FK-280-2865 DC motor [33]	0.036	1520.5	0.0152	2.65	160
Maxon DC motor [33]	0.038	546.6	0.0127	2.10	45
Aeroflex Brushless DC motor [33]	0.256	421	0.0098	0.241	4.0
Kannan Brushless DC motor [33]	0.600	521.5	0.08	0.838	17

[1] [60, 33, 65, 89, 16]

Clues as to the effective selection of design parameters for a resonator assembly are found in Stansfield's discussion of underwater acoustic transducer elements [80]. These parameters include the values of the head and tail masses, the resonator's natural frequency, and the effective stiffness of the transducer. Another important resonator parameter is the mechanical quality factor, Q_M, which describes the ratio of the assembly's resonant frequency to the acoustic bandwidth (Serway) [77]. Stansfield stresses the need for a wide bandwidth, and a correspondingly low quality factor, to facilitate impedance matching with the acoustic source over a wide frequency range [80]. Using a lumped mass approximation of the resonator assembly, the mechanical quality factor is related to the design parameters by the following equation:

$$Q_M = \frac{\omega_S M_H}{R_r M_B}(M_H + M_B) \tag{2.1}$$

where ω_S is the assembly's natural frequency, and M is the mass of the respective horn *(H)* and base *(B)* [80]. Acoustic radiation resistance, denoted by R_r, is the real portion of the complex acoustic radiation impedance [80]. In the case where the end radius of the horn is small in compared to the wavelength λ of the emitted sound, R_r is expressed as:

$$R_r = \frac{2\pi\rho c}{\lambda^2} A_p^2 \tag{2.2}$$

where ρ is the density of the horn material, and c is the speed of sound in that material [80]. The quantity A_p denotes the area of the output face of the horn. The natural frequency is related to the equivalent stiffness of the transducer and its support members by:

$$\omega_S^2 = k_{eq}\frac{(M_H + M_B)}{M_H M_B} \tag{2.3}$$

A center bolt typically maintains the transducer in compression between the horn and base masses [80]. The equivalent stiffness, k_{eq}, is derived by considering the dynamic equivalence of the bolt/ceramic material assembly. That is, the bolt and the ceramic material are considered to be in parallel, because they deflect the same amount. Published values of transducer stiffness are available from manufacturers, but they are highly dependent upon test conditions. Using an iterative approach and equations 2.1 and 2.3, the horn and base mass values can be calculated.
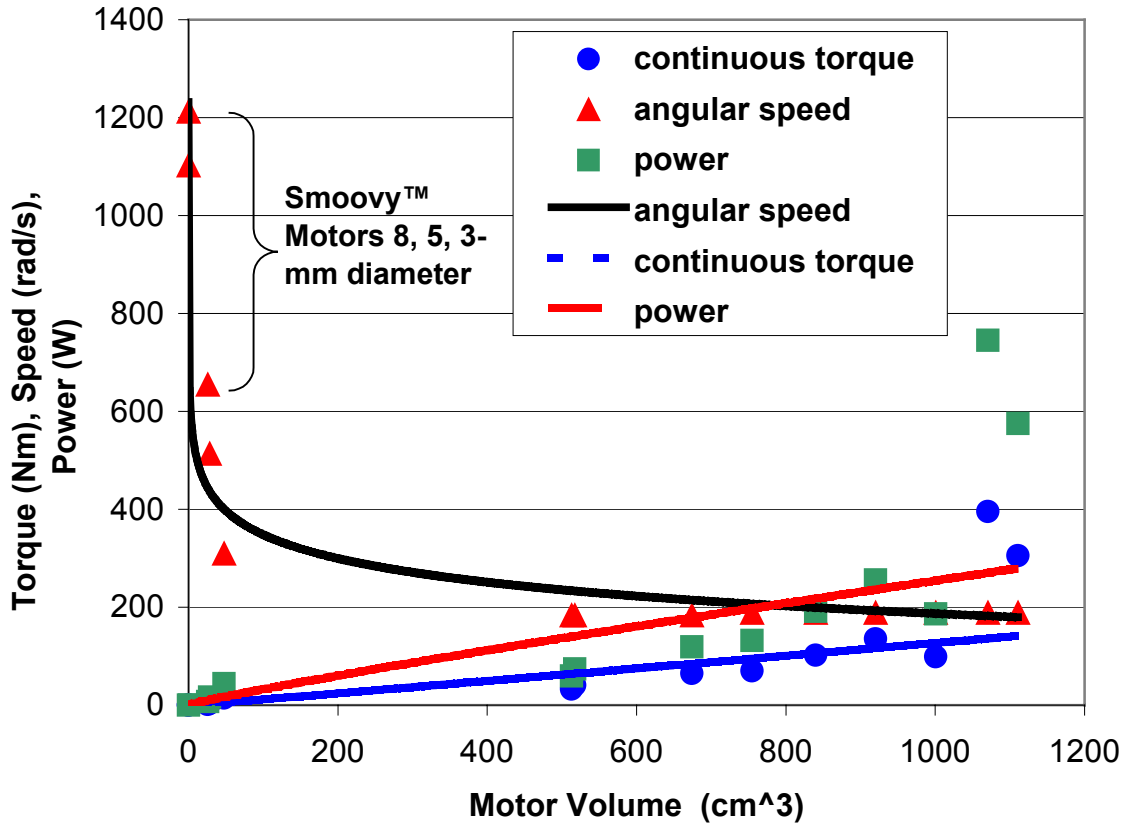
<u>Figure 2.8</u>. **Limited survey of EM motor performance vs. volume (DC motors distributed by McMaster-Carr Corporation, and miniature Smoovy™ motors with 8, 5, and 3-mm diameter) [60]**

When the resonator of a mode conversion USM is energized, a standing elastic wave develops. The standing wave is considered to be the superposition of two equal sinusoids traveling in opposite directions in time on a Cartesian *xy* coordinate plane within the medium [77]. The sinusoids have the following expressions:

$$y_a = A\sin\left(\left(\frac{2\pi x}{\lambda}\right) - (2\pi f t)\right)$$
$$y_b = A\sin\left(\left(\frac{2\pi x}{\lambda}\right) + (2\pi f t)\right)$$

(2.4)

where *f* denotes frequency, *t* is time, λ is wavelength as in the previous segment, and *A* is the amplitude [77]. Adding equations 2.4 and applying trigonometric identities yields the superposed waveform:

$$y = \left(2A\sin\left(\frac{2\pi x}{\lambda}\right)\right)\cos(2\pi f t)$$

(2.5)

19

Figure 2.9 depicts Sashida's model of the rotor/stator interface of the mode conversion USM as relayed by Uchino [88]. Imagine a simplified version of the L/T coupler of the USM shown in Figure 2.5 angled by an amount θ and pressed against a *xy* plane representing the rotor [88]. Here, the L/T coupler is represented as a long, slender beam that deflects when pressed into the rotor face with an initial interference, Δ_i [88]. The deflection is assumed small in comparison to the coupler's length. For simplicity, assume the resonator produces the sinusoid in the horizontal *x* direction given by $A_0\sin(2\pi ft+\alpha)$, and that the natural frequencies of the resonator and coupler are well matched [88]. The resulting horizontal and vertical displacement locus of the L/T coupler tip describes an ellipse denoted by the following:

$$x = A_0 \sin(2\pi ft + \alpha)$$
$$y = A_1 \sin(2\pi ft + \beta)$$

(2.6)

where α and β are phase angles [88]. This relationship is plotted in Figure 2.10. Upon inspection, it is
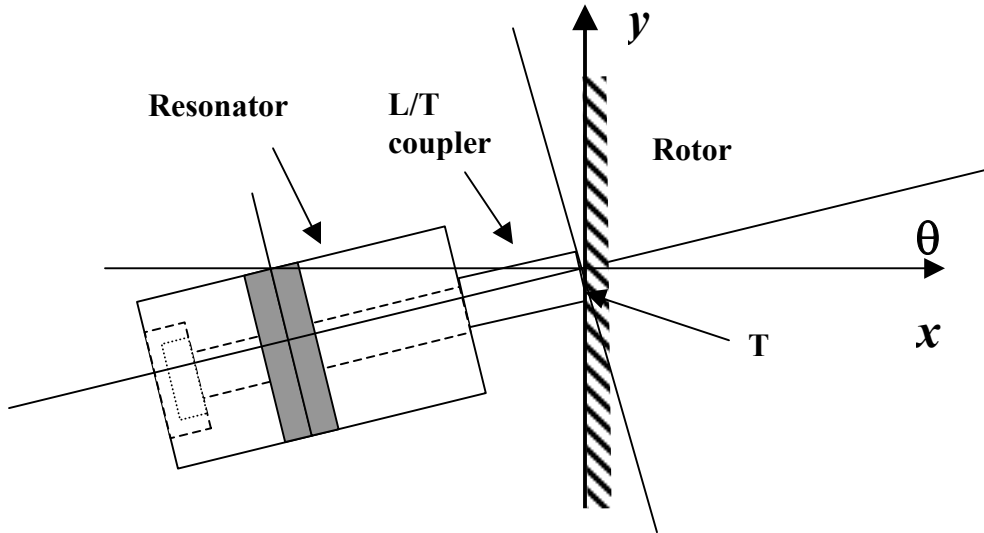
Figure 2.9. **Standing wave USM rotor/coupler contact model [88]**

20
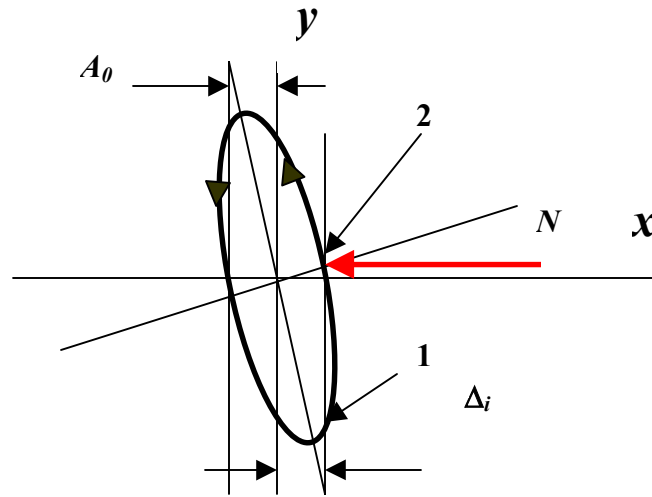
Figure 2.10. **L/T coupler tip point displacement locus [88]**

evident that the rotor exerts a normal force N on the coupler as it passes through segment 1-2 only. Thus, the frictional torque on the rotor is *not* constant during the operational cycle. It is also apparent that the greater the interference Δ_I between coupler and rotor, the larger the normal force N, assuming the rotor and resonator are constrained against motion in the positive and negative x directions, respectively. Although the wave mechanics are simplified, this model and the associated observations provide insight into designing for optimal torque. The next segment reports associated research that investigates vibratory coupler design.

Figure 2.11 illustrates examples of vibratory couplers that have been modeled and prototyped in the last decade. Figure 2.11 (b) is the so-called "windmill" configuration created by Koc, Bouchilloux, and Uchino (Koc, Bouchilloux, and Uchino) [48]. It has been used in mode conversion USM's as small as three millimeters in diameter [48]. When bonded to a ring-shaped transducer, the structure resonates in the radial direction, at a frequency that is matched to the bending mode shape of the four arm projections [48]. The radial displacement, coupled with the bending action of the arms, creates the required elliptical displacement locus at the tips [48].

When a conical projection of the output shaft is pressed against the tips, shaft torsion occurs. The dynamic tip response was verified and plotted using finite element analysis with free and constrained boundary conditions applied at the tips (Koc, Xu, and Uchino) [49]. Figure 2.12 depicts a cross-sectional view of the prototype USM, and a free body diagram of the stator arm. The tangential and normal force components

<div align="center">(a)   (b)   (c)</div>
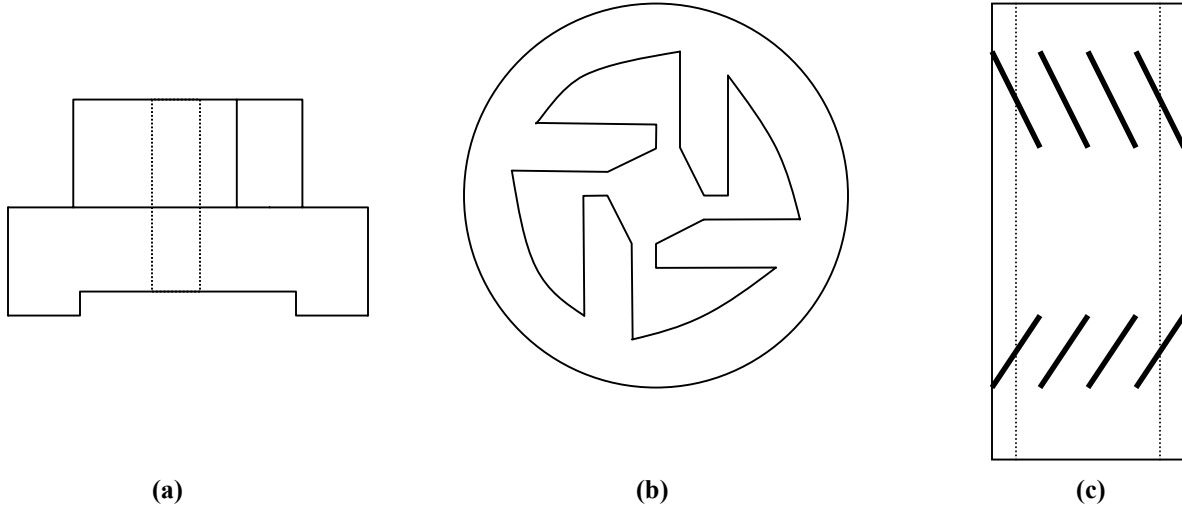
<u>Figure 2.11</u>. **Vibratory coupler prototypes: a.) Kumada, [52] b.) Koc, Bouchilloux, and Uchino; [48] c.) Tsujino, Ueoka, Otoda, and Fujimi [86]**

transmitted from the stator tip to the rotor as shown in Figure 2.12 (b) are expressed as [48]:

$$T_2 = F_A \cos\varphi \sin(\theta + \varphi)$$
$$N_2 = F_A \cos\varphi \cos(\theta + \varphi)$$

<div align="right">(2.7)</div>

where F_A is the dynamic radial force due to transducer displacement, θ is the angle between the center O and the base of the arm, and φ is the angle between the base and the rotor contact point. Normal force N_2 is resolved in the vertical plane depicted in Figure 2.12 (a) by the following:

$$N_3 = F_A \cos\varphi \cos(\theta + \varphi)\cos\alpha$$

<div align="right">(2.8)</div>

where α is the angle of the rotor cone [48]. As normal force N_3 determines the magnitude of frictional traction on the rotor, inspection of Figure 2.12 (a) also suggests that it is balanced in the vertical plane by pre-load force F_N. Considering static equilibrium of the rotor in the vertical direction yields:

$$F_N = n N_3 \sin\alpha$$

<div align="right">(2.9)</div>

were n denotes the number of arms in contact with the rotor. Static torque is expressed in terms of the pre-load by the following [48]:

$$\tau_s = \mu_s \frac{F_N}{\sin\alpha}\left(\frac{R_0 + R_i}{2}\right)$$

<div align="right">(2.10)</div>
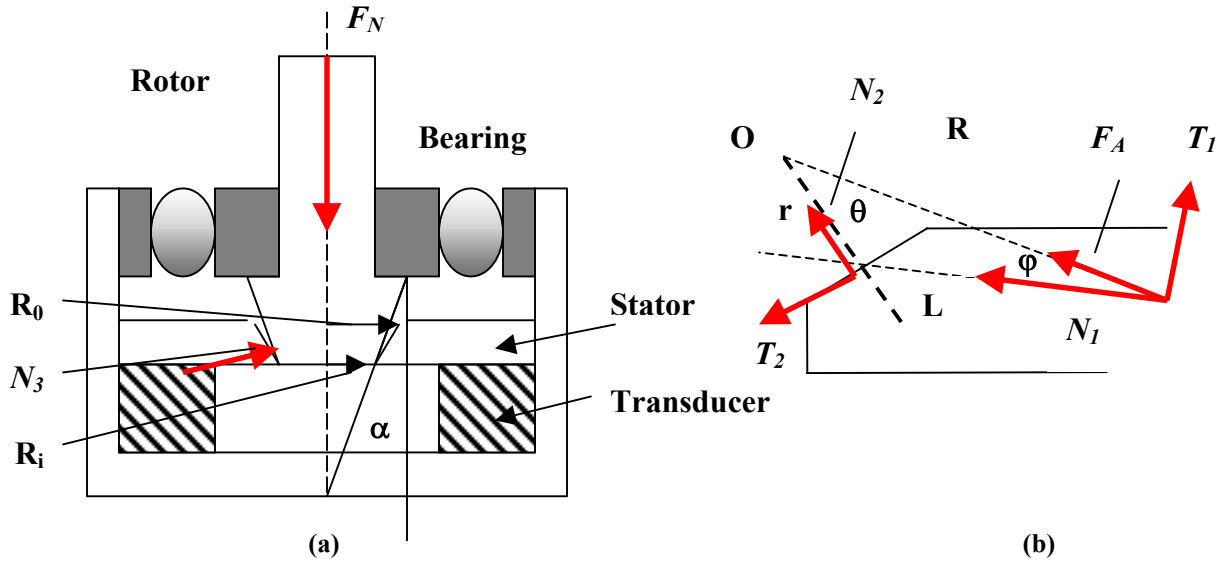
Figure 2.12. **a.) Windmill USM prototype cross section, [48] b.) Stator arm free body diagram (top) [48]**

where μ_s is the coefficient of static friction between rotor and stator. Figure 2.11 (c) illustrates the L/T coupler reported by the Tsujino group (Tsujino, Ueoka, Otoda, and Fujimi) [86]. This coupler outputs torsoinal vibration by virtue of sets of angled slits arranged about its circumference [86]. Unlike the windmill coupler, this device converts longitudinal displacement to an elliptical profile at the output face of the cylinder [85]. Although little static or dynamic modeling is offered, this development is significant in that prototype USM's using 60-mm diameter versions of the coupler yielded static torques in excess of 20 Nm [85]. Finite element models of the interaction between rotor and stator that predict the performance of USM's are offered by Ragulskis (Ragulskis, Bansevicius, Barauskas, and Kulvietis) [72]. A specific formulation is discussed in the following segment.

Finite element analysis is used extensively in USM research, mainly for modeling the dynamic response of the stator under harmonic excitation. Notable contributors include Tonshoff and Stegmann; Dong, Wang, Shen, and Li; and Koc, Xu, and Uchino [83, 20, 49]. The work of Ragulskis is significant since it presents a general dynamic finite element model of the contact between rotor and stator [72]. First, the finite element model generates performance metrics that are directly related to the input parameters [72]. The performance formulas listed below pertain to continuous motion rotary USM's, operating in the steady state,

and driven by a single, continuous, harmonic signal [72]. According to these assumptions, the average angular velocity of the rotor is defined as:

$$\overline{\omega} = \frac{1}{T}\int_0^T \omega \, dt \tag{2.11}$$

where ω is the angular velocity, and T is the period of vibration [72]. Average (continuous) torque is given by:

$$\tau_c = \sum_i \frac{R^i}{T}\int_0^T P_1^{ABi} \, dt \tag{2.12}$$

where R^i is the radius of the rotor between contact element i and the axis of rotation, and P is the component of the nodal contact force relative to the tangential direction in the local coordinate system. Superscript AB indicates force acting from member A to member B at node i [72]. Pre-load between rotor and stator is expressed as:

$$F_N = \frac{1}{T}\int_0^T P_3^{ABi} \, dt \tag{2.13}$$

Here, subscript 3 refers to the vertical direction of the local coordinate system [72]. Efficiency is related by the following:

$$\eta = \frac{A_u}{\left(A_u + A_T + A_e + A_h\right)} \tag{2.14}$$

Useful work from the USM in a single period, denoted by A_u, is written as follows:

$$A_u = \int_0^T \tau_c \omega \, dt \tag{2.15}$$

Work due to tangential (friction) forces in the same period is:

$$A_T = \int_0^T \left(P_1^{BAi}\left(R^i\omega - \delta_1^{bi} - [a]_1^i U^{Ai}\right) - P_2^{BAi}\left(\delta_2^{bi} + [a]_2^i U^{Ai}\right)\right) dt \tag{2.16}$$

where δ represents displacement of a node within body A or B along a specific axis relative to the local coordinate frame. Applying the coordinate transformation matrix $[a]$ relates matrix δ to corresponding displacements in the global coordinate system [72]. The quantities A_{el} and A_h refer to the work of electricity,

and dissipated heat, respectively. Figure 2.13 illustrates the finite element model of a rotary USM where interaction between rotor and stator occurs at discrete points through contact elements [72]. Each contact
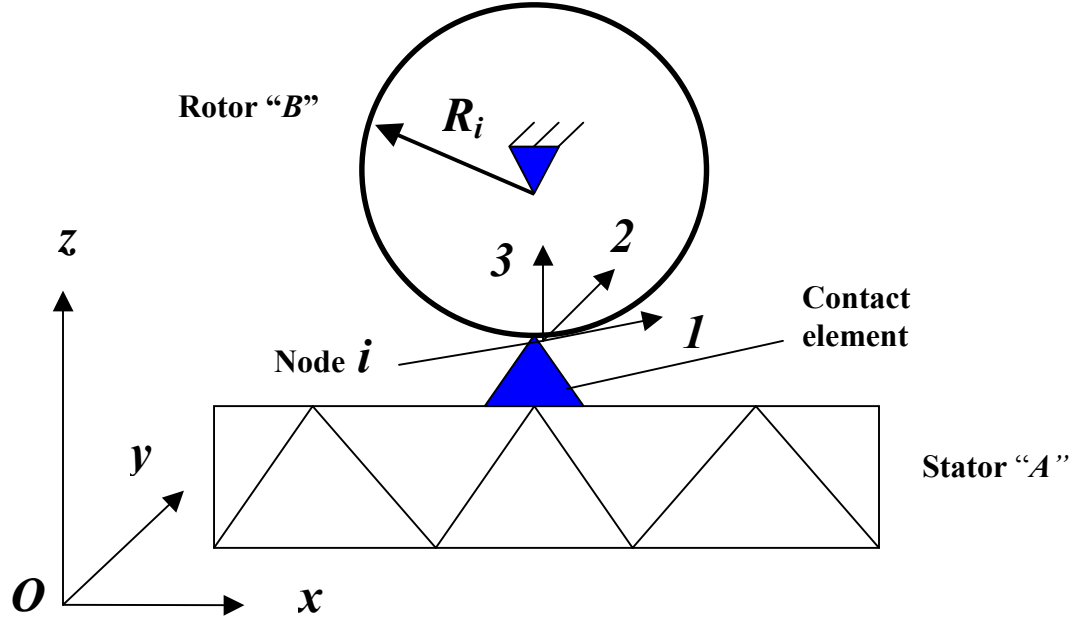
Figure 2.13. **FE model of a rotary USM with discrete contact between rotor and stator [72]**

element has parallel stiffness and damping components in local coordinate directions *1* and *3*, the normal and tangential directions with respect to the rotor surface. Local coordinate direction *2* meanwhile is parallel to the axis of rotation of the rotor. Additionally, the model assumes the rotor is rigid, and its radius varies through its thickness [72]. Furthermore, assuming the length of the contact element is relatively small, we may conclude:

$$P^{BAi} = -P^{ABi} \tag{2.17}$$

The displacements in the local coordinate frame should satisfy the following relationship [72]:

$$[K_C]\delta^{bi} + [C_C]\dot{\delta}^{bi} = P^{BAi} \tag{2.18}$$

where K_C and C_C are the matrices of stiffness and damping of the contact element at node *i*. They are written in matrix form as follows:

$$K_C = \begin{bmatrix} k_{c1}^i & 0 & 0 \\ 0 & k_{c2}^i & 0 \\ 0 & 0 & k_{c3}^i \end{bmatrix}$$

$$C_C = \begin{bmatrix} c_{c1}^i & 0 & 0 \\ 0 & c_{c2}^i & 0 \\ 0 & 0 & c_{c3}^i \end{bmatrix}$$

(2.19)

Matrices P^{Bai} and δ^{bi} are written as:

$$P^{BAi} = \begin{bmatrix} P_1^{BAi} \\ P_2^{BAi} \\ P_3^{BAi} \end{bmatrix}$$

$$\delta^{bi} = \begin{bmatrix} \delta_1^{bi} \\ \delta_2^{bi} \\ \delta_3^{bi} \end{bmatrix}$$

(2.20)

Nodal displacements and forces are related to the global coordinate system using the transformation matrix $[a]$ [72]. Thus:

$$\delta^{bi} = [a]^i U^{bi}$$
$$\delta^{Ai} = [a]^i U^{Ai}$$
$$F^{ABi} = [a]^i P^{ABi}$$
$$F^{BAi} = [a]^i P^{BAi}$$

(2.21)

With these parameters defined, the equations of motion of the system are [72]:

$$[M_A]\ddot{U}^A + [C_A]\dot{U}^A + [K_A]U^A = F^A + \sum_i \begin{bmatrix} 0 \\ \cdot \\ F^{BAi} \\ \cdot \\ 0 \end{bmatrix}$$

$$J\ddot{\theta} + c\dot{\theta} = -M_C \operatorname{sgn}(\dot{\theta}) + \sum_i R^i P_1^{ABi}$$

(2.22)

The first equation of the system 2.22 describes the dynamic action of the stator with respect to the global coordinate frame. It is assigned mass, damping, and stiffness matrices M_A, C_A, and K_A, respectively. Vector F_A accounts for the nodal forces generated within the stator by the deformation of the transducer [72]. The last

26

term on the right hand side represents a summation across the contact elements of contact force vectors acting from the rotor (body *B*) to the stator (body *A*) [72]. The response of the rotor is captured by the second equation 2.22, where *J* is the polar mass moment of inertia, *c* denotes a damping coefficient, and θ represents the angular coordinate [72]. Counterclockwise rotation is assumed positive. On the right hand side, M_C is a resistance (frictional) torque that is depends on the sign of the rotation [72]. Supplementing equations 2.17, 2.18, and 2.21, the following boundary conditions apply:

$$
\begin{aligned}
&1\!\left(\delta_3^{Ai},\delta_3^{bi},G^i,P_3^i\right)\!\left(-[a]_3^i\left(U^{Ai}\right)-\delta_3^i+G^i\right)=0 \\
&1\!\left(\delta_3^{Ai},\delta_3^{bi},G^i,P_3^i\right)\!\left(\delta_3^{bi}k_{c3}^i+\delta_3^{bi}c_{c3}^i\right)=P_3^i \\
&P_3^i\mu_k\,\mathrm{sgn}\!\left(R^i\dot\theta-[a]_1^i U^{Ai}-\delta_1^{bi}\right)=P_1^i \\
&P_3^i\mu_k\,\mathrm{sgn}\!\left(-[a]_1^i U^{Ai}-\delta_1^{bi}\right)=P_2^i
\end{aligned}
\tag{2.23}
$$

where μ_k represents the coefficient of kinetic friction, and G^i denotes the length of the *i*th contact element [72]. The unit function $1\!\left(\delta_3^{Ai},\delta_3^{bi},G^i,P_3^i\right)$ in the boundary conditions 2.23 describes whether or not the rotor and stator are in physical contact at node *i*. It returns a one or a zero if the following are true [72]:

$$
1\!\left(\delta_3^{Ai},\delta_3^{bi},G^i,P_3^i\right)=\left\{\begin{aligned}&1,\left(-\delta_3^{Ai}-\delta_3^{bi}+G^i<0\right)\bigcap\left(P_3^i<0\right)\\ &\qquad\qquad 0\end{aligned}\right\}
\tag{2.24}
$$

Additional considerations, which are out of the scope of this section, are required to implement the computational discrete contact model. These introduce alternative conditions that are needed to circumvent the signum function (*sgn*). Moving beyond the analyses reviewed thus far, Ueha and Tomikawa have published a quantitative algorithm that facilitates the design of USM's for maximum torque and velocity [87]. Torque optimization is described below.

Ueha and Tomikawa developed a design algorithm based upon their hybrid transducer USM [87]. It is a multiple transducer, standing wave USM whose construction is similar to that depicted in Figure 2.3. A review of the algorithm reveals some practical tools that are useful for optimization of similar, single transducer constructions. The design algorithm for the hybrid transducer USM is based upon an equivalent circuit model of the motor, one that represents the conversion of torsional vibration of the stator into frictional torque at the rotor [87]. Figure 2.14 exhibits the equivalent circuit. Independent transducers in the stator portion produce torsional and longitudinal vibration with very little coupling. The left portion of Figure 2.14 is the circuit
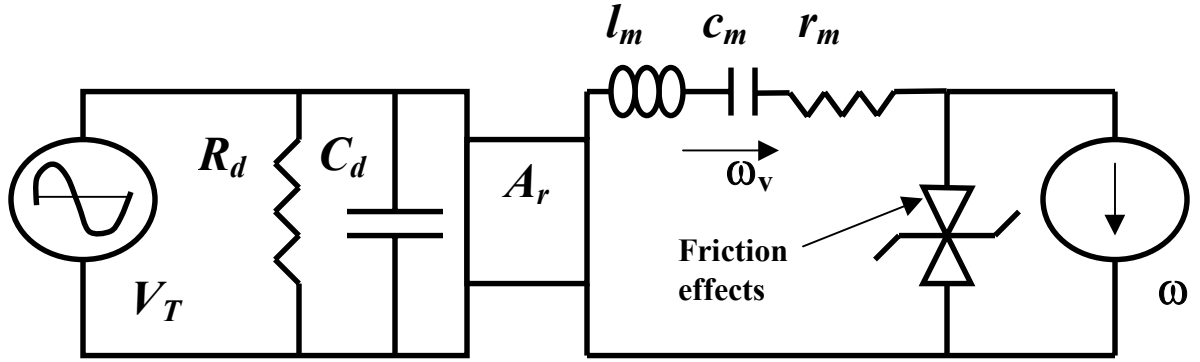
Figure 2.14. **Hybrid Transducer USM equivalent circuit model for electromechanical conversion [87]**

representation of the torsional portion of the resonator. It is driven by a voltage source V_T in the form of a cosine wave. Quantities R_d and C_d account for dielectric loss and damped capacitance in the torsional transducer [87]. On the right side of Figure 2.14, the mechanics of the rotor are modeled. Tandem Zener diodes approximate Coulomb friction at the rotor/stator interface. Conceptually, if rotor velocity is analogous to current, and torque to voltage, the rotor is stationary at torques greater than $-\tau_z$ (the "threshold torque"), and less than $+\tau_z$. In all other regions, the rotor operates, and is depicted as a current source with magnitude ω. It follows that slip between rotor and stator is defined as the difference between the angular velocity of the rotor and that of the torsional vibration ω_V, and the instantaneous torque produced by the rotor varies accordingly [87]. Components l_m, c_m, and r_m constitute the rotor moment of inertia, torsional stiffness, and mechanical loss. In practice, reactive elements l_m, and c_m are neglected [87]. Electromechanical transfer function A_r joins the two halves of the circuit [87]. Motor performance can be calculated using the equivalent circuit model with the understanding that the elliptical displacements of the stator will cause a periodic fluctuation in the instantaneous magnitude of pre-load f_N [87]. A simple approximation is to assume the instantaneous pre-load varies sinusoidally, and ϕ_c marks the fraction of the period where rotor and stator are in contact [87]. Consider the case when ϕ_c is less than 2π. It follows that instantaneous pre-load is written as:

$$f_N = \begin{cases} \beta\left(\cos at - \cos\left(\dfrac{\phi_c}{2}\right)\right), \left(0 \le at \le \dfrac{\phi_c}{2}, 2\pi - \dfrac{\phi_c}{2} \le at \le 2\pi\right) \\ 0, (no\ contact) \end{cases} \qquad (2.25)$$

where β describes a constant amplitude. It is reasonable to conclude that the average of the time-varying pre-load is equal to the static pre-load, F_N. Substituting this result into 2.25 yields an expression for the amplitude [87]:

$$\beta = \frac{\pi F_N}{\sin\dfrac{\phi_c}{2} - \dfrac{\phi_c}{2}\cos\dfrac{\phi_c}{2}} \qquad (2.26)$$

With the expressions for pre-load defined, equations for instantaneous (continuous) torque follow. When slip between the rotor and stator is zero, continuous torque is written as:

$$\tau_c = A_r V_T \cos at - r_m \omega \qquad (2.27)$$

If drive voltage V_T is low, the second term in 2.27 may be omitted [87]. In the case where positive slip occurs, i.e. the velocity of the torsional vibration is greater than the velocity of the rotor, continuous torque becomes:

$$\tau_c = \mu_k f_N R \qquad (2.28)$$

where μ_k is the coefficient of kinetic friction between contacting surfaces, and R is the mean radius of the contact area. Conceptually, Equation 2.28 indicates that for the short time the rotor and stator are in contact in any given period, the torsional wave will "pull" the rotor along with a frictional torque of magnitude equal to $\mu_k f_N R$. Conversely, if the rotor velocity is greater than that of the torsional vibration, slip is negative, and the right side of Equation 2.28 changes sign, suggesting a braking effect on the rotor [87]. A calculation of maximum static torque is realized by the following procedure. Let ϕ_c assume a target value of π. Thus, for relatively low drive voltage, static torque is the time average of the instantaneous torque given by 2.27. This result is written as follows [87]:

$$\tau_s = \bar{\tau}_c = \frac{A_r V_T}{\pi}\sin\frac{\phi_c}{2} \qquad (2.29)$$

As drive voltage is increased, static torque will rise proportionally to a limit determined by the following:

$$\tau_s = \mu_k F_N R \qquad (2.30)$$

Ueha and Tomikawa propose the following design procedure. It is based on the previously described model [87]:

- Assign a static torque limit, a drive voltage, and a USM radius that leads to mean contact radius, R.

- Calculate the required static pre-load from Equation 2.30 given the coefficient of kinetic friction for the materials selected.

- Determine ϕ_c using F_N and the parameters of the longitudinal component of the resonator design.

- Calculate the required electromechanical transfer function A_r from 2.29.

- Lastly, use A_r to specify the design of the torsional component of the resonator.

Successfully applying this algorithm to single transducer mode conversion USM's may require an investigation to determine how the action of the vibratory coupler affects parameters such as the contact duration, ϕ_c. In other words, the Ueha-Tomikawa model yields different results in systems where the rotor and stator come out of contact during the period of the input signal than in cases where contact is continuous.

The literature reviewed in this segment underscores the exhaustive nature of research and development in the field of rotary ultrasonic motors. However, comparatively little work has been established focusing on torque optimization of single transducer USM's with vibratory couplers. Furthermore, few studies consider the impact of miniaturization on USM performance. A brief review of physical analyses considering scale relationships in the field of motor design is discussed in the next segment.

2.3 Physical Analysis Considering Scale Relationships

2.3.1 Introduction and Overview of Scale Modeling Theory

Creating robust mechatronic systems at unprecedented miniature scales implies that engineers must assemble and draw upon a new body of knowledge that includes an understanding of the changes in fundamental physical phenomena with size. Feynman stresses this point in his discussion of the engineering and manufacturing challenges associated with creating micro and nano-scale products [32]. Although it is true that in the past, engineers creating very large structures such as dams and offshore oil drilling platforms have been forced to address scale effects, it was in the opposite sense than they are faced with today. The most recent and perhaps the most widely known experience with the physical effects of miniaturization is in the field of microelectronics. In the past three decades, many resources have been devoted to predicting the performance implications of ever-smaller gate oxide thickness in transistors. The 20th century saw rapid development and deployment of three principal mathematical resources to aid technologists in designing products on extreme scales. These resources include Geometric Transformations and Dilation, Similarity Theory or Similitude, and Dimensional Analysis, which is also a fundamental part of Similarity (Baker) [4]. Computer aided design and

associated computer graphics software utilize the mathematics of Geometric Transformations and Dilations to accurately and efficiently transform, scale, and redisplay objects in three-dimensional space (Mortenson) [58]. Similarity theory is highly effective in designing for scales that make prototype evaluation impractical or impossible. Rooted in Dimensional Analysis complimented by the Buckingham Pi Theorem (a dimensional theory developed in 1914 by Edgar Buckingham), engineers may use Similarity methods to test conveniently sized physical models to predict prototype performance [4]. Moreover, in the analysis of systems where a theoretical background is not available, or is too complex, non-dimensional parameters called Pi terms may be derived using the Buckingham Pi Theorem [4]. Experiments are subsequently devised to show meaningful relationships between Pi terms, leading to valuable insight into system behavior (Munson, Young, and Okiishi) [62]. Sedov and Langhaar contributed to the predominant area for the application of Similarity theory: Fluid Mechanics (Sedov) [76], (Langhaar) [53]. Consequently, Similarity methods in scale modeling have been used extensively in the petroleum and aerospace industries over the past fifty years. Applications are not limited to this discipline, however. Goodier et al. demonstrated Similarity methods in solving problems in Elasticity in 1944 [4]. In the field of life sciences, McMahon and Bonner used this approach to study the effects of size on skeletal mechanics [56]. In the context of miniaturization, Dimensional Analysis fundamentally involves the study of physical systems in terms of dimensionless scale factors (Skoglund) [79, 53, 4]. This approach is used widely in recent publications concerning scale behavior of actuators and motors, and it is implemented in this program to evaluate the effects of size on piezomotor performance.

2.3.2 Studies of Actuator and Motor Performance vs. Size

Detailed dimensional analyses that describe the performance of electromagnetic motors with size have been published (Wallace and Selig) [95]. To a lesser degree, other researchers have applied this method to piezoelectric actuators and ultrasonic motors. The following segment illustrates which actuation principles scale favorably to the micro domain. First, a brief synopsis of some basic concepts of Similarity and Dimensional Analysis are listed below (see Baker) [4].

Many of the arguments that impact the size on motors are founded on the derivation of geometric scale factors. To understand scale factors, we must first review some of the attributes of similar systems. Figure 2.15 illustrates a simple example of a pair of right triangles. Imagine the leftmost triangle to be a conveniently sized

h_m

h_p
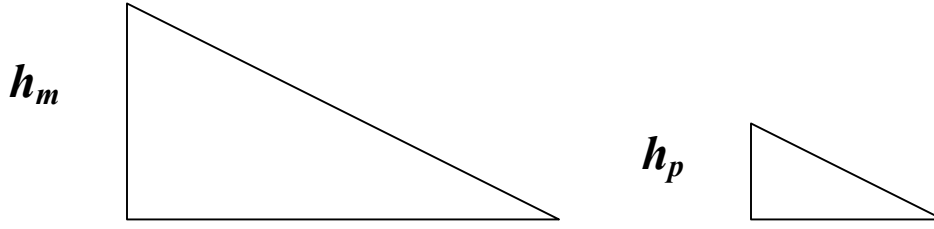
Figure 2.15. **Geometrically similar triangles**

model of the much smaller prototype at the right. Inspection of the figure indicates that dimensions h_m and h_p describe the height of corresponding sides, but their values are clearly not equal. These dimensions are thus considered *homologous* [4]. A scale factor may be defined as the ratio of the homologous dimensions as follows [53]:

$$s_h = \frac{h_m}{h_p} \qquad (2.31)$$

Since s_h involves the ratio of two lengths, it is non-dimensional. A powerful attribute of scale factors is that they permit comparisons that are independent of artifact-based systems of measure [4]. In addition to 2.31, scale factors s_b and s_{hyp} may be written which describe the ratios of the homologous dimensions of the base and hypotenuse, respectively. If s_h, s_b, and s_{hyp} are equal, the model is said to be geometrically similar to the prototype [4]. Note that other parameters such as force, time, or temperature may also be homologous, leading to other forms of similarity. Examples include kinematic, dynamic and constitutive (which involves homologous material properties) [4]. With the attributes of similar systems established, relationships between scale factors will now be explored. Consider Figure 2.15 with a set of geometrically similar circles substituted for the right triangles. Let s_r denote the scale factor for the homologous radii. Given that the area of a circle involves the square of the radius, it may be concluded that the area of a circle scales as s_r^2. This reasoning is applied repeatedly in the literature (Pisano) [69], (Trimmer and Jebens) [84, 95], to predict how forces and other physical quantities change with the size of a device.

Several notable papers establish scale factors to illustrate the impact of size on the effectiveness of electromagnetic motors [84, 95]. Trimmer and Jebens begin with an investigation of the impact of scale on

various forces, ultimately demonstrating the diminished effectiveness of electromagnetic motors as size approaches the micro scale [95]. Table 2.4 lists their findings on how a geometric scale factor *s* (similar to those discussed above) varies with respect to certain forces [84]. Supplementary information compiled by Pisano regarding geometric scale effects on the parameters of dynamic systems is also included [69]. For example, the force produced by a hydraulic actuator is determined in part by the area of the piston, a fact that is

Table 2.4 **Geometric Scale Factor Relationships**

Force	Varies As	If Linear Dimension Changes By A Factor Of:	Force Changes By A Factor Of:
Surface Tension	s^1	10	10
Hydraulic/Pneumatic/Pressurized Fluid Force or Muscle Force	s^2	10	100
Magnetics*	s^3, s^4	10	1,000;10,000
Dynamic Parameter	**Varies As**	**Depends On**	
Mass	s^3	Volume	
Spring Constant (cantilever beam)	s	Length, moment of inertia, Young's modulus	
Natural Frequency	s^{-1}	Spring constant, mass	
Viscous Damping	s^2	Velocity, area	
Harmonic Velocity	s^0	Natural frequency, displacement	
Harmonic Acceleration	s^{-1}	Natural frequency, displacement	
Harmonic Work Per Cycle	s^3	Force, displacement	
Harmonic Power	s^2	Force, velocity	
Kinetic Energy	s^3	Mass, velocity	
Potential Energy of a Linear Spring	s^3	Spring constant, deflection	

* Depending on current density model (discussed below)

affirmed by Pascal's Law [77]. Therefore, from the previous discussion, it is obvious that the force in this case will vary as s^2. Practically speaking, this relationship implies that if the radius of the piston is decreased by ten

times, the hydraulic force will decrease by a factor of one hundred [84]. The torque output of DC motors depends on the magnetic moment applied to the rotor by the stator. Consequently, they investigate size effects on magnetic force using the elementary model of adjacent current carrying conductors shown in Figure 2.16. The magnetic force on wire *b* is expressed as [84]:

$$F_b = \frac{\mu_0 L}{2\pi D} I_a I_b + \frac{I_b L}{2\pi D c^2} \left[\int \frac{\partial E}{\partial t} dA_c \right] \tag{2.32}$$

where I_a and I_b are the currents in the respective wires, A_c is their cross-sectional area, E is the electric field, c is a constant from Maxwell's equation, and μ_0 is the permeability of free space [84]. Current is the product of the current density J, and the cross-sectional area A_c. If current density is considered invariant with size, then the current scales with the area, which varies as s^2 [84]. Substituting the appropriate relationships for *L, D, I_a,* and
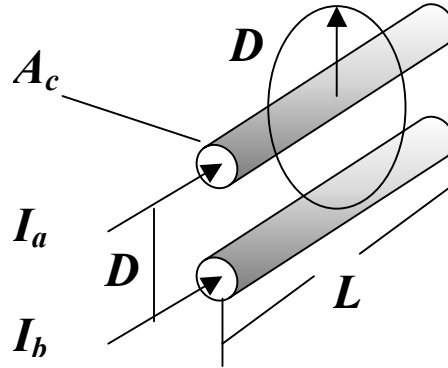
Figure 2.16. **Magnetic interaction of adjacent current-carrying conductors**

I_b in the first term of 2.32, the scale relationship for force is calculated as follows:

$$F_b = \frac{[s]}{[s]} [s^2][s^2] = s^4 \tag{2.33}$$

With these assumptions, a ten-fold decrease in the radius of the wire may reduce the magnetic force by ten thousand times! Using a similar procedure, the authors go on to show how electrostatic forces do not suffer the same fate as size approaches the micro domain [84]. Wallace and Selig move this analysis a step further by deriving advanced Dimensional Analysis to examine electromagnetic motor performance standards over a wide range of frame size.

Wallace and Selig recently published an investigation that applies an advanced dimensional analysis to determine the torque requirements for direct drive electromagnetic motors for microrobots [95]. Their technique involves creating a set of geometric transformations using Lie Algebra. Several relevant conclusions are made. First, as robotic linkages are reduced in size and mass, the required actuation torque at the joints decreases at a *greater rate* than the output of direct-drive electromagnetic motors. Thus, microrobots will have a greater capacity to do useful work. Second, the motor constant (defined as the constant of proportionality between input power and the square of the torque) decreases with size. This point is illustrated in their "motor universe" plot mentioned earlier [95]. In the process, a so-called *Q*-Factor is proposed as a useful tool for comparison of motors of vastly different sizes on the basis of motor constant. It is expressed as the following:

$$Q = \frac{K_M}{m^n} \tag{2.34}$$

where K_M is the motor constant, and m is the mass. This formula is essentially the slope of the motor universe plot with an important modification. The authors prove that the motor constant varies with a motor's geometric scale factor as $s^{5/2}$. Recalling that mass varies as s^3 and substituting these relationships into 2.34 yields:

$$Q = \frac{[s^{5/2}]}{[s^3]} = s^{5/6} \tag{2.35}$$

It follows that assigning exponent n in 2.34 a value of 5/6; Q becomes *scale-invariant* [95]. That is, it is compensated for differing motor size [95].

Other groups conducting electromagnetic motor scale research echo many of the notable findings discussed above. Rabinovici [71] focused on scaling of switched reluctance motors (SRM's) and found that torque varies as the cube of the rotor radius. Binns and Shimmin conducted a scale study of rare earth permanent magnet motors that also considered the effects of size on frame temperature (Binns and Shimmin) [8]. They discovered that in motors of this construction, torque is proportional to the product of the magnet volume and the rotor diameter raised to the ¼ power. The relationship accounts for a numerical estimate of the temperature rise in larger frames [8].

Dimensional analysis of piezoelectric transducers was performed by Shih, Shih, and Aksay [78] in 1997. They examined the effect of size on the axial displacement of RAINBOW and Moonie transducers [78]. Figure 2.17 depicts these devices. Referring to Figure 2.17 (a), the RAINBOW transducer, originally developed

by Haertling, is modeled as a composite piezoelectric/non-piezoelectric strip of thickness t, characteristic half-length L, and radius of curvature r [78]. The Sugawara Group's Moonie, shown in cross section in Figure 2.17 (b) realizes displacement amplification by means of a brass cap bonded to a transducer disk of diameter L. The assembly has an initial dome thickness of t [78]. In each instance a normalized axial displacement is defined as the dimensionless ratio of the axial displacement, Δh, and the respective thickness parameter t. Invoking the Theory of Elasticity to enforce stress-related boundary conditions in the RAINBOW model, the authors arrive at the following relation for normalized axial displacement and applied potential V [78]:

$$\frac{\Delta h}{t} = \frac{3L^2 d_{31} V}{16 t^3} \tag{2.36}$$

Piezoceramic

Non-piezoceramic

Brass cap

Piezoceramic

(a)   **(b)**
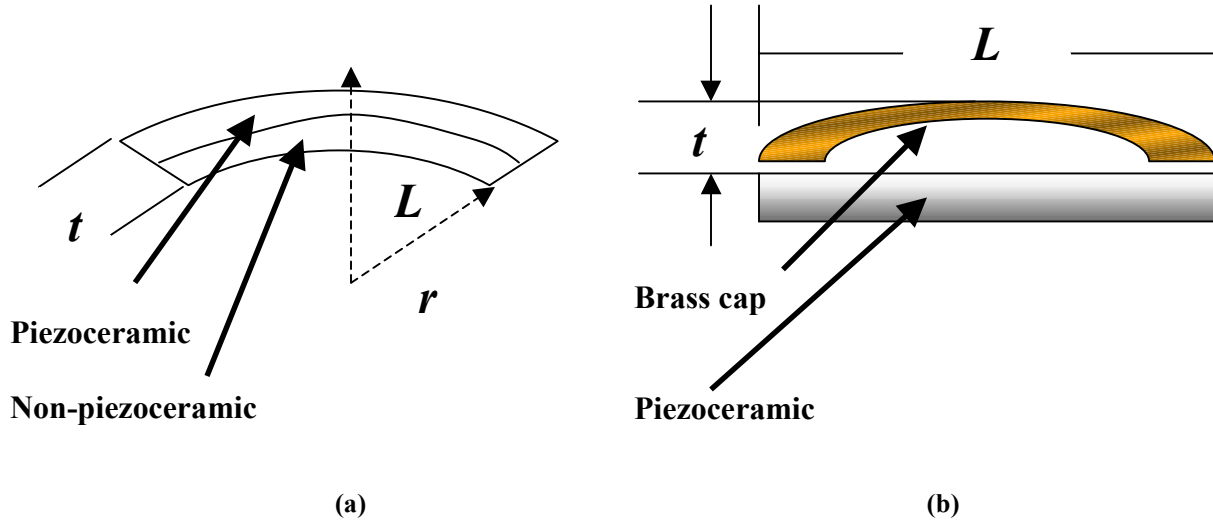
Figure 2.17. **Transducer models [78] a.) RAINBOW™, b.) Moonie™**

where d_{31} denotes the piezoelectric coefficient. Assuming geometric similarity holds for scaled versions of the RAINBOW, the geometric scale factors for length and thickness are equal to factor s as before. Substituting into 2.36 yields the following:

$$\frac{\Delta h}{t} = \frac{3[s^2] d_{31} V}{16 [s^3]} \tag{2.37}$$

Therefore, if potential is held constant, the normalized axial displacement varies as s^{-1}. By approximating the deformed geometry of the Moonie in the presence of and electric field E, the following relation holds [78]:

$$\frac{\Delta h}{t} = -\frac{d_{31}EL^2}{2t^2} \quad\quad\quad (2.38)$$

The same procedure generates the conclusion that for constant electric field, normalized axial displacement in the Moonie varies as s^0, indicating the relationship with electric field is scale invariant. Equations involving alternate parameters may yield different results.

Nakamura and Ueha illustrate graphically the variation in performance measures versus diameter and mass of their hybrid transducer USM (Nakamura and Ueha) [65]. In the course of the investigation, they constructed a series of prototypes ranging from eighty to five millimeters in stator diameter [65]. Static torque, no-load angular velocity of the rotor, and maximum output power were recorded. The following conclusions are noted:

- Static torque varies as the cube of the transducer and stator diameter [65]. Note this conclusion agrees with many of the findings concerning electromagnetic motors.

- The maximum pre-load that can be applied, is limited by material properties. It follows that pre-load varies as the square of the transducer and stator diameter [65].

- No-load angular velocity varies as the inverse of the transducer and stator diameter [65]. It follows that since maximum output power is the product of the static torque and no-load speed, it varies as the square of the diameter [65].

To date, no literature has been identified in which formal Dimensional Analysis procedures are applied in rotary USM size investigations.

A review of the literature presented in this segment reveals the opportunity for focused research using Dimensional Analysis to evaluate the effects of piezomotor size on performance. In regard to linear piezomotors using THUNDER™ stressed unimorph technology, an investigation of displacement, stiffness, and actuator type blocked force versus size may be unprecedented. Moreover, the current body of literature opens the possibility for a unique study of static torque performance with size in mode conversion, single transducer USM's. Particular items of interest include the impact of scale on frictional torque and steady state velocity.

Chapter 3

Design, Modeling, and Characterization of A Linear Piezomotor Based On Stressed Unimorph Technology

3.0 Introduction

Recent research activity at the N. C. State Center for Robotics and Intelligent Machines (CRIM) has focused on the development of miniature, autonomous mobile robots that mimic amphibian and insect species in size, locomotion, and intelligence. The cornerstone of this research is the study of direct drive mechanisms for energy storage and quick-release. Such mechanisms are inherent in jumping animals and insects, such as

locusts (Chapman and Joern) [13]. A major goal of the N.C. State research effort was the production of a cost-effective jumping robot that used a novel, high energy density, linear piezomotor designed specifically to store elastic energy and to release it quickly. For this reason, a linear piezomotor design using planar fabrication techniques from the semiconductor industry was adopted.   The reasons that support this decision are as follows: (1.) piezoelectric transducers were identified as having the force capability necessary to realize practical linear piezomotors for direct drive robotics, (2.) certain classes of planar piezoelectric transducers are supplied in a variety of geometric shapes and (3.), these transducers allowed the scalability issues to be addressed. Based on the results obtained, the principal contributions of this research include:

- Flexible pre-stressed unimorph piezoelectric transducers arranged in parallel and used in the novel linear piezomotor design generated greater than ten newtons of blocked force.

- Transducers mounted using non-constrained end conditions produced an amplified step displacement.

- A simple passive latching mechanism was implemented to control transducer displacement and linear piezomotor motion.

This chapter documents the design, modeling, and characterization of a prototype linear piezomotor referred to as the THUNDERWORM. Subsequent segments address the details of a model that attempts to quantify and ultimately predict displacement losses in the piezomotor mechanism.

3.1 THUNDERWORM Design

Many of the numerous piezoelectric linear motors reviewed and documented in Chapter 2, Section 2.2.2.1, embodied a stepper motor architecture for control. When this control architecture is coupled to a piezoelectric transducer acting as an extender, and to a set of active latches, a simple linear piezomotor is produced. Figure 3.1 illustrates a high-level control algorithm that can be used to actively control a linear piezomotor designed with two active latches and one transducer. The latches are arranged in the device such that the extender forces one portion of the linear piezomotor to move relative to the other. The resulting motion emulates that of an inchworm motion along a rod or fixed guide. To achieve active control, additional transducers would be required to operate the latches, adding complexity to the control circuitry (active control is not addressed in this dissertation). Moreover, the microscopic strains produced demand elaborate

1. Apply a potential voltage to activate the rear latch.

2. Remove the potential voltage from the front latch.

3. Apply a potential voltage to the piezoelectric transducers of the linear piezomotor.

4. Apply a potential voltage to activate the front latch.

5. Remove the potential voltage from the rear latch.

6. Allow the stiffness of the deflected piezoelectric transducer to return the transducer to its equilibrium position, producing forward motion of the linear piezomotor.

7. Repeat 1.

Figure 3.1. **High-level control algorithm for an "inchworm" linear piezomotor**

designs, requiring very fine tolerances. To avoid losses in mountings and ensure consistent end conditions, it would be necessary to mount the transducers within the latch housings. The N. C. State THUNDERWORM linear piezomotor did not require active latches. Adopting passive latches eliminated the need for active control, thereby simplifying the design. Figure 3.2 shows a THUNDERWORM prototype. Analogies of passive latches are currently utilized in consumer and industrial products (Drake) [21]. Review of references indicated that the motion of the passive latch in the so-called "non-binding" direction causes the pawl, seen in Figure 3.2 (opposite page), to naturally rotate to an open position, permitting the linear piezomotor to translate along the rod. Motion in the direction indicated is achieved with minimal friction, i.e., the least resistance to motion. The opposite is true when the latches operate in the reverse direction, here the latches bind, i.e., a high resistance to linear motion. When operating in the reverse direction, the pawl's rotation results in a braking action, interfering with the linear piezomotor's relative motion along the rod. A prototype linear piezomotor, designed and constructed using this principle of operation, contained twenty mechanically coupled THUNDER™ transducers and two passive latches (see Figure 3.2). Here, the THUNDER™ module *contracts* with the application of electric potential. With this action, the following simultaneous reactions occur: (1.) the rear latch moves ahead, and (2.) the forward latch binds, forming an anchor that pulls the linear piezomotor forward. Upon removal of the potential, the THUNDERS relax, and the module *expands,* pushing the forward

Passive latch pawl

THUNDER™ transducer module

Spring-loaded rod

Forward

Passive latch housing
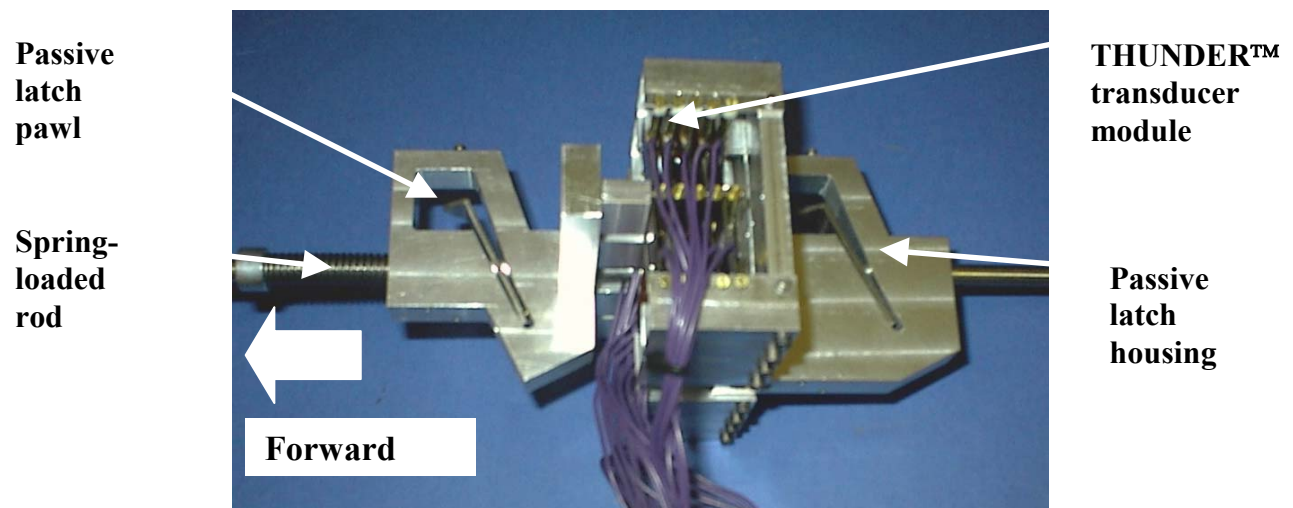
<u>Figure 3.2</u>. **Prototype THUNDERWORM linear piezomotor (showing THUNDERS mounted in parallel and passive latches)**

latch ahead. In this mode of operation, the rear latch binds and blocks a reactionary displacement, i.e., a linear translation to the rear. A mechanical analysis of the passive latch is detailed later in this chapter.

An apparatus was designed and constructed allowing a comprehensive set of experiments to be carried out on the THUNDERWORM, e.g. work was performed on a variable load provided by a set of calibrated coil springs. Moreover, the apparatus was easily retrofitted to accept subsequent design modifications. The apparatus was planned to be a standard vehicle for measuring the performance of prototype linear piezomotors. Since no standard test-bed or protocol appeared to be available, characterization tests were devised. Characterization required the following measurements to be recorded:

- Actuator velocity versus drive signal frequency

- Blocked force versus drive signal frequency

- Energy density of the prototype in joules per kilogram

To supplement the items listed above, the experimental setup also included a means of determining displacement losses in the passive latches under varying load. Linear Variable Differential Transformers (LVDT's) were attached to the body of the piezomotor to measure these losses. Lastly, energy density measurements were recorded to serve as a reference for comparison against other linear piezomotor technologies.

3.2 THUNDERWORM Test and Analysis

The THUNDERWORM system analysis has three distinct objectives. First, the equation for the effective stiffness of the linear piezomotor is derived, and associated stiffness relationships are detailed. Second, an empirical model is derived to predict the blocked force of the THUNDER™ transducer module separate from the latch assemblies. Lastly, the mechanics of the passive latch are studied to clarify their operating principle and predict their suitability for use in scalable linear piezomotors.

Figure 3.3 shows the design of an early linear piezomotor assembly; one that used four sets of five model 8R THUNDER™ transducers mounted in parallel. It should be noted that with this linear piezomotor assembly, the end conditions permitted both rotation and translation of the latches simultaneously. Experimental work carried out on the early prototype shown in Figure 3.3 showed that unrestricted end conditions yielded greater transducer flexural displacements (Mulling, Usher, Dessent, Palmer, Franzon, Grant, and Kingon) [61]. From equivalent dynamic systems theory, we know that the effective actuator stiffness, K_{eq}, is the sum of the stiffnesses of the individual THUNDERS working in parallel. This relationship is expressed as follows:

$$K_{eq}(V) = \sum_{i=1}^{n} k_i(V) \tag{3.1}$$

Stiffness k_i in the transducers is a function of the applied potential, V. This notation reflects the tendency for stiffness to increase with tensile stress in the stainless steel substrate as it flexes during actuation (Gere and Timoshenko) [31].

Early in this investigation, the N.C. State research team established that the blocked force of a THUNDER™ module can be classified in two ways: (1.) the *free mass* type, F_1, denotes a load level at which all flexural displacement of the module ceases, and, more importantly, (2.) the *actuator* type blocked force, F_2, causes static deflection equal to the no-load flexural displacement, δ_0 (Palmer, Dessent, Mulling, Usher, Grant, Eischen, Kingon, and Franzon) [67]. Consequently, a load of this magnitude reduces the elastic rebound of the module to zero with no net forward motion of the actuator. This quantity is the product of δ_0 and the zero-potential equivalent stiffness, $K_{eq}(0)$:

$$F_2 = \delta_0 K_{eq}(0) \tag{3.2}$$
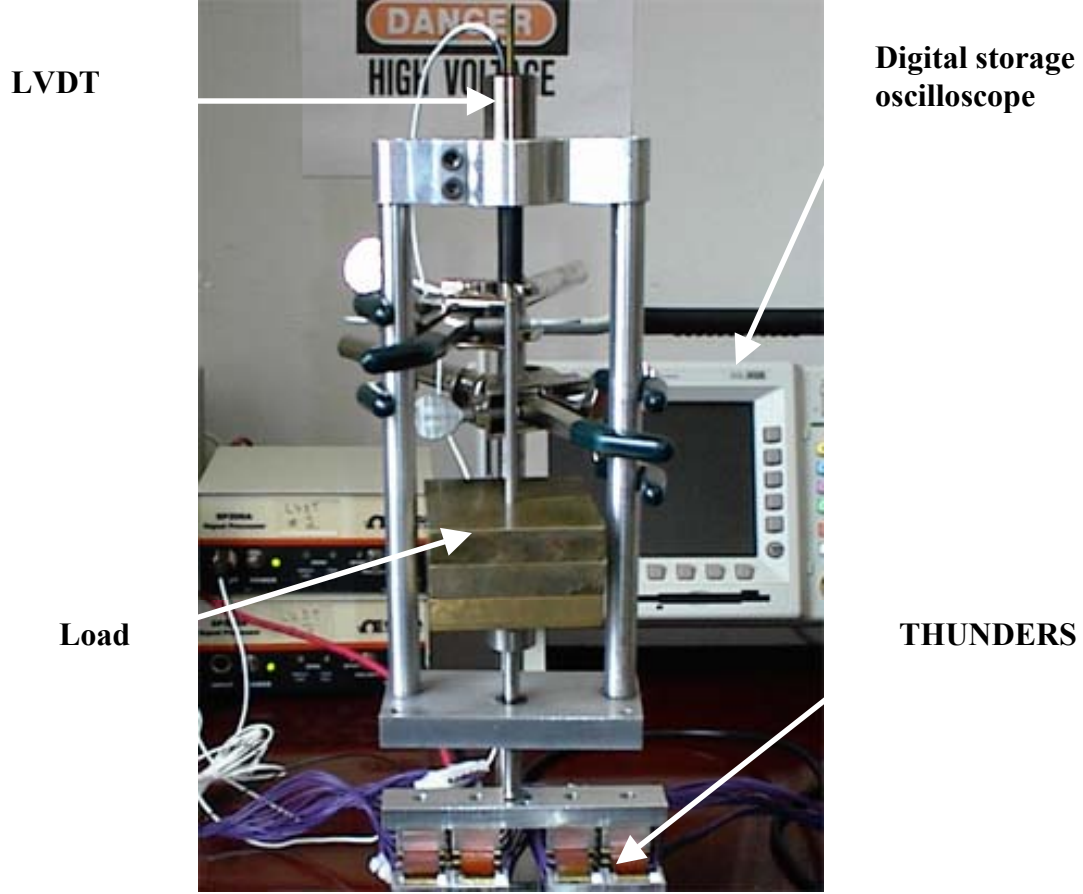
Figure 3.3. **Test rig showing a THUNDER™-based linear piezomotor transducer module under test [67]**

Blocked force types F_1 and F_2 are predicted empirically from the plot of upper-surface position versus load over a range of potential. This procedure is discussed in a later segment.

Figure 3.4 depicts the static equilibrium of the portion of the latch mechanism known as the pawl, at the onset of motion in the negative x direction as indicated. The force F due to the contact of the latch housing on the pawl, and its horizontal component (F_x) act at point C. Pre-load force Q, provided by a spring or elastic band, maintains the pawl in firm contact with the rod at an angle θ relative to the rod centerline. Contact of the edges of the pawl slot with the rod cause binding forces N and N', and corresponding frictional forces F_f and F_f', respectively. The weight of the pawl, W, acts at the centroid as indicated. Enforcing static equilibrium in the x and y planes yields equations for the binding forces as follows:

$$\sum F_x = \mu_s N + \mu_s N' - F \sin\theta + Q \sin\theta = 0 \qquad (3.3a)$$

$$\sum F_y = N - N' - W + F\cos\theta - Q\cos\theta = 0 \qquad (3.3b)$$

$$N = \frac{1}{2}\left[(F - Q)\left(\frac{\sin\theta}{\mu_s} - \cos\theta \right) + W \right]$$

$$N' = \frac{1}{2}\left[(F - Q)\left(\frac{\sin\theta}{\mu_s} + \cos\theta \right) - W \right] \qquad (3.3c)$$
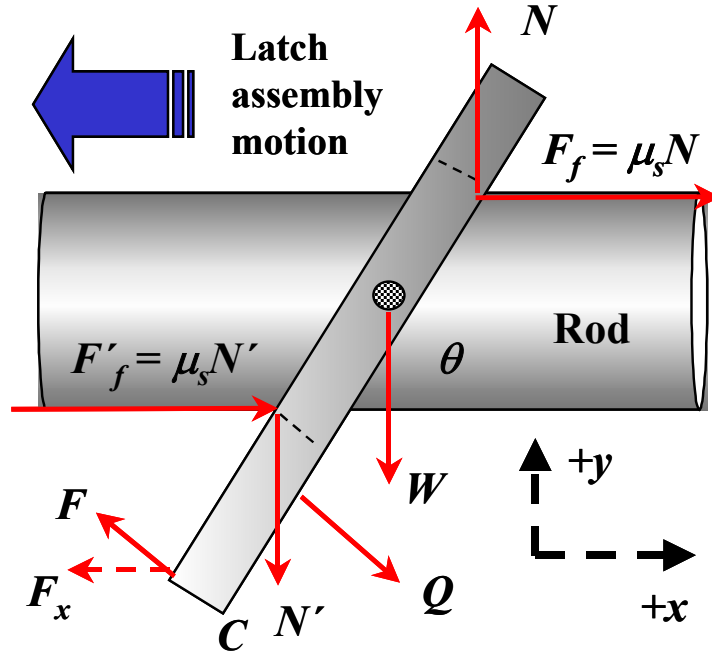
Figure 3.4. **Free body diagram of the impending motion of a passive latch pawl**

From Figure 3.4 it should be noted that the thickness of the pawl determines the horizontal distance between the

rod contact points. As the ratio of the pawl thickness to rod diameter approaches unity, the binding action

diminishes due to the deflection of the rod by these forces. Hence, if the pawl is too thick, the rod will simply

deflect away from the contact points, and motion will not be arrested as required. Displacement loss due to

relative motion between the rod and pawl in the direction indicated in Figure 3.4 is referred to as *back slip*.

Back slip losses are manifested by several factors, including kinetic friction, contact deformation at the

pawl/rod interface, pawl deflection, and deformation of the rod and latch housing. As load level approaches

44

that of the actuator blocked force, flexural displacement upon relaxation of the THUNDER™ module declines. Actuator failure ensues when the back slip equals the amount of flexural displacement.

3.2.1 Experimental Procedure

Three specific experiments were developed to allow us to evaluate THUNDERWORM linear piezomotors. The experimental test-bed provides data that: (1.) empirically models the THUNDER™ modules equivalent stiffness and actuator blocked force, (2.) is the measured velocity and, (3.) is the performance of the THUNDERWORM under load with associated latch slip losses, a variant of velocity measurement. In each of the experimental procedures the THUNDERWORM was controlled from a square wave input generated by a PC-based LABVIEW™ program.   The maximum control signal that was applied directly to the THUNDERWORM was 480 volts. During our testing we confirmed that unlike the mechanical analysis, the electrical load of the THUNDER™ module was capacitive.

The test apparatus for the THUNDER™ module characterization appears in Figure 3.3. Motion of the module is converted to a measurable voltage by a calibrated LVDT. Once the LVDT was interfaced to a virtual digital multi-meter in LABVIEW™, data was recorded. The stylus column of the test apparatus was loaded to a maximum of approximately 10 N, incrementally for each test. A sequence of voltages was then applied to the THUNDER™ module for each increment of the applied load. Stylus positions were measured from the LVDT at each voltage. Actuator blocked force was determined from the plot of stylus position versus load as shown in Figure 3.5 below. The slope of each series is the reciprocal of stiffness, or compliance. A difference in slopes indicates stiffness varying with potential.

A photo of the velocity and load test set up is displayed in Figure 3.6. During velocity testing, a digital storage oscilloscope captured the output of the LVDT, and plots it with respect to the drive signal.   The actuator's displacement per cycle with no applied mechanical load was again measured using the oscilloscope. Velocity is the product of the step displacement and drive signal frequency.   Load characterization involved compressing the calibrated coil springs with the THUNDERWORM linear piezomotor mounted in the test stand shown.   To monitor back slip, it was necessary to include a second LVDT in the experimental test rig. This second LVDT was used to capture the relative motion between the forward and rear passive latches. Oscilloscope traces of the LVDT signals were once again analyzed to determine the displacement of the latches
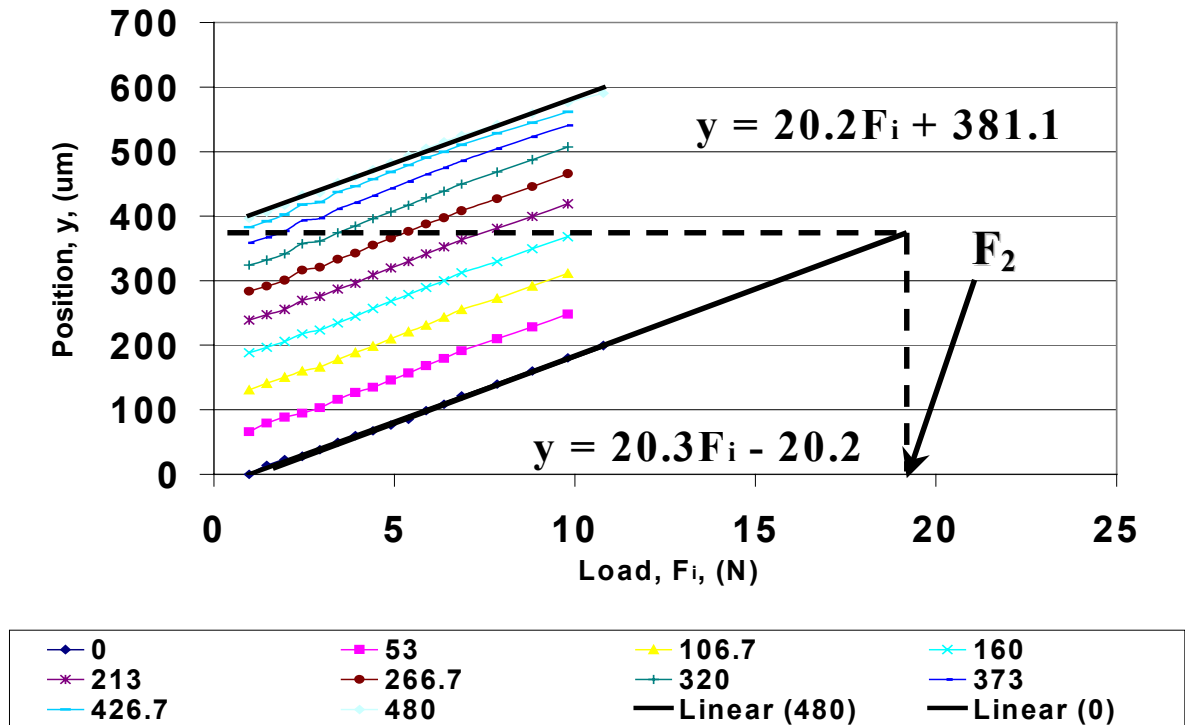
Figure 3.5. **Position vs. load and voltage for a module containing 20 type 8R THUNDERS [67]**
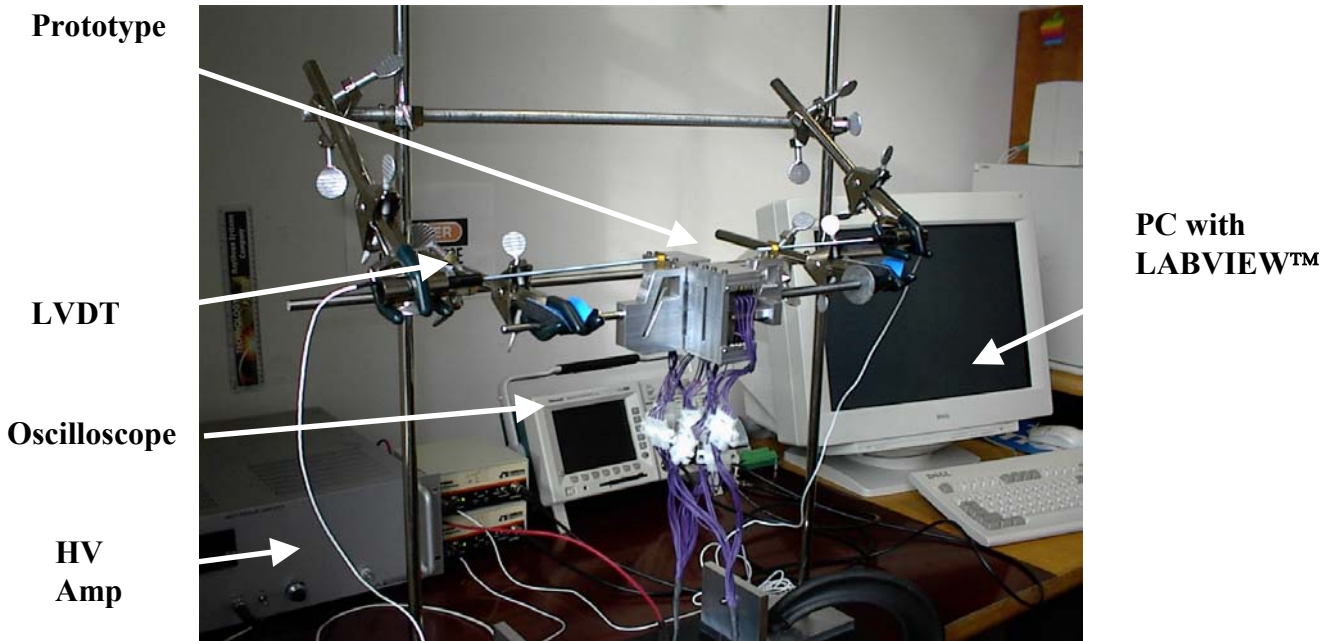
Figure 3.6. **Velocity and load characterization test apparatus [67]**

46

at various loads. This procedure was repeated to create plots of maximum force versus frequency, and latch slip versus load.

3.3 Results

The following segment summarizes the results of the THUNDERWORM characterization trials using the experimental procedures outlined above. The plot of empirical model results shown in Figure 3.5, in conjunction with Equation 3.2, predicts an actuator blocked force of 19.8 N, and a corresponding no-load flexural displacement of 401 microns (determined by the difference of the *y*-intercepts of the 0 and 480V trend lines). The stiffness of the THUNDER™ module was calculated at 0 volts and 480 volts which yielded a transducer stiffness of 49.2 N/mm and 49.4 N/mm respectively. At 2.5 N/mm and 2.7 N/mm, the stiffness values measured for a single 8R THUNDER™ are one twentieth that of the complete module. In addition to the velocity data, the characterization trial results include the observed maximum load of the prototype at various frequencies. This data was compared to the actuator type blocked force stated above. These results facilitate comparisons and discussion regarding differences in the actual and predicted force output. Loss mechanisms are quantitatively described.

A digital storage oscilloscope captured the output of a single LVDT shown in the velocity and load test apparatus (see Figure 3.6). This displacement output signal was plotted with respect to the drive signal. The step displacement per cycle of the actuator, with no applied mechanical load, was measured directly from the oscilloscope. The measurement of velocity was also obtained from the oscilloscope, since velocity is the product of the step displacement and drive signal frequency.

Load characterization of the THUNDERWORM involved compressing calibrated coil springs that were mounted onto the test-bed as indicated in Figure 3.6. To monitor back slip, a second LVDT was mounted onto the test-bed to capture the relative motion between the forward and rear latches. Analysis of the oscilloscope traces of the LVDT signals determined the displacement of the latches at various loads. This procedure was repeated to create plots of maximum force versus frequency, and latch slip versus load. The following segment summarizes the results of the THUNDERWORM characterization trials using the experimental procedures outlined here.

A plot of no-load velocity versus drive signal frequency is illustrated in Figure 3.7. The results of two independent trials indicate that maximum velocity is realized at or near 100 Hz. The highest velocity observed was 161 mm/s. Evaluation of the prototype at frequencies greater than 200 Hertz was beyond the scope of the development program, due to limitations of portable drive circuitry. However, tests at higher frequencies may
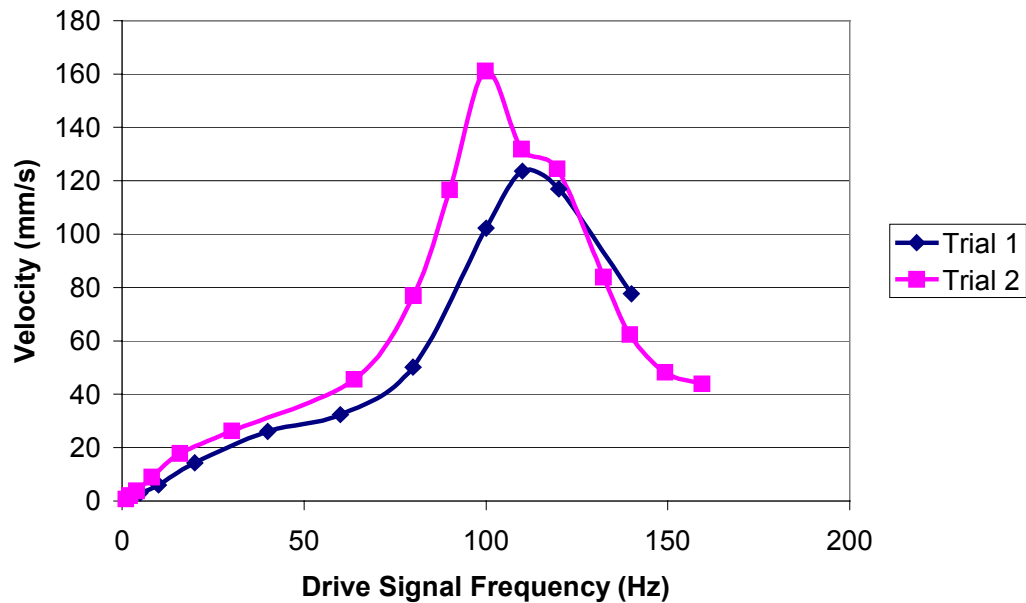
Figure 3.7**. THUNDERWORM velocity vs. drive signal frequency [67]**

reveal that greater velocities are possible once the system passes through higher-order structural resonant modes. In the process of evaluating maximum blocked force, an LVDT was connected to both the forward and rear latch assemblies as previously stated. The no-load velocity testing using this set-up indicated that the transfer of linear momentum from the rear latch assembly to the forward half of the prototype consistently increased step displacement.

Figure 3.8 is a plot of maximum blocked force over a range of drive signal frequency [67]. The greatest blocked force observed in both trials was 13.9 N at 50 Hz. This value was markedly lower than the actuator-blocked force of the THUNDER™ module predicted earlier. Back slip, introduced in Section 3.2, reduces the net displacement of the prototype to zero at load levels less than the actuator type blocked force.
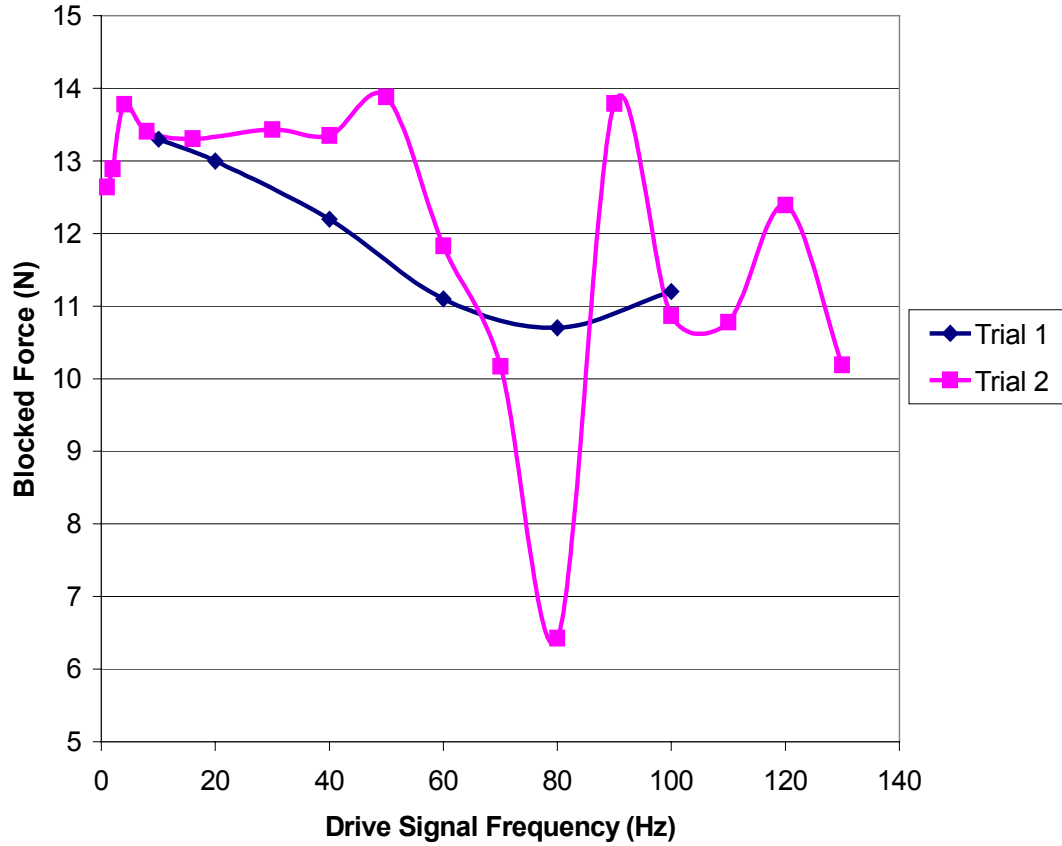
Figure 3.8. **Maximum blocked force vs. frequency [67]**

Back slip is modeled and discussed in detail in Section 3.4. Energy density of the THUNDERWORM is expressed as the product of the no-load flexural displacement of the THUNDER™ module, and the maximum blocked force; divided by the mass of the prototype. Module displacement is used to avoid bias from inertial effects in the prototype displacement data. Based on the data reported earlier, and with a prototype mass of 850 grams, the energy density of the THUNDERWORM is 0.0066 joules per kilogram. Multiplying the energy density by the drive signal frequency yields the power density. At 100 Hertz the THUNDERWORM power density is 0.66 W/kg.

3.4 Investigation of Back Slip Losses

Examination of the latch displacement waveforms in Figure 3.9 clearly indicates the presence of measurable amounts of back slip (denoted by δ_{bs}) in the latches. Consequently, a percentage of the
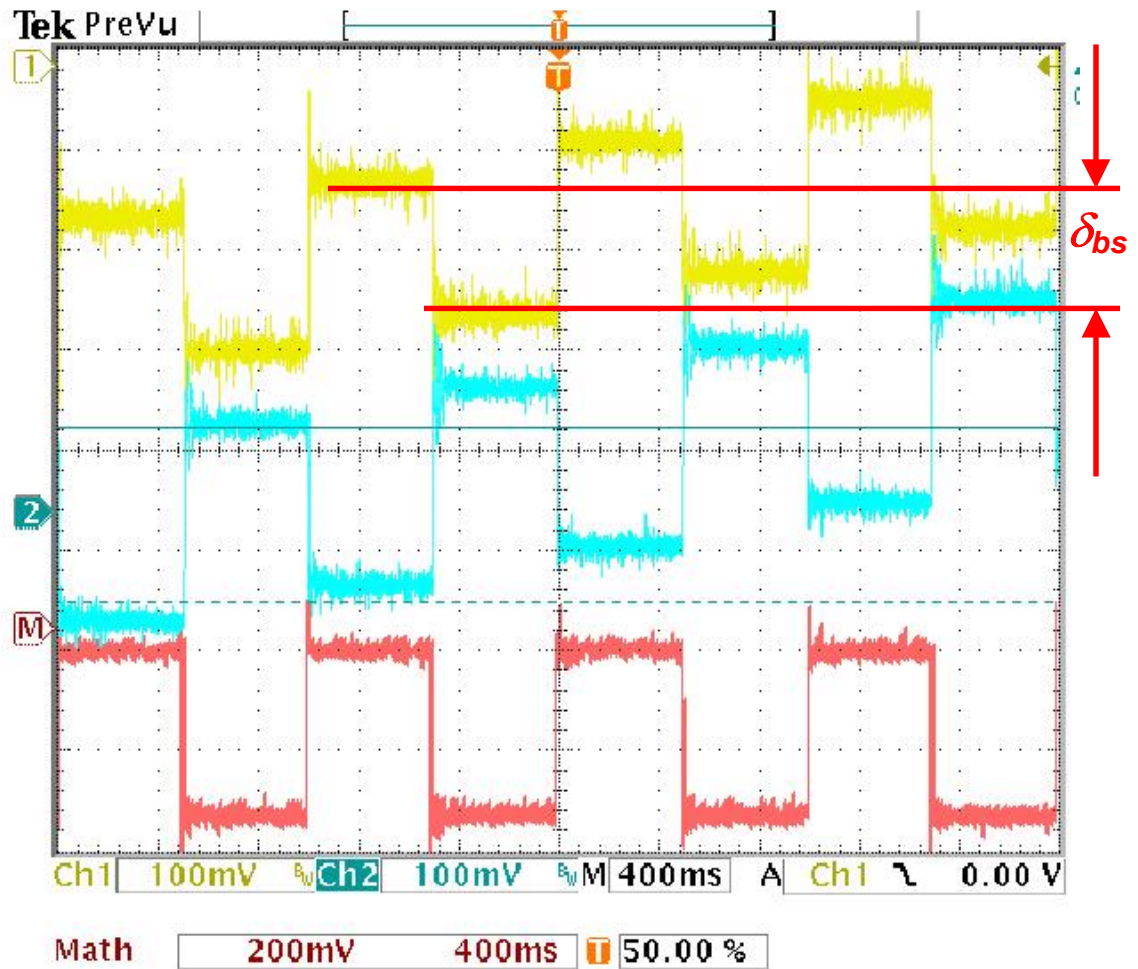
Legend

Horizontal Scale: Time (400ms per division), Vertical Scale: Displacement (100mV per division = 66.7 μm per division), Yellow trace (top): position of front half of piezomotor, Cyan trace (middle): position of rear half, Red trace (bottom): front position minus rear position, or net THUNDER™ output.

Figure 3.9. **Waveform plot showing forward and rear latch displacements [67]**

THUNDER™ module flexural displacement per cycle is lost due to one latch sliding backward prior to binding. Here, we define displacement efficiency as the ratio of net forward displacement to THUNDER™ flexural displacement per cycle. Figures 3.10 and 3.11 show how the output displacement of the THUNDERS decreases, and how back slip increases, with increasing load. Under these conditions, the THUNDERWORM
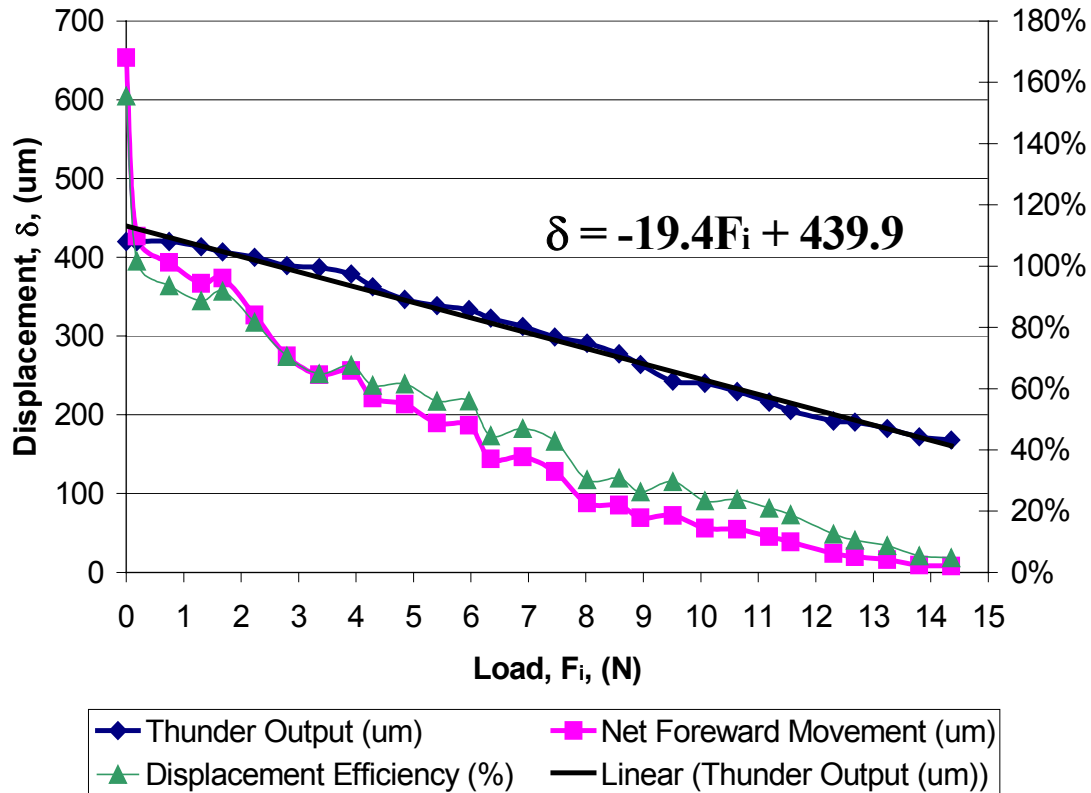
Figure 3.10. **THUNDERWORM displacement and efficiency vs. load [67]**

maximum blocked force is limited by the displacement efficiency of the latches to a level 30% less than the predicted capability.   Note that in Figure 3.11, negative latch slip denotes relative motion in the forward direction by a mechanism called kinetic forward slip, which is discussed in Section 3.4.2.5. The following segment explains the formulation of a model that quantifies back slip, and may be useful as a tool in predicting back slip levels in similar passive latch prototypes.
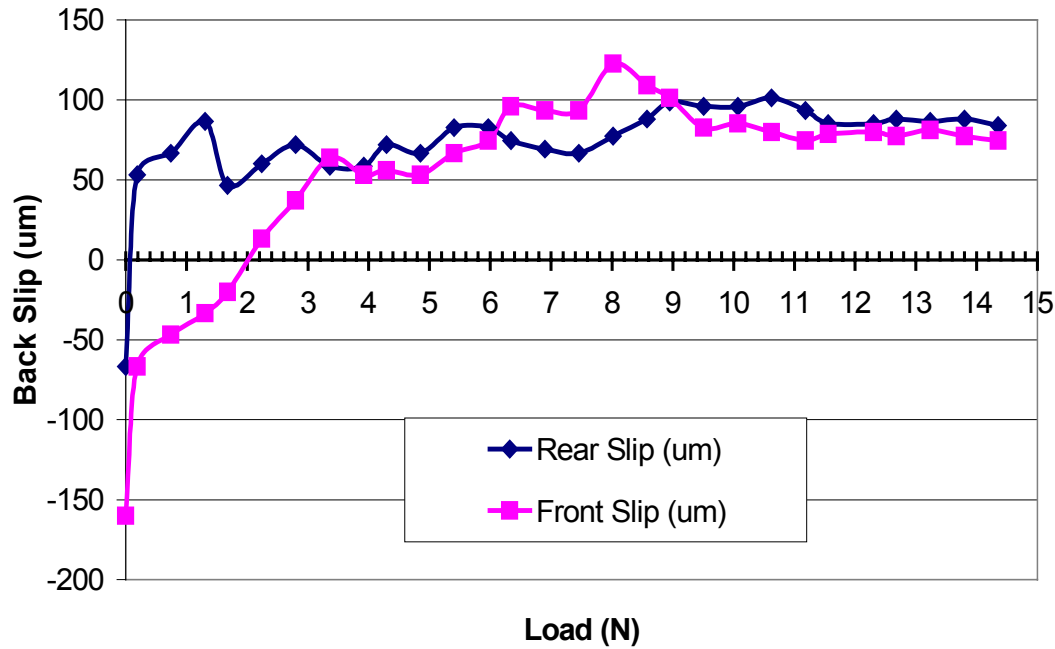
<u>Figure 3.11</u>. **THUNDERWORM latch slip vs. load [67]**

3.4.1 Slip Mechanisms

Slip losses are defined by two categories, forward slip, and back slip. The following paragraphs describe these static slip mechanisms. Forward slip refers to displacement losses associated with forward motion of the latch assembly. It includes slip due to momentum transfer within the piezomotor, and the effect of pawl rotation to the "open" position. This action of the pawl is illustrated in Figure 3.12. The pre-load force maintains the pawl in firm contact with the rod at points on the upper and lower surfaces as indicated (position 1). At this instant, the latch is locked in position, and cannot move to the left (backward). At the start of forward motion of the piezomotor in the direction indicated, the housing separates from the pawl in the pre-load area, and the latter subsequently rotates counterclockwise about the lower point of contact with the rod (position 2). Rotation continues past the point where the coefficient of static friction between the rod and pawl is overcome, and relative sliding motion occurs. Motion ceases when the friction forces and the increasing pawl pre-load balance each other. The forward linear displacement of the latch housing required to open the pawl to the point of relative sliding motion quantifies the forward slip. In order for the latch to bind during the next
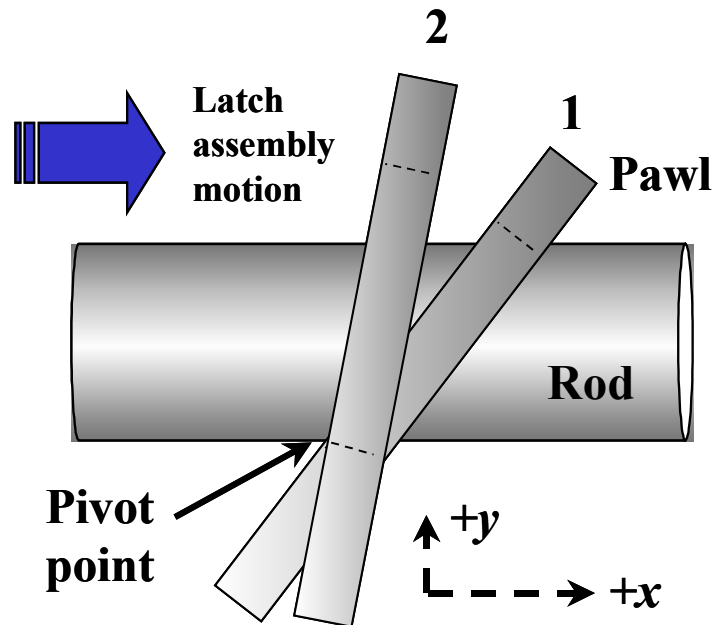
<u>Figure 3.12</u>. **Forward slip motion cycle**

contraction sequence of the THUNDER™ module, the pawl must rotate *clockwise*, returning to its starting position. This return rotation is facilitated by the *rearward* motion of the latch housing, and is the major contributor to back slip.

Slip losses incurred in a direction opposite to the forward progress of the piezomotor is quantified by back slip. Back slip occurs during the binding operation of the latch (see the free body diagram of Section 3.2, Figure 3.4). Several factors contribute to the measurable level of back slip. They are listed below:

- Latch housing deflection (Section 3.4.2.1)

- Contact deformation (Section 3.4.2.2)

- Pawl deflection (Section 3.4.2.3)

- Rotation of the pawl from the open configuration described in the previous segment, to a closed or binding position (Section 3.4.2.4)

- Rod deflection

Back slip due to rod deflection is considered negligible if the ratio of the pawl thickness to rod diameter is much less than one. As the ratio approaches unity, the rod simply deflects away from the action of the pawl, and no

binding occurs.   Back slip in a given passive latch design may be predicted by the superposition of the contributions from these static mechanisms. The superposition model is described in the following segment.

3.4.2 Static Back Slip Superposition Model

Figure 3.13 exaggerates the effects of contact deformation, and pawl/ latch housing deflection. Either, or both contributes to the total back slip in varying levels as the applied load increases. Under low-load, or an unloaded condition, these elastic effects are negligible when compared to the slip caused by consistent momentum transfer between the forward and rear portions of the piezomotor (see Section 3.4.2.5). This process reduces pawl return rotation, which generally dominates back slip at low load levels. The following sections develop models that collectively determine back slip over the full load spectrum.
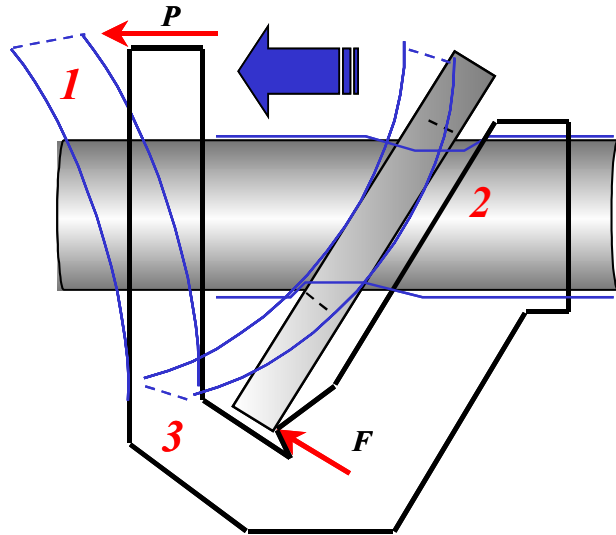
Figure 3.13. **Back slip loss mechanisms: 1.) Latch housing deflection, 2.) Pawl/rod contact deformation, 3.) Pawl deflection**

3.4.2.1 Latch Housing Deflection

The second-generation U-shaped latch housing shown above may be idealized as a curved beam for purposes of modeling the rearward horizontal deflection of the point of application of load *P*. The model is shown below (Ugural and Fenster) [92].   Referring to Figure 3.14 (a), load *P* denotes the force of the THUNDER™ transducer module acting rearward at the centroid *C′* of the rectangular latch housing cross-

section shown. Load *P* is the *reaction* force generated by the transducer module as it pulls itself and the rear latch assembly forward after the THUNDER™ module is energized. Figure 3.14 (b) shows the free body diagram of the beam segment described by angle θ and cut *a-a'*. It includes the radial shear force *V*, tangential force *N*, and moment *M* [92]. Enforcing static equilibrium in the radial and tangential coordinate directions yields the following:

$$V = P\cos\theta \tag{3.4}$$

$$N = P\sin\theta \tag{3.5}$$

(a)   (b)
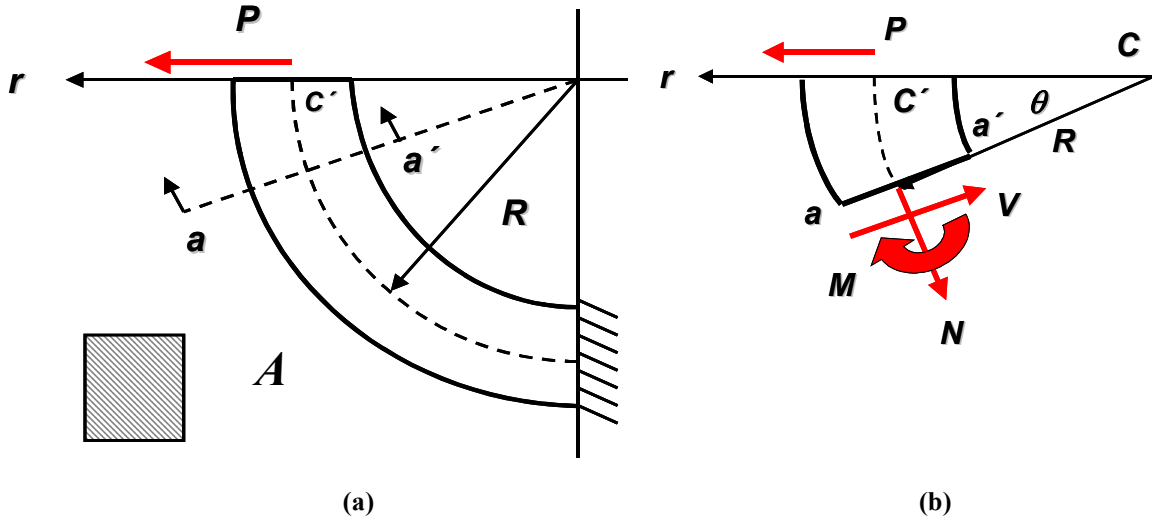
Figure 3.14. **a.) Latch housing curved beam idealization, b.) Beam segment free body diagram**

Similarly, expressing moment equilibrium results in:

$$M = PR\sin\theta \tag{3.6}$$

From Castigliano's theorem, the total strain energy *U* in the system may be written as the sum of contributions from tensile, shear, bending, and torsional loads [92]:

$$U = \int\frac{N^2}{2AE}dx + \int\frac{M^2}{2EI}dx + \int\frac{\alpha V^2}{2AG}dx + \int\frac{T^2}{2JG}dx \tag{3.7}$$

where *A* is the cross-sectional area, *E* is Young's modulus, *I* denotes the cross-section moment of inertia, *G* represents the shear modulus, and *J* is the polar moment of inertia. For the rectangular cross-section, the form factor for shear, α, in 3.7 is equal to 6/5 [92]. Since there are no torsional effects in the model, the last term of

3.7 is neglected. Substituting $rd\theta$ for dx, differentiating with respect to load P, and integrating each term from zero to $\pi/2$ yields radial displacement δ_1, and thus the component of back slip due to deflection of the housing [92]:

$$\delta_1 = \frac{PR\pi}{4AE} + \frac{PR^3\pi}{4EI} + \frac{6PR\pi}{20AG} \tag{3.8}$$

Simulation of this result reveals that the contributions of the first and third terms are small in comparison to that of pure bending, represented by the second term. The next segment lists derives back slip attributed to Hertzian contact deformation between the rod and pawl.

3.4.2.2 Contact Deformation

Figure 3.15 illustrates a magnified view of the region of contact between the rod and pawl. In the
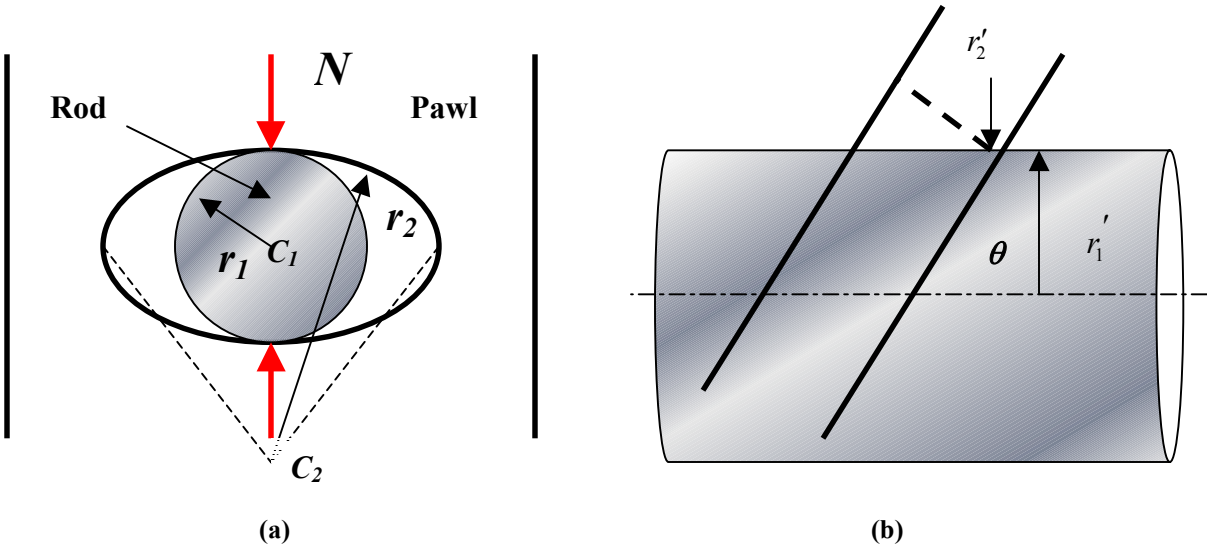
Figure 3.15. **Rod/pawl contact region: a.) Front view, b.) Side view**

orientation shown, the razor-like edge of the pawl slot "digs" into the rod at a tangent point on its curved surface. As the load on the latch mechanism increases, contact stress and deflection develops at the interface. Contact deflection consequently contributes to the total back slip. Assuming the bodies in contact are elastic and isotropic materials, the amount of that contribution is quantifiable using a Hertzian contact model.

Referring to Figure 3.15, the relative approach, or change in distance between center points C_1 and C_2 under normal force N is desired (Johnson) [44]. Table 3.1 defines the radii of the two bodies and the associated sign convention. The algorithm presented by Johnson describes the geometry of the contact footprint as elliptical [44]. Figure 3.15 (a) and (b) depict the orientation of the contacting bodies in specific planes, denoted by the r and r' notation [44]. In the r' plane, the bodies are oriented by angle θ with respect to each other. With

<u>Table 3.1</u> **Parameter Definitions and Sign Convention for Contacting Bodies**

Body 1: Rod	Sign	Comment
r_1	Positive	Radius of the rod
r_1'	N/A	Rod axial profile (infinite radius)
Body 2: Pawl		
r_2	Negative	Pawl slot radius
r_2'	Positive	Slot edge radius $\left(r_2' << r_2\right)$

this established, the relative approach of the centers is:

$$\delta_c = \left(\frac{9N^2}{16E^{*^2} R_e} \right) F_2(e)$$

(3.9)

where E^* refers to the following function of the modulus of elasticity of the rod material (steel) and Poisson's Ratio:

$$E^* = \frac{E}{(1-\upsilon^2)}$$

(3.10)

Function $F_2(e)$ is called the eccentricity correction factor [44]. Its value is determined using graphical data presented by Johnson [44]. Quantity R_e is the equivalent relative curvature, which is written as:

$$R_e = \frac{1}{2\sqrt{AB}}$$

(3.11)

The ratio of parameters B and A indicate the eccentricity of the contact ellipse [44]. Parameter A is defined by:

$$A = \frac{1}{2}\left(\frac{1}{r_1} + \frac{1}{r_1'} + \frac{1}{r_2} + \frac{1}{r_2'} \right)$$

(3.12)

Likewise, parameter B is written as follows:

$$B = \frac{1}{2}\left[\left(\frac{1}{r_1} - \frac{1}{r_1'}\right)^2 + \left(\frac{1}{r_2} - \frac{1}{r_2'}\right)^2 + 2\left(\frac{1}{r_1} - \frac{1}{r_1'}\right)\left(\frac{1}{r_2} - \frac{1}{r_2'}\right)\cos 2\theta\right]^{1/2} \tag{3.13}$$

Given the relative approach of the centers, the resulting back slip is determined by the following.

Figure 3.16 illustrates the change in the orientation of the pawl following contact deformation. A simple approximation assumes the contact point on the pawl moves in the negative y direction with a corresponding displacement of point C in the negative x direction. Hence the back slip is as follows:
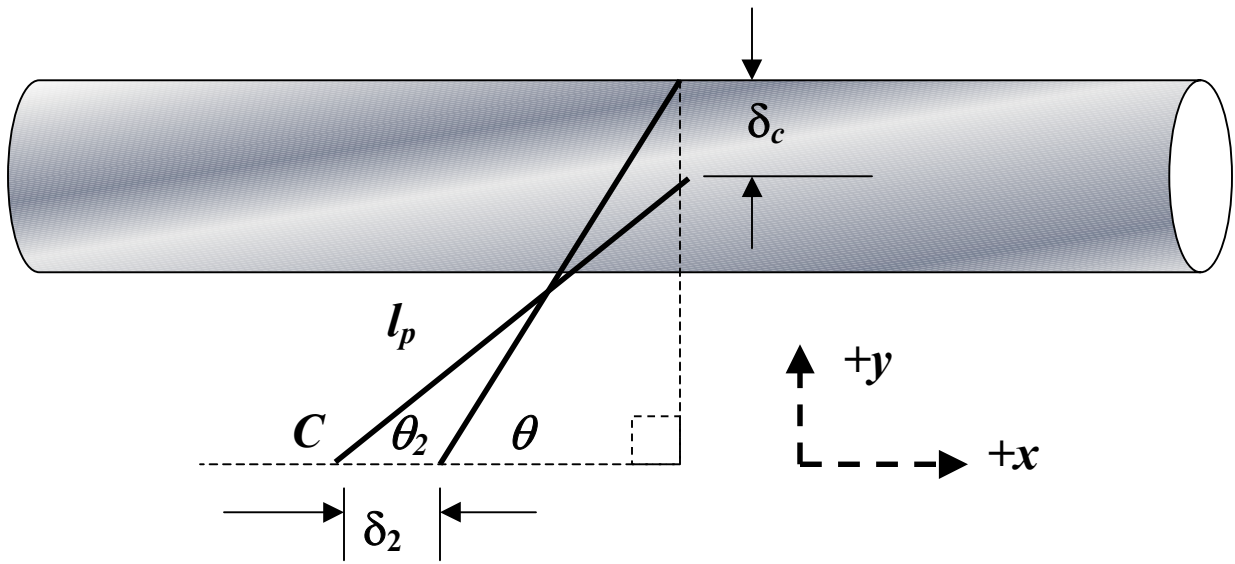
Figure 3.16. **Geometric model relating back slip due to contact deformation to the relative approach of the centers**

$$\delta_2 = l_p\left(\cos\theta_2 - \cos\theta\right) \tag{3.14}$$

where angle θ_2 may be expressed in terms of pawl length l_p, and angle θ as follows:

$$\theta_2 = \sin^{-1}\left[\frac{\left(l_p \sin\theta - \delta_c\right)}{l_p}\right] \tag{3.15}$$

3.4.2.3 Pawl Deflection

The following static model of the passive latch pawl used the loading shown in Figure 3.4. This model developed a qualitative expression for the deflection of the pawl at the latch housing interface, point *C*. The pawl deflection is a component of the load-dependent back slip in the latch mechanism.

In the binding configuration, the pawl is considered to be a cantilever beam with a rectangular cross-section (see Figure 3.17). A datum is placed through the center of gravity, perpendicular to the axis as
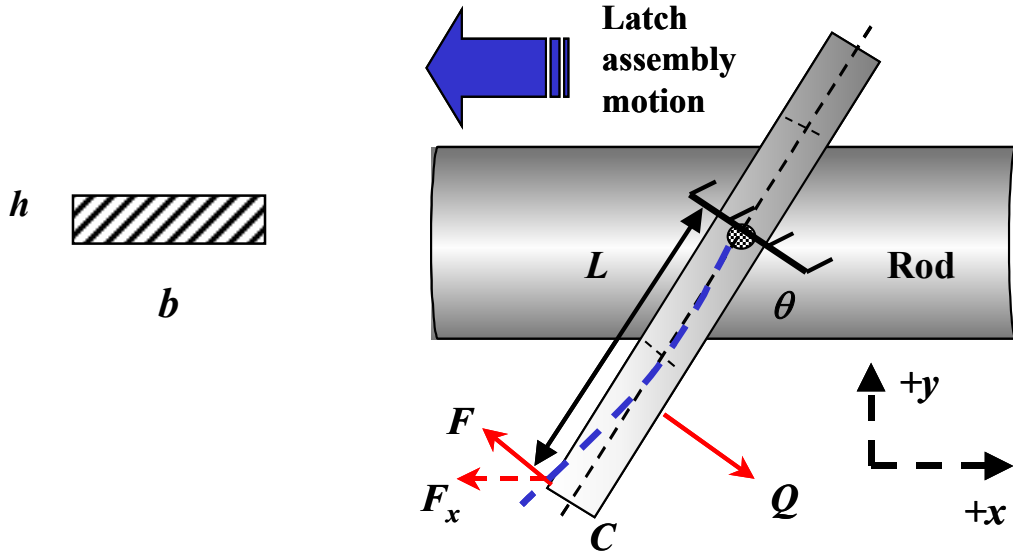
Figure 3.17. **Pawl cantilever beam idealization**

indicated. Tip load *F* and pre-load *Q* act as shown. The distance from the datum to the tip is length *L*. In practice, the position of the datum relative to the lower edge of the pawl slot is assumed to be one-half the slot height. Positive deflection of the pawl is in the direction of latch assembly motion. The superposition approach documented by Gere and Timoshenko is adopted here to determine the expression for the deflection at point *C* [31]. Figure 3.18 illustrates the two beam loadings that are added to construct the model [31]. Referring to Figure 3.18 (a), the beam theory approach adopted to determine the deflection at point *B* is written as:

$$\delta_B = \frac{FL^3}{3EI} \tag{3.16}$$
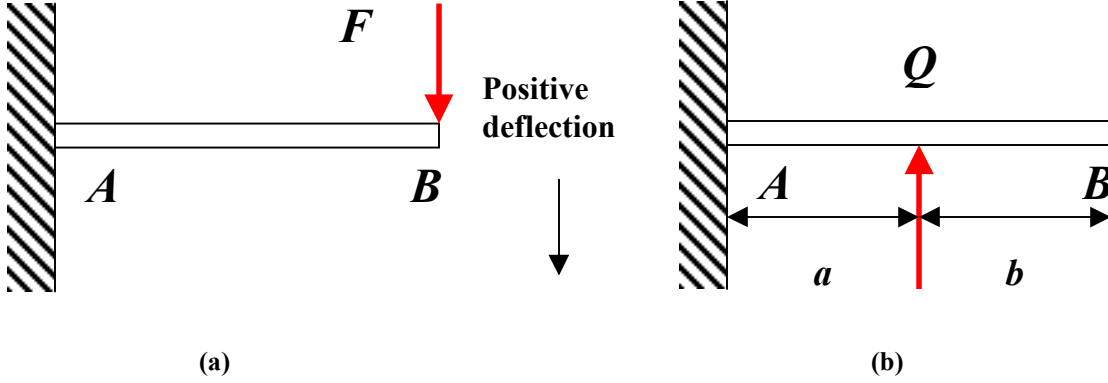
Figure 3.18. **Superposed beam loadings for pawl deflection derivation [31]**

where E is the modulus of elasticity, and I denotes the moment of inertia of the cross-section shown in Figure 3.17 [31]. The same deflection for the loading shown in Figure 3.18 (b) is given by:

$$\delta_B = \frac{Qa^2}{6EI}(3L - a)$$

(3.17)

In the THUNDERWORM passive latch design, a is assumed to equal to $L/2$. In Figure 3.18 (b), force Q causes a deflection in the negative direction. After substituting for a, and adding Equation 3.17 to 3.16, the pawl deflection equation [31] becomes:

$$\delta(L) = \frac{FL^3}{3EI} - \frac{5QL^3}{48EI}$$

(3.18)

Finally, by considering the component of deflection along the global x-axis (see Figure 3.17) the contribution to the total back slip is as follows:

$$\delta_3 = \delta(L)\sin\theta$$

(3.19)

3.4.2.4 Pawl Return Rotation

Rotation of the pawl as it transitions from its open configuration to the binding configuration impacts significantly on the latch back slip. Expanding on Figure 3.12, Figure 3.19 traces the change in the line of action of the pre-load force with respect to pawl orientation. In one half-cycle of operation, energizing (or de-energizing) the THUNDER™ transducer module causes the point of attachment of the pawl pre-load and the latch housing to shift a distance equal to d_{TH} in the positive x direction. This quantity is the THUNDER™ transducer module step displacement, and as Figure 3.10 indicates, it is proportional to the applied load. Back

slip associated with pawl return rotation is denoted by δ_4. It may be estimated from the oblique triangle formed by the pawl's leftmost edge in each configuration. Applying the Law of Cosines yields the following:

$$\delta_4 = \sqrt{s_1^2 + s_0^2 - 2s_1 s_0 \cos\varphi} \tag{3.20}$$

Parameters s_0, s_1, and φ are expressed from further trigonometric constructions, given d_{TH}, and the pawl arm l_t, which is the distance from the pawl lower face to the edge of the slot.

Side s_0 is determined from the right triangle that includes the radius of the rod r_1, and angle θ. The relation is as follows:

$$s_0 = \frac{r_1}{\sin\theta} \tag{3.21}$$

Figure 3.19. **Pawl rotation during the return from the open configuration**

Likewise, side s_1 is determined by:

$$s_1 = \frac{r_1}{\sin(\theta + \varphi)} \tag{3.22}$$

where φ represents the pawl return rotation angle. Applying the Law of Sines to triangle OXY in Figure 3.20 yields an expression for this angle:

$$\varphi = \sin^{-1}\left[\frac{d_{TH}\sin\theta}{s_t}\right] \qquad (3.23)$$

Parameter s_t is calculated from the Law of Cosines:

$$s_t = \sqrt{l_t^2 + d_{TH}^2 - 2l_t d_{TH}\cos\theta} \qquad (3.24)$$
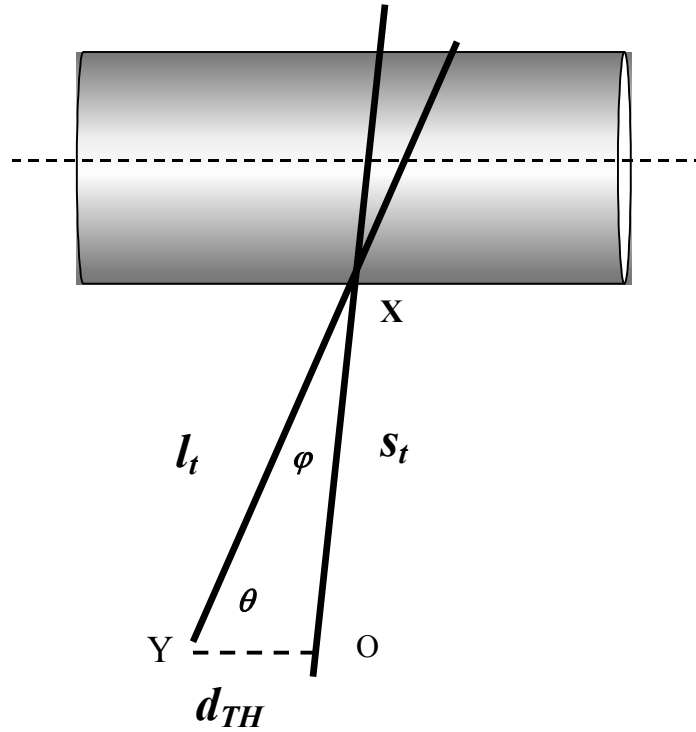
Figure 3.20. **Pawl return rotation angle construct**

At this point it is appropriate to note that when implementing this algorithm, angle θ does not remain constant over the range of piezomotor load. In fact, it may assume the value of angle θ_2 described in Section 3.4.4.2 due the effects of contact deformation.

3.4.2.5 Kinetic Forward Slip

Experiments with the unloaded THUNDERWORM at frequencies less than 20 Hz generated *negative* values of back slip (see Figure 3.11). Here, the magnitude of *kinetic forward slip* is greater than the combined effect of the back slip. Kinetic forward slip defines the supplemental forward displacement resulting from momentum transfer between the forward and rear portions of the piezomotor. In other words, one part of the THUNDERWORM can effectively "bump" the entire assembly forward. The following model quantifies kinetic forward slip in the forward latch assembly, and relates it to the total back slip.

Figure 3.21 shows kinetic forward slip in the plot of forward latch assembly displacement versus time, for the THUNDERWORM driven at ten hertz under increasing load. The LVDT displacement trace in Figure

(a)   (b)
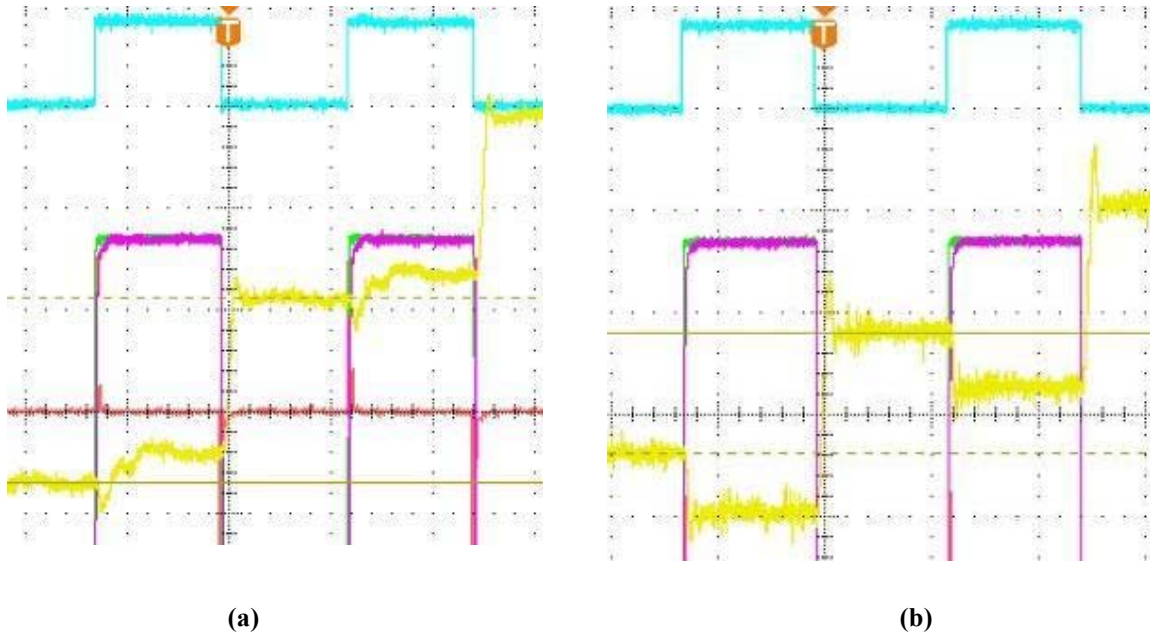
Figure 3.21. **Waveform plot of forward latch assembly displacement (yellow) with drive signal (cyan) at 10 Hz: a.) Low-load, b.) Increasing load [67]**

3.21 (a) moves upward (indicating forward motion of the latch assembly) during the drive signal period when there is no relative displacement from the transducer module. This motion is diminished at greater loads, as seen in Figure 3.21 (b). Table 3.2 explains this behavior by representing piezomotor motion at significant stages in the drive signal period. At the left, the THUNDERWORM is depicted as two masses joined by a

spring with variable stiffness $K_{eq}(V)$. The center column contains the drive signal trace. Forward latch assembly displacement is shown at the right. At the onset of the leading edge of the drive pulse, the transducer module is energized and contracts. This action causes the forward pawl to rotate "closed" with measurable back slip, δ_4. With the forward latch in the binding configuration, the rear portion of the piezomotor is pulled forward, ultimately "bumping" the forward latch assembly. The concurrent transfer of linear momentum moves the piezomotor ahead a distance δ_k. When the trailing edge of the drive signal occurs, the transducer module is powered down. The elastic relaxation of the module propels the forward latch assembly ahead, following the return rotation of the rear pawl. As the THUNDERS reach the limit of their step displacement, the excess kinetic energy of the forward latch assembly causes it to "overshoot," pulling the piezomotor forward slightly, and introducing elastic strain in the THUNDERS.   Ultimately this strain acts as a critically damped recoil mechanism, pulling the forward latch rearward to an equilibrium position. The Principle of Work and Energy, combined with the Conservation of Linear Momentum provide a means of expressing the kinetic forward slip associated with the leading edge of the drive signal (Beer and Johnston) [7].   That is, the distance the THUNDERWORM moves ahead following the collision between the rear and forward assemblies.
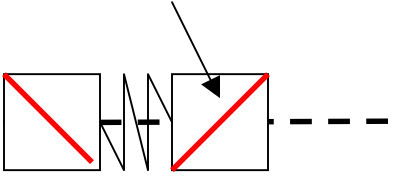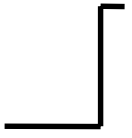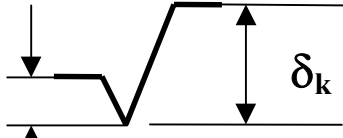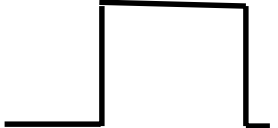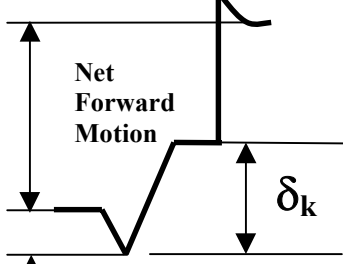
Figure 3.22 illustrates the sequence of events leading to kinetic forward slip at the leading edge of the drive signal. Assuming conservation of energy, the total energy of the rear latch and transducer module assembly at point 2 must equal that of the forward latch assembly at the same instant. This condition is expressed as the following:

$$T_1 + U_{12} = T_2 \qquad (3.25)$$

At system position 1 shown in Figure 3.22 (a), the kinetic energy T_1 of the stationary rear latch and transducer module assembly is zero. The transducer module performs work U_{12} by moving the rear latch assembly from position 1 to position 2. It is equal in magnitude and *opposite* in sign to the (negative) work performed by the force of friction between the rod and pawl [7]. Figure 3.23 illustrates a quasi-static free body diagram of the rear latch assembly and rod during relative motion. In the open configuration, a single friction force, F'_f, resists movement. Enforcing static equilibrium in the vertical direction gives rise to an expression for the friction in terms of known parameters W (the weight of the pawl), and Q (the pawl pre-load force delivered by a spring attached to the latch housing shown in Figure 3.2):

64

$$\sum F_y = N' - W - Q\cos\theta = 0 \tag{3.26}$$

Table 3.2 **THUNDERWORM Low-Load Motion Sequence**

THUNDERWORM Motion	Drive Signal	Forward Latch Assembly Displacement Signal
 $K_{eq}(V)$ • Forward pawl closes • Rear latch assembly is pulled forward • Rear portion "bumps" the piezomotor ahead		 **Pawl return** δ_4
  • Rear pawl rotates closed • Forward latch assembly is pushed forward • Forward latch assembly "overshoots" and pulls entire piezomotor ahead • Forward latch assembly recoils		 **Pawl return** δ_4

Solving this expression for N' and multiplying by the coefficient of kinetic friction results in:

$$F'_f = (W + Q\cos\theta)\mu_k \tag{3.27}$$

65
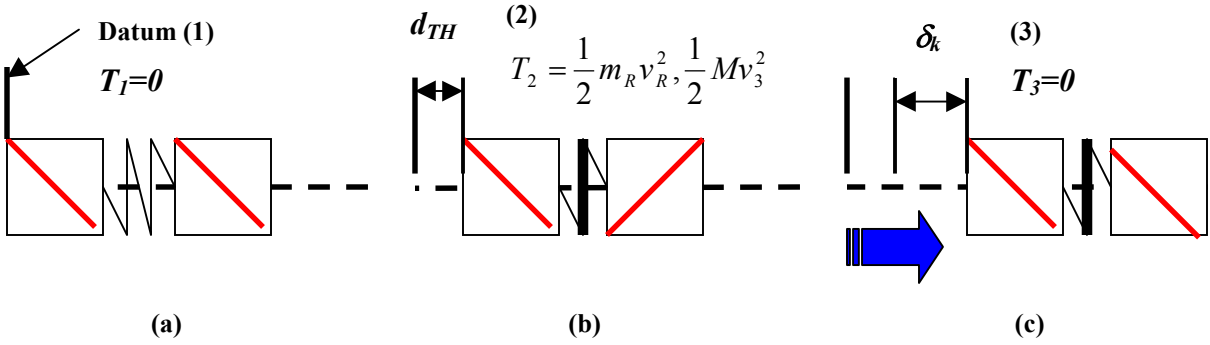
Figure 3.22. **Motion sequence for kinetic forward slip on the drive signal leading edge: a.) Position 1, b.) Position 2, c.) Position 3**
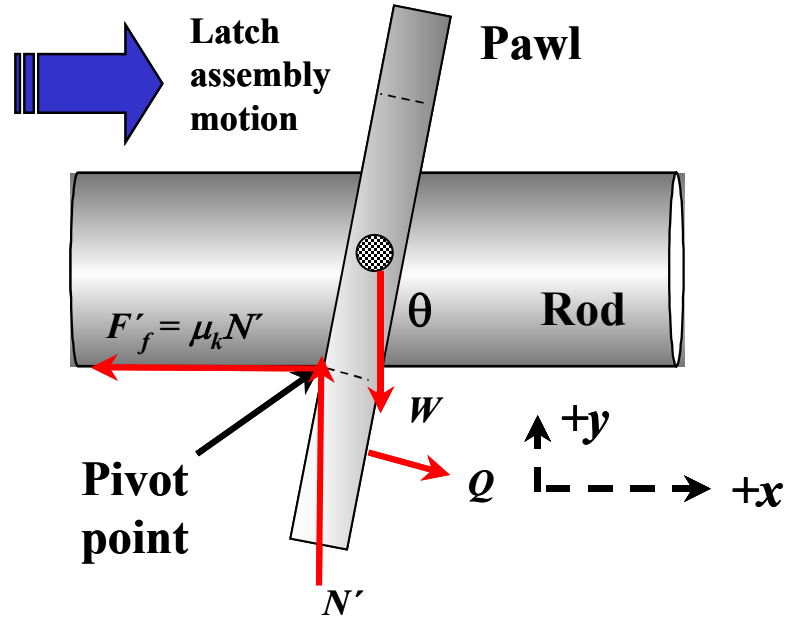
Figure 3.23. **Quasi-static free body diagram of the pawl in the open configuration during forward motion of the latch assembly**

Summing forces in the x direction yields the following:

$$\sum F_x = R - F'_f = 0 \qquad (3.28)$$

where R is the resultant force of the transducer module acting on the latch assembly. By inspection of 3.28, R is equal to the force of friction, and the work expression is written as:

$$U_{12} = Rd_{TH} = F'_f d_{TH} = (W + Q\cos\theta)\mu_k d_{TH} \tag{3.29}$$

Once in motion, the rear portion of the piezomotor attains the kinetic energy T_2 at position 2, shown in Figure 3.22 (b). Kinetic energy in this position is:

$$T_2 = \frac{1}{2}m_R v_R^2 \tag{3.30}$$

where m_R is the mass of the rear portion, and v_R is the corresponding velocity. Substituting 3.29 and 3.30 into 3.25, and solving for v_R yields an equation for the velocity of the rear portion:

$$v_R = \sqrt{\frac{2F'_f d_{TH}}{m_R}} \tag{3.31}$$

The transfer of linear momentum between the rear and forward sections of the piezomotor may be compared to a perfectly plastic collision of two particles moving in one dimension [7]. This idealization is justified in that the forward and rear portions are linked by the THUNDER™ transducer module, and remain in contact moving as a single particle following impact. Invoking the Principle of Conservation of Linear Momentum, a relation between the prior and post-impact velocities is realized [7]:

$$m_F v_F + m_R v_R = (m_F + m_R)v_3 \tag{3.32}$$

Given the forward portion initially at rest, and substituting the total mass of the piezomotor M for the sum on the right hand side, 3.32 is re-written as the following:

$$m_R v_R = Mv_3 \tag{3.33}$$

Solving for the post-impact velocity v_3 results in:

$$v_3 = \frac{m_R v_R}{M} \tag{3.34}$$

Hence the kinetic energy of the piezomotor immediately after the collision is:

$$T_2^+ = \frac{1}{2}Mv_3^2 \tag{3.35}$$

Following the collision, the unit travels forward a distance equal to the kinetic forward slip, until it comes to rest at position 3 in Figure 3.22 (c). Parameter U_{23} designates the sum of the work performed by the piezomotor against the load spring from position 2 to 3, and the work dissipated by friction. It may be written as follows:

$$U_{23} = U_{23}^e + U_{23}^f \tag{3.36}$$

Work performed on the load spring is found by evaluating the (trapezoidal) area under the load versus deflection curve as the spring is compressed an amount equal to the kinetic forward slip with load increasing from an initial magnitude of F_{Lmin} to final magnitude F_{Lmax}. In this case, the work is considered negative, and the expression is as follows:

$$U_{23}^e = -\frac{1}{2}\left(F_{L\,min} + F_{L\,max}\right)\delta_k \tag{3.37}$$

As the piezomotor moves to position 3, the forward and rear pawls slide along the rod in their fully open configuration. The corresponding force of friction acting on each pawl is:

$$F_f^* = \left(W + Q\cos(\theta + \varphi)\right)\mu_k \tag{3.38}$$

This result factors in the following expression for the work dissipated by friction:

$$U_{23}^f = -2F_f^*\delta_k \tag{3.39}$$

Substituting 3.39 and 3.37 into 3.36 leads to the total work between positions 2 and 3:

$$U_{23} = -\left(\frac{1}{2}(F_{L\,min} + F_{L\,max})\delta_k + 2F_f^*\delta_k\right) \tag{3.40}$$

Expressing the Principle of Work and Energy between positions 2 and 3 results in:

$$T_2^+ + U_{23} = T_3 = 0 \tag{3.41}$$

Replacing F_{Lmax} in 3.40 with the product of the load spring stiffness k_L and the kinetic forward slip, substituting the result with 3.35 into 3.41, and re-arranging terms yields a second-order polynomial that is easily solved for the kinetic forward slip:

$$-\left(\frac{k_L}{2}\right)\delta_k^2 - \left(\frac{F_{L\,min}}{2} + 2F_f^*\right)\delta_k + \frac{1}{2}Mv_3^2 = 0 \tag{3.42}$$

Note the solution to 3.42 is dual-valued.

The total back slip in the system is the difference between the so-called steady state, and transient kinetic values:

$$\delta_{bs} = \sum_{n=1}^{4}\delta_n - \delta_k \tag{3.43}$$

where δ_n denotes the steady state contributions described in sections 3.4.2.1 through 3.4.2.4. Back slip superposition model results are listed in the paragraphs that follow.

3.4.2.6 Back Slip Superposition Model Results

A plot comparing back slip superposition model results to the forward latch back slip data of Figure 3.11 is shown in Figure 3.24, below. The experimental data is bounded by curves calculated by varying the pawl arm parameter, l_t. Recall that in the model formulation, this dimension is the distance from the pawl lower face to the edge of the slot (see Figure 3.20). It determines pawl return rotation, which influences the magnitude of the total back slip. A more concise definition of the pawl arm is the distance from the point of contact between the pawl and the latch housing, and the edge of the slot. In the prototype, this point varies with the configuration of the pawl. The following items were not considered in the model applied to the THUNDERWORM prototype:

- Due to the fact that the THUNDERWORM latch housing was a continuous piece unlike the succeeding design shown in Figure 3.13, latch housing deflection was omitted from the model.

- The recoil of the forward latch assembly shown in Table 3.2 was omitted.

Figure 3.24 shows that good agreement between the data and the superposition model is achieved in the low-load regime. The superposition model tends to under predict the back slip at load levels greater than 5 N. Error increases with load, and decreases rapidly after 8 N as the displacement of the transducers falls below 300 microns (see Figure 3.10). This situation reflects a limitation in the superposition model, in that it assumes the pivot point X shown in Figure 3.20 remains fixed as the pawl rotates to the binding configuration. The data suggests contrary to the idealization that the pivot point slides backward prior to binding. Sliding is attributed to variance in the binding forces N and N' (see Figure 3.4) during pawl rotation. At load levels in excess of 8 N, pawl rotation and the sliding motion is diminished as transducer displacement continues to decrease. Sliding is expected to be less prevalent in the rear latch, which is not directly loaded. Inspection of the rear latch back slip in Figure 3.11 reveals less error between 5 and 8 N, which supports this hypothesis. Figure 3.11 also shows a distinction between the forward and rear latch in kinetic forward slip behavior at low loads; this is attributed to the difference in mass between the portions of the THUNDERWORM. Since back slip levels at high load are of primary importance, a separate investigation of kinetic forward slip in the rear latch assembly was not
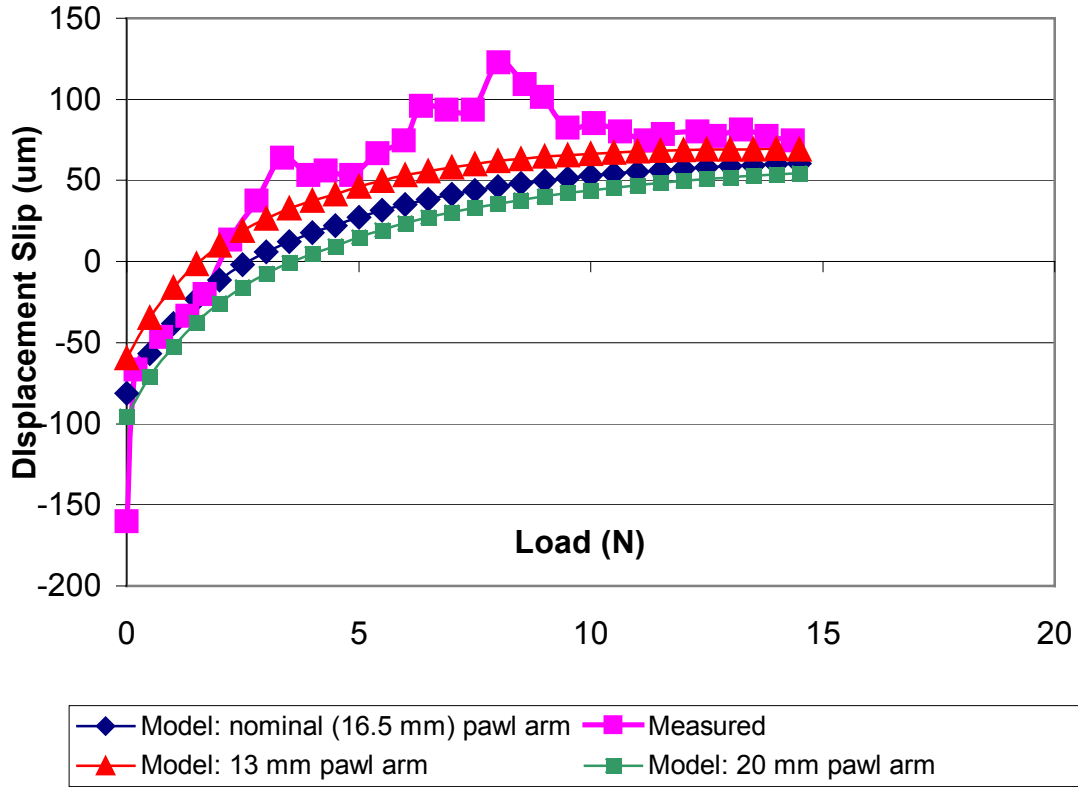
Figure 3.24. **Back slip superposition model results for THUNDERWORM forward latch**

undertaken. It is important to note that kinetic forward slip is a low-frequency phenomenon. Plots of forward latch displacement at low loads and drive frequencies greater than 20 Hz confirm that kinetic effects become negligible. One argument supports this observation: at high frequency, THUNDER™ transducer module displacement per half cycle tends to decrease, and curtails the momentum transfer between the forward and rear portions of the piezomotor.

3.5 Conclusion and Suggestions For Future Work

Trials conducted with the THUNDERWORM linear piezomotor were based on inchworm-style motion. The linear piezomotor compressed a calibrated spring, and the latches ensured that the energy was stored so that it could be used to do useful work when required. Using this arrangement, numerous optimized performance metrics were extracted, e.g., maximum velocity, maximum blocked force, energy density, and

back slip losses. These metrics were determined over a range of working frequencies and incremental loading. The THUNDERWORM produced a maximum velocity of 161 mm/s at a frequency of 100 Hz under no-load conditions [67]. The maximum blocked force achieved experimentally is 14 N, which is close to the 19.8 N actuator type blocked force value predicted from an empirical model devised prior to the linear piezomotor being fabricated [67]. Experiments with the THUNDERWORM linear piezomotor showed that under high-load conditions, the motion efficiency reduced, and that the predicted actuator type blocked force was not realized due to the passive latch operation.

Back slip levels in the passive latches are predicted using a superposition approach. The model quantifies back slip caused by a combination of pawl rotation, static deflection, and momentum transfer at low load levels. Agreement in the high-load regime may be improved by adding an empirical allowance for sliding in the forward latch. Analysis of the back slip mechanisms used in the passive latches of the linear piezomotor has led to the formulation of design criteria for such latches. Based on a combination of modeling and experimentation, it is concluded that a balance must be achieved in the length to thickness ratio of the pawl. Analysis proved that the major contributing factor to back slip, i.e., pawl return rotation, was reduced when the pawl length was increased. Knowledge gained from modeling methods indicated that an adverse length to thickness ratio alteration badly affects the pawl tip deflection, which is an undesirable feature in the linear piezomotor design. Although the level of back slip measured was consistently less than 100 microns, it was enough to effect motion efficiency, because the THUNDER™ transducers produce deflections much less than 400 microns under high load. The combination of the two effects means poor motion efficiency.

With design changes to the linear piezomotor, improved motion efficiency can be achieved at higher loads. One example is substituting THUNDER™ transducers with circular geometry for the rectangular ones. Experiments with round THUNDERS show that their stiffness is significantly greater than that of comparably sized rectangular transducers. The same results indicate that the negative aspect of using round transducers is that their displacements are comparably smaller. Overall, it is concluded that latch efficiency must be improved if linear piezomotor motion efficiency is to improve. Similarly, a radical miniaturization of the linear piezomotor to the meso (millimeter) scale might also improve motion efficiency and energy density.

Chapter 4

Investigation of Dimensional

Relationships and Performance in A

Miniature Linear Piezomotor

4.0 Introduction

Chapter 3 demonstrated the THUNDERWORM linear piezomotor; a direct drive actuation system using rectangular beam-shaped THUNDER™ transducers. The next step in development of the miniature robotic platform drive system was to introduce a smaller, more dimensionally compatible linear piezomotor based on the THUNDERWORM concept. Boosting the blocked force output of the smaller prototype was also of interest.

Tests with the THUNDERWORM revealed that advantages in stiffness and blocked force are realized by constructing a linear piezomotor using circular transducer geometry (Mulling) [60]. Figure 4.1 is a view of the annular THUNDER™ transducer. Table 4.1 lists comparison data for single-transducer stiffness, displacement, and actuator type blocked force (see Section 3.2 for details). Inspection of the data reveals that the increased stiffness comes at the expense of smaller free (no-load) displacement. However, the no-load

Piezoceramic layer   **Steel substrate**
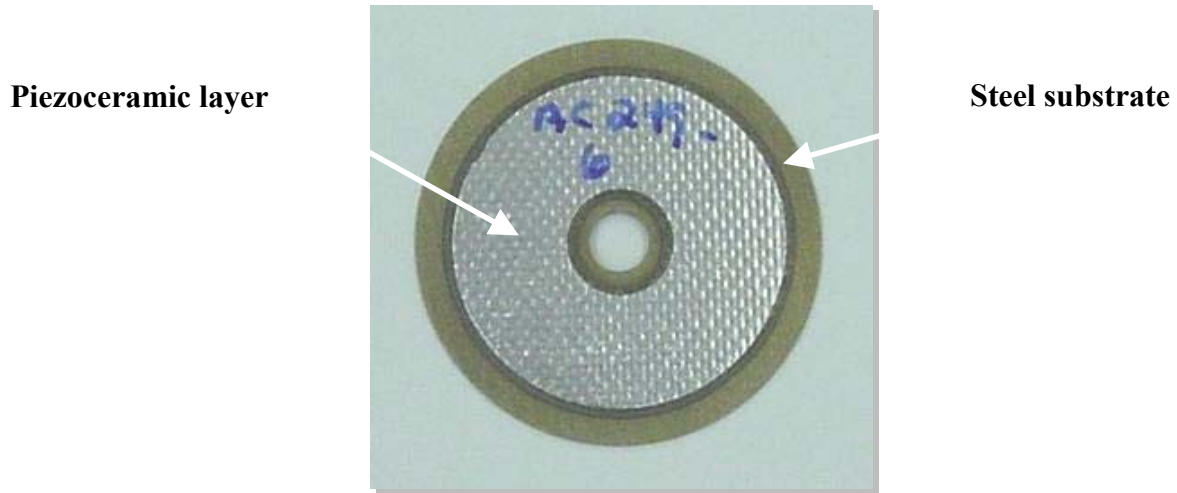
Figure 4.1. **Annular THUNDER™ piezoelectric transducer**

Table 4.1 **Performance Comparison Data With Type 8R Transducers [61]**

Parameter	1.75-in. Diameter Annular	Type 8R Beam-Shaped	Comparison
No-load flexural displacement, δ_0, (μm)	126	410	3.25X smaller
Zero-potential stiffness, k_0, (N/mm)	58.4	2.55	23X larger
Actuator type blocked force, F_2, (N)	7.3	1.05	7X larger

displacement was considered large enough to construct a miniature linear piezomotor.

The size of the prototype linear piezomotor detailed in this chapter was established principally by manufacturing resource limitations. In the interest of future work, it was considered valuable to devise an analytical method to determine how small the linear piezomotor could be constructed while maintaining acceptable velocity and blocked force. This need was addressed by applying Dimensional Analysis to assess the scalability of the performance of critical piezomotor components, specifically, the annular THUNDER™

transducers. Dimensional Analysis involves the comparative study of similar physical systems in terms of dimensionless scale factors (Skoglund) [79], (Langhaar) [53], (Baker) [4]. As Chapter 2 relates, scale factors represent the ratio of homologous dimensions. A simple example is the ratio of the lengths of corresponding (but not necessarily equal) sides of a pair of geometrically similar polygons. In such a case, similarity implies that all members of the set of geometric scale factors associated with the polygons are equal [4]. This chapter documents a dimensional analysis that considers the variation of elastic deflection and other performance measures across a set of annular THUNDER™ transducers of varying size. The dimensional analysis included the following:

- Analytical expressions for the elastic deflection and stiffness of the transducers under powered (piezoelectric) actuation, and unpowered (static) deflection were derived.

- The expressions were compared to experimental data to determine their validity, and understand their limitations.

- Scale factors for transducer and piezomotor performance parameters were established based on the preceding steps, and the consequences of the scale relationships are discussed.

The prototype miniature linear piezomotor, introduced in the next segment, was characterized to measure its performance relative to predictions, and to identify failure modes. Chapter 6 discusses the conclusions that were drawn from the characterization results.

4.1 Milliworm Annular THUNDER™-Based Linear Piezomotor

The Milliworm 3A miniature linear piezomotor was constructed from 0.525-inch diameter annular THUNDER™ transducers. It is pictured in Figure 4.2. Figure 4.2 (b) depicts a section view of the extender module assembly. Up to three transducers are supported at the perimeter by brass "C" rings which are mounted to the base plate and housing. The transducers are coupled in the center by a tube with thin plastic spacers providing separation. The housing and base plate is joined to a passive mechanical latch at the rear, while the center assembly connects to a passive latch at the front. Carefully arranged electrical insulation is not shown. Milliworm 3A is approximately 1 inch in length, and one half inch in diameter, weighing 10 grams. When powered by a 480-volt square wave at 50 Hz, the device generates inchworm motion along the rod (not shown). The characterization of the device is presented in Section 4.3.

(a)	**(b)**
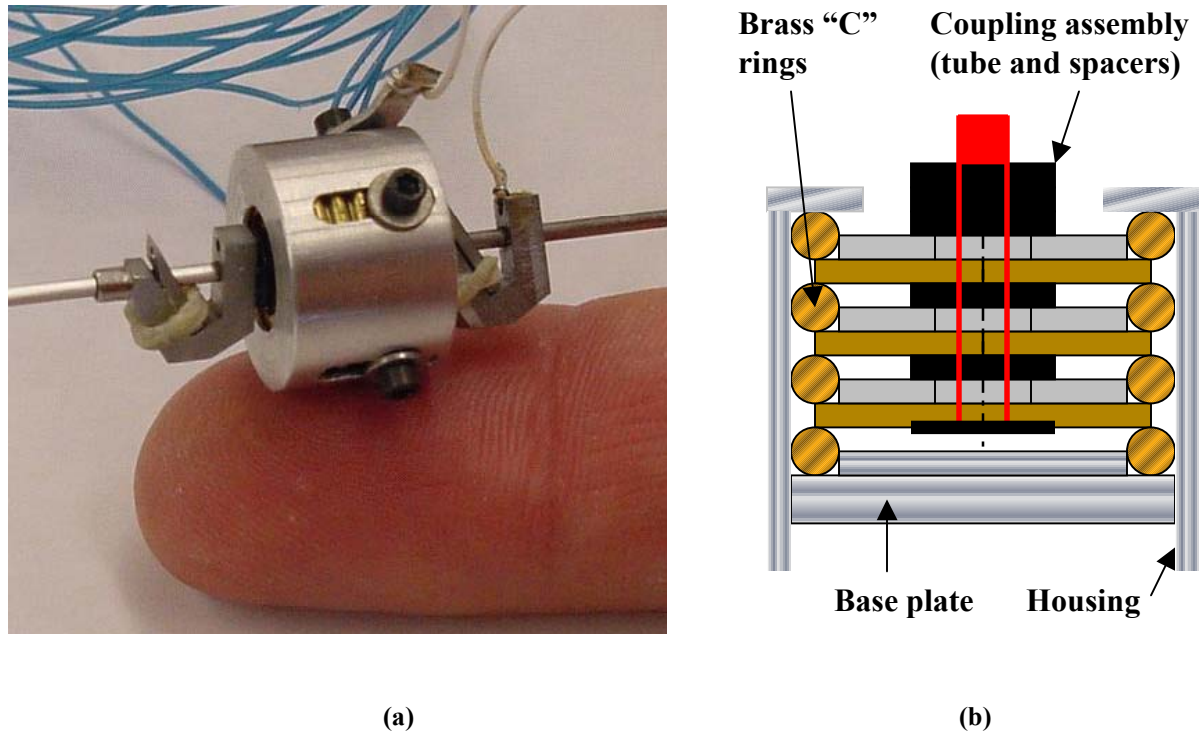
Figure 4.2. **Milliworm 3A: a.) Side view, b.) Extender module section view**

4.2 Dimensional Analysis of Annular THUNDERS

A set of annular THUNDERS was constructed with outer diameters ranging from 44 mm (1.75 in.) to 13.2 mm (0.525 in.). Figure 4.3 (a) illustrates three of the four sizes considered. Figure 4.3 (b) identifies the variables assigned to the structural dimensions. The outer radius of the substrate is designated r_o, while r_i denotes the outer radius of the overlying piezoceramic layer. In order to simplify the elastic deflection model, the inner radius of the piezoceramic layer is considered equal to the hole radius, r_h. Later, it will be demonstrated that this assumption has little effect on the model results. The total thickness of the transducer is represented by h, where h_m and h_p indicate the individual substrate and piezoceramic layer thicknesses, respectively. Table 4.2 lists the actual dimensions for each of the four transducer sizes. The right most columns identify scale factors including s_{ro}, which is the ratio of homologous outer radii; s_{ri} corresponding to the piezoceramic inner radii; s_h, the ratio of homologous hole radii; and finally s_t, the ratio of homologous total thickness. For example, the value of scale factor s_{ro} listed in the second row of Table 4.2 is equal the ratio of r_o for transducer 1 (22 mm), and r_o for transducer 2 (11 mm), or 0.5. Inspection of the table shows that the set

75

(a)

(b)
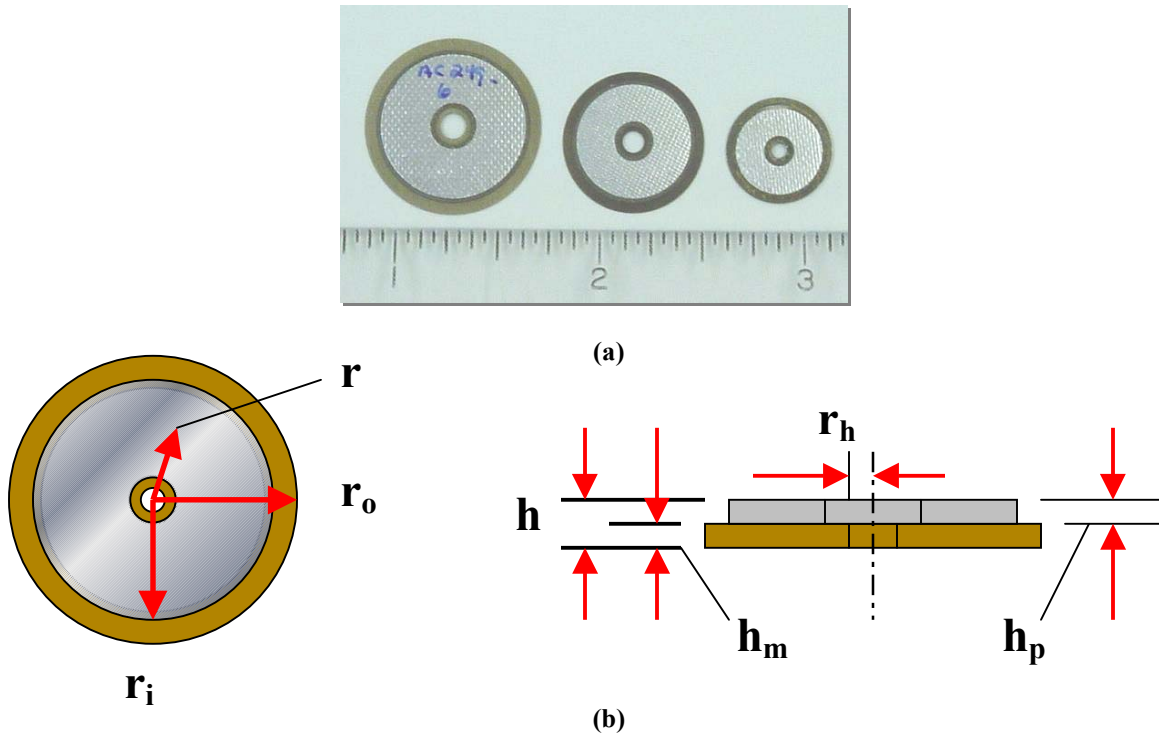
Figure 4.3. **a.) Annular THUNDERS of varying size, b.) Dimensional variable assignments**

Table 4.2 **Transducer Dimensions**[*]

Transducer	r_o	r_i	r_h	h_p	h_m	s_{ro}	s_{ri}	s_h	s_t
1	22	19	3.1	0.3	0.2				
2	11	9.6	1.6	0.3	0.2	0.50	0.51	0.52	1
3	8.9	7.6	1.3	0.3	0.2	0.81	0.79	0.81	1
4	6.6	5.8	0.84	0.3	0.2	0.74	0.77	0.65	1

*All dimensions in millimeters.

deviates from geometric similarity, most notably in the area of thickness. The total thickness was held constant to preclude bias in deflection performance due to varying thickness across the transducers. In the following sections, the scale factor s_{ro} will be used as a building block to construct dimensional relationships associated with piezomotor performance measures supported by the analytical expressions for elastic deflection of the transducers.

4.2.1 Elastic Deflection Model

An analytical model of the annular THUNDER™ was formulated to predict the deflection as a function of size measured by the outer radius. Considering the relatively small diameters of the test samples shown in Table 4.2, it is reasonable to assume that the dome-shape the devices acquire during thermal processing is small, and consequently these transducers may be treated as thin composite plates (Coorpender, Finkel, Kyzar, Sims, Smirnova, Tawhid, Bouton, and Smith) [18]. Using this approach allows a subset of the Theory of Plates and Shells to describe the elastic deflection of the annular THUNDER™ under specific loading and boundary conditions (Timoshenko and Woinowsky-Krieger) [82]. The same theory is the foundation for a model developed by Coorpender et al. who consider deflection under piezoelectric actuation [18].   The Coorpender-Smith model is adapted to the annular THUNDER™ geometry by invoking the Principle of Superposition [82]. Relevant assumptions follow.

4.2.1.1 Assumptions

The following conditions are assumed in describing the elastic deflection of the annular THUNDER™ under piezoelectric and external loads [82]:

- The total thickness of the device is small relative to its outer radius. Referring to Table 4.2, the outer radius of the smallest device in the series is in excess of ten times the total thickness.

- Deflections are less than one-half the total thickness [82]. The deflection of the 1.75-inch annular THUNDER™ listed in Table 4.1 corresponds to one quarter of the total thickness. Inasmuch as deflections of smaller devices are anticipated to be less, this assumption is justified.

- There exists a neutral plane in the deformed composite structure that does not experience strain. In uniform plates, the neutral plane coincides with the mid-plane of the cross-section [82].

- Points lying on lines normal to the neutral plane prior to bending remain in place thereafter, i.e. the effect of internal shear forces is not considered [82].

- Normal stress components acting transverse to the neutral plane are disregarded [82].

- Material properties in the piezoceramic and substrate layers are homogeneous.

In addition to the assumptions listed above, the inner radius of the piezoceramic layer is considered equal to the hole radius. The thin adhesive layer that fastens the piezoceramic to the substrate is omitted from the composite structure analysis.

4.2.1.2 Model Constraints and Sign Convention

To support the objective of determining deflection as a function of size, the equation of the deflected profile in static equilibrium is derived (see Figure 4.4 (a)). This configuration is representative of the device constraints in the miniature piezomotor. As the figure illustrates, the annular THUNDER™ is simply supported at the outer perimeter, and is subjected to a uniform load q distributed over the upper surface area. By the Principle of Superposition, the deflection curve of the configuration of Figure 4.4 (a) is expressed as the sum of the deflections of the three sub models shown in Figure 4.4 (b) (Beer and Johnston) [7, 82].   Sub Model 1 represents the simply supported case without a hole.   The effect of the hole is realized by adding the contributions of sub models 2 and 3 as shown. Sub Model 2 simulates pure bending under radial moments M_1 and M_2, where M_1 acts at the edge of the hole. Sub Model 3 expresses the shear force distribution Q_h along the inner edge of the hole.

A sign convention considers deflection $w(r)$ in the downward direction *negative* [18]. Similarly, loads oriented in the downward direction are also considered negative. Moments acting clockwise about the axis normal to the page are denoted as positive. The sign convention is reflected in the sub model derivations presented in the next segment.

4.2.1.3 Sub Model 1 Derivation

Relationships describing bending behavior in the uniformly loaded composite disk represented by Sub Model 1 (see Figure 4.4 (b)) are formed by analyzing the structure in two distinct segments [18]. The first is the ring of substrate material that lies between points r_i and r_o in Figure 4.3 (b). A unique equation governs bending in the second segment, a composite disk occupying the domain ($0 \leq r \leq r_i$.) The bending relations in each segment are related by enforcing a set of continuity boundary conditions described later in this section [18].

Bending in a thin, elastic, circular plate, with the assumptions listed above, varies with radial position r, and is determined by the following equation [82]:

$$\frac{d}{dr}\left[\frac{1}{r}\frac{d}{dr}\left(r\frac{dw(r)}{dr}\right)\right] = \frac{qr}{2D}$$

(4.1)

(a)

(b)
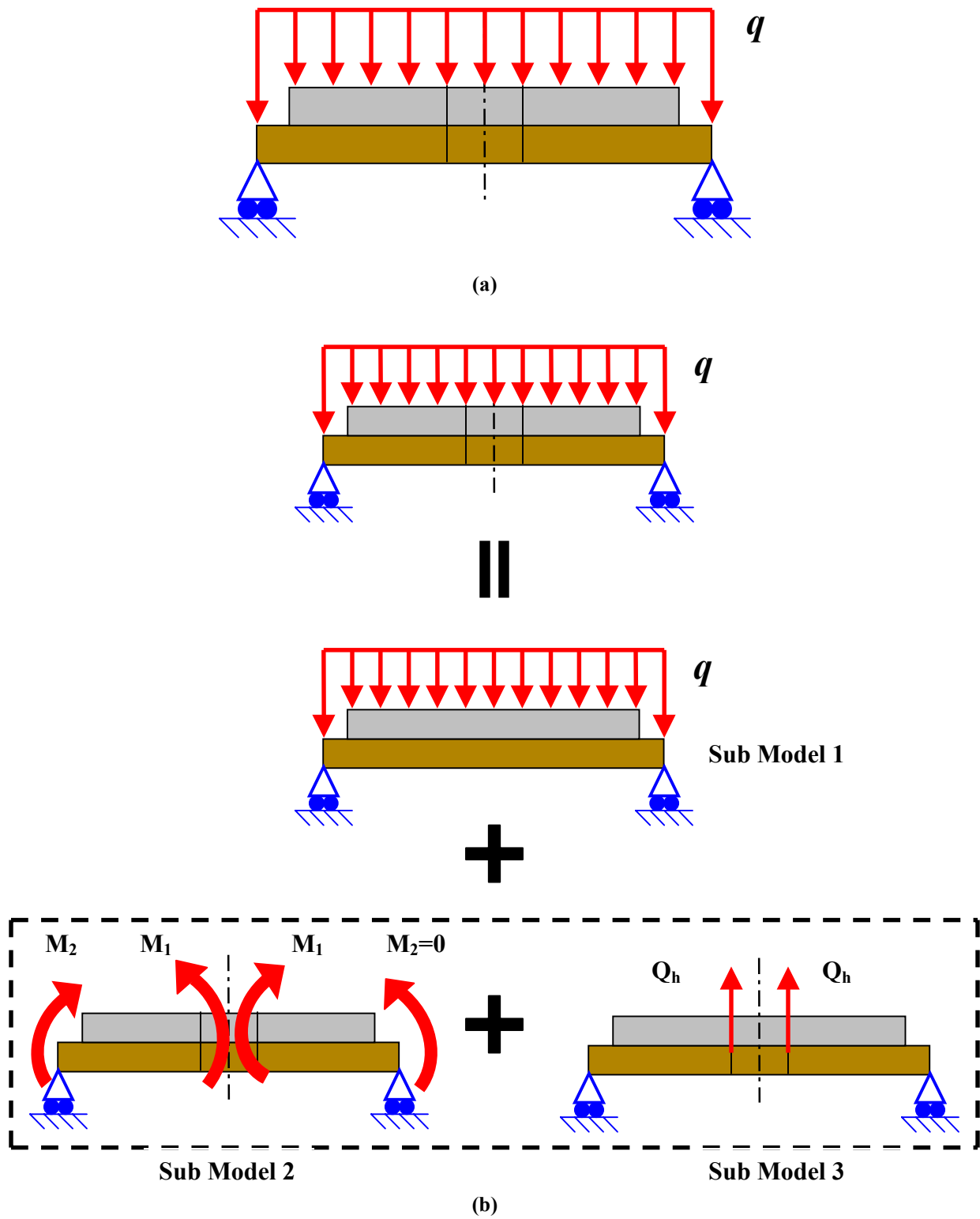
Figure 4.4. **a.) Model loads and constraints, b.) Superposition sequence**

where the quantity D is the flexural rigidity of the structure [82]. Considering the outer ring of substrate material, the flexural rigidity is denoted by D_s, which is defined as:

$$D_s = \frac{E_m h_m^3}{12(1 - \upsilon_m^2)} \tag{4.2}$$

where E_m is the modulus of elasticity, and υ_m is Poisson's ratio [82]. Its distinctive form facilitates the task of integrating of Equation 4.1 to solve for $w(r)$. Integrating twice, and appropriately moving "r" terms to the right hand side yields the following expression for the slope of the deflection curve:

$$\frac{dw(r)}{dr} = \frac{qr^3}{16D_s} + C_1 \frac{r}{2} + \frac{C_2}{r} \tag{4.3}$$

where C is a constant. The final integration reveals the deflection formula valid over the domain shown [82]:

$$w(r) = \frac{qr^4}{64D_s} + C_1 \frac{r^2}{4} + C_2 \ln\left(\frac{r}{r_o}\right) + C_3 \qquad (r_i < r \le r_o) \tag{4.4}$$

To represent deflection in the composite disk, Equation 4.4 is rewritten as the following:

$$w(r) = \frac{qr^4}{64D_c} + C_4 \frac{r^2}{4} + C_5 \ln\left(\frac{r}{r_o}\right) + C_6 \qquad (0 \le r \le r_i) \tag{4.5}$$

The quantity D_c denotes the flexural rigidity of the laminate expressed as [18]:

$$D_c = \frac{1}{3}\left(\frac{E_p}{1 - \upsilon_p^2}\right)\left[(h_m + h_p - z_n)^3 - (h_m - z_n)^3\right] + \frac{1}{3}\left(\frac{E_m}{1 - \upsilon_m^2}\right)\left[(h_m - z_n)^3 - (-z_n)^3\right] \tag{4.6}$$

where the subscript p designates the piezoceramic layer. The location of the neutral surface z_n in the laminate is defined by (Gere and Timoshenko) [31], [18]:

$$z_n = \frac{E_p h_p\left(\dfrac{h_p}{2} + h_m\right) + E_m\left(\dfrac{h_m^2}{2}\right)}{E_p h_p + E_m h_m} \tag{4.7}$$

This quantity is measured upward from the datum attached to the lower edge of the substrate. Equation 4.1 is derived from the static equilibrium of an infinitesimal wedge-shaped piece of the uniform circular plate [82]. The equilibrium expression includes contributions from the radial moment acting along the curved

circumference of the wedge $M_r(r)$, and the tangential moment $M_\theta(r)$, acting along its sides. Dimensionally speaking, these are *moments per unit length*, and are written as follows [82, 18]:

$$M_r(r) = D\left(\frac{d^2w(r)}{dr^2} + \frac{\upsilon}{r}\frac{dw(r)}{dr}\right) \tag{4.8a}$$

$$M_\theta(r) = D\left(\frac{1}{r}\frac{dw(r)}{dr} + \upsilon\frac{d^2w(r)}{dr^2}\right) \tag{4.8b}$$

Tailoring equations 4.8 to model the outer substrate ring and the composite disk involve replacing D and υ with D_s and υ_m in the first instance, and D_c and υ_c in the latter. Note υ_c denotes Poisson's ratio for the substrate/piezoceramic laminate, and is assigned a value of 0.3 [18].

Table 4.3 is a list of boundary conditions associated with Sub Model 1. Applying them leads to solutions for the six unknown constants. One constant, C_5, must be assigned a value of zero at the outset to avoid the singularity that occurs when r equals zero in Equation 4.5. The first and second boundary conditions describe attributes of the simply supported edge, where deflection and radial moment $M_r(r_o)$ are identically zero. The third boundary condition in Table 4.3 is implicit and therefore does not aid in determining any of the remaining constants. Boundary conditions 4 through 6 enforce continuity of deflection, slope, and moments at

Table 4.3 **Sub Model 1 Boundary Conditions**

1.) $w(r_o) = 0$	3.) $\dfrac{dw(0)}{dr} = 0$	5.) $\dfrac{dw(r_i^-)}{dr} = \dfrac{dw(r_i^+)}{dr}$
2.) $M_r(r_o) = 0$	4.) $w(r_i^-) = w(r_i^+)$	6.) $M_T(r_i) = M_r(r_i)$

the junction of the outer substrate ring (+) and the composite section (-), respectively. The quantity $M_T(r)$ represents the total moment in the transducer. It includes the constant external moment M_{rp} applied to the composite section by piezoelectric actuation. Since there are three sub models involved in the superposition solution process, we assign each *one third* of the total piezoelectric moment. Equation 4.9 expresses static moment equilibrium:

$$\sum M_r = -M_r(r) + \frac{M_{rp}}{3} + M_T(r) = 0 \tag{4.9}$$

Solving for $M_T(r)$ yields:

$$M_T(r) = M_r(r) - \frac{M_{rp}}{3} \tag{4.10}$$

To define the piezoelectric moment, it is necessary to introduce the piezoelectric strain coefficient, d_{31} [18]. This coefficient relates the strain due to lattice expansion in the vertical (z) direction (and corresponding radial constrictive strain) per unit of electric field applied to the piezoceramic [18]. With this in mind, the piezoelectric moment is given by the following:

$$M_{rp} = \frac{E_p V d_{31}}{2(1 - \upsilon_p)} \left(h_p - 2z_n + 2h_m \right) \tag{4.11}$$

where V denotes electric potential. The reader is referred to Coorpender for a detailed derivation of Equation 4.11 [18]. Expressions for the constants were developed and checked from the boundary conditions using MAPLE™. Excerpts of the results for this sub model are included in Appendix B.

4.2.1.4 Sub Model 2 Derivation

Sub models 2 and 3 are formulated such that their loadings effectively *cancel* the shear and moment distributions at the edge of the hole when superposed with Sub Model 1 [82]. It follows that one of the six boundary conditions for Sub Model 2 specifies that the radial moment M_1 in Figure 4.3 (b) must be equal and opposite to the radial moment $M_r(r_h)$ calculated from Sub Model 1 and Equation 4.8 (a). Accordingly, we assign moment M_h to denote $-M_r(r_h)$. Table 4.4 lists the boundary conditions for Sub Model 2. The corresponding deflection expressions for the two domains follow. Aside from the third, the same boundary

Table 4.4 Sub Model 2 Boundary Conditions

1.) $w(r_o) = 0$	3.) $M_1 = M_h$	5.) $\dfrac{dw(r_i^-)}{dr} = \dfrac{dw(r_i^+)}{dr}$
2.) $M_r(r_o) = M_2 = 0$	4.) $w(r_i^-) = w(r_i^+)$	6.) $M_T(r_i) = M_r(r_i)$

$$w(r) = -C_7 \frac{r^2}{4} - C_8 \ln\left(\frac{r}{r_o}\right) + C_9 \qquad (r_i < r \leq r_o) \qquad (4.12)$$

$$w(r) = -C_{10} \frac{r^2}{4} - C_{11} \ln\left(\frac{r}{r_o}\right) + C_{12} \qquad (0 < r \leq r_i) \qquad (4.13)$$

conditions for Sub Model 1 apply here. An important distinction exists in the fact that all six of the boundary conditions in Table 4.4 must be satisfied. This requirement requires the derivation of an explicit solution for constant C_{11}, which creates a singularity when r is equal to zero. Consequently, the domain of Equation 4.13 is restricted to exclude this point. Since one of the sub models is invalid at zero, the same condition must apply to the top-level model in Figure 4.4 (a). Calculations for Sub Model 2 are included in Appendix B.

4.2.1.5 Sub Model 3 Derivation

Sub Model 3 simulates the shear load Q_h about the edge of the hole that is equal and opposite of the shear present at the same location in Sub Model 1. This shear load per unit length is written as [82]:

$$Q_h = \frac{-q\pi r_h^2}{2\pi r_h} = -\frac{qr_h}{2} \qquad (4.14)$$

The numerator of the middle term in the previous equation is designated P_3, the resultant of the shear distribution about the inner diameter of the hole [82]:

$$P_3 = -q\pi r_h^2 \qquad (4.15)$$

The resultant load is included in the deflection expressions for Sub Model 3 listed below [82]:

$$w(r) = \frac{P_3 r^2}{8\pi D_s}\left(\ln\left(\frac{r}{r_o}\right) - 1\right) - C_{13}\frac{r^2}{4} - C_{14}\ln\left(\frac{r}{r_o}\right) + C_{15} \qquad (r_i < r \leq r_o) \qquad (4.16)$$

$$w(r) = \frac{P_3 r^2}{8\pi D_c}\left(\ln\left(\frac{r}{r_o}\right) - 1\right) - C_{16}\frac{r^2}{4} - C_{17}\ln\left(\frac{r}{r_o}\right) + C_{18} \qquad (0 < r \leq r_i) \qquad (4.17)$$

Note the singularity at $r = 0$ holds in this case also. Boundary conditions are shown in Table 4.5 below. Calculations for Sub Model 3 are included in Appendix B.

<u>Table 4.5</u> **Sub Model 3 Boundary Conditions**

1.)	$w(r_o) = 0$	3.)	$M_r(r_o) = 0$	5.)	$\dfrac{dw(r_i^-)}{dr} = \dfrac{dw(r_i^+)}{dr}$
2.)	$M_r(r_h) = 0$	4.)	$w(r_i^-) = w(r_i^+)$	6.)	$M_T(r_i) = M_r(r_i)$

4.2.1.6 Deflection Model Analytical Verification

Adding equations 4.5, 4.13, and 4.17, and substituting Equation 4.15 yields the complete deflection expression for the top-level annular THUNDER™ model shown in Figure 4.4 (a). For the domain of the laminate section, the expression is as follows:

$$w(r) = \frac{qr^4}{64D_c} + C_4\frac{r^2}{4} + C_6 - C_{10}\frac{r^2}{4} - C_{11}\ln\left(\frac{r}{r_o}\right) + C_{12} - \frac{qr_h^2 r^2}{8D_c}\left(\ln\left(\frac{r}{r_o}\right) - 1\right)$$
$$- C_{16}\frac{r^2}{4} - C_{17}\ln\left(\frac{r}{r_o}\right) + C_{18} \qquad (0 < r \le r_i) \tag{4.18}$$

To simplify the previous expression, we define the constants C_{19}, C_{20}, and C_{21} by the following:

$$C_{19} = C_4 - C_{10} - C_{16} \tag{4.19a}$$

$$C_{20} = -\left(C_{11} + C_{17}\right) \tag{4.19b}$$

$$C_{21} = C_6 + C_{12} + C_{18} \tag{4.19c}$$

Making these substitutions reduces Equation 4.18 to:

$$w(r) = \frac{qr^4}{64D_c} - \frac{qr_h^2 r^2}{8D_c}\left(\ln\left(\frac{r}{r_o}\right) - 1\right) + C_{19}\frac{r^2}{4} + C_{20}\ln\left(\frac{r}{r_o}\right) + C_{21} \qquad (0 < r \le r_i) \tag{4.20}$$

The expression for total moment at the top level is listed below.

$$M_T(r) = M_r(r) - M_{rp} \tag{4.21}$$

Independent verifications of the complete deflection model were performed. The first confirms that the model satisfies the top-level boundary conditions listed in Table 4.6. Other verifications involve modifying the model parameters to compare results with a documented solution in two separate configurations [82].

<u>Table 4.6</u> **Top-level Model Boundary Conditions**

1.) $w(r_o) = 0$	3.) $M_r(r_o) = 0$	5.) $\dfrac{dw(r_i^-)}{dr} = \dfrac{dw(r_i^+)}{dr}$
2.) $M_T(r_h) = 0$	4.) $w(r_i^-) = w(r_i^+)$	6.) $M_T(r_i) = M_r(r_i)$

One case considers the static (zero electric potential) deflection of the annular THUNDER™ with a 1.75-inch outer diameter under the following conditions:

- The hole is virtually eliminated by assigning the radius a value that is several orders of magnitude smaller than the outer radius of the device.

- The material properties of the piezoceramic are modified to such that they are identical to the substrate.

- A unit load is applied ($q = -1$).

- The outer radius of the piezoceramic layer is equal to the outer radius of the substrate ($r_i = r_o$).

The last case repeats the previous one with the exception that the piezoceramic layer thickness is set to zero. Results of the comparative verifications appear in Table 4.7. Comparing the deflection of the (small hole

<u>Table 4.7</u> **Comparative Verification Results [82]**

Configuration	Deflection $w(r_h)$	Published Model	Difference (%)
Identical material layers	$-0.391148551 \times 10^{-8}$	$-0.391148549 \times 10^{-8}$	0
Zero piezoceramic thickness	$-0.101846456 \times 10^{-6}$	$-0.101846456 \times 10^{-6}$	0

radius) model under piezoelectric actuation to published results from Coorpender show good agreement despite different boundary conditions and the fact that the value of d_{31} was undocumented [18]. Details of these results are provided in Appendix B. Additional piezoelectric simulations run at 600V revealed that with the dimensions listed in Table 4.2, the presence of the hole effects the device deflection by no greater than 2.3%.

4.2.1.7 Experimental Verification

Trials were conducted to experimentally verify the transducer deflection expressions and to establish scale relationships for piezomotor performance parameters. Deflection testing of the annular THUNDER™ transducers described in Table 4.2 was performed using the LVDT apparatus shown in Figure 3.3 in Chapter 3. A non-conductive polycarbonate stylus was used to prevent ground faults, and eliminate bias caused by the presence of insulation at the tip. The deflection of each sample was recorded under increasing values of electric potential and static load (see Appendix B). Figure 4.5 illustrates the cylindrical test fixture. Figure 4.6 is a plot of deflection at the edge of the hole versus outer diameter for 480V actuation with no applied load (*q=0*). This
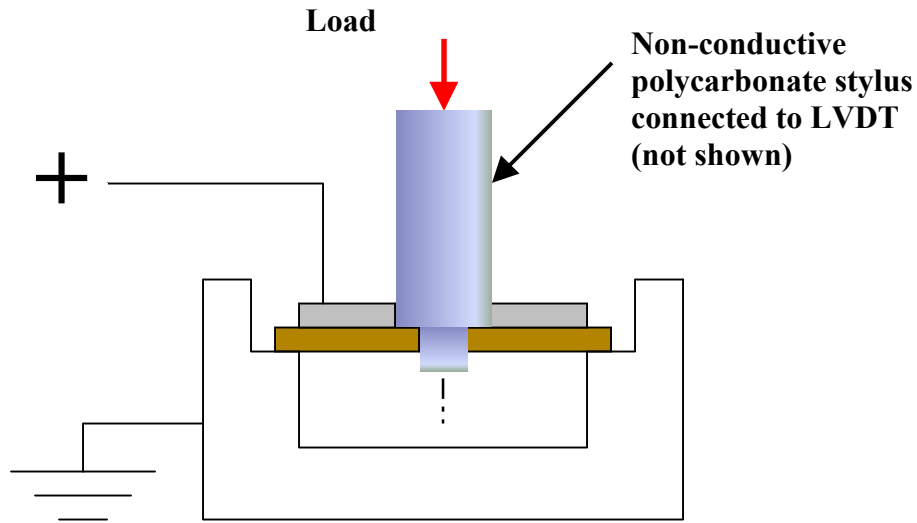
Figure 4.5. **Deflection test fixture**

condition allowed measured values to be plotted with the results of Equation 4.20 for a range of values of the piezoelectric strain coefficient. Error bars are included to reflect uncertainty in the LVDT calibration constant. Complete details of the deflection measurement and data processing procedure are included in Appendix B. The data confirms the model for outer diameters up to and including 0.875 inches. Agreement was poor in the case of the 1.75-inch transducer. Several attributes were considered in determining the root cause of the deficiency. First, the piezoceramic and substrate thickness of the transducers was verified to be consistent with the analytical values. Literature [82] was consulted to confirm that the greatest predicted deflection of 203 microns was less than one-half the total transducer thickness according to assumptions. The stiffening effect of
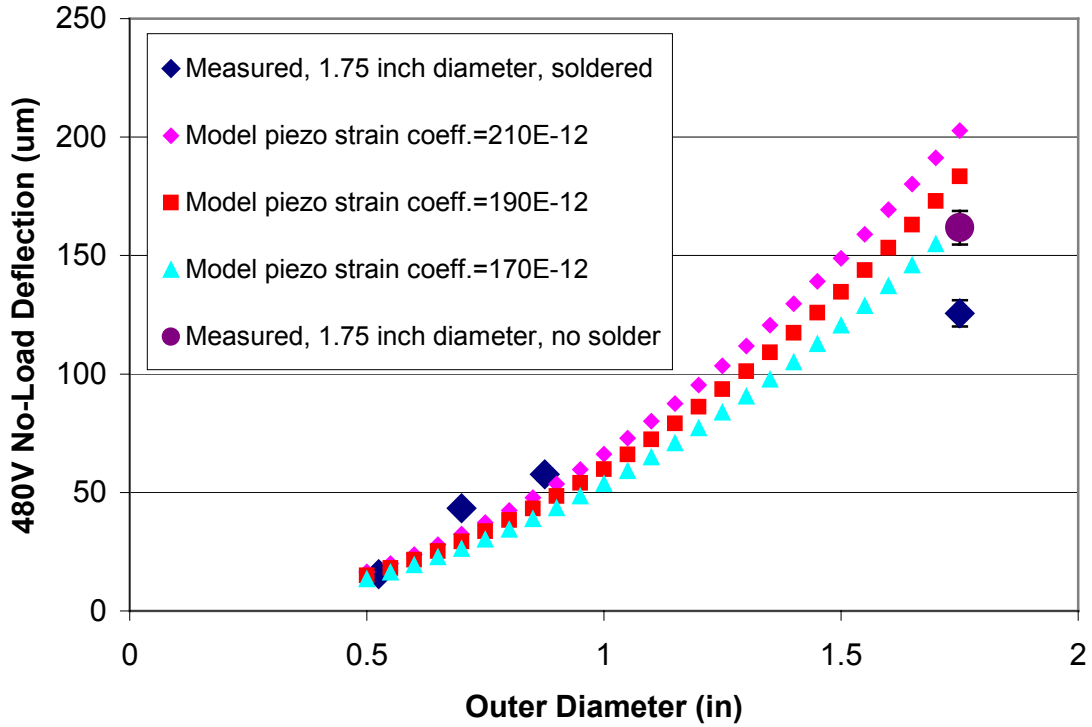
<u>Figure 4.6</u>. **Deflection vs. outer diameter for unloaded piezoelectric actuation at 480 volts**

substrate curvature (dome height) was also investigated without conclusive results (Young) [103]. Finally, electrical connections were checked. Since the 1.75-inch transducer was the only device tested that included soldered leads, it was postulated based on experience with piezoelectric materials (Uchino) [88] that the high-temperature process had altered the piezoelectric strain coefficient. To evaluate this theory, deflection testing was repeated on a 1.75-inch transducer and electrical lead attached with conductive tape. Results show that while there was little change in stiffness, deflection improved by nearly 30% (see Figure 4.6). Although agreement with the analytical expressions improves without soldering, it follows that there is insufficient evidence to support the validity of the deflection expression for transducers larger than 0.875 inches in diameter.

Experimental data for stiffness based on static deflection at zero volts is plotted in Figure 4.7. In this case, a range of load is applied to the stylus (see Figure 4.5), and the stiffness is best represented using Equation 4.17 (Sub Model 3). Deriving the stiffness involves solving for the load P_3 that produces a deflection of unity
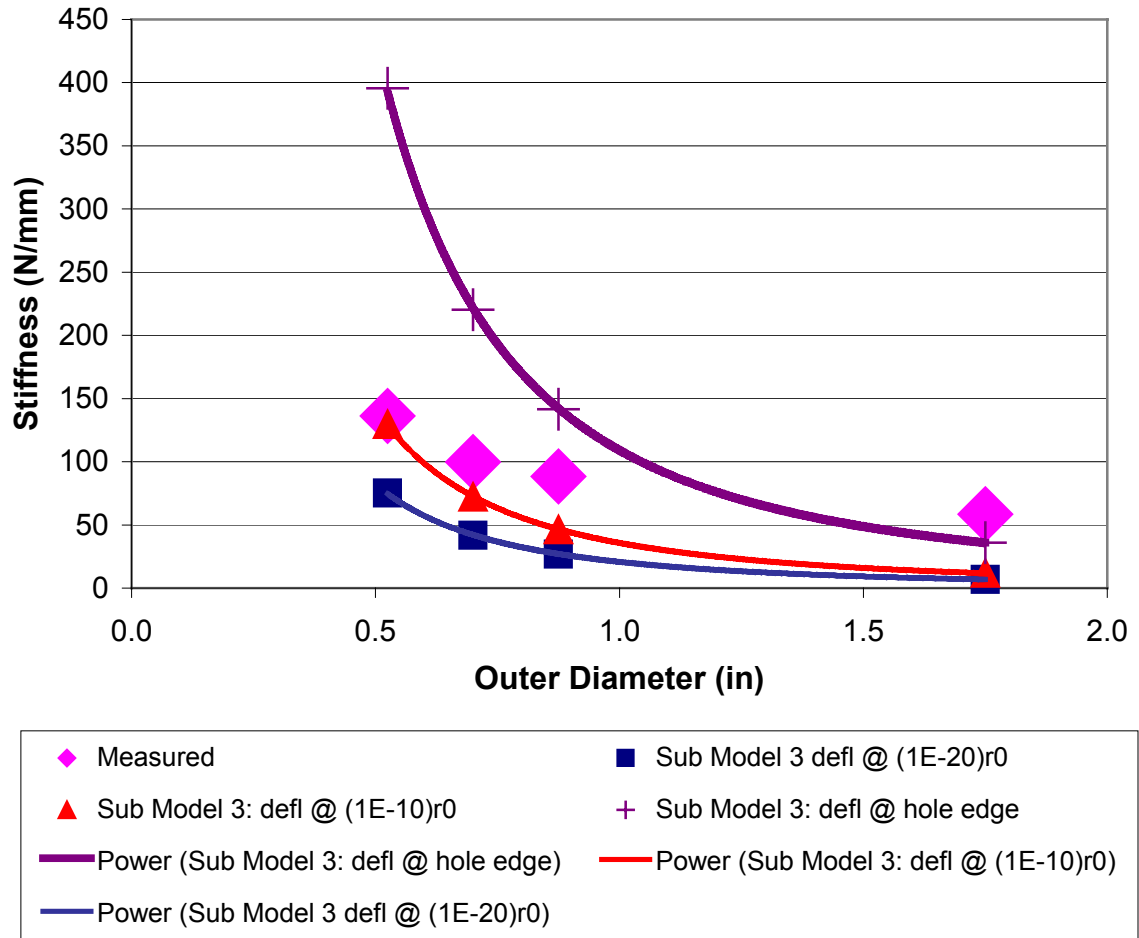
Figure 4.7. **Stiffness vs. outer diameter for static deflection at zero electric potential**

[31]. Three solution curves are plotted for different values of radial position *r*. The topmost curve in Figure 4.7 represents stiffness corresponding to deflection at the edge of the hole, r_h. Moving inward from the edge of the hole towards the center of the transducer, the deflection equation approaches a singular point. Consequently, the stiffness prediction for the 0.525-inch diameter transducer varies significantly when deflection is evaluated in closer proximity to the center. The best agreement with the measured stiffness data is observed when deflection is calculated at a radial position equal to $1 \times 10^{-10} r_o$. At $1 \times 10^{-20} r_o$, the stiffness falls below the measured values. Due to the discrepancy in the deflection measurements, the equation is not valid for predicting the stiffness of transducers larger than 0.875 inches in diameter.

4.2.2 Scale Factor Development

Consider the case of deflection at the edge of the hole under unloaded piezoelectric actuation at 480 volts. Setting the applied load q equal to zero and substituting r_h for r in Equation 4.20 yields:

$$w(r_h) = C_{19} \frac{r_h^2}{4} + C_{20} \ln\left(\frac{r_h}{r_o}\right) + C_{21} \qquad (0 < r_h \le r_i) \tag{4.22}$$

To determine the relationship between device performance and size, an expression that relates $w(r_h)$ to the outer radius r_o is derived. Inspection of Table 4.2 reveals that the hole radius and the outer radius of the piezoceramic layer are related to the outer radius of the device by constant fractions. Specifically, r_h is $0.142r_o$, and r_i is $0.865r_o$. Assigning values to the material properties and making the aforementioned substitutions in the expressions for constants C_{19}, C_{20}, and C_{21} reveal the following (see Appendix B for details):

$$C_{19} = a_0 \tag{4.23a}$$

$$C_{20} = a_1 r_o^2 \tag{4.23b}$$

$$C_{21} = a_2 r_o^2 \tag{4.23c}$$

where a_0, a_1, and a_2 are constants. Substituting these expressions into (4.22) results in:

$$w(0.142r_o) = \left(\frac{a_0 (0.142)^2}{4} + \ln(0.142) a_1 + a_2 \right) r_o^2 \tag{4.24}$$

Equation 4.24 suggests that the deflection of the annular THUNDER™ is directly proportional to the square of the outer radius. This finding is in agreement with documented results for the maximum deflection of a simply supported homogeneous circular plate under a central point load [82].

4.2.2.1 Scale Factor For Deflection

The relationship between deflection and outer radius can be expressed in terms of the scale factors defined in Section 4.2. Let scale factor s_w define the ratio of the homologous deflections at the edge of the hole between two annular THUNDER™ transducers of differing size and constant piezoceramic thickness. The implication of Equation 4.24 is that s_w is related to the scale factor for the outer radius as follows:

$$s_w \propto s_{ro}^2 \tag{4.25}$$

89

In this case, the constant of proportionality is the ratio of the term in parentheses in Equation 4.24 corresponding to each device. The next section explains how this process is extended to derive scale relationships for piezomotor performance measures such as zero potential equivalent stiffness, and actuator type blocked force.

4.2.2.2 Scale Factors For Stiffness and Piezomotor Blocked Force

As Section 4.2.1.7 explains, the stiffness of the annular THUNDER™ is derived from the deflection of Sub Model 3 at zero potential under a load P_3 acting very close to the center. Note that P_3 acts in the downward or negative sense in this case. To accurately simulate stiffness associated with deflection at the center, the radial position r was assigned a value of $1 \times 10^{-10} r_o$. In a manner similar to the previous segment, material property values are assigned, and r_h and r_i are defined as constant fractions of r_o. Making the appropriate substitutions in the expressions for the constants, and subsequently Equation 4.17, we arrive at the following relation:

$$w(0^+) = bP_3 r_o^2 \tag{4.26}$$

where b is a constant. Solving this expression for P_3 with a deflection of unity yields the stiffness:

$$k_i(0) = \frac{1}{b_0 r_o^2} \tag{4.27}$$

Thus, the zero potential stiffness is inversely proportional to the outer radius. It follows that the scale factor for stiffness, s_k, is related by the following:

$$s_k \propto s_{ro}^{-2} \tag{4.28}$$

The actuator type blocked force, introduced in the previous chapter, defines the limiting output force in a THUNDER™-based linear piezomotor. Alternatively, F_2 can be written as:

$$F_2 = mk_i(0)\delta_{0+} \tag{4.29}$$

where m denotes the number of transducers in parallel, and δ_{0+} signifies the near-center deflection under unloaded piezoelectric actuation at 480 volts. To find the scale factor for actuator type blocked force, the following substitution is made in Equation 4.29:

$$s_{F_2} \propto s_{ro}^{-2} s_{ro}^2 = s_{ro}^0 \tag{4.30}$$

This result implies that the actuator type blocked force is *invariant* with the outer radius, requiring that a scale factor based on another dimension must be developed. The thickness (height) of the device is the likely alternative. The total device thickness, h, is the sum of the substrate and piezoceramic layer thickness. Repeating the previous procedure generates the following relationship:

$$k_i(0) = b_1 h^3 \tag{4.31}$$

where b_1 is a constant. Similarly, the relationship for deflection under *unloaded piezoelectric actuation* is:

$$\delta_{0+} = \frac{b_2}{h^2} \tag{4.32}$$

Substituting these results in Equation 4.29 gives:

$$F_2 = mb_1b_2h \tag{4.34}$$

Thus, the scale factor may be redefined as:

$$s_{F_2} \propto s_t \tag{4.35}$$

Recall s_t is the ratio of homologous total thickness. It follows that actuator type blocked force varies directly with the total thickness, which suggests that F_2 should remain constant across the set of devices tested in this investigation. Due to the constant thickness of the test devices, the scale factor for actuator type blocked force could not be confirmed in this investigation, and is reserved for future work. Table 4.8 summarizes the scale factor findings. The consequences of the scale relationships are discussed in Chapter 6.

Table 4.8 **Scale Factor Summary**

Parameter	Scale Factor	Proportional To
Unloaded deflection under 480V actuation	s_w	s_{ro}^2
Zero potential device stiffness	s_k	s_{ro}^{-2}
Actuator type blocked force	s_{F_2}	s_t

4.3 Milliworm Characterization

The blocked force performance of the Milliworm 3A prototype was determined using the characterization apparatus shown in Figure 4.8.   The test setup includes a spring-loaded LVDT to apply load to the forward portion of the piezomotor, while a second LVDT captures displacement at the rear.   Table 4.9 lists performance data for the prototype containing three 0.525-inch THUNDERS, and compares it to predictions. The measured performance was far less than expected in all categories.   Moreover, performance was highly degraded when transducers were assembled in the module.   The next segment discusses this and other performance limitations.

Spring-loaded LVDT
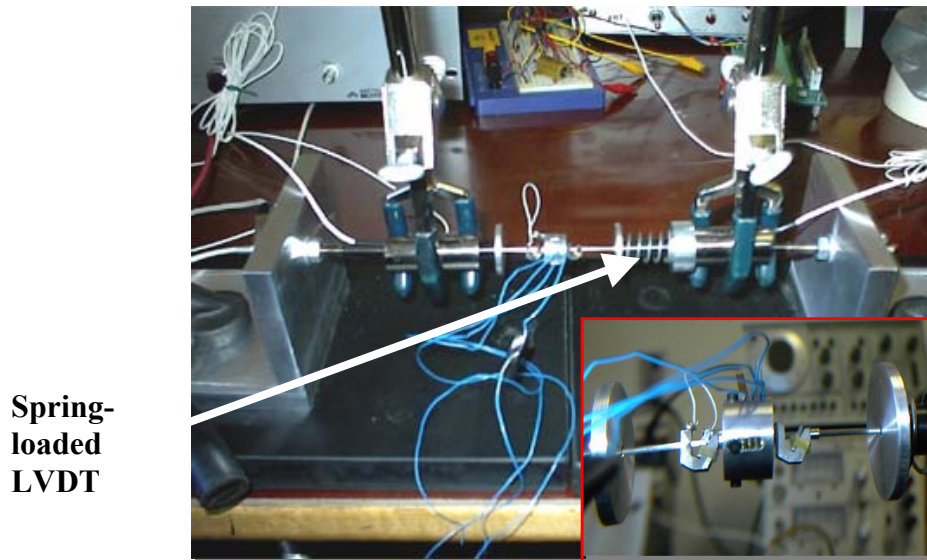
Figure 4.8. **Characterization apparatus**

Table 4.9 **Milliworm 3A Performance Summary**

Measure	Measured Value	Predicted Value: Three Transducers In Module	Predicted Value: Single Transducer Outside of Module
Average blocked force (N)	0.23	0.44	2.12
Maximum velocity (mm/s)	1 mm/s @ 100 Hz	1.7 mm/s @ 100 Hz	1.5 mm/s @ 100 Hz
Power density (mW/kg)	9.4	36.3	4035.9

4.4 Conclusions

The blocked output force of the Milliworm 3A prototype is curtailed by limiting factors in several aspects of the design, including the module, the latches, and the straightness of the rod. These factors work in concert to reduce the stiffness of the piezomotor, reduce its step displacement under load, and increase the level of frictional resistance. As the previous chapter explains, the piezomotor performs work against a load during the portion of the drive signal period when there is no electric potential on the THUNDER™ transducers. During this time, the elastic rebound of the THUNDERS pushes the forward latch against the load. Inasmuch as the extender module stiffness is large enough to push the latch against the load with enough displacement to overcome back slip in the latches, the blocked force will be greater than the resistance level encountered. This fact leads to the following observation regarding the stiffness of the Milliworm 3A extender module:

> *Even when pressed tightly together, gaps and compliant parts in the coupling and "C" ring assemblies contribute to settling in the extender module, which dramatically reduces its stiffness.*

Figure 4.9 compares the plots of stylus position (see Figure 4.5) versus load for the unpowered static deflection of a single 0.525-inch annular THUNDER™ in the case where it is mounted in the extender module, and when it is not. The data shows that the stylus moves much further downward when load is applied to the THUNDER™ mounted in the module. This condition suggests that the compliance of the module is greater than that of the free standing device. Since compliance is the inverse of stiffness, it follows that stiffness is reduced by nearly 80%. Back slip losses in the passive latches reduce the displacement output of the extender module in a given cycle. The amount of displacement loss depends on the load level. A trial was conducted to determine the amount of back slip versus load in the Milliworm 3A prototype with a single THUNDER™ mounted in the module. The LVDT displacement traces of the forward and rear latches were recorded via digital storage oscilloscope over a range of load. One such trace is shown in Figure 4.10. Constant patterns of back slip were not detected, and thus the greatest observed back slip was recorded in each case. It should also be noted that back slip levels less than 5 microns were difficult to capture due to noise in the displacement traces. Results show the greatest observed back slip was 9 microns on average. Excluding kinetic effects, the superposition model (see Chapter 3) predicted an average of 3.6. The high level of compliance in the extender module may contribute to the apparent lack of kinetic forward slip behavior. The pattern of low back slip
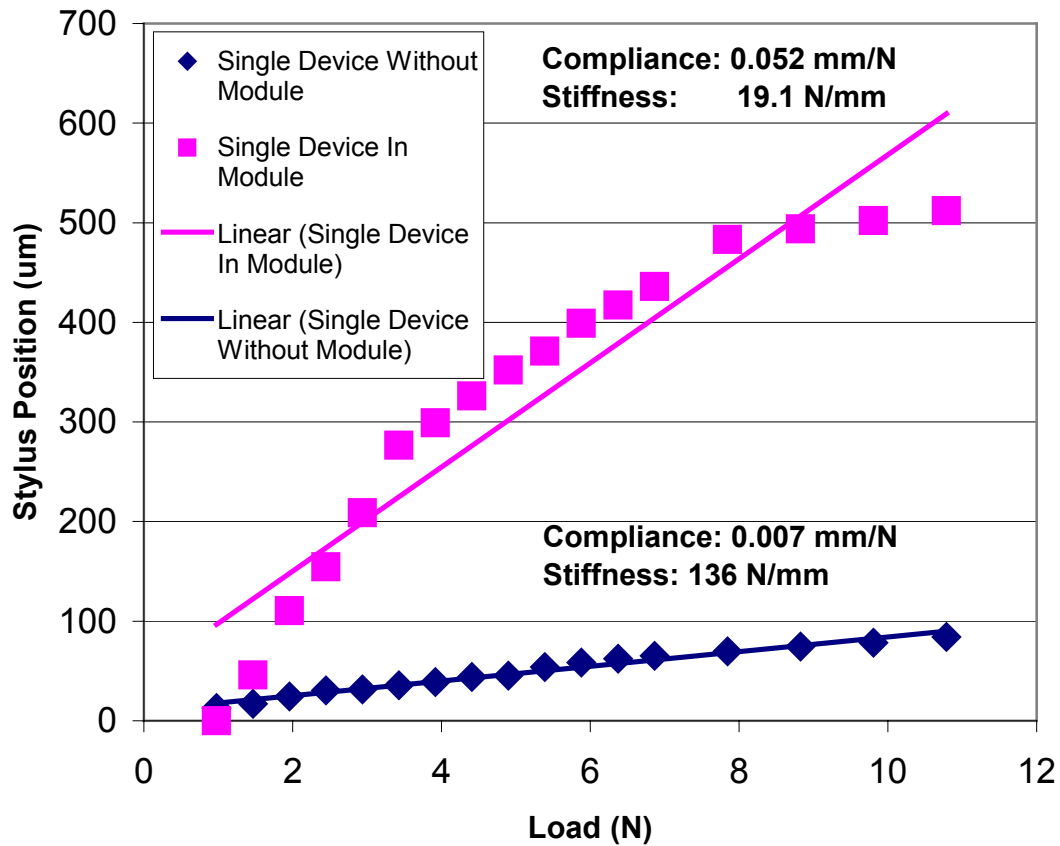
Figure 4.9. **Stylus position vs. load for static deflection at zero potential for a single 0.525" annular THUNDER™ mounted in, and outside of the extender module**

prediction is consistent with trials performed with previous piezomotors, and suggests that there exists an additional portion of back slip that the model does not address. Extra slip may likely be due to a small amount of sliding motion of the pawl relative to the rod prior to rotating to a closed position. Although an increase in pawl pre-load can remedy this condition, heavy pre-load levels tended to bind the piezomotor, and were not applied. Another significant limitation of the Milliworm 3A prototype is its high sensitivity to waviness in the rod. Even under tension, the piezomotor encountered many areas of high drag on the rod due to slight bends or high spots. Consequently, characterization trials were performed along short stretches of the rod where low friction was detected.
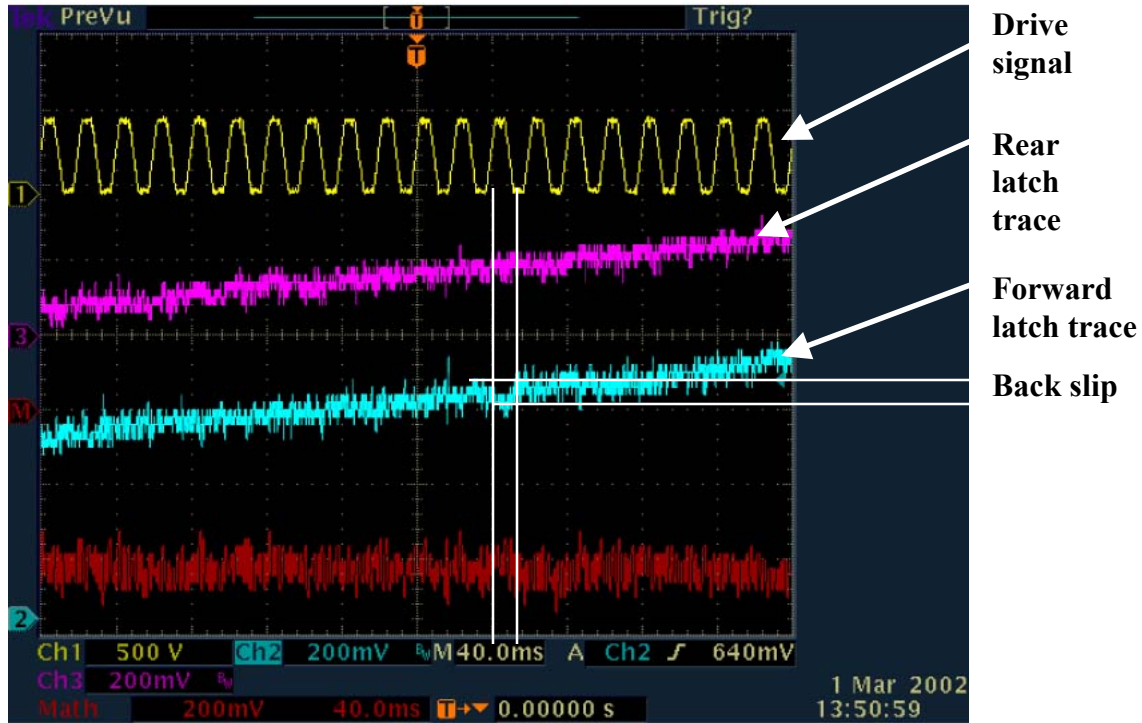
Figure 4.10. **Oscilloscope screen capture of forward and rear latch displacement traces showing evidence of back slip**

4.5 Future Work

The implementation the Milliworm 3A prototype demonstrates that a linear piezomotor can be realized at the millimeter scale using THUNDER™ stressed unimorph piezoelectric transducers. To be practical, the construction of the system must be improved to fully overcome what has been the Achilles heel of non-ultrasonic linear piezomotors. Namely, micron-size displacements are very difficult to harness without cumbersome amplification and clamping systems under exacting external control. The apparent loss of stiffness in the Milliworm 3A extender module can be curbed by introducing precision engineered components to eliminate gaps, and prevent settling under load. Additional benefits may arise from integrating the base plate, housing, and rear latch into a single component.

Chapter 5

Development and Analysis of A

Miniature Mode Conversion Rotary

Ultrasonic Motor

5.0 Introduction

Chapter 2 discussed the background and operational principles of rotary ultrasonic motors (USM's). That chapter established that a "motor gap" (see Figure 2.8) exists in the state of the art of miniature mechatronic technology (Mulling) [60]. In other words, there is a lack of miniature, high-torque, low-speed, rotary motor systems for use in direct drive microrobots. One objective of this chapter is to evaluate the torque capacity of a miniature mode conversion type rotary USM for the drive system of the N. C. State robotic jumping platform. A detailed discussion of the mode conversion design is included to supplement the basic principles covered in Chapter 2. Furthermore, an analysis is presented that predicts the dynamic characteristics of a miniature prototype, and identifies design parameters that influence torque.   These results are compared to characterization data.   The information presented in this chapter classifies the performance of the mode conversion design with (1.) size and (2.), commercially available electromagnetic and ultrasonic motors [60].

5.0.1 Justification

The decision to develop a miniature mode conversion design is supported by several arguments. First, the literature shows that the Kumada mode conversion design exhibits greater static torque density than USM's of comparable mass [60], (Glenn and Hagood) [33]. Its "tonpilz" transducer design is well understood and modeled by investigators such as Stansfield (Stansfield) [80]. Furthermore, the resonator assembly contains only a few components, a clear advantage for miniaturization. A design tradeoff exists in the fact that the mode conversion motor is reversible with frequency, whereas hybrid transducer USM's alter direction more easily by shifting the relative phase of multiple drive signals (Ueha and Tomikawa) [87]. Based on the results obtained, the principal contributions of this work are summarized as follows:

- A solid state, miniature, mode conversion type rotary ultrasonic motor has been created and characterized with the primary objective of optimizing static torque density. Static torque density is defined by the ratio of static (stalled rotor) torque to motor mass.

- In support the primary objective, a series of miniature prototypes with various L/T coupler designs were constructed to determine the impact of L/T coupler design on torque. The static torque, maximum power, and efficiency of the prototypes were measured.

- Expressions for the dynamic behavior of the system were developed to identify parameters that influence performance. Computational results are compared to experimental data for accuracy.

This motor is intended for use in direct drive miniature and micro robots up to 3 cubic centimeters in volume. Without external gearing, conventional electromagnetic motors exhibit low static torque capabilities in this size range (Khatib, Craig, and Lozano-Perez) [46, 60]. A comparative study of electromagnetic and rotary ultrasonic motor performance [60] suggests that the mode conversion design, with its attributes of high static torque and relatively simple construction, is well suited for miniature robotic applications.

5.0.2 Prototype Description

Figure 5.1 depicts the N.C. State prototype mode conversion USM. The tonpilz resonator (enclosed by dashed lines) includes an annular stack-type piezoelectric transducer bonded to a set of steel masses [80]. The head mass (or "horn") is at the forward edge of the stack, the tail mass (or "base") is located at the rear [80]. A center bolt (brass), is threaded through the center of the masses, and maintains the required compressive stress on the stack. This assembly with the L/T coupler comprises the *stator*. The stator produces longitudinal
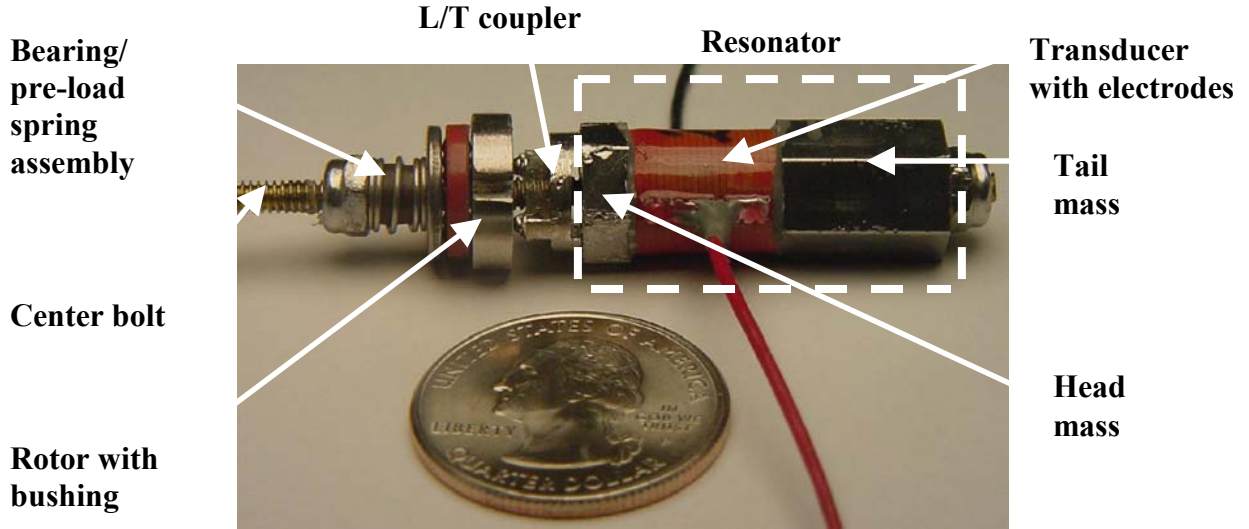
Figure 5.1. **N. C. State miniature mode conversion USM prototype**

resonant vibrations that are converted to elliptical displacement at the tip of the L/T coupler. The *rotor* assembly receives the elliptical displacement and corresponding frictional couple produced by the stator, and outputs useful torque. It includes the rotor, and the forward pre-load assembly, consisting of a coil spring, thrust bearing, and lock nut. The pre-load assembly delivers a normal force (referred to as the *static pre-load*) that presses the rotor against the L/T coupler. The following sections detail the rotor and stator designs.

5.0.2.1 Resonator Design

Resonator design involves selecting two key parameters: (1.) the center bolt size and material, and (2.) the size of the masses. To prevent tensile damage, the transducer manufacturer recommends the stack be loaded in compression (see www.physikinstrumente.com for details). The total compressive force must be 20% of the compressive load limit of 500 N, or 100 N (PI Corporation). The support member that delivers the load (in this case, the center bolt) should have a stiffness 10% that of the stack (PI Corporation). Thus, if the published stack stiffness is 1×10^8 N per meter (PI Corporation), the center bolt material and dimensions are determined by iterating on the expression for the equivalent stiffness of an axially loaded rod (Rao) [73]:

$$k_{cb} = \frac{E_{cb} A_T}{L_{cb}} \tag{5.1}$$

where k_{cb} is the stiffness, E_{cb} is the elastic modulus, A_T is the tensile area of the threaded center bolt (Avallone and Baumeister) [3], and L_{cb} denotes its length. In this program, a UNC 4-40 center bolt with a tensile area of 4×10^{-6} square meters was initially proposed [3]. The portion passing through the resonator was planned to be at least 14 mm in length. Substituting these values and the required bolt stiffness into (5.1) and solving for the elastic modulus yields a minimum value of 35 GPa. This result suggested that a soft metal such as aluminum or brass is appropriate. Machining considerations ultimately led to the use of free cutting brass, similar to UNS C36000 (see www.matweb.com for details). Stansfield provides the following guidelines for sizing the masses (see Chapter 2) [80]. First, the tail mass should be designed with a volume and inertia greater than the head mass in order to direct kinetic energy forward toward the rotor [80]. Second, the resulting resonator should have a low quality factor, and therefore a wide bandwidth. Noting these guidelines, a trial and error approach was adopted here, one where the performance of a series of prototypes with varying mass combinations was observed. The set that delivered the most noticeable improvement in torque and velocity output was ultimately chosen. Table 5.1 lists the dimensions and performance specifications of the final resonator design calculated from equations 2.1, 2.2, and 2.3. The resonator was assembled as follows. First, the tail mass was

<u>Table 5.1</u> **Resonator Specifications**

Parameter	Value	Units	Comment
Head Mass, M_H	0.003	kg	
Tail Mass, M_B	0.0094	kg	
Resonator Length	0.030	m	L_{cb} (this value is approximately $\lambda/4$)
First Natural Frequency, ω_l	2.37×10^5	rad/sec	37.8 kHz, calculated from Equation 2.3
Acoustic Wavelength, λ	0.136	m	
Acoustic Radiation Resistance, R_r	82.3	kg/sec	Calculated from Equation 2.2
Mechanical Quality Factor, Q_M	1.8		Calculated from Equation 2.1
Bandwidth, $\Delta\omega$	1.3×10^5	rad/sec	21 kHz

threaded onto the center bolt. The stack was then bonded to it using a high stiffness epoxy. This step was repeated for the head mass. Lastly, the masses were carefully tightened against the stack to provide compressive stress without damaging it.

5.0.2.2 L/T Coupler Design

The L/T coupler (see Figure 2.6) is mounted to the head mass at the outer perimeter. The beam or spine segment on the upper portion of the L/T coupler is offset from the longitudinal plane of symmetry by an angle of twenty-six degrees. As discussed in Chapter 2, this unique geometry converts the longitudinal vibration of the resonator to elliptical displacement at the outlying edges of the beam where embedded ball bearings make point contact with the rotor assembly. The hardened steel ball bearings are mounted in holes in the top face of the beam, and fixed with epoxy. Point contact was observed to enhance prototype performance by transmitting acoustic energy more efficiently than planar contact. To facilitate development trials, the L/T coupler was not bonded to the resonator. Consequently, this interface represented a potential source of energy loss in the system. L/T coupler dynamics are explored further in Section 5.1.

5.0.2.3 Rotor Assembly Design

The rotor pivots about a nylon bushing mounted to the center bolt. Notches cut in the side allow the rotor to be interfaced with an external load for torque testing, and provide for optical velocity measurements. A thrust bearing reduces friction between the rotor and the pre-load assembly components. The magnitude of the static pre-load is adjusted by turning the lock nut, which compresses the pre-load spring. Use of a lock nut is essential, as the vibration of the center bolt causes common nuts to shake loose. Section 5.1 discusses the role of pre-load as an essential ingredient for developing torque in the USM.

5.1 Analysis

Two separate mechanisms were studied to aid the understanding of the operating principles of the prototype mode conversion USM. First, the dynamic response characteristics of the stator assembly were determined. The dynamic response defines the operating frequencies, and characterizes the elliptical displacement pattern of the L/T coupler. Second, the equation of motion of the USM was derived. This yielded the static torque, and rotor velocity profile.

5.1.1 Stator Frequency Response

The experimental portion of the program included a study to observe the response spectrum of the stator. Specific objectives of the study included identifying the resonant frequencies, and measuring the amplitudes and phase difference of the longitudinal and tangential (torsional) displacements at the tip of the L/T coupler. Figure 5.2 illustrates the test apparatus constructed to measure the stator response to a range of
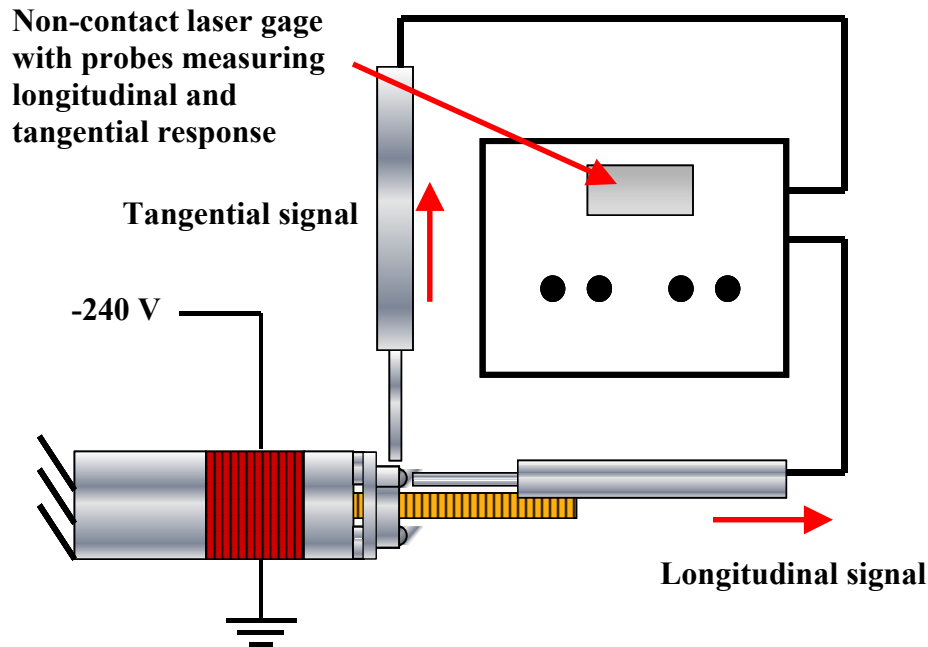
Figure 5.2. **Non-contact laser gage apparatus for measuring stator frequency response**

sinusoidal inputs. The PI model P305.10 stack transducer was powered by a set of amplifiers generating greater than 240 volts peak-to-peak with negative polarity. The two-stage amplifier system (not shown) included a lock-in amplifier generating a 5-volt ultrasonic signal, connected to a high voltage amplifier with a gain of 60. The longitudinal and tangential displacement over the range of 15 to 80 kHz was measured using a non-contact laser gage interfaced to a digital storage oscilloscope (not shown). The response spectrum is plotted in Figure 5.3. The plot confirms the presence of a strong resonance near 43 kHz. It is characterized by a longitudinal signal with amplitude greater than 3.5 microns peak to peak that leads the tangential signal. The tangential signal has a peak to peak amplitude greater than 1.5 microns. The data listed in Table 5.1 suggests that this
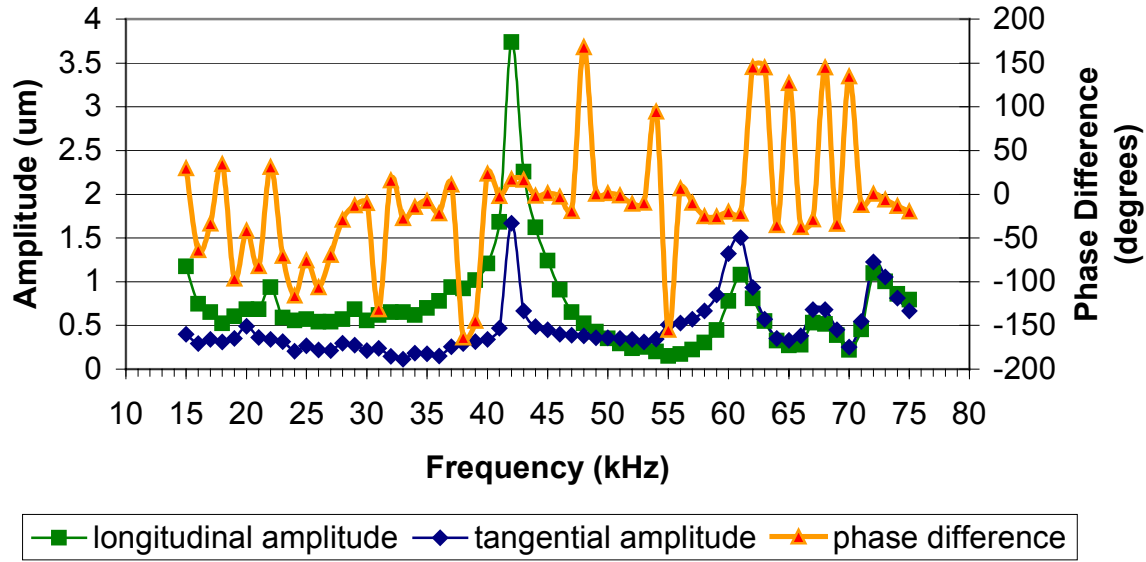
Figure 5.3. **Stator response spectrum for standard L/T coupler**

peak corresponds to the fundamental frequency of the resonator assembly. A dynamic finite element model of the stator agrees with the vibration experiments (Palmer, Kennedy, Mulling, Gruverman, Grant, Kingon, Franzon, and Eischen) [68], and indicates that the L/T coupler mode shape at this frequency corresponds to that shown in Figure 2.6 (Chapter 2). Although it can run at any resonant frequency with the correct mode shape, the USM prototype ran most reliably near 43 kHz. Hereafter, this is referred to as the *primary operating frequency*.

The phase difference between the longitudinal and tangential response was measured with the lock-in amplifier, which allowed comparisons to be made between the input signal, and feedback from the oscilloscope. A Lissajous figure, which is the plot of the tangential versus longitudinal signals, was used to display the shape of the displacement locus at the tip of the L/T coupler (Tsujino, Suzuki, and Takeuchi) [85], (Ueha and Tomikawa) [87]. The displacement locus at the primary operating frequency, with the standard L/T coupler, lacked clarity. However, well-defined elliptical patterns were observed at the primary operating frequency in alternate L/T coupler designs (see Figure 5.4 (d)). Figures 5.4 (a), (b), and (c) illustrate how the ellipse changes shape and orientation with phase angle. At 0 and 180 degrees, the ellipse collapses and becomes a line (Figure 5.4 (a), (c)), indicating a pattern of "jackhammer" impulses (Uchino) [88]. Conversely, a phase angle of 90 or

(a)

(b)

(c)

(d)
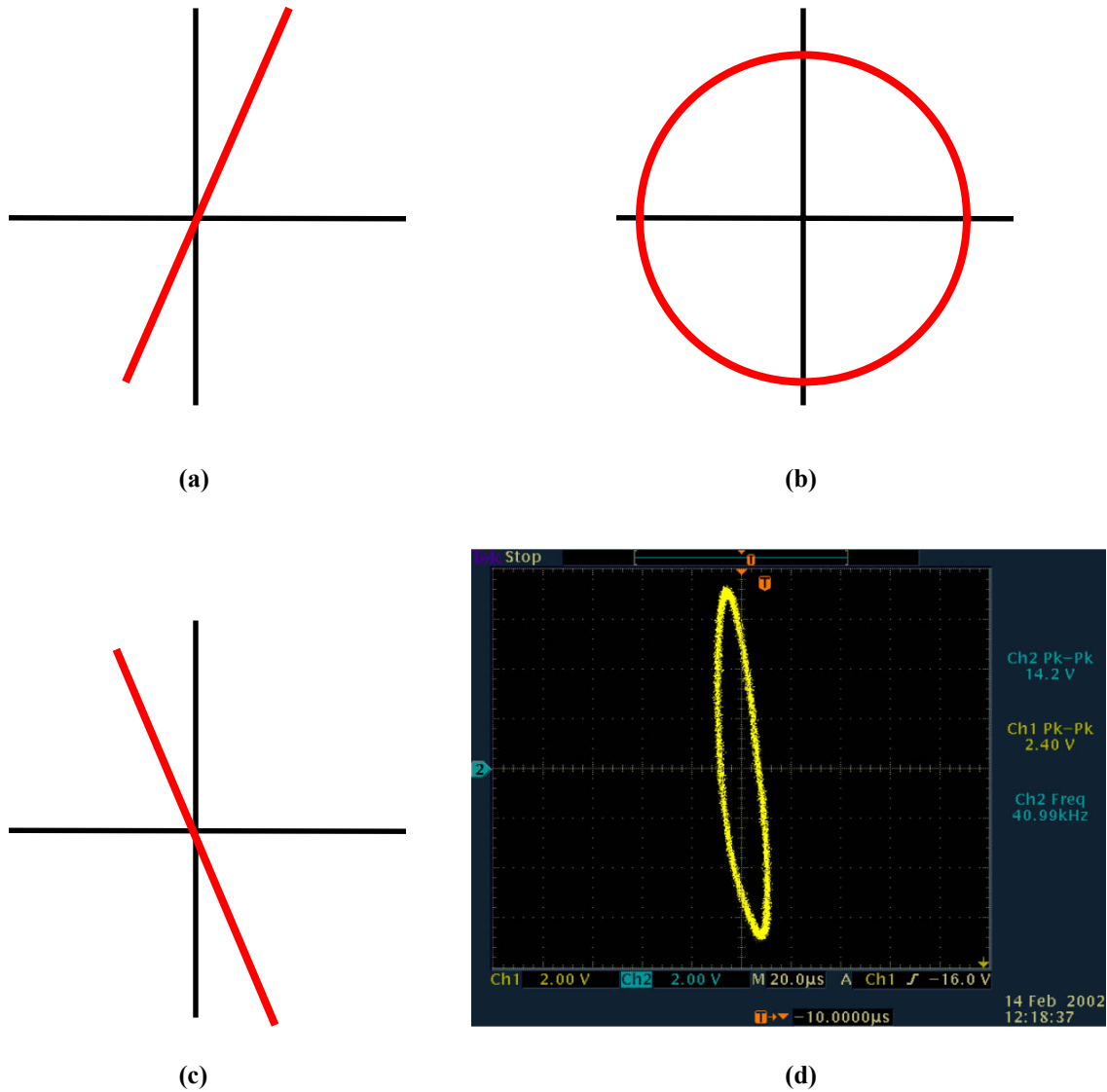
<u>Figure 5.4</u>. **L/T coupler elliptical displacement locus for various phase angles: a.)   0/360 degrees, b.) 90/270 degrees, c.)   180 degrees, d.)   Oscilloscope Lissajous screen capture (alternate tall beam L/T coupler design near the primary operating frequency)**

270 degrees traces a circular locus. In experiments with the prototype USM, the phase angle (and the shape of the ellipse) changes when the drive signal frequency is varied. This in turn alters the L/T coupler mode shape [85, 87, 88]. As Section 5.1.2 explains, a non-zero phase difference is necessary for the USM to operate if factors such as pre-load assembly response and variations in friction are not considered.

5.1.2 Equation of Motion

The equation of motion of the USM was derived for the purpose of predicting the maximum steady state rotor velocity, and the frictional torque exerted by the stator. Figure 5.5(a) depicts the quasi-static free body diagram of the rotor/stator interface, while Figure 5.5(b) is a dynamic free body diagram of the rotor.

(a)   (b)
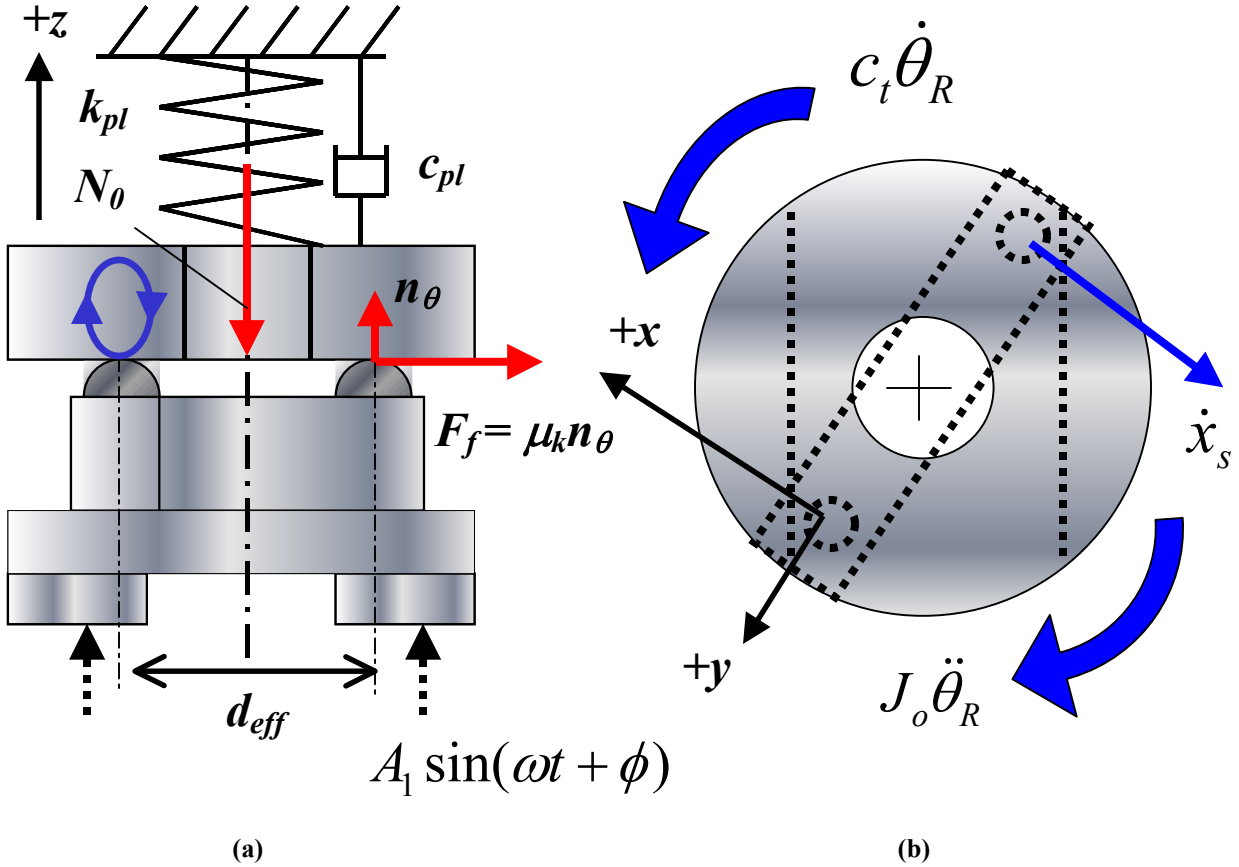
Figure 5.5. **USM free body diagrams: a.) Rotor/Stator quasi-static (side view), b.) Rotor dynamic (top view looking down on L/T coupler)**

Referring to Figure 5.5 (a), the rotor and pre-load assembly is represented by a single degree of freedom damped mass-spring system [73]. The transient response of the rotor/pre-load assembly was not considered in the model. It was assumed to move in phase with the stator, and that it remains in continuous contact at all times (Bauer) [5, 87, 88]. This assumption simplified the model derivation, but imposes a restriction on how a time varying pre-load is simulated.

As the stator oscillates in the longitudinal (axial) direction, the magnitude of the static pre-load force exerted on the stator varies due to contributions from inertial and non-inertial (i.e. static) effects. To understand these contributions, consider the expression for longitudinal stator vibration in the z direction:

$$z_s = A_1 \sin(\omega t + \phi) \tag{5.2}$$

where A_1 is the longitudinal amplitude, ω is the frequency in radians per second, and ϕ is the phase difference relative to the input signal measured in radians (assumed to be zero in initial runs of the model). The motion of the stator causes the pre-load to oscillate about its static magnitude, N_0, according to the following function:

$$n_{\theta s} = z_s k_{pl} + N_o \tag{5.3a}$$

where $n_{\theta s}$ is the dynamic or time-varying pre-load due to non-inertial forces, and k_{pl} is the stiffness of the pre-load spring. Since A_1 is on the order of microns, the amplitude of the dynamic pre-load is very small, and may be neglected. Greater amplitude arises if the inertial force of the rotor is addressed. As the rotor is accelerated upward by the stator (see Figure 5.5 (a)), its resistance to a change in velocity (its inertia) generates a force proportional to the acceleration according to Newton's Second Law (Serway) [77]. Differentiating Equation 5.2 twice with respect to time and multiplying by the rotor assembly mass (approximately 4 grams) yields:

$$n_{\theta_d} = \begin{cases} -M_R A_1 \omega^2 \sin(\omega t + \phi) + N_0 & \sin(\omega t) > 0 \\ N_0 & \sin(\omega t) \le 0 \end{cases} \tag{5.3b}$$

where $n_{\theta d}$ is the dynamic pre-load due to inertial forces, and m_R is the mass of the rotor assembly (the spring is assumed to be massless). The pre-load amplitude resulting from Equation 5.3 (b) is greater than 500 N, and leads to very high torsional impulses on the rotor. Simulation data shows that neither equation yields accurate results. As a compromise, the following pre-load function is adapted from the literature [87, 88, 5]:

$$n_\theta = N_0(1 + \sin(\omega t + \phi)) \tag{5.3c}$$

An investigation of the specific mechanism(s) that limit the amplitude of the pre-load is reserved for future work. In this case, use of Equation 5.3 (c) according to prior art produces a consistent estimate of the dynamic friction force F_f shown in Figure 5.5.

Frictional contact between the rotor and stator results in a couple exerted on the rotor when the tip of the L/T coupler deflects in the positive x direction. Hence the instantaneous torque is written as:

$$\tau_i = \mu_k n_\theta d_{eff} \tag{5.4}$$

where μ_k is the coefficient of kinetic friction (assumed constant 0.47, dry mild steel on aluminum [3]), and d_{eff} is the effective rotor diameter described by the distance between the L/T coupler contact points. Likewise, the continuous torque is the time average of the instantaneous torque over the drive signal period (Ragulskis, Bansevicius, Barauskas, and Kulvietis) [72]. Theoretical maximum torque involves the static pre-load, and is defined as follows [87]:

$$\tau_{i_{max}} = \mu_k N_0 d_{eff} \tag{5.5}$$

Equations 5.4 and 5.5 represent theoretical estimates of USM torque performance. Actual performance is gauged by measuring static torque (see Section 5.2). With equations 5.3 through 5.5 established, the model hypothesis may now be stated:

- The period of the stator vibration may be divided into two segments: the *drive stroke* and the *return stroke*. The drive stroke occurs over the first half of the drive signal period, while the return stroke takes place over the latter half of the drive signal period.

- During the drive stroke, the stator expands upward in the positive z direction, while the tip of the L/T coupler deflects in the positive x direction. Assuming the rotor is rigid, the upward expansion increases the magnitude of the dynamic pre-load force n_θ exerted on the rotor according to Equation 5.3 (c) (see Figure 5.5).

- During the return stroke, the L/T coupler returns to its original shape. The stator works *against* the rotor during the return stroke. However, the contraction of the stator reduces the magnitude of the dynamic pre-load.

- Assuming there is a nonzero phase difference between the longitudinal and tangential components of the stator displacement, the average magnitude of the dynamic pre-load is larger on the drive stroke than on the return. Hence there is a resultant frictional torque available to drive the rotor.

Mathematically, the hypothesis implies that the instantaneous torque changes its sense from positive to negative during the drive signal period. This condition is expressed using the *signum* function, [72, 5, 88]:

$$\text{sgn}(x) = \begin{cases} 1 & (x > 0) \\ -1 & (x < 0) \\ 0 & (x = 0) \end{cases} \tag{5.6}$$

In this case, the argument of the signum function is the relative velocity of the rotor and the stator. The equation of motion of the USM incorporates this function, and is listed below:

$$J_0\ddot{\theta}_R + c_t\dot{\theta}_R = \text{sgn}\left[\dot{\theta}_R - \dot{\theta}_S\right]\mu_k n_\theta d_{eff} \tag{5.7}$$

where J_0 is the polar mass moment of inertia of the rotor [73], and c_t is the coulomb damping coefficient (the sign of this quantity is negative). Simulation of damping was omitted in this program, and c_t is assigned a value of zero accordingly. The subscript R denotes the angular position of the rotor, and S, the stator. The rotational velocity of the stator involves differentiating the tangential displacement as follows:

$$\dot{\theta}_S = \frac{2A_2\omega}{d_{eff}}\cos(\omega t + \phi + \varphi) \tag{5.8}$$

where A_2 is the measured peak-to-peak tangential amplitude, and φ represents the phase difference between the longitudinal and tangential displacements.

In theory, a non-zero phase difference between the longitudinal and tangential stator displacements is necessary for the USM to produce constant velocity and torque. Consider the stator waveforms shown in Figure 5.6. The longitudinal stator displacement is shown in phase with the tangential waveform in Figure 5.6 (a). This phase relationship corresponds to the "jackhammer" displacement locus (see Figure 5.4 (a)). The portion of the dynamic pre-load curve marked by red lines represents the return stroke (a period of decreasing pre-load). Concurrently, the portion of the tangential displacement curve marked by green dashed lines indicates tangential displacement of the tip of the L/T coupler in the negative x direction. By inspection, it is evident that while the stator is driving the rotor in the negative x direction, the magnitude of the dynamic pre-load changes from a maximum to a minimum value. More importantly, the exact *opposite* occurs when the stator drives the rotor in the positive x direction. Consequently, equal and opposite torsional impulses are applied to the rotor during the period of stator vibration, and the net torsional impulse is zero. The rotor will oscillate forward and reverse, but will not turn continuously. Figure 5.6 (b) illustrates a 90-degree phase difference between the tangential and pre-load waveforms. In this case, tangential motion of the stator in the negative x direction occurs while the pre-load amplitude is above its static value. Thus, there is a larger torsional impulse applied in one direction than the other, and the rotor turns continuously. To support this argument, an investigation was conducted in which the dynamic analysis was run for longitudinal/tangential phase difference varying between 0 and 180 degrees. Results indicate a parabolic relationship between phase angle and steady state velocity,

(a)   **(b)**
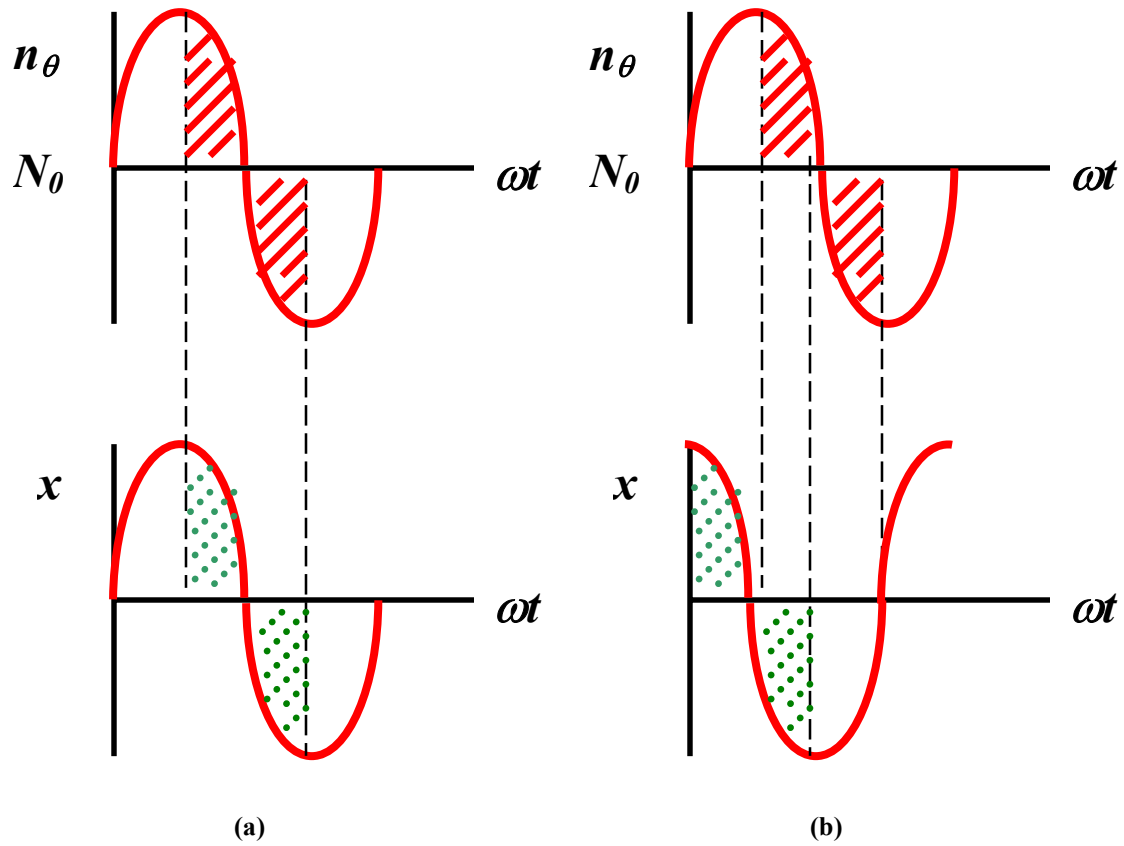
Figure 5.6. **Comparison of stator phase relationships: a.) 0° phase difference, b.) 90° phase difference**

where the greatest steady state velocity occurs at 90 degrees (see Appendix C). At this point, it is important to note that one cannot conclude from this argument alone that the jackhammer displacement locus will not drive the rotor in the USM prototype. On the contrary, it may work in more realistic conditions where the response of the rotor assembly affects the dynamic pre-load level during the return stroke, and the coefficient of kinetic friction changes with the direction and velocity of the rotor [3].

5.2 Prototype Characterization

In support of the research objectives stated in Section 5.1, an experimental program was conducted to characterize the performance of the prototypes with various L/T coupler designs, and verify the accuracy of the system model. An apparatus was developed to measure parameters leading to the static torque, power, and efficiency of the prototypes (see Section 5.2.1). The following segment introduces the test apparatus and

procedure, followed by a discussion of the prototype L/T coupler designs and the associated stator frequency response. Finally, torque performance data is presented, and compared to model results.

5.2.1 Torque Test Apparatus and Procedure

Figure 5.7 depicts the torque test apparatus. The torque test procedure involved applying a load to the
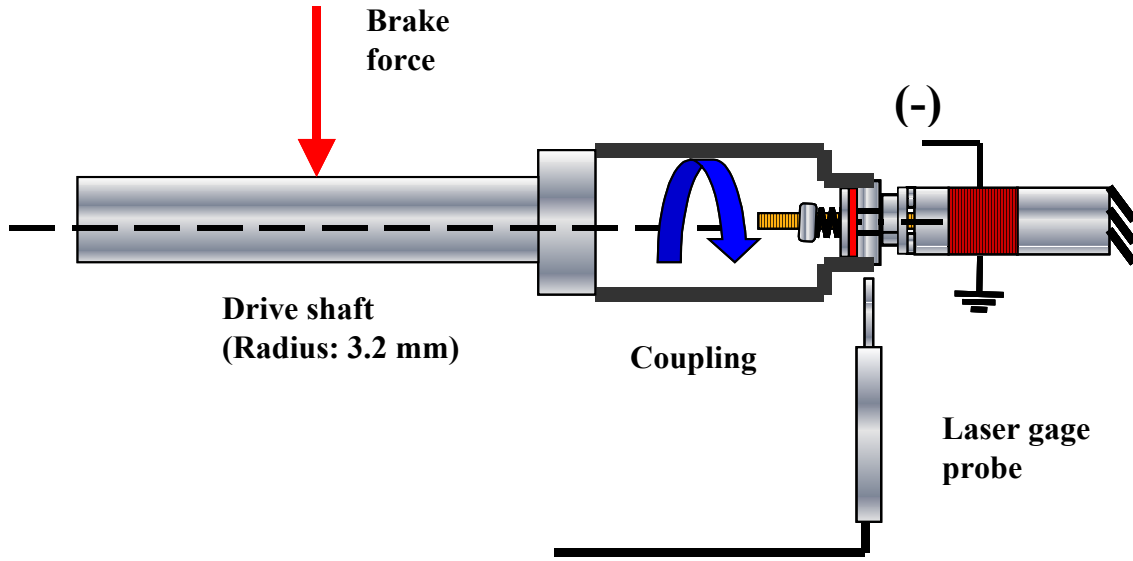
Figure 5.7. **Torque test apparatus**

rotor, then starting the prototype from rest and measuring the corresponding steady state velocity using the non-contact laser gage (see Figure 5.2). A battery-driven dynamic circuit provided power to the USM. The rotor load was varied by mounting a series of weights on a brake shoe pressed against a drive shaft coupled to the rotor of the prototype. The static or stalled rotor torque, τ_s, was extrapolated from the linear plot of rotor velocity versus brake force. The instantaneous mechanical power is written as follows:

$$P_i = \mu_k mgr_s \omega \qquad (5.9)$$

where m is the applied mass (kg), g is the local gravitational acceleration (9.81 m/s^2), and r_s is the driveshaft radius in meters (see Figure 5.7) [77]. Note that the coefficient of kinetic friction in Equation 5.9 is reassigned to reflect dry contact between steel and aluminum. A mechanical power curve for the USM can be derived from Equation 5.9 and the rotor velocity versus brake force plot. Multiplying the slope and intercept of this plot

by the appropriate constants and rewriting the linear expression results in the following relationship between rotor velocity and the load torque:

$$\omega = C(\mu_k mgr_s) + D \tag{5.10}$$

where C and D are constants (note that C is a negative slope). Solving Equation 5.10 for the quantity in parentheses and substituting the result in Equation 5.9 yields:

$$P_i = \left[\frac{\omega^2 - \omega D}{C} \right] \tag{5.11}$$

Equation 5.11 reveals that the power curve is parabolic. Differentiating with respect to ω, setting the result equal to zero, and subsequently solving for ω identifies the maximum of the power curve. Substituting the result in Equation 5.11 reveals the maximum power:

$$P_{out} = \left[\frac{\left(\frac{D}{2}\right)^2 - \left(\frac{D}{2}\right)D}{C} \right] = -\frac{D^2}{4C} \tag{5.12}$$

Static torque and power data was recorded for the set of USM prototypes with alternate L/T couplers described in the following segment.

5.2.2 Alternate L/T Coupler Designs

A set of three L/T couplers was fabricated to determine if alternate designs could improve static torque performance. Designs were selected based on dynamic finite element model data [68] that indicated which combination of parameters relative to the standard configuration led to (1) greater longitudinal and tangential displacements near the primary operating frequency, and (2) enhancement of higher order modes (see Figure 2.6). The following design parameters were varied with the strategy of creating and/or improving displacement amplification structures:

- Height of the beam/spine
- Thickness of the base
- Position of the contact points with the rotor

The final designs are pictured in Figure 5.8. The "winglet" design at the left of Figure 5.8 features rotor contact points that are displaced approximately 2 mm tangentially from the standard position. The so-called tall beam
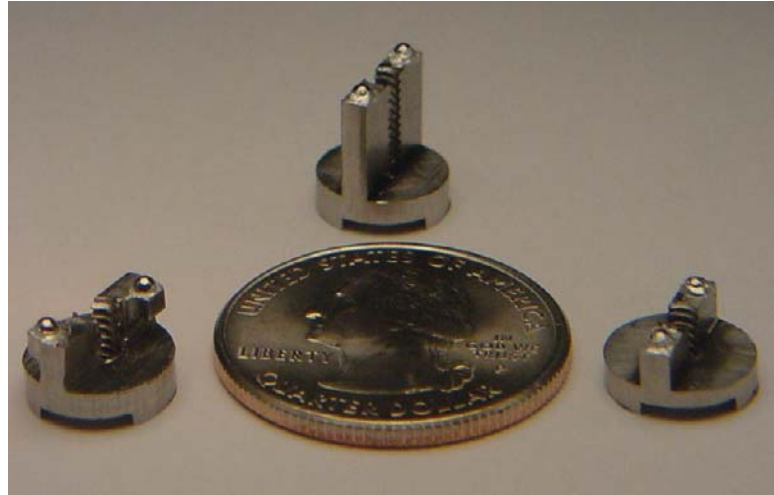
Figure 5.8. **Alternate L/T couplers: tall beam (top), displaced contacts or "winglet" (left), and thin base (right)**

design at the top of the figure has a beam height that is 2.5 times larger than the standard. Lastly, the designation of "thin base" is given to the design shown on the right. Its base thickness is 1.5 times less than the nominal dimension. The displacement spectra for each L/T coupler are shown in Figure 5.9. Inspection of the plots reveals that the tall beam design shown in Figure 5.9 (b) exhibits the greatest longitudinal and tangential displacement at the primary operating frequency relative to the standard. The winglet and thin base designs amplify tangential displacement at the primary operating frequency, and cause strong tangential peaks at 60 kHz. All designs maintain a similar phase relationship at the primary operating frequency. Section 5.2.3 shows how the tall beam design is associated with increased static torque density.

5.2.3 Experimental Results

Figure 5.10 shows the response spectrum between 30 and 50 kHz for the prototype with the rotor and tall beam L/T coupler assembled. The red diamonds in the figure denote, on an arbitrary scale, how well the motor ran at a particular frequency, with 5 signifying continuous operation with high steady state velocity. Inspection of the plot reveals that with regard to the tall beam prototype, best performance is associated with a peak in both longitudinal and tangential displacement. The addition of the rotor changed the value of the longitudinal/tangential phase difference at any given frequency, although the pattern of phase difference changes was preserved in portions of the frequency band shown.
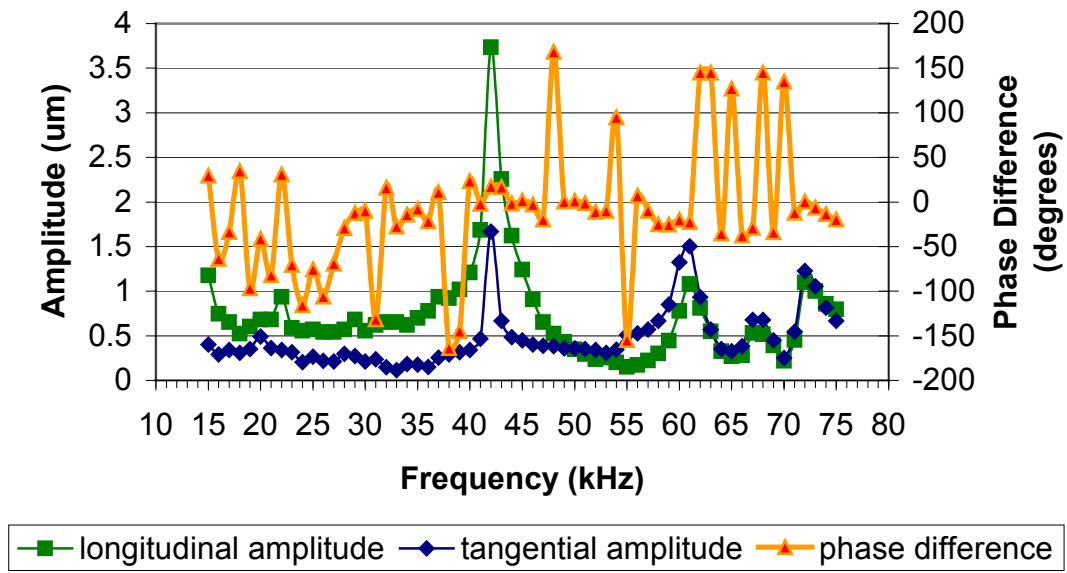
(a)
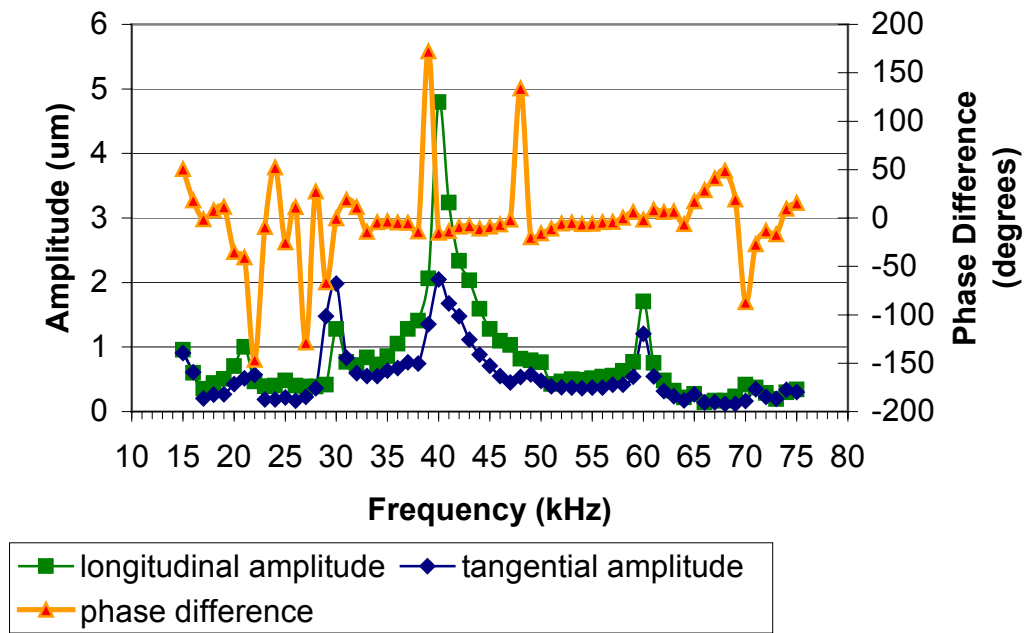
(b)

<u>Figure 5.9</u>. **Frequency response spectra for alternate L/T coupler prototypes: a.) Winglet, b.) Tall beam, c.) Thin base**
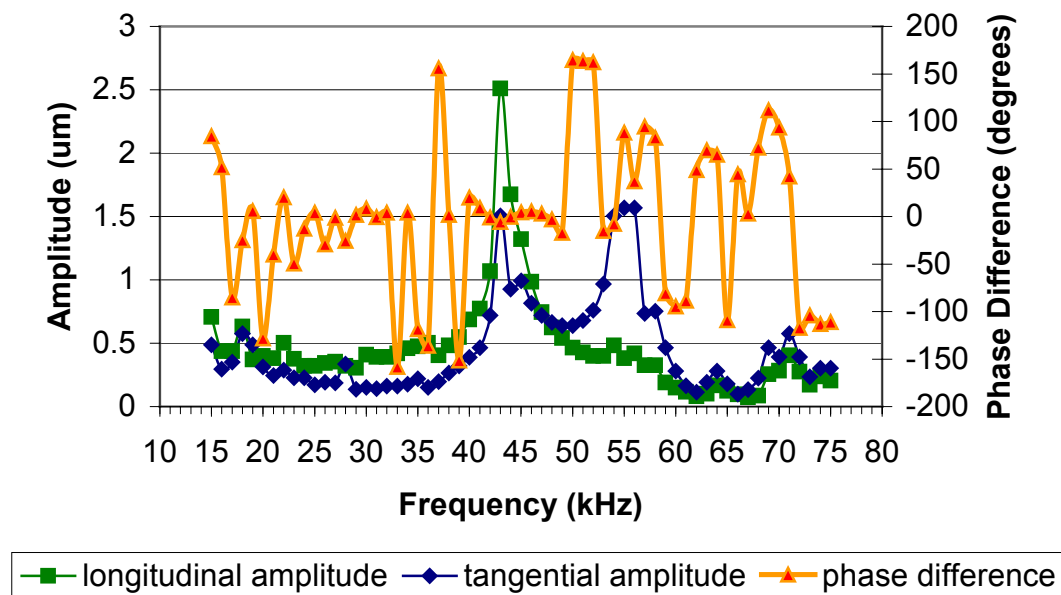
(c)

Figure 5.9. **(Continued)**

Table 5.2 lists velocity and torque characterization results for the standard and alternative L/T coupler designs. Plots of rotor velocity versus brake force appear in Appendix C. The magnitude of the static pre-load was continuously adjusted during the tests, ranging as high as 7 N, corresponding to a theoretical maximum torque of 20 mNm. The mass of each USM prototype was 30.5 grams. Efficiency is defined as the ratio of peak output mechanical power to input electrical power. Efficiency results are discussed in detail in Section 5.3.1. Results show that the tall beam L/T coupler improved static torque density by greater than 15% relative to the standard design, with an 82% increase in peak shaft power. In general, greater peak shaft power was observed in designs with higher unloaded steady state velocities. In direct drive applications however, greater peak power at low speed is more desirable. From this standpoint, the tall beam design is also advantageous.

Of the designs tested, the tall beam and winglet prototypes exhibited consistent operation at shaft loads greater than 8 mNm. Significant pre-load was necessary for high torque operation. Equations 5.4 and 5.5 suggest that torque is directly proportional to static pre-load. Additional torque trials were conducted to
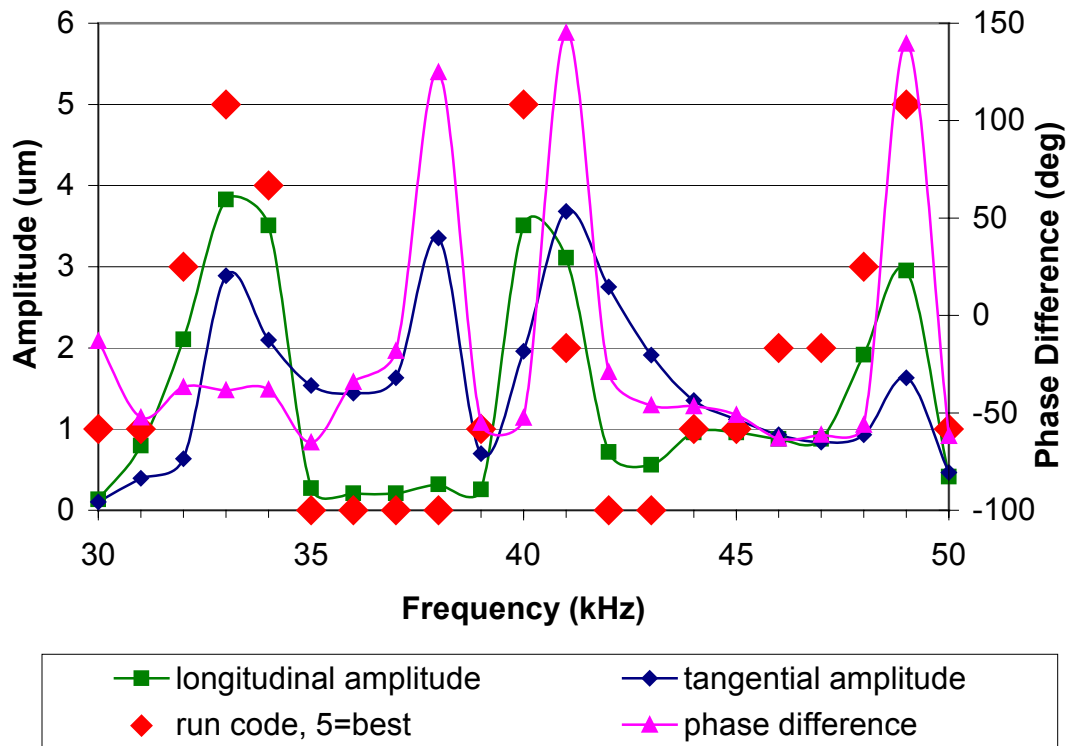
Figure 5.10. **Frequency response spectrum for USM prototype with tall beam L/T coupler and rotor assembled**

Table 5.2 **Prototype USM Static Torque Characterization Results**

L/T Coupler Design	Maximum Speed (< 0.5 N Static Pre-Load) (rpm)	Static Torque * (mNm)	Static Torque Density (Nm/kg)	Peak Shaft Power (mW)	Efficiency (%)
Standard	721 @ 44 kHz	9.7	0.32	110 @ 216 rpm	1.5
Winglet	1423 @ 59 kHz	9.1	0.30	287 @ 599 rpm	8.6
Tall Beam	3372 @ 31 kHz	11.3	0.37	200 @ 336 rpm	1.5
Thin Base	2252 @ 56 kHz	7.9	0.26	251@ 605 rpm	2.2

*Drive frequency and static pre-load were adjusted during the tests to maintain operation under increasing load.

confirm this relationship. Results are shown in Figure 5.11. Further experiments proved that the friction generated by a large static pre-load also reduces the unloaded steady state rotor velocity. A plot appears in Appendix C. Experimental results are compared to the equation of motion in Section 5.2.4.

114
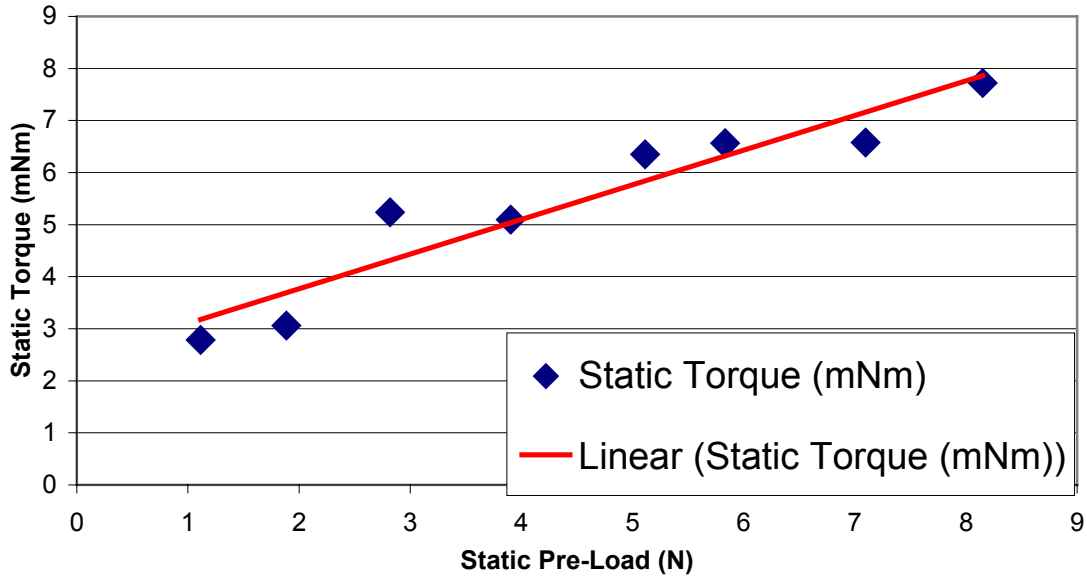
Figure 5.11. **Static torque vs. static pre-load for tall beam L/T coupler design**

5.2.4 Theoretical Results Comparison

Equation 5.7 was solved numerically using a fourth-order Runge-Kutta technique (Van Irwaarden) [93]. Figure 5.12 shows the theoretical rotor velocity profile for the standard L/T coupler prototype (Appendix C lists the values assigned to the system parameters). The steady state velocity is determined from the mean of the band that is caused by the alternating sign of the torsional impulse. Table 5.3 compares theoretical and measured maximum velocity results for a range of peak-to-peak tangential displacement amplitude. Good agreement is achieved in two cases. The highest velocities suggest tangential amplitudes that are greater than the measured values. Characterization data revealed that the actual rotor velocity is more sensitive to changes in static pre-load than the dynamic model suggests (see Appendix C). This limitation is a consequence of using Equation 5.3 (c) to simulate the dynamic pre-load function. Static torque is predicted by adding a constant load term to Equation 5.7:

$$ J_0\ddot{\theta}_R + c_t\dot{\theta}_R = \text{sgn}\left[\dot{\theta}_R - \dot{\theta}_S\right]\mu_k n_\theta d_{eff} - \mu_{k_{Al}} Mgr_{shaft} \tag{5.13} $$

Simulating Equation 5.13 repeatedly for increasing load yields a theoretical rotor velocity versus brake force plot from which the static torque is extrapolated. The static torque calculation for each prototype involved
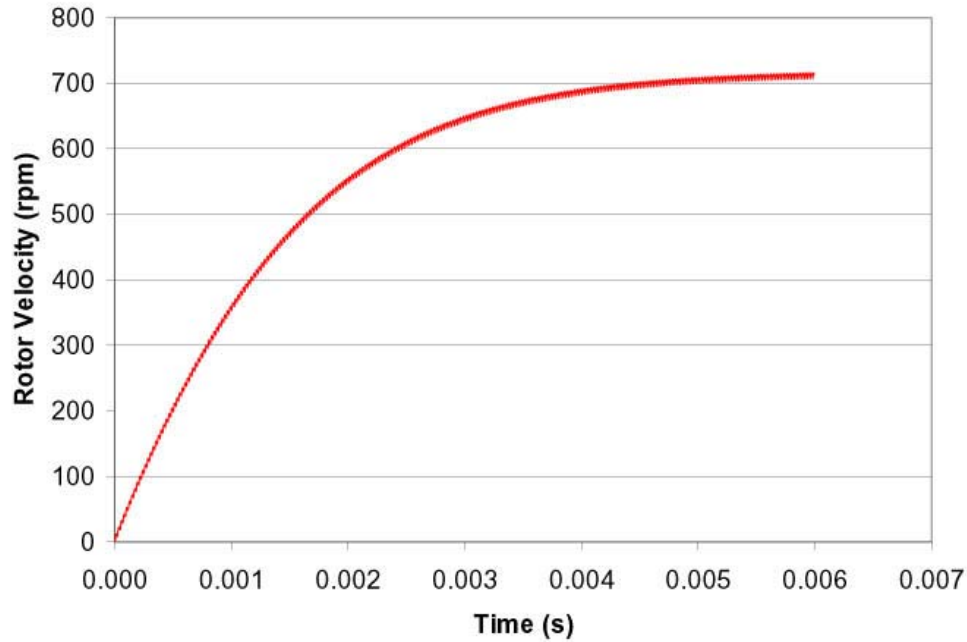
Figure 5.12. **Theoretical maximum rotor velocity profile for the USM system with standard L/T coupler (see Appendix C for parameter values)**

holding the drive frequency, static pre-load, and phase difference constant at arbitrarily selected values of 43 kHz, 10 N, and 150 degrees, respectively. Only the tangential displacement amplitude was varied according to experimental data. The constant parameters led to a uniform static torque of 8 mNm, and a corresponding static torque density of 0.26 Nm/kg. The result illustrates how static torque is independent of tangential displacement amplitude and rotor velocity. Greater static torque was measured in the tall beam prototype because the large amplitude of the longitudinal vibration allowed the static pre-load to be increased during the trial (see Appendix C). Model calculations support this observation: if the tall beam prototype model is run at 43 kHz with a phase difference of 150 degrees as before, but with a larger static pre-load, say 15 N versus ten, a static torque of 12.5 mNm is calculated.

<u>Table 5.3</u> **Comparison of Measured and Predicted Maximum Rotor Velocity Data**

L/T Coupler Design	Predicted Value (rpm) (Measured Displacement Amplitude)	Measured Maximum Speed (< 0.5 N Static Pre-Load) (rpm)	Predicted Value (rpm) (High Displacement Amplitude)
Standard	714 (1.3 um)	721 @ 44 kHz	817 (1.5 um)
Winglet	1356 (2.2 um)	1423 @ 59 kHz	1514 (2.5 um)
Tall Beam	2235 (6.1 um)	3372 @ 31 kHz	3422 (9.5 um)
Thin Base	1179 (1.6 um)	2252 @ 56 kHz	2537 (3.5 um)

5.3 Conclusions

Based on the results of the theoretical investigation and prototype characterization, the following conclusions regarding static torque performance in the mode conversion USM are supported:

- Four prototypes of a miniature mode conversion rotary ultrasonic motor have been created with alternate L/T coupler designs. The L/T couplers convert axial vibration of the resonator to elliptical displacement at the points of contact with the rotor mechanism. The ellipsoid is characterized by a non-zero longitudinal/tangential phase difference near the primary operating frequency of 43 kHz in all prototypes. Theoretical results indicate the greatest steady state rotor velocity is associated with a circular (90-degree phase difference) locus. Rotor velocity is proportional to the amplitude of the tangential stator vibration, which is determined by the L/T coupler geometry and the axial displacement of the resonator. Steady state rotor velocity does not determine static torque performance.

- The following factors directly influence static torque in the mode conversion USM: (1.) static pre-load, (2.) diametric distance between the rotor contact points and, (3.) the coefficient of kinetic friction. Static pre-load was directly controlled in the characterization trials, yielding greater static torque results that are supported by the dynamic model.

- Characterization data shows that assembling the rotor under a non-zero pre-load attenuates the longitudinal stator displacement (see Figure 5.10). Thus, a prototype that produces greater axial displacement can sustain a larger static pre-load, and produces greater static torque. Of the

prototypes tested, the tall beam L/T coupler design exhibited the greatest axial displacement amplitude, which allowed for static pre-load to be increased during the torque characterization. Consequently, the tall beam design generated the largest measured static torque.

5.3.1 Performance Comparison

Table 5.4 compares the static torque and static torque density results of the tall beam prototype USM with that of comparably sized commercial motors listed in Table 2.3. The large diameters of the ring-type traveling wave motors listed in Table 5.4 provide a clear advantage in static torque [33]. This fact suggests that

Table 5.4 **Torque Performance Comparison for Prototype and Commercial USM's**

Motor	Type	Mass (g)	Static Torque (mNm)	Static Torque Density (Nm/kg)
Piezosystems RU30-001 [60]	Traveling wave rotary USM	20	100	5
Canon EF 300/2.8L Ring-type [33]	Traveling wave rotary USM	45	160	3.6
N. C. State	**Mode conversion rotary USM**	**30.5**	**11.3**	**0.37**
Mabuchi FK-280-2865 [33]	Electromagnetic	36	15.2	0.42
Maxon [33]	Electromagnetic	38	12.7	0.33

in addition to an increase in static pre-load, future development of the N. C. State prototype may require a change of aspect ratio to match the disk profile of the traveling wave USM's.

Another important comparison is in the area of power consumption and efficiency. The motor constant, K_M, defines the constant of proportionality between the square of the continuous torque and the power consumed (see Section 2.2.2.2 and Appendix C for details) (Wallace and Selig) [95]. As a basis of comparison, consider the Pittman Series 6000™ model 6X12 commercial DC brush motor (www.pittmannet.com, Bulletin LC2). It has a mass of 42.5 grams, a published continuous torque of 5.7 mNm, and a corresponding motor constant of 4.66×10^{-3} NmW$^{-1/2}$. Similarly, the tall beam prototype USM has a mass of 30.5 grams, and a theoretical continuous torque of 25.2 mNm calculated from the time average of Equation 5.5 and parameters

listed in Appendix C (with the static pre-load function given by Equation 5.3 (c), the continuous torque is equal to the theoretical maximum) [72]. As a more equitable alternative, the starting torque defined by the product of the rotor inertia and the slope of the transient portion of the rotor velocity profile (see Appendix C for parameters) is substituted for the continuous torque. At 43 kHz, the starting torque is equal to 6 mNm. The average power consumption of the prototype has been estimated at 12.92 watts (Xu) [99]. This results in a motor constant of 1.7×10^{-3} NmW$^{-1/2}$, more than half that of the DC motor. This difference indicates that the USM requires more electrical power than the DC motor to produce the same amount of torque, and underscores the design challenges associated with improving drive circuit efficiency, and limiting mechanical losses in the USM, as the next segment describes.

5.3.2 Limitations

Efficiency of the mode conversion USM is limited by two major thermal energy dissipation mechanisms: (1.) friction between the rotor and stator and (2.), high frequency switching in the drive circuit [99]. An investigation into quantifying these losses and identifying possible design-based remedies is out of the scope of this chapter. However, some commercial USM manufacturers address the wear and heating issues at the rotor/stator interface by fabricating the contact members from ceramic materials [88].

Experimental and theoretical results show that the static torque is limited by the magnitude of the static pre-load, which, as the preceding paragraphs explain, depends on the amplitude of the longitudinal vibration. It follows that a strategy for improving torque performance in the USM should include optimization of the stator design to maximize the longitudinal amplitude. Manufacturing issues associated with the L/T coupler also curbed the sustainable level of static pre-load in the torque characterization trials. Specifically, high static pre-loads caused shear failure in the ball bearings embedded in the L/T coupler by epoxy. An estimate of the shear stress associated with epoxy failure is obtained by calculating the ratio of the friction force on the stator contact point to the surface area of one-half of the embedded steel ball bearing. Assuming a failure pre-load of 12 N, and a ball bearing radius of 0.75 mm, the failure shear stress is 1.43 MPa. Machining integral contact points on the face of the L/T coupler, albeit expensive, eliminates this problem.

5.4 Future Work

The following items are recommended for future research:

- The resonator design must be optimized to yield the largest longitudinal displacement amplitude in the smallest package. This research would require a series of resonators to be constructed to evaluate the performance of various head and tail masses and epoxy systems in terms of the acoustic parameters described in Table 5.1. The dynamic finite element model of the stator was constructed to facilitate this effort [68]. Compiled using the ANSYS™ 5.7 software package, the batch input file for the stator model includes variable part dimensions and material properties that allow for an optimization subroutine to be applied. The output of the subroutine predicts the frequency response spectrum of a practical stator design that satisfies the optimization objective [68].

- An investigation of the dynamic response of the pre-load assembly and center bolt is necessary to determine their individual and collective influence on the stator displacement locus. Preliminary calculations suggest that transient oscillations of the rotor and pre-load spring system occur as the rotor velocity increases prior to the steady state. These oscillations may influence the dynamic pre-load waveform. Furthermore, calculations show that the first transverse harmonic of the center bolt is active near the primary operating frequency. These oscillations may interfere with the stator displacement locus. To mitigate this effect, the center bolt length was increased to move the center bolt resonance away from the primary operating frequency.

- Lastly, the accuracy of the model can benefit by improvements in two areas. First, the effects of coulomb damping between the rotor and its bushing should be simulated. Second, the mechanics of the rotor/stator contact must be modeled with the objective of developing a more accurate expression for the dynamic pre-load waveform that more closely emulates the variation of steady state rotor velocity with static pre-load. This expression must account for the amplitude of the longitudinal stator displacement.

Chapter 6

Conclusions and Future Work

6.0 Conclusions

Chapter 6 draws on the results of the research presented in the preceding chapters to develop conclusions on the effectiveness of using piezoelectric transducers to produce high force/torque actuation systems for miniature robots. A comparison of the performance metrics and scalability results obtained with both linear and rotary piezomotors lead to additional conclusions regarding the characteristics of smaller versions of these systems, and how they can be improved. Finally, future directions for this research are considered, including methods for integrating these piezomotors in robotic actuation systems at the millimeter and micro scales.

6.0.1 Scalability of Prototypes

Chapter 4 derived scale factors for key parameters that impact on the performance of linear piezomotors such as the Milliworm. The dimensional analysis technique applied in the linear piezomotor research was extended to parameters associated with the mode conversion USM. Based on the results, conclusions are drawn regarding the scalability of the mode conversion USM system.

Appendix D lists the dimensions utilized in a simulation that calculated the static torques and steady state rotor velocities of a set of geometrically similar mode conversion USM's. This dynamic analysis was discussed in Chapter 5. In constructing the simulation, the following USM dimensions were scaled linearly by an arbitrary factor of three quarters.

- Radial and axial dimensions, including the distance between the L/T coupler ball bearing contacts, the outer and inner radius of the rotor, and the rotor, head mass, and tail mass thickness.

- In Chapter 2 it was reported that the axial displacement of a simple, single-layer, piezoelectric transducer is related to its length by the piezoelectric strain coefficient (Uchino) [88]. Considering this prior knowledge, the axial and tangential displacement of the USM stator was also scaled linearly by the same factor.

- The magnitude of the static pre-load was scaled by this factor to reflect the change in axial displacement amplitude.

Reducing the size (and the mass) of the resonator causes the primary operating frequency to increase (Rao) [73]. To simulate this effect, Equation 2.3 was utilized to estimate the primary operating frequency given the scaled dimensions of the head and tail masses. A new equivalent stiffness of the transducer was calculated to improve the accuracy of the equation relative to the measured primary operating frequency of the prototype. Figure 6.1 is a plot of static torque and unloaded steady state rotor velocity versus the radius of the L/T coupler ball

The curve labels in the figure read:

$$d\theta_R/dt = 8627.9 r_{eff}^{-1.6}$$

$$d\theta_R/dt = 0.8 r_{eff}^{2.1}$$
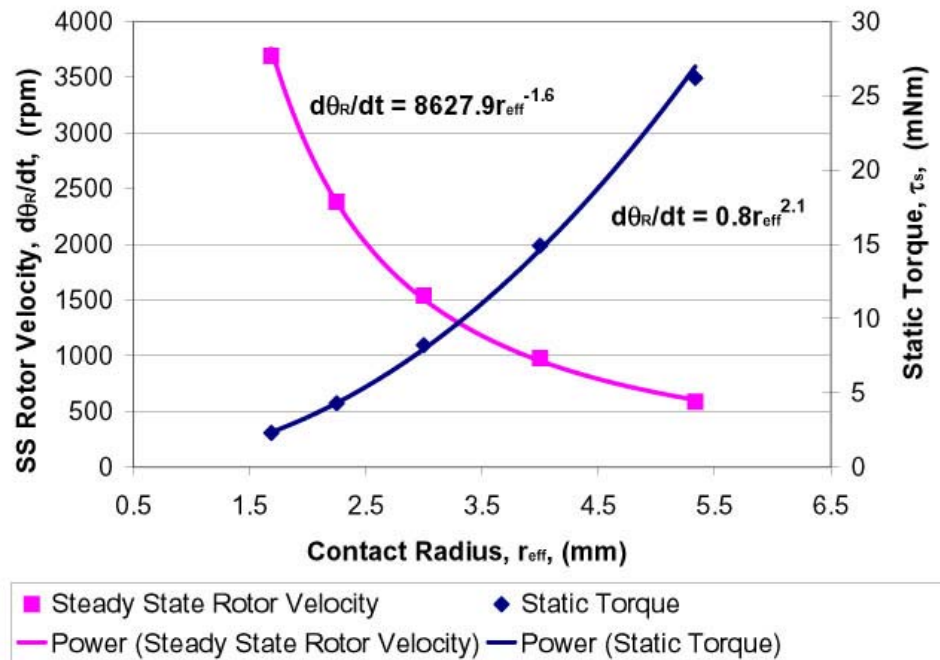
Figure 6.1. **Static torque and steady state rotor velocity vs. contact radius**

bearing contacts. If s_r is the ratio of homologous contact radii (see Section 2.3), Figure 6.1 shows that the static

torque varies as s_r^2, and steady state rotor velocity as $s_r^{-\frac{3}{2}}$. Thus, if the radius of the USM is halved, the static

torque decreases by one quarter. Furthermore, miniaturization will cause the steady state rotor velocity to

increase by a power of three halves. The dimensional analysis results for both the rotary USM and the linear

piezomotor are summarized in Table 6.1.

An advantage of the THUNDER™-based Milliworm is the invariance of the actuator type blocked

Table 6.1 **Dimensional Analysis Summary**

Prototype	Parameter	Scale Factor	Proportional To
Milliworm linear piezomotor	Unloaded deflection under 480V actuation	s_w	s_{ro}^2
	Zero potential device stiffness	s_k	s_{ro}^{-2}
	Actuator type blocked force	s_{F_2}	s_t
	Passive latch back slip (pawl return rotation only)*	s_{δ_4}	s_{ro}^2
	Passive latch back slip* (pawl deflection only)	s_{δ_3}	$s_{t_{pawl}}^{-3}$
Mode conversion rotary USM	Static torque	s_{τ_s}	s_r^2
	Steady state rotor velocity	$s_{\dot{\theta}_R}$	$s_r^{-\frac{3}{2}}$

* See Appendix D for details.

force with the outer radius. If the transducer thickness remains constant, the blocked force will remain constant

as the radius of the piezomotor varies. However, it should be noted that the deflection model becomes invalid

when the transducer geometry deviates from that of a disk. Moreover, it is realistic to assume that the

piezoceramic layer thickness will reduce in thickness with the dimensions of the transducer during

manufacturing, and that the reduction in blocked force would conform to a moderate, linear relationship.

Characterization trials with the Milliworm illustrated the difficulties associated with producing piezomotor

actuation based on micron-sized transducer displacements. It is anticipated that the cost associated with

precision engineering of transducer modules will climb as transducer displacements decrease as the square of the outer radius. Another drawback associated with reduced transducer size is the inevitable loss in step displacement and velocity during piezomotor operation. Table 6.1 lists the scale factors associated with back slip components (see Appendix D for details). Although back slip due to pawl return rotation scales favorably with reduced step displacements, miniaturization leads to challenges regarding the design of the pawl. On the micro scale, as the diameter of the rod approaches that of a human hair, Section 3.4.1 explains how the thickness of the pawl must be smaller for binding to occur. Equation 3.18 shows that pawl deflection is proportional to $1/EI$ such that if the pawl thickness is halved without a similar reduction in length, the deflection *increases* by a factor of eight. Consequently, miniaturization of the rod and passive latch requires that the length of the pawl be reduced by at least the same factor as the thickness to avoid large deflections. Material changes must also be considered to avoid brittle fracture of a very thin pawl. From a manufacturing standpoint, this information alone indicates that the mode conversion rotary USM design is more scalable than the Milliworm, because the USM mechanism eliminates many of the problems associated with harnessing micron step displacements. Considering performance, USM miniaturization reduces static torque by a power of two with its radius. If a cylinder of radius r and length l represents the geometry of the USM, its volume is proportional to r^2l. It follows that miniaturization will cause the USM mass to decrease according to a cubic relationship, and *static torque density* may actually increase linearly. It is thereby concluded that the mode conversion rotary USM design is more scalable than the linear piezomotor. It should be noted, however, that the results in Table 6.1 suggest that implementing a micro-scale version of the USM prototype in the jumping mechanism will require operating speed to be reduced. This could be a barrier to using the miniature mode conversion USM as a direct drive system.

6.0.2 Motor System Comparison

The following segment compares performance data for the two prototype motors discussed in this dissertation. The objectives of the comparison are: (1.) to determine which prototype exhibits the greatest power density for driving the robotic locomotion system and, (2.) to compare the performance and scalability results to those of comparable commercial systems of a similar size and/or mass. Power density values are the common standard for such comparisons.

Table 6.2 lists the measured performance data of the Milliworm linear piezomotor, and the mode conversion USM prototype with tall beam L/T coupler. Static torque and actuator type blocked force data is included. Results show that although the mode conversion USM has three times the mass of the Milliworm, its peak power density is larger by three orders of magnitude. The measured static torque is more than one-tenth the estimated 350 mNm (~20 N of linear force) required to directly charge the springs of the prototype robotic platform. It is concluded that neither prototype is capable of directly driving the jumping locomotion system in its current configuration.

<u>Table 6.2</u> **Prototype Performance Comparison**

Prototype	Mass (g)	Actuator Type Blocked Force (mN)	Static Torque (mNm)	Power Density (mW/kg)
Milliworm linear piezomotor	10	230		9.4
Mode conversion rotary USM (tall beam L/T coupler)	30.5		11.3	6,560 (peak) @ 336 rpm

Simulation results support the conclusion that smaller versions of the prototype mode conversion USM exhibit greater static torque density and lower steady state speed than electromagnetic (EM) motors of similar size. Table 6.3 lists performance data associated with a simulated mode conversion USM with a 1.7-mm contact radius, and a 3-mm diameter Smoovy™ EM motor (Mulling) [60]. The Smoovy™ generates greater

<u>Table 6.3</u> **Performance Data Comparison for Simulated Micro-Scale Rotary Motors [60]**

Parameter	Simulated Mode Conversion Rotary USM (1.7-mm contact radius, 5.6 N static pre-load, 2.4 um displ. (p-p), 150° phase diff @ 102 kHz)	3-mm diameter Smoovy™ EM motor
Mass (g)	3 (estimated)	0.33
Steady state rotor velocity (rpm)	3,691	72,000
Static torque (mNm)	2.3	0.035
Static torque density (Nm/kg)	0.77	0.11
Power density (W/kg)	81 (peak) @ 1978 rpm	1,340

power due to its higher steady state speed. Although the Smoovy™ has a significant advantage in mass, the static torque density remains seven times smaller than the USM.

As a final comparison, Table 6.4 lists the same performance data for the Milliworm linear piezomotor versus the shape memory alloy-based Electric Piston™ [60]. Here, operational frequency is listed as an analogy to rotor velocity in Table 6.3. The Electric Piston™ exhibits a blocked force that is 100 times greater than the Milliworm, but activation of the shape memory effect requires approximately 15 seconds [60]. Combined with a limited stroke [60], this cycle time makes the shape memory actuation system an unacceptable alternative for the robotic platform.

<u>Table 6.4</u> **Performance Data Comparison for Linear Motors [60]**

Parameter	Milliworm 3A Linear Piezomotor (measured)	Electric Piston™
Mass (g)	10	10
Operational frequency (Hz)	100	0.067
Blocked force (N)	0.23	25.4 (extrapolated)
Power density (W/kg)	0.0094	3.9

6.0.3 Summary

The conclusions of this dissertation are:

- Two prototype miniature piezoelectric motor systems have been characterized, one linear and one rotary. The motors were designed for integration with the drive mechanism of a miniature robot. Each prototype demonstrates measurable force and torque.

- Neither the linear nor the rotary prototype possesses adequate force/torque capacity to directly drive the locomotion system in their current form.

- The miniature mode conversion rotary ultrasonic motor demonstrates power density that is nearly 1,000 times greater than the linear piezomotor. Thus its capability for directly driving the locomotion system is greater than that of the linear prototype.

- The mode conversion USM design is predicted to have greater scalability, and is therefore more suitable for miniaturization than the linear piezomotor. On the micro scale, (contact radius less

than 1 mm) the USM will not be effective as a direct drive motor, as the unloaded rotor velocity is expected to rise above 4,000 rpm. Increasing the static pre-load (preferred), or adding a gearbox can reduce the rotor velocity. Both methods amplify static torque.

- Dynamic simulation data indicates that a geometrically similar micro-scale version of the mode conversion USM prototype would possess greater static torque density and lower steady state rotor velocity than one of the smallest commercial EM motors currently available: the 3-mm diameter Smoovy™. This result supports the literature (Ueha and Tomikawa) [87, 88] in the claim that with respect to torque and speed, rotary USM's are more effective than EM motors in miniature direct drive robotics applications.

6.1 Future Work

The following are final recommendations on the jumping robotic platform and miniature piezoelectric motor program.

6.1.1 Next Generation Motor Designs

The following objectives are recommended for the design of the next generation mode conversion USM: (1.) miniaturization and (2.), static torque improvements. A simple design change that will boost static torque output is increasing the radius of the ball bearing contacts. Implementing this change while maintaining a miniature profile will necessitate altering the aspect ratio of the USM such that it acquires a disk shape (if the resonator design permits). To boost axial displacement while limiting failure under high static pre-load, the embedded ball bearing contacts must be integrated with the tall beam L/T coupler. Further miniaturization requires an alternative means of fastening the stator components to the center bolt. One solution is to weld or epoxy the components together (Avallone and Baumeister) [3]. Manufacturing parts with complex geometry such as the L/T coupler on the micro scale can be accomplished using precision electric discharge machining (EDM) [3], or LIGA technology (Kovacs) [50].

In the near term, engineering of the Milliworm linear piezomotor must focus on improving the precision of the outer and inner C-ring spacers that separate the THUNDERS within the transducer module (see Section 4.2.1). The brass wire should be replaced with a non-conducting material to reduce ground faults. Furthermore, exact tolerances regarding thickness, flatness, and parallelism of the spacers must be implemented to curtail stiffness losses. Due to the loss of transducer displacement with diameter, and the difficulty in

coupling it, Chapter 4 showed that the 0.525-inch prototype represents the limit of miniaturization in the Milliworm design.

6.1.2 Micro-Scale Robotic Platform

Efforts to miniaturize of the N. C. State robotic actuation systems will lead engineers away from the folding leg design in favor of a more simple approach. Coil springs will be replaced by composite flexures and tendons for energy storage. Design modifications are also necessary to promote self-assembly and eliminate the need for fasteners. Alternate actuation systems may also be considered. For example, a drive system based on piezoelectric motors may be traded for a high force, long stroke pneumatic or hydraulic reaction micro motor with a compact piezoelectric compressor. These steps are part of what is anticipated to be a decades-long evolution in micro robotics that requires dramatic innovations in smart materials, motors, power supplies, and electronics. This dissertation has presented evidence illustrating how the performance of piezomotors changes with size. Disseminating this information enforces the paradigm shift that is necessary to create effective engineering systems in the micro regime.

REFERENCES

[1] Adriaens, J.M.T.A., de Koning, W.L. and Banning, R. "Design and Modeling of a Piezo-Actuated Positioning Mechanism." Proceedings of the IEEE 36th Conference on Decision and Control (1997): 1978-1983.

[2] Asada, H. and Youcef-Toumi, K. (1987) Direct-Drive Robots Theory and Practice. Cambridge, Massachusetts: The MIT Press.

[3] Avallone, E. A., and Baumeister, T. (1987). Mark's Standard Handbook for Mechanical Engineers, 9th ed. New York: McGraw-Hill Inc.

[4] Baker, W.E., Westine, P.S. and Dodge, F.T. (1991). Similarity Methods in Engineering Dynamics. New York: Elsevier.

[5] Bauer, M. G. "Design of A Linear High Precision Ultrasonic Piezoelectric Motor." Dissertation, North Carolina State University, 2001.

[6] Baumgartner, H. "When Bugs Are The Machine." Mechanical Engineering 123, 4 (2001): 108.

[7] Beer, F. P. and Johnston, E. R. (1988). Vector Mechanics for Engineers: Statics and Dynamics, 5th ed. New York: McGraw-Hill Book Company.

[8] Binns, K.J., and Shimmin, D.W. "The Relationship Between Performance Characteristics and Size of Permanent Magnet Motors." IEE Electrical Machines and Drives 412 (1995): 423-427.

[9] Bizzigotti, R.A. "Electromechanical Translation Apparatus." United States Patent 3,902,085 (1975).

[10] Boylestad, R., and Nashelsky, L. (1989). Electronics: A Survey. Englewood Cliffs, NJ: Prentice- Hall.

[11] Brand, L. "The Pi Theorem of Dimensional Analysis." Archive for Rational Mechanics and Analysis I 1 (1957): 36-45.

[12] Bryant, R. G., Evans, S. A., Long, E. R., and Fox, R. L. "Thermal and Mechanical Characterization of NASA High Displacement Actuators For Satellite Instrumentation." Proceedings of SPIE 3991 (2000): 195-201.

[13] Chapman, R.F. and Joern, A. (1990). Biology of Grasshoppers. New York: John Wiley and Sons.

[14] Chen, Q., Yao, D., Kim, C.J. and Carman, G.P. "Development of Mesoscale Actuator Device with Microinterlocking Mechanism." Journal of Intelligent Material Systems and Structures 9 (1998): 449 - 457.

[15] Chen, Q., Yao, D., Kim, C.J. and Carman, G.P. "Mesoscale Actuator Device: Micro Interlocking Mechanism to Transfer Macro Load." Sensors and Actuators 73 (1999): 30-36.

[16] Chow, S., and Thackery, S. "Miniature Ultrasonic Motor." Horological Journal 141, 2 (1999): 56-58.

[17] Clephas, B. and Janocha, H. "New Linear Motor With Hybrid Actuator." SPIE Smart Structures and Integrated Systems 3041 (1997): 316-325.

[18] Coorpender, S., Finkel, D., Kyzar, J., Sims, R., Smirnova, A., Tawhid, M., Bouton, C., and Smith, R.C. "Modeling and Optimization Issues Concerning a Circular Piezoelectric Actuator Design." Adaptive Structures and Materials Systems 1999 (1999): 199-204.

[19] Dong, S., Li, L., Gui, Z., Zhou, T., and Zhang, X. "A New Type of Linear Piezoelectric Stepper Motor." IEEE Transactions on Components, Packaging, and Manufacturing Technology-Part A 18 (1995): 257-260.

[20] Dong, S., Wang, S., Shen, W., and Li, L. "A Miniature Piezoelectric Ultrasonic Motor Based On Circular Bending Vibration Mode." IEEE/ASME Transactions on Mechatronics 5 (2000): 325– 330.

[21] Drake, J. "Bar Clamp For Single-Hand Operation." United States Patent number 5,853,168, (1998).

[22] Drexler, K.E. (1986). Engines of Creation. Garden City, N.Y. : Anchor Press/Doubleday.

[23] Edwards, Jr., C. H., and Penney, D. E. (1993). Elementary Differential Equations with Boundary Value Problems, 3rd ed. Englewood Cliffs, NJ: Prentice-Hall.

[24] Ervin, J.D. and Brei, D. "Recurve Piezoelectric-Strain-Amplifying Actuator Architecture." IEEE/ASME Transactions on Mechatronics 3 (1998): 293-301.

[25] Evans, E.B. "Piezoelectric Linear Actuator." United States Patent 3,551,764 (1970).

[26] Fasick, J. C. "Development of A Nanometer Resolution Constant Velocity Piezotranslator." Thesis, North Carolina State University, 1998.

[27] Feynman, R.P. "There's Plenty of Room at the Bottom." Journal of Microelectromechanical Systems 1 (1992): 60-66.

[28] Fiorini, P., Hayati, S., Heverly, M., and Gensler, J. "A Hopping Robot for Planetary Exploration." Aerospace Conference, 1999 Proceedings 1999 IEEE 2 (1999): 153 –158.

[29] Flynn, A.M., Tavrow, L.S., Bart, S.F., Brooks, R.A., Ehrlich, D.J., Udayakumar, K.R., and Cross, L.E. "Piezoelectric Micromotors for Microrobots." Journal of Microelectromechanical Systems 1 (1992): 44-50.

[30] Frank, J., Mockensturm, E.M., Chen, W., Koopmann, G.H., and Lesieutre, G.A. "Roller-Wedgeworm: A Piezoelectrically-Driven Rotary Motor." 10th International Conference on Adaptive Structures and Technologies (1999): 1-11.

[31] Gere, J.M., and Timoshenko, S.P. (1997). Mechanics of Materials. 4th ed. New York: PWS Publishing.

[32] Gilbert, H.D. (1961). Miniaturization. New York: Reinhold Publishing Corporation.

[33] Glenn, T.S., and Hagood, N.W. "Development of a Two-Sided Piezoelectric Rotary Ultrasonic Motor For High Torque." SPIE Smart Structures and Integrated Systems 3041 (1997): 326-338.

[34] Glumac, D. "A Planar Unimorph-Based Actuator with Large Vertical Displacement Capability." IEEE Transactions on Ultrasonics, Ferroelectrics, and Frequency Control 45, 5 (1998): 1145-1150.

[35] Goul, A.S. "Fast Clamp." United States Patent Number 4,874,155, (1989).

[36] Gould, P.L. (1988). Analysis of Shells and Plates. New York: Springer-Verlag.

[37] Groves, I.D. (1981). Acoustic Transducers. Stroudsburg, PA: Hutchinson Ross Publishing Company.

[38] Hameyer, K., and Belmans, R. "Design of Very Small Electromagnetic and Electrostatic Micro Motors." IEEE Transaction on Energy Conversion 14, 4 (1999): 1241 -1246.

[39] Henke, A., Kummel, M.A. and Wllaschek, J. "A Piezoelectrically Driven Wire Feeding System for High Performance Wedge-Wedge-Bonding Machines." Mechatronics '98 : Proceedings of The 6th UK Mechatronics Forum International Conference (1998): 147-152.

[40] Hyder, C., Horner, G., and Clark, W. "Linear Traveling Wave Motor." SPIE Conference on Industrial and Commercial Applications of Smart Structures Technologies 3674 (1999): 205-211.

[41] Ikuta, K., Kawahara, A. and Tsutsui, Y. "Development of Miniature Cybernetic Actuator Driven by Piezoelectric Device." IEEE/RSJ International Workshop on Intelligent Robots and Systems (1991): 1151-1156.

[42] Isaacson, E. de St Q. and Isaacson, M. de St Q. (1975). Dimensional Methods in Engineering and Physics London: Edward Arnold Publishers Ltd.

[43] Judy, J.W., Polla, D.L. and Robbins, W.P. "A Linear Piezoelectric Stepper Motor With Submicrometer Step Size and Centimeter Travel Range." IEEE Transactions on Ultrasonics, Ferroelectrics, and Frequency Control 37 (1990): 428-437.

[44] Johnson, K.L. (1985). Contact Mechanics. New York: Cambridge University Press.

[45] Kawai, Y., Asai, K., Naito, S., Fukui, T., Adachi, Y., Handa, N., Ikeda, K., and Tsuda, K. "High Power Travelling-Wave Type Ultrasonic Motor." Japanese Journal of Applied Physics 34 (1995): 2711-2714.

[46] Khatib, O., Craig, J.J. and Lozano-Perez, T. (1992). The Robotics Review 2. Cambridge, Massachusetts: The MIT Press.

[47] Kline, S.J. (1965). Similitude and Approximation Theory New York: McGraw-Hill.

[48] Koc, B., Bouchilloux, P., and Uchino, K. "Piezoelectric Micromotor Using A Metal-Ceramic Composite Structure." IEEE Transactions on Ultrasonics, Ferroelectrics, and Frequency Control 47 (2000): 836-843.

[49] Koc, B., Xu, Y., and Uchino, K. "Ceramic/Metal Composite Piezoelectric Motors." 1998 IEEE Ultrasonics Symposium (1998): 687-690.

[50] Kovacs, G. T. A. (1998). Micromachined Transducers Sourcebook. Boston: McGraw-Hill.

[51] Kumada, A. "Piezoelectric Revolving Motors Applicable for Future Purpose." 7th International Symposium on Applications of Ferroelectrics, 1990, IEEE (1991): 213 –219.

[52] Kumada, A. "Ultrasonic Motor Using Bending, Longitudinal and Torsional Vibrations." United States Patent 4,642,509 (1987).

[53] Langhaar, H.L. (1951). Dimensional Analysis and Theory of Models New York: John Wiley and Sons.

[54] Leonard, J.W. (1988). Tension Structures: Behavior and Analysis. New York: McGraw-Hill.

[55] May, W.G. Jr. "Peizoelectric Electromechanical Translation Apparatus." United States Patent 3,902,084 (1975).

[56] McMahon, T.A. and Bonner, J.T. (1983). On Size and Life. New York: W.H. Freeman and Co.

[57] Ming, Y., and Peiwen, Q. "Performances Estimation of a Rotary Traveling Wave Ultrasonic Mortor Based On Two-Dimension Analytical Model." Ultrasonics 39 (2001): 115-120.

[58] Mortenson, M.E. (1995). Geometric Transformations. New York: Industrial Press.

[59] Mossi, K. M., Selby, G. V., and Bryant, R. G. "Thin-layer Composite Unimorph Ferroelectric Driver and Sensor Properties." <u>Materials Letters</u> 35 (1998): 39-49.

[60] Mulling, J.F. "Compiled Performance Metrics for Linear and Rotary Actuators and Motors." North Carolina State University Center for Robotics and Intelligent Machines, Technical Report NCSU-CRIM-TR-2002-0202, 2002.

[61] Mulling, J., Usher, T., Dessent, B., Palmer, J., Franzon, P., Grant, E., and Kingon, A. "High Displacement Piezoelectric Actuators: Characterization At High Load with Controlled End Conditions." <u>Sensors and Actuators A</u> 94 (2001) 19-24.

[62] Munson, B.R., Young, D.F., and Okiishi, T.H. (1990). Fundamentals of Fluid Mechanics. New York: Wiley and Sons.

[63] Nakamura, K., Kurosawa, M., Kurebayashi, H., and Ueha, S. "An Estimation of Load Characteristics of an Ultrasonic Motor by Measuring Transient Responses." <u>IEEE Transactions on Ultrasonics, Ferroelectrics, and Frequency Control</u> 38 5 (1991): 481-485.

[64] Nakamura, K., Kurosawa, M., and Ueha, S. "Design of a Hybrid Transducer Type Ultrasonic Motor." <u>IEEE Transactions on Ultrasoinics, Ferroelectrics, and Frequency Control</u> 40 (1993): 395-401.

[65] Nakamura, K., and Ueha, S. "Performances of a Hybrid Transducer-Type Ultrasonic Motor as a Function of the Size." <u>1994 Ultrasonics Symposium</u> (1994): 557-560.

[66] Okubo, H., Nakano, E. and Handa, M. "Design of a Jumping Machine Using Self-Energizing Spring." <u>IEEE/RSJ Int. Conf. on Intelligent Robots and Systems</u> (1996): 186-191.

[67] Palmer, J. A., Dessent, B., Mulling, J. F., Usher, T., Grant, E., Eischen, J. W., Kingon, A. I., and Franzon, P. D. "The Design and Characterization of a Novel Piezoelectric Transducer-Based Linear Motor." (not published).

[68] Palmer, J. A., Kennedy, C.J., Mulling, J. F., Gruverman, A., Grant E., Kingon, A. I., Franzon, P. D., and Eischen, J.W. "Torque Optimization of a Miniature Mode Conversion Rotary Ultrasonic Motor." (not published).

[69] Pisano, A.P. "Resonant-Structure Micromotors." <u>IEEE Micro Electro Mechanical Systems, 1989, Proceedings, An Investigation of MicroStructures, Sensors, Actuators, Machines and Robots</u> (1989): 44-48.

[70] Pohl, D.W. "Dynamic Piezoelectric Translation Devices." <u>Rev. Sci. Instrum.</u> 58 (1987): 54-57.

[71] Rabinovici, R. "Scaling of Switched Reluctance Motors." <u>IEE Proceedings on Electric Power Applications</u> 142 (1995): 1-4.

[72] Ragulskis, K., Bansevicius, R., Barauskas, R., and Kulvietis, G. (1988). Vibromotors for Precision Microrobots. New York: Hemisphere Publishing Corporation.

[73] Rao, S. S. (1995). Mechanical Vibrations, 3rd ed. Reading, Massachusetts: Addison-Wesley Publishing Company.

[74] Ruxton, A.D. "The Design and Implementation of A Constant Velocity Piezoelectric Actuation Motor." Thesis, North Carolina State University, 1996.

[75] Schaaf, U. "Piezoelectric Motors and Their Electronic Supply." <u>IEE Colloquium on Innovative Actuators for Mechatronic Systems</u> (1995): 9/1 – 9/3.

[76] Sedov, L.I. (1993). Similarity and Dimensional Methods in Mechanics 10th ed. Boca Raton: CRC Press.

[77] Serway, R.A. (1990). Physics for Scientists and Engineers. Philadelphia: Saunders College Publishing.

[78] Shih, W.Y., Shih, W.H., and Aksay, I.A. "Scaling Analysis for the Axial Displacement and Pressure of Flexitensional Transducers." Journal of the American Ceramic Society 80 (1997): 1073-78.

[79] Skoglund, V.J. (1967). Similitude Theory and Applications Scranton, PA: International Textbook Company.

[80] Stansfield, D. (1991). Underwater Electroacoustic Transducers: A Handbook for Users and Designers. Bath, UK: Bath University Press.

[81] Tainhong, C., Liding, W., Qiongying, L., and Xaiodong, T. "Theoretical Analysis and Design of Ultrasonic Micromotors." 5th International Symposium on Micro Machine and Human Science, 1994. Proceedings (1994): 115-118.

[82] Timoshenko, S., and Woinowsky-Krieger, S. (1959). Theory of Plates and Shells, 2nd ed. New York: McGraw-Hill, Inc.

[83] Tonshoff, H.K., and Stegmann, A. "FEM Analysis of a Bimodal Linear Piezo-Friction Motor." SPIE Smart Structures and Materials 1997 3041 (1997): 339-345.

[84] Trimmer, W. and Jebens, R. "Actuators for Micro Robots." Proceedings, 1989 IEEE International Conference on Robotics and Automation 3 (1989): 1547 -1552.

[85] Tsujino, J., Suzuki, R., and Takeuchi, M. "Load Characteristics of Ultrasonic Rotary Motor Using A Longitudinal-Torsional Vibration Converter With Diagonal Slits. Large Torque Ultrasonic Rotary Motor." Ultrasonics 34 (1996): 265-269.

[86] Tsujino, J., Ueoka, T., Otoda, K., and Fujimi, A. "One-Dimensional Longitudinal-Torsional Vibration Converter with Multiple Diagonally Slitted Parts." Ultrasonics 38 (2000): 72-76.

[87] Ueha, S. and Tomikawa, Y. (1993). Ultrasonic Motors: Theory and Applications. Oxford : Clarendon Press ; New York : Oxford University Press.

[88] Uchino, K. (1997). Piezoelectric Actuators and Ultrasonic Motors. Boston : Kluwer Academic Publishers.

[89] Uchino, K. "Piezoelectric Ultrasonic Motors: Overview." Journal of Smart Materials and Structures 7 (1998): 273-285.

[90] Uchino, K. "Recent Trend of Piezoelectric Actuator Developments." 1999 International Symposium on Micromechatronics and Human Science (1999): 3-9.

[91] Udayakumar, K.R., Bart, S.F., Flynn, A.M., Chen, J., Tavrow, L.S., Cross, L.E., Brooks, R.A., and Ehrlich, D.J. "Ferroelectric Thin Film Ultrasonic Micromotors." Micro Electro Mechanical Systems, 1991, MEMS '91, Proceedings. An Investigation of Micro Structures, Sensors, Actuators, Machines and Robots. IEEE , 1991 (1991): 109-113.

[92] Ugural, A.C., and Fenster, S.K. (1995). Advanced Strength and Applied Elasticity. Englewood Cliffs, NJ: PTR Prentice Hall.

[93] Van Iwaarden, J. L. (1985). Ordinary Differential Equations with Numerical Techniques. San Diego: Harcourt Brace Jovanovich Publishers.

[94] Wallace, R.S. "Miniature Direct Drive Rotary Actuators II: Eye, Finger and Leg." Proceedings: IEEE (1994): 1496-1501.

[95] Wallace, R.S. and Selig, J.M. "Scaling Direct Drive Robots." IEEE Int. Conf. on Robotics and Automation (1995): 2947-2953.

[96] Wallaschek, J. "Contact Mechanics of Piezoelectric Ultrasonic Motors." Smart Materials and Structures 7 (1998): 369-381.

[97] Wise, S. A. "Displacement Properties of RAINBOW and THUNDER Piezoelectric Actuators." Sensors and Actuators A 69 (1998): 33-38.

[98] Wojcik, G.L., Vaughan, D.K., Abboud, N., and Mould, J., Jr. "Electromechanical Modeling Using Explicit Time-Domain Finite Elements." IEEE Ultrasonics Symposium (1993): 1107-1112.

[99] Xu, J. "A Resonant Driver Circuit For The Standing Wave Rotary Piezoelectric Motor." North Carolina State University Center for Robotics and Intelligent Machines, Technical Report NCSU-CRIM-TR-2002-0203, 2002.

[100] Xu, W., and King, T.G. "Piezomotors using Flexure Hinged Displacement Amplifiers." IEE Colloquium on Innovative Actuators for Mechatronic Systems 11 (1995): 1-5.

[101] Yao, K., Koc, B., and Uchino, K. "Longitudinal-Bending Mode Micromotor Using Multilayer Piezoelectric Actuator." IEEE Transactions on Ultrasonics, Ferroelectrics and Frequency Control 48, 4 , (2001): 1066 –1071.

[102] Yen, K., Yang, C. and Roig, G. "Linear Piezoelectric Step Motors." Proceedings IEEE Southeastcon 1990 (1990): 21-24.

[103] Young, W.C. (1989). Roark's Formulas for Stress and Strain, 6th ed. New York: McGraw-Hill.

[104] Zhang, B., and Zhu, Z. "Developing a Linear Piezomotor With Nanometer Resolution and High Stiffness." IEEE/ASME Transactions on Mechatronics 2 (1997): 22-29.

Appendices

Appendix A

Back Slip Superposition

Model Calculations

A.1 THUNDERWORM Back Slip Calculations

Superposition model calculations were performed using a spreadsheet. Figure A.1 is an excerpt showing model parameters. Figures A.2 through A.7 display excerpts of the spreadsheet calculations for significant components of the total back slip.   Transducer module displacement versus load is calculated from the curve fit of the empirical deflection data shown in Figure 3.10.

Dimensional	Value	Units	Comments
Rod Diameter, D	0.0064	m	1/4 in
Rod Moment of Inertia, Ic	1.287E-08	m^4	
Pawl Volume, *V*	8.27E-07	m^3	calculated by hand 9/28/99 notes
Pawl Hole Diameter, th	7.50E-03	m	
Pawl Thickness, tc	1.62E-03	m	
Pawl Length, lp	0.02404	m	pawl length not including release portion
Pawl Moment of Inertia, Ixxp	4.464E-12	m^4	
Pawl Pre-load Attachment Length, lpr	2.800E-03	m	point of spring attachment measured from lower edge
Pawl Arm, lt	1.650E-02	m	distance from lower edge to lower rod contact point
Initial Pawl Rear Edge -To-C.L., s0	3.434E-03	m	rear edge distance from lower contact point to rod C.L.
Latch L.O.A. length, L	0.00767	m	LATCH line of action length
Latching Angle, θ, θc	1.19923	rad	angle pawl plane makes with rod axis
LATCH Housing Effective Radius, R		m	
LATCH Housing Width		m	
LATCH Housing Depth		m	
LATCH Housing Cross-Sectional Area, A		m^2	LATCH HOUSING DEFL OMITTED FOR TWORM!!
LATCH Housing Moment of Inertia, Ixxc		m^4	
Contact Radius, r1	3.20E-03	m	rod radius, r1' corresponds to the rod axial profile, and is infinite
Pawl Slot Radius, r2	-3.20E-03	m	matches the rod radius
Radius of the slot edge in contact with rod, r2'	1.00E-05	m	assigned an arbitrarily small value
Contact Deformation Coefficient, m	4.00E-05		
Contact Deformation Coefficient, A	5.00E+04		
Contact Deformation Coefficient, B	5.03E+04		
F2(e)	1.003E+00		using this quantity, F2(e) is found from the plot in Johnson, p.97

Figure A.1. **THUNDERWORM back slip superposition model: spreadsheet parameter table**

Material	Value	Units	Comments
Density, ρ	7895	kg/m^3	density of 410 SS
Coefficient of Static Friction, μs	0.74		mild steel on mild steel (dry), see Mark's 3-26
Coefficient of kinetic Friction, μk	0.57		mild steel on mild steel (dry), see Mark's 3-26
Poisson's Ratio, ν	0.32		stainless steel (ref: www.physics.uwstout.edu)
Modulus of Elasticity, E	2.07E+11	Pa	stainless steel (ref: www.physics.uwstout.edu)
Shear Modulus of Elasticity, G	8.000E+10	Pa	stainless steel (ref: www.physics.uwstout.edu)
Loading	**Value**	**Units**	**Comments**
Pawl Static Pre-Load, Q	3.94	N	
Pre-Load Spring Constant, k	1929.70	N/m	
Load Spring Constant, kl	733.79	N/m	4.19 lbf/in
Spring Initial Length, l0	0.0090	m	
Pawl Weight, W	5.89E-02	N	
Motor	**Value**	**Units**	**Comments**
THUNDER extender module initial displacement, dth	4.400E-04	m	480V-experimental displacement value
Mass of Rear Latch/Extender Module Assembly, mR	4.730E-01	kg	
THUNDERWORM mass	6.163E-01	kg	This must exclude the rod
Extender module 480V equivalent stiffness, Keq(480)	4.940E+04	N/m	

Figure A.1. **(Continued)**

LATCH LOADING

Spring Load, Q, (N)	Latch Thrust Load, P, (N)	Upper Normal Force, N, (N)	Lower Normal Force, N', (N)
0.000	0.000	-1.736E+00	-3.225E+00
0.500	0.441	-1.538E+00	-2.867E+00
1.000	0.883	-1.340E+00	-2.509E+00
1.500	1.324	-1.142E+00	-2.151E+00
2.000	1.766	-9.446E-01	-1.793E+00
2.500	2.207	-7.468E-01	-1.435E+00

Figure A.2. **THUNDERWORM back slip spreadsheet excerpt: latch loading**

138

THUNDER MODULE DISPLACEMENT   EMPIRICALLY DETERMINED FROM PLOT

Spring Load, Q, (N)	THUNDER module displacement, dth (m)
0.00	4.400E-04
0.50	4.302E-04
1.00	4.205E-04
1.50	4.107E-04
2.00	4.010E-04

Figure A.3. **THUNDERWORM back slip spreadsheet excerpt: module displacement**

PART II: ROD/PAWL HERTZIAN CONTACT DEFLECTION MODEL

Upper Normal Force, N, (N)	δc (m)	$\theta 2$ (rad)	Spring Load, Q, (N)	$\delta 2$ (m)
-1.736E+00	1.4729E-06	1.19906	0.00	3.78E-06
-1.538E+00	1.35877E-06	1.19907	0.50	3.49E-06
-1.340E+00	1.23962E-06	1.19908	1.00	3.18E-06
-1.142E+00	1.11444E-06	1.19910	1.50	2.86E-06
-9.446E-01	9.81782E-07	1.19911	2.00	2.52E-06

Figure A.4. **THUNDERWORM back slip spreadsheet excerpt: contact deflection**

PART III: PAWL STATIC DEFLECTION MODEL

Spring Load, Q, (N)	$\delta 3$ (m)
0.000	-3.46E-06
0.500	-2.22E-06
1.000	-9.78E-07
1.500	2.62E-07
2.000	1.50E-06

Figure A.5. **THUNDERWORM back slip spreadsheet excerpt: pawl deflection**

A.2 Milliworm Back Slip Calculations

Parameters for the Milliworm back slip calculations are shown in Figure A.8. Spreadsheet calculations for the back slip components are performed in the same manner as the THUNDERWORM, and are omitted.

LOW-LOAD REGIME: KINETIC BACK SLIP COMPONENTS

Spring Load, (N)	THUNDER module displacement, dth (m)	Lower Pawl Friction Force, F'f, (N)	Rear Latch/Extender Assembly Velocity, vR, (m/s)
0.000	4.400E-04	8.4895E-01	3.974E-02
0.500	4.302E-04		3.930E-02
1.000	4.205E-04		3.885E-02
1.500	4.107E-04		3.840E-02
2.000	4.010E-04		3.794E-02

		Quadratic Formula Parameter Calculations		Forward Latch
Post-Impact Motor Velocity, v3f (m/s)	a [kl (1,2,3)]	b	c	Kinetic Forward Slip, δk, (m)
3.050E-02	-3.669E+02	-1.592E+00	2.867E-04	1.731E-04
3.016E-02		-1.845E+00	2.803E-04	1.476E-04
2.982E-02		-2.097E+00	2.740E-04	1.278E-04
2.947E-02		-2.350E+00	2.676E-04	1.119E-04
2.912E-02		-2.602E+00	2.613E-04	9.904E-05

Figure A.6. **THUNDERWORM back slip spreadsheet excerpt: kinetic back slip**

PART IV: PAWL FORWARD HALF-CYCLE ROTATION: GEOMETRIC BACK SLIP CONTRIBUTION

Spring Load, Q, (N)	s0	s1'	φ	θ^*	s1	$\delta4$
0.00	3.4340E-03	1.6345E-02	2.5085E-02	1.2243E+00	3.4022E-03	**9.1451E-05**
0.50	3.4346E-03	1.6349E-02	2.4518E-02	1.2236E+00	3.4031E-03	**8.9545E-05**
1.00	3.4346E-03	1.6352E-02	2.3959E-02	1.2230E+00	3.4038E-03	**8.7521E-05**
1.50	3.4346E-03	1.6355E-02	2.3401E-02	1.2225E+00	3.4044E-03	**8.5498E-05**
2.00	3.4345E-03	1.6359E-02	2.2842E-02	1.2219E+00	3.4051E-03	**8.3474E-05**

Figure A.7. **THUNDERWORM back slip spreadsheet excerpt: pawl return rotation**

MILLIWORM MODEL DATA

Dimensional	Value	Units	Comments
Rod Diameter, D	0.0012	m	0.047 in
Rod Moment of Inertia, Ic	8.482E-11	m^4	
Pawl Volume, *V*	7.88E-09	m^3	from Pro\E
Pawl Hole Diameter, th	0.001524	m	0.060 in slot height
Pawl Thickness, tc	0.000508	m	0.020 in thickness
Pawl Length, lp	0.00450	m	pawl length not including release portion
Pawl Moment of Inertia, Ixxp	2.742E-14	m^4	
Pawl Pre-load Attachment Length, lpr	1.400E-03	m	point of elastic attachment measured from lower edge (high error!)
Pawl Arm, lt	3.000E-03	m	distance from lower edge to lower rod contact point
Initial Pawl Rear Edge -To-C.L., s0	6.530E-04	m	rear edge distance from lower contact point to rod C.L.
Latch L.O.A. length, L	0.00161	m	clamp line of action length
Latching Angle, θ, θc	1.16528	rad	angle pawl plane makes with rod axis
LATCH Housing Effective Radius, R	0.0054	m	models clamp housing as a curved beam, determined graphically
LATCH Housing Width	0.00203	m	0.080 inch
LATCH Housing Depth	0.00251	m	0.099 inch
LATCH Housing Cross-Sectional Area, A	5.10E-06	m^2	0.080 x 0.099 in cross section
LATCH Housing Moment of Inertia, Ixxc	1.75E-12	m^4	
Contact Radius, r1	6.00E-04	m	rod radius, r1' corresponds to the rod axial profile, and is infinite
Pawl Slot Radius, r2	-6.00E-04	m	matches the rod radius
Radius of the slot edge in contact with rod, r2'	1.00E-05	m	assigned an arbitrarily small value
Contact Deformation Coefficient, m	4.00E-05		
Contact Deformation Coefficient, A	5.00E+04		
Contact Deformation Coefficient, B	5.14E+04		
F2(e)	1.014E+00		using this quantity, F2(e) is found from the plot in Johnson, p.97

Figure A.8. **Milliworm back slip superposition model spreadsheet parameter table**

Material	Value	Units	Comments
Density, ρ	7895	kg/m^3	density of 410 SS
Coefficient of Static Friction, μs	0.74		mild steel on mild steel (dry), see Mark's 3-26
Coefficient of kinetic Friction, μk	0.57		mild steel on mild steel (dry), see Mark's 3-26
Poisson's Ratio, ν	0.32		stainless steel (ref: www.physics.uwstout.edu)
Modulus of Elasticity, E	2.07E+11	Pa	stainless steel (ref: www.physics.uwstout.edu)
Shear Modulus of Elasticity, G	8.000E+10	Pa	stainless steel (ref: www.physics.uwstout.edu)
Loading	**Value**	**Units**	**Comments**
Pawl Static Pre-Load, F0	0.75	N	force generated by a nominal 4 oz dental elastic
4 oz. Dental Elastic Spring Constant, k	235.40	N/m	as measured 1/2001 see RTPZT_MW3A\lvdt_calibration.xls
Load Spring Constant, kl	452.01	N/m	4.19 lbf/in
Dental Elastic Initial Length, l0	0.0029	m	as measured from Pro/E
Pawl Weight, W	6.10E-04	N	
Motor	**Value**	**Units**	**Comments**
THUNDER extender module initial displacement, dth	1.60E-05	m	480V-experimental displacement value (compromise between 022402-m & back slip vs. load file)
Mass of Rear Latch/Extender Module Assembly, mR	1.153E-02	kg	*This includes the mass of LVDT core and face plate! (12.93g)
MILLIWORM 3A mass	2.620E-02	kg	Excludes rod BUT includes mass of LVDT core+face plate (21.4g)
Extender module 480V equivalent stiffness, Keq(480)	1.900E+04	N/m	19 N/mm @ 0 V - Elastic rebound drives the forward step!!

Figure A.8. **(Continued)**

Appendix B

Annular THUNDER™

Transducer Analysis and

Milliworm Characterization

B.1 Sub Model 1 MAPLE™ Excerpt

The deflection expressions for the annular THUNDER™ transducer were derived using the MAPLE™ mathematics software package. The following is a listing of the MAPLE™ commands used to calculate the constants of integration for Sub Model 1. Some output (shown in blue) is included for clarity.

JEREMY PALMER
ROUND THUNDER DEFLECTION MODEL
1-07-02
CALCULATION OF CONSTANTS PART 1

```
> restart;
> C5:=0;
> q:=0;
> w(r):=((q*(r^4))/(64*Ds))+((C1*(r^2))/4)+(C2*ln(r/r0))+C3;
```

$$w(r) := \frac{1}{64}\frac{q\,r^4}{Ds} + \frac{1}{4}C1\,r^2 + C2\ln\left(\frac{r}{r0}\right) + C3$$

```
> wc(r):=((q*(r^4))/(64*Dc))+((C4*(r^2))/4)+(C5*ln(r/r0))+C6;
```

$$wc(r) := \frac{1}{64}\frac{q\,r^4}{Dc} + \frac{1}{4}C4\,r^2 + C5\ln\left(\frac{r}{r0}\right) + C6$$

```
> w(r0):=eval(w(r),r=r0);
> w(ri):=eval(w(r),r=ri);
> wc(ri):=eval(wc(r),r=ri);
> dwdr:=diff(w(r),r);
> dwcdr:=diff(wc(r),r);
> d2wdr2:=diff(dwdr,r);
> d2wcdr2:=diff(dwcdr,r);
> dwcridr:=eval(dwcdr,r=ri);
> dwridr:=eval(dwdr,r=ri);
> Mr(r):= simplify(Ds*(d2wdr2+((nu/r)*dwdr)));
> Mr(r0):=eval(Mr(r),r=r0);
> Mr(ri):=eval(Mr(r),r=ri);
> Mrc(r):=simplify(Dc*(d2wcdr2+((nuc/r)*dwcdr)));
> Mrc(ri):=eval(Mrc(r),r=ri);
> MT(ri):=Mrc(ri)-(Mrp/3);
>
bcs:={w(r0)=0,Mr(r0)=0,w4(ri)=wc(ri),dwridr=dwcridr,MT(ri)=Mr(
ri)};
> vars:={C1,C2,C3,C4,C6};
> simplify(solve(bcs,vars));
```

B.2 Sub Model 2 MAPLE™ Excerpt

The following is a listing of the MAPLE™ commands used to calculate the constants of integration for

Sub Model 2. Some output (shown in blue) is included for clarity.

JEREMY PALMER
ROUND THUNDER DEFLECTION MODEL
1-07-02
CALCULATION OF CONSTANTS PART 2b: SIMPLY-SUPPORTED ANNULAR
COMPOSITE WITH MOMENT LOADS

```
> restart;
> w(r):=((-C7*(r^2))/4)-(C8*ln(r/r0))+C9;
```

$$w(r) := -\frac{1}{4}C7\,r^2 - C8\ln\left(\frac{r}{r0}\right) + C9$$

```
> wc(r):=((-C10*(r^2))/4)-(C11*ln(r/r0))+C12;
```

$$wc(r) := -\frac{1}{4}C10\,r^2 - C11\ln\left(\frac{r}{r0}\right) + C12$$

```
> w(r0):=eval(w(r),r=r0);
> w(ri):=eval(w(r),r=ri);
> wc(ri):=eval(wc(r),r=ri);
> dwdr:=diff(w(r),r);
> dwcdr:=diff(wc(r),r);
> dwridr:=eval(dwdr,r=ri);
> dwcridr:=eval(dwcdr,r=ri);
> d2wdr2:=diff(dwdr,r);
> d2wcdr2:=diff(dwcdr,r);
> d2wcridr2:=eval(d2wcdr2,r=ri);
> Mr(r):= simplify(Ds*(d2wdr2+((nu/r)*dwdr)));
> Mr(r0):=eval(Mr(r),r=r0);
> Mr(ri):=eval(Mr(r),r=ri);
> Mrc(r):=simplify(Dc*(d2wcdr2+((nuc/r)*dwcdr)));
> Mrc(ri):=eval(Mrc(r),r=ri);
```

Mh IS DERIVED FROM THE RESULTS OF THE SUB MODEL 1.

```
> Mh:=1/48*(-3*nuc*nu^2*ri^4*q*Ds+16*nuc*nu*r0^2*Dc*Mrp-
16*nuc*nu*ri^2*Dc*Mrp+3*nuc*nu^2*r0^2*ri^2*q*Ds-
3*nuc*r0^2*ri^2*q*Ds-3*r0^2*ri^2*Dc*nuc^2*q-
3*nu*r0^2*ri^2*Dc*nuc^2*q+3*nu*ri^4*Dc*nuc^2*q-
3*Dc*nuc^2*q*ri^4+16*nuc*r0^2*Dc*Mrp+16*nuc*Dc*Mrp*ri^2+3*nuc*
q*ri^4*Ds-
3*nuc*rh^2*q*ri^2*Ds+3*q*rh^2*Dc*r0^2*nuc^2+3*nu*q*rh^2*Dc*r0^
2*nuc^2-
3*q*rh^2*nu*ri^2*nuc^2*Dc+9*q*rh^2*r0^2*Ds+9*q*rh^2*Dc*r0^2+9*
rh^2*q*ri^2*Dc-
9*rh^2*q*ri^2*Ds+3*rh^2*Dc*nuc^2*q*ri^2+3*nuc*q*rh^2*r0^2*Ds-
3*nuc*q*rh^2*nu^2*r0^2*Ds+3*nuc*rh^2*nu^2*ri^2*q*Ds+12*q*rh^2*
Dc*r0^2*nuc-
9*q*rh^2*nu^2*r0^2*Ds+12*nu*q*rh^2*Dc*r0^2*nuc+9*nu*q*rh^2*Dc*
r0^2+9*rh^2*nu^2*ri^2*q*Ds+12*rh^2*Dc*nuc*q*ri^2-
```

```
12*q*rh^2*nu*ri^2*nuc*Dc-9*q*rh^2*nu*ri^2*Dc-3*nu^2*ri^4*q*Ds-
18*Dc*nuc*q*r0^4-6*Dc*nuc*q*ri^4-
6*Dc*nu*q*r0^4+3*nu*q*ri^4*Dc+16*nu*r0^2*Dc*Mrp-
16*nu*ri^2*Dc*Mrp+3*nu^2*r0^2*ri^2*q*Ds+3*nu*r0^2*ri^2*q*Dc+16
*r0^2*Dc*Mrp+16*Dc*Mrp*ri^2-3*r0^2*ri^2*q*Ds+3*r0^2*ri^2*q*Dc-
3*q*ri^4*Dc-18*Dc*q*r0^4-
6*Dc*nuc*nu*q*r0^4+6*nu*ri^4*Dc*nuc*q+3*q*ri^4*Ds)/(-
nuc*Dc*ri^2-Dc*r0^2*nuc-r0^2*Ds-Dc*r0^2-Dc*ri^2-
Dc*nu*r0^2+nu*ri^2*Dc+nu^2*r0^2*Ds-nu*r0^2*nuc*Dc-
nu^2*ri^2*Ds+nu*ri^2*nuc*Dc+ri^2*Ds)+1/3*Mrp;
> MT(r):=Mrc(r)-(Mrp/3);
> MT(ri):=eval(MT(r),r=ri);
> MT(rh):=eval(MT(r),r=rh);
>
bcs:={w(r0)=0,Mr(r0)=0,w(ri)=wc(ri),dwridr=dwcridr,MT(ri)=Mr(r
i),MT(rh)=Mh};
> vars:={C7,C8,C9,C10,C11,C12};
> solve(bcs,vars);
```

B.3 Sub Model 3 MAPLE™ Excerpt

The following is a listing of the MAPLE™ commands used to calculate the constants of integration for

Sub Model 3. Some output (shown in blue) is included for clarity.

JEREMY PALMER
ROUND THUNDER DEFLECTION MODEL
1-08-01
CALCULATION OF CONSTANTS PART 2c: SIMPLY-SUPPORTED ANNULAR
COMPOSITE WITH SHEAR LOADS
NOTES:
C17 is currently in here.

```
> restart;
> P3:=-q*pi*rh^2;
```

$$P3 := -q\,\pi\,rh^2$$

```
> w(r):=(((P3*(r^2))/(8*pi*Ds))*((ln(r/r0))-1))-
((C13*(r^2))/4)-(C14*ln(r/r0))+C15;
```

$$w(r) := -\frac{1}{8}\frac{q\,rh^2\,r^2\left(\ln\left(\frac{r}{r0}\right)-1\right)}{Ds} - \frac{1}{4}C13\,r^2 - C14\ln\left(\frac{r}{r0}\right) + C15$$

```
> wc(r):=(((P3*(r^2))/(8*pi*Dc))*((ln(r/r0))-1))-
((C16*(r^2))/4)-(C17*ln(r/r0))+C18;
```

$$wc(r) := -\frac{1}{8}\frac{q\,rh^2\,r^2\left(\ln\left(\frac{r}{r0}\right)-1\right)}{Dc} - \frac{1}{4}C16\,r^2 - C17\ln\left(\frac{r}{r0}\right) + C18$$

```
> w(r0):=eval(w(r),r=r0);
> w(ri):=eval(w(r),r=ri);
> wc(ri):=eval(wc(r),r=ri);
> dwdr:=diff(w(r),r);
> dwridr:=eval(dwdr,r=ri);
> dwcdr:=diff(wc(r),r);
> dwcridr:=eval(dwcdr,r=ri);
> d2wdr2:=diff(dwdr,r);
> d2wridr2:=eval(d2wdr2,r=ri);
> d2wcdr2:=diff(dwcdr,r);
> d2wcridr2:=eval(d2wcdr2,r=ri);
> Mr(r):= simplify(Ds*(d2wdr2+((nu/r)*dwdr)));
> Mr(r0):=eval(Mr(r),r=r0);
> Mr(ri):=eval(Mr(r),r=ri);
> Mrc(r):=simplify(Dc*(d2wcdr2+((nuc/r)*dwcdr)));
> Mrc(ri):=eval(Mrc(r),r=ri);
> MT(r):=Mrc(r)-(Mrp/3);
> MT(ri):=eval(MT(r),r=ri);
> MT(rh):=eval(MT(r),r=rh);
>
bcs:={w(r0)=0,MT(rh)=0,Mr(r0)=0,w(ri)=wc(ri),dwridr=dwcridr,MT
(ri)=Mr(ri)};
> vars:={C13,C14,C15,C16,C17,C18};
> simplify(solve(bcs,vars));
```

B.4 Top-Level Model Output Verifications

A series of four independent verifications of the output of the top-level deflection model were undertaken. The MAPLE™ command listings and results follow. Note that in each case, the complete expressions for the constants of integration were too large to be reprinted in this document, and are omitted.

B.4.1 Identical Material Layers

The following command listing compares the output of the top-level deflection expressions to that of the Timoshenko model (Timoshenko and Woinowsky-Krieger) [82] for the case of the 1.75-inch diameter transducer with piezoceramic and substrate layers assigned identical material properties, and a very small hole radius.

JEREMY PALMER
ROUND THUNDER MODEL VERIFICATION #2
1-16-02

HERE, WE CONSIDER THE 1.75 INCH NO-HOLE CASE (TOP-LEVEL MODEL)
WHERE THE PZT LAYER IS CHANGED TO BE THE SAME MATERIAL
AS THE SUBSTRATE, AND ri=r0. WE COMPARE THE DEFLECTION FOR A UNIT
LOAD WITH TIMOSHENKO'S RESULT
DATA (METRIC UNITS USED THROUGHOUT)

```
> restart;
> unassign('q','Ds','Dc','nu','nuc','Mrp','ri','rh');
> q:=-1;
> nu:=0.27;
```
NOMINAL: 0.27
```
> nuc:=0.27;
> nup:=0.27;
```
GOT THIS FROM ANSYS INPUT FILE
```
> hm:=0.2E-03;
```
CHANGED FOR TESTING 1/13/02
```
> hp:=0.4E-03;
```
CHANGED FORTESTING 1/13/02
```
> Ep:=2E+11;
```
GOT THIS FROM PIEZOSYSTEMS
```
> Em:=2E+11;
```
NOMINAL 2E+11 (STEEL)
```
> V:=0;
```
NOMINAL 480V
```
> d31:=190E-12;
```
GOT THIS FROM PIEZOSYSTEMS
EQUATIONS
```
> zns:=((Ep*hp*((hp/2)+hm))+(Em*hm*(hm/2)))/((Ep*hp)+(Em*hm));
> Ds:=(Em*(hm^3))/(12*(1-(nu^2)));
> Dc:=(((1/3)*(Ep/(1-(nup^2))))*(((hm+hp-zns)^3)-((hm-
zns)^3)))+(((1/3)*(Em/(1-(nu^2))))*(((hm-zns)^3)-((-zns)^3)));
> Mrp:=(Ep*V*d31*(hp-(2*zns)+(2*hm)))/(2*(1-nup));
> r0:= 0.022;
```
CHANGED FROM 1.75 IN. RADIUS 1/13/02
```
> ri:=r0;
```
NOMINAL: 0.857r0
```
> rh:=0.00001*r0;
```
NOMINAL: 0.23r0

$$C4 := .00004011654168$$

$$C6 := -.3911485492\ 10^{-8}$$

$$C10 := -.4011654165\ 10^{-14}$$

$$C11 := -.1688961359 \, 10^{-17}$$

$$C12 := -.4854101543 \, 10^{-18}$$

$$C16 := .1791136120 \, 10^{-14}$$

$$C17 := .3020795782 \, 10^{-26}$$

$$C18 := .9708203052 \, 10^{-18}$$

> `C19:=C4-C10-C16;`

$$C19 := .00004011654168$$

> `C20:=-C11-C17;`

$$C20 := .1688961356 \, 10^{-17}$$

> `C21:=C6+C12+C18;`

$$C21 := -.3911485491 \, 10^{-8}$$

> `wc(r):=((q*(r^4))/(64*Dc))-`
`(((q*(rh^2)*(r^2))/(8*Dc))*((ln(r/r0))-`
`1))+((C19*(r^2))/4)+(C20*ln(r/r0))+C21;`

$$wc(r) := -.004023871528 \, r^4$$

$$+ .1558043056 \, 10^{-14} \, r^2 \, (\ln(45.45454545 \, r) - 1)$$

$$+ .00001002913542 \, r^2 + .1688961356 \, 10^{-17} \, \ln(45.45454545 \, r)$$

$$- .3911485491 \, 10^{-8}$$

> `wc(rh):=eval(wc(r),r=rh);`

$$wc(.22 \, 10^{-6}) := -.3911485510 \, 10^{-8}$$

TIMOSHENKO MODEL (68), p.57

>
`w_timo_max:=((5+nuc)*q*(r0^4))/(64*(1+nuc)*((Em*((hm+hp)^3))/(`
`12*(1-(nuc^2))))));`

$$w\_timo\_max := -.3911485494 \, 10^{-8}$$

> `ff:=w_timo_max/wc(rh);`

$$ff := .9999999959$$

THIS AGREES WITH TIMOSHENKO'S RESULT!

B.4.2 Zero Piezo Layer Thickness

The following command listing compares the output of the top-level deflection expressions to that of the Timoshenko model [82] for the case of the 1.75-inch diameter transducer with zero piezoceramic layer thickness and a very small hole radius.

```
JEREMY PALMER
ROUND THUNDER MODEL VERIFICATION #3
1-19-02

HERE, WE CONSIDER THE 1.75 INCH NO-HOLE CASE WHERE THE PZT LAYER
THICKNESS IS CHANGED TO ZERO,
 AND ri=r0.  WE COMPARE THE DEFLECTION FOR A UNIT LOAD WITH
TIMOSHENKO'S RESULT
DATA (METRIC UNITS USED THROUGHOUT)
> restart;
>
unassign('q','Ds','Dc','nu','nuc','Mrp','ri','rh','wc(r)','wc(
rh)');
> q:=-1;
> nu:=0.3;
NOMINAL: 0.27
> nuc:=0.3;
> nup:=0.15;
GOT THIS FROM ANSYS INPUT FILE
> hm:=0.2E-03;
CHANGED FOR TESTING 1/13/02
> hp:=0;
CHANGED FORTESTING 1/13/02
> Ep:=6.6E+10;
GOT THIS FROM PIEZOSYSTEMS
> Em:=2E+11;
NOMINAL 2E+11 (STEEL)
> V:=0;
NOMINAL 480V
> d31:=190E-12;
GOT THIS FROM PIEZOSYSTEMS
EQUATIONS
> zns:=((Ep*hp*((hp/2)+hm))+(Em*hm*(hm/2)))/((Ep*hp)+(Em*hm));
> Ds:=(Em*(hm^3))/(12*(1-(nu^2)));
> Dc:=(((1/3)*(Ep/(1-(nup^2))))*(((hm+hp-zns)^3)-((hm-
zns)^3)))+(((1/3)*(Em/(1-(nu^2))))*(((hm-zns)^3)-((-zns)^3)));
> Mrp:=(Ep*V*d31*(hp-(2*zns)+(2*hm)))/(2*(1-nup));
> r0:= 0.022;
CHANGED FROM 1.75 IN. RADIUS 1/13/02
> ri:=r0;
```

NOMINAL: 0.857r0
> `rh:=1E-22*r0;`
NOMINAL: 0.23r0

$$C4 := .001048162500$$

$$C6 := -.1018464562 \, 10^{-6}$$

>

$$C10 := -.1048162503 \, 10^{-46}$$

>

$$C11 := -.4710741752 \, 10^{-50}$$

>

$$C12 := -.1268276628 \, 10^{-50}$$

>

$$C16 := .4446750000 \, 10^{-47}$$

>

$$C17 := .3760253026 \, 10^{-92}$$

>

$$C18 := .2536553250 \, 10^{-50}$$

> `C19:=C4-C10-C16;`

$$C19 := .001048162500$$

> `C20:=-C11-C17;`

$$C20 := .4710741752 \, 10^{-50}$$

> `C21:=C6+C12+C18;`

$$C21 := -.1018464562 \, 10^{-6}$$

> `wc(r):=((q*(r^4))/(64*Dc))-`
`(((q*(rh^2)*(r^2))/(8*Dc))*((ln(r/r0))-`
`1))+((C19*(r^2))/4)+(C20*ln(r/r0))+C21;`

$$wc(r) := -.1066406250 \, r^4$$

$$+ .4129125000 \, 10^{-47} \, r^2 \, (\ln(45.45454545 \, r) - 1)$$

$$+ .0002620406250 \, r^2 + .4710741752 \, 10^{-50} \, \ln(45.45454545 \, r)$$

$$- .1018464562 \, 10^{-6}$$

> `wc(rh):=eval(wc(r),r=rh);`

$$wc(.22\ 10^{-23}) := -.1018464562\ 10^{-6}$$

TIMOSHENKO MODEL (68), p.57
>
`w_timo_max:=((5+nuc)*q*(r0^4))/(64*(1+nuc)*((Em*((hm+hp)^3))/(
12*(1-(nuc^2)))));`

$$w\_timo\_max := -.1018464563\ 10^{-6}$$

> `ff:=w_timo_max/wc(rh);`

$$ff := 1.000000001$$

>
THIS AGREES WITH TIMOSHENKO'S RESULT!
NOTE: HAD TO MAKE NU = NUC TO GET AGREEMENT!

B.4.3 Coorpender-Smith Example

The following MAPLE™ excerpt compares deflection results with those published by Coorpender et al. (Coorpender, Finkel, Kyzar, Sims, Smirnova, Tawhid, Bouton, and Smith) [18]. The Coorpender-Smith example considers unloaded piezoelectric actuation at 1 volt of a 4 mm diameter circular THUNDER™ with no hole and clamped end conditions. Since the model derived in this dissertation considers free end conditions, the predicted deflection should be slightly *larger* than the Coorpender-Smith example.

JEREMY PALMER
ROUND THUNDER DIMENSIONAL ANALYSIS
1-19-02

HERE, WE'RE PLOTTING wc(rh) vs. r0 TO OBSERVE THE SCALING RELATIONSHIP.
DATA (METRIC UNITS USED THROUGHOUT)
> `restart;`
> `unassign('q','Ds','Dc','nu','nuc','Mrp','ri','rh');`
> `q:=0;`
> `nu:=0.34;`
NOMINAL: 0.27 (COORPENDER-SMITH EXAMPLE ASSUMES A HARDENED
BRASS SUBSTRATE)
> `nuc:=0.3;`
> `nup:=0.15;`
GOT THIS FROM ANSYS INPUT FILE
> `hm:=49.85e-06;`
CHANGED FOR TESTING 1/13/02
> `hp:=0.20E-03;`
CHANGED FORTESTING 1/13/02
> `Ep:=6.6E+10;`

GOT THIS FROM PIEZOSYSTEMS
> **Em:=104E+09;**
NOMINAL 2E+11 (STEEL)
> **V:=1;**
NOMINAL 480V
> **d31:=190E-12;**
GOT THIS FROM PIEZOSYSTEMS
EQUATIONS
> **zns:=((Ep*hp*((hp/2)+hm))+(Em*hm*(hm/2)))/((Ep*hp)+(Em*hm));**
> **Ds:=(Em*(hm^3))/(12*(1-(nu^2)));**
> **Dc:=(((1/3)*(Ep/(1-(nup^2))))*(((hm+hp-zns)^3)-((hm-zns)^3)))+(((1/3)*(Em/(1-(nu^2))))*(((hm-zns)^3)-((-zns)^3)));**
> **Mrp:=(Ep*V*d31*(hp-(2*zns)+(2*hm)))/(2*(1-nup));**
> **r0:= 4e-03;**
CHANGED FROM 1.75 IN. RADIUS 1/13/02
> **ri:=3.67e-03;**
NOMINAL: 0.857r0
> **rh:=0.00001*r0;**
NOMINAL: 0.23r0

$$C4 := .002418199128$$

$$C6 := -.9582332193 \, 10^{-8}$$

$$C10 := -.002418199129$$

$$C11 := .4496010612 \, 10^{-20}$$

$$C12 := -.9582332181 \, 10^{-8}$$

$$C16 := -.002418199127$$

$$C17 := .2248005307 \, 10^{-20}$$

$$C18 := -.9582332183 \, 10^{-8}$$

$$C19 := .007254597384$$

$$C20 := -.6744015919 \, 10^{-20}$$

$$C21 := -.2874699655 \, 10^{-7}$$

> **wc(r):=((C19*(r^2))/4)+(C20*ln(r/r0))+C21;**

$$wc(r) := .001813649346 \, r^2 - .6744015919 \, 10^{-20} \ln(250.0000000 \, r)$$
$$- .2874699655 \, 10^{-7}$$

> **wc(rh):=eval(wc(r),r=rh);**

$$\text{wc}(.4\ 10^{-7}) := -.2874699655\ 10^{-7}$$

RALPH SMITH GOT -22.54 nm WITH SAME PARAMETERS BUT CLAMPED END
CONDITIONS (NOT SURE WHAT HE USED FOR d31 THOUGH)! THIS IS
CONSISTENT WITH THE ANTICIPATED RESULT IN THAT THE PREDICTION FOR
FREE END CONDITIONS SHOULD BE SLIGHTLY LARGER.

B.5 Annular THUNDER™ Transducer Deflection Data Processing

This segment describes the annular THUNDER™ data processing procedure. Data for the 1.75-inch

diameter transducer is presented as an example. Annular THUNDER™ deflection was measured using the test

apparatus shown in Figure 4.5, according to the procedure outlined in Section 3.2.1. LVDT data for stylus

position versus load and voltage was compiled and averaged in a spreadsheet for up to six trials performed on

each of the transducer sizes listed in Table 4.2. The unloaded deflection under piezoelectric actuation at 480 V

was determined from the plot of displacement versus load. To understand this procedure, consider the

displacement plot for the 1.75-inch diameter annular THUNDER™ shown in Figure B.1. The unloaded

deflection corresponds to the point where the 480-volt curve crosses the *y*-axis. However, in the 1.75-inch case

shown in Figure B.1, the deflection behavior is non-linear at low loads and different values for the unloaded

deflection are possible depending on which portion of the curve is linearly extrapolated to the axis. For

example, if the portion of the curve from 0.724 to 1.7 N is extrapolated, an unloaded displacement of 134

microns results. Alternatively, considering the portion from 2.6 to 4.1 N yields an unloaded displacement of

103 microns. To reconcile this difference, the deflection corresponding to 0.724 N is reported. The physical

interpretation of this choice is that using the deflection at 0.724 N adequately filters out a portion of the effects

of settling in the test fixture, while acknowledging that this non-linear behavior occurred uniformly at various

voltage levels, and was reproducible. This method was preferred to averaging the two values, because it led to

better agreement with the prediction. Figure B.2 shows that this non-linear behavior was unique to the 1.75-

inch transducer, and the unloaded deflection for smaller transducer sizes (the 0.7-inch diameter transducer is

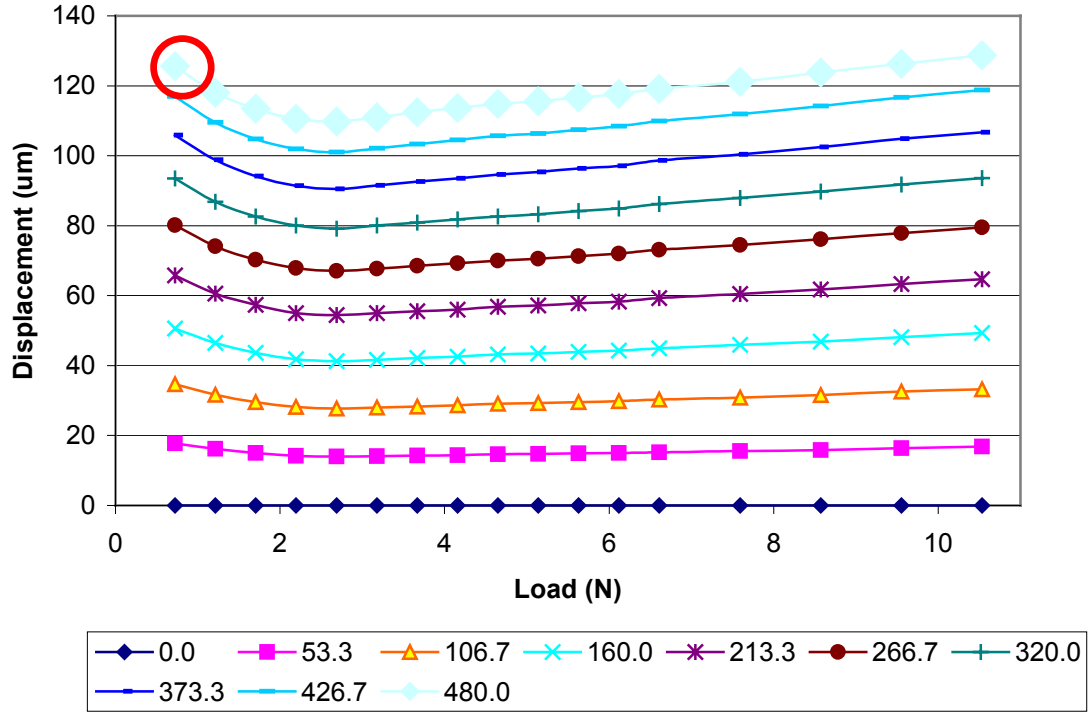shown in Figure B.2) was not impacted by this interpretation.

Figure B.1. **Deflection vs. load for 1.75-inch outer diameter annular THUNDER™**
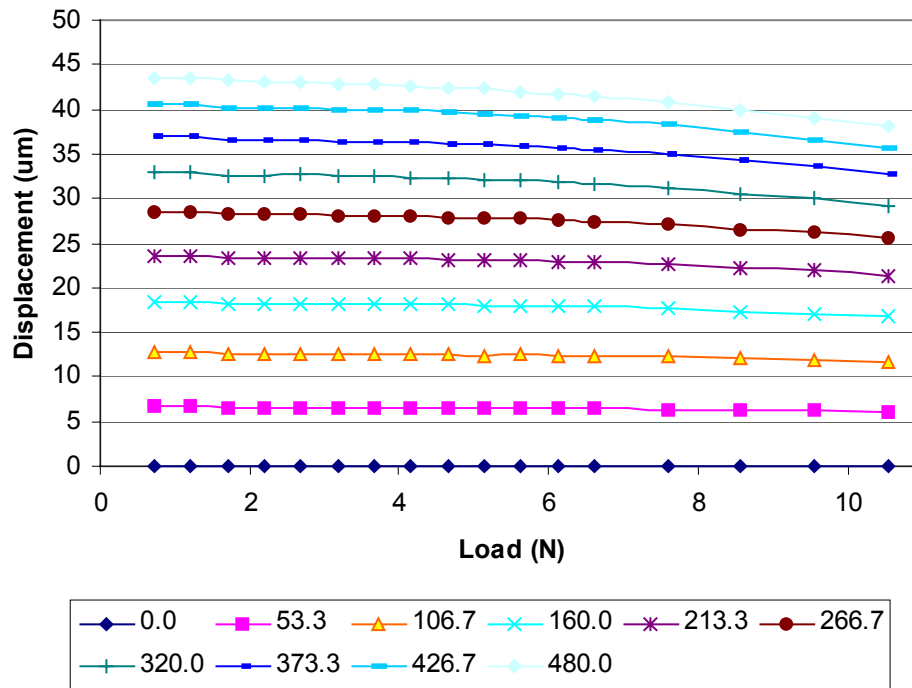

Figure B.2. **Deflection vs. load for the 0.7-inch outer diameter annular THUNDER™**

Stiffness at zero volts was measured from the plot of stylus position versus load. The plot for the 1.75-inch diameter transducer is shown in Figure B.3, below. Here, the stiffness corresponds to the inverse of the slope of the linear portion of the zero-volt plot. In all trials, the most linear portion was observed to be above 2 newtons of applied load.
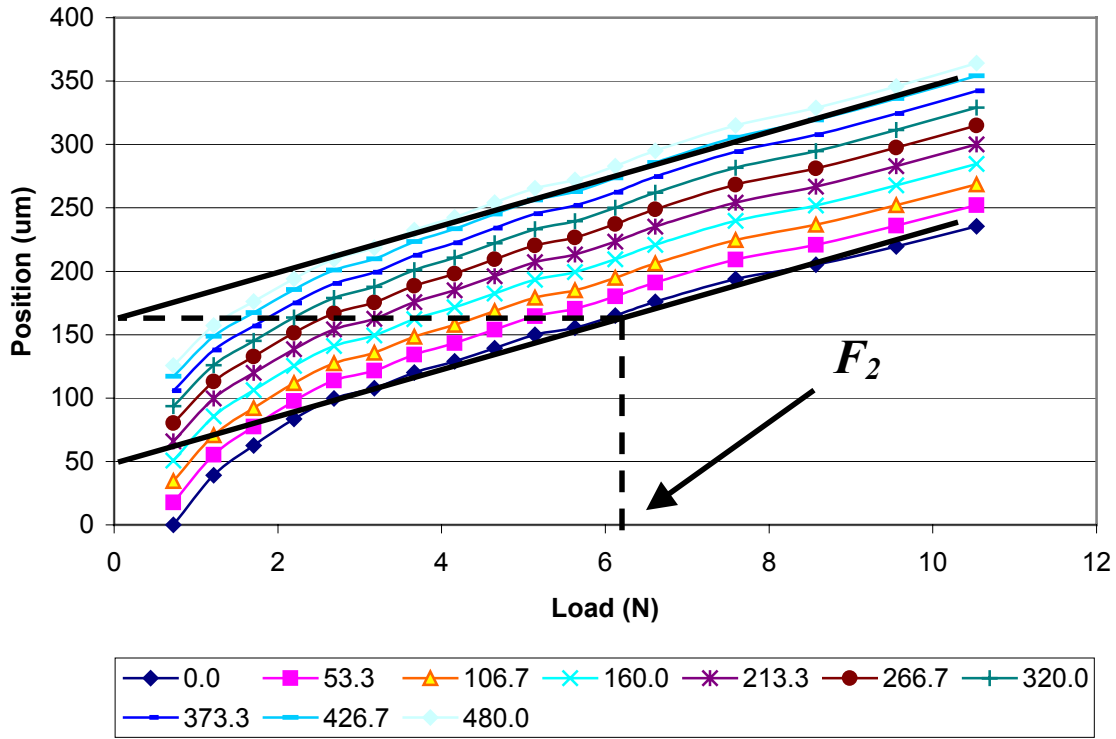

Figure B.3. **Stylus position vs. load for 1.75-inch outer diameter annular THUNDER™**

B.6 Scale Factor Development

Determining the scale relationships for transducer deflection and stiffness using MAPLE™ involved two steps: (1.) assigning material properties, piezoelectric actuation parameters, and thickness dimensions and, (2.) assigning radial dimensions such that they were constant multiples of the outer radius, r_o. The following sections show the MAPLE™ dimensional analysis results. Note that the complete expressions for the constants of integration are omitted due to their length.

B.6.1 Scale Factor For Deflection

The dimensional analysis for transducer deflection produced the following MAPLE™ output leading to

equations 4.23, and 4.24:

JEREMY PALMER
ROUND THUNDER DIMENSIONAL ANALYSIS
3-06-02

HERE, WE'RE PLOTTING wc(rh) vs. r0 TO OBSERVE THE SCALING RELATIONSHIP.
CONDITIONS: ZERO LOAD, 480 V PIEZOELECTRIC ACTUATION
DATA (METRIC UNITS USED THROUGHOUT, ALL LENGTHS IN METERS)

```
> restart;
> unassign('q','Ds','Dc','nu','nuc','Mrp','ri','rh');
> q:=0;
> nu:=0.27;
```
NOMINAL: 0.27
```
> nuc:=0.3;
> nup:=0.15;
```
GOT THIS FROM ANSYS INPUT FILE
```
> hm:=0.2e-03;
> hp:=0.30E-03;
> Ep:=6.6E+10;
```
GOT THIS FROM PIEZOSYSTEMS
```
> Em:=190E+09;
```
NOMINAL 190E+09 (STEEL)
```
> V:=480;
```
NOMINAL 480V
```
> d31:=190E-12;
```
GOT THIS FROM PIEZOSYSTEMS
EQUATIONS
```
> zns:=((Ep*hp*((hp/2)+hm))+(Em*hm*(hm/2)))/((Ep*hp)+(Em*hm));
> Ds:=(Em*(hm^3))/(12*(1-(nu^2)));
> Dc:=(((1/3)*(Ep/(1-(nup^2))))*(((hm+hp-zns)^3)-((hm-
zns)^3)))+(((1/3)*(Em/(1-(nu^2))))*(((hm-zns)^3)-((-zns)^3)));
> Mrp:=(Ep*V*d31*(hp-(2*zns)+(2*hm)))/(2*(1-nup));
> ri:=0.865*r0;
```
THE 0.8 FACTOR REFLECTS THE POSITION OF THE SUPPORTS IN THE TEST
FIXTURE
```
> rh:=0.142*r0;
```
THE 0.8 FACTOR REFLECTS THE POSITION OF THE SUPPORTS IN THE TEST
FIXTURE

$$C4 := .5190819933$$

$$C6 := -.1266170581\, r0^2$$

$$C10 := -.5187520050$$

$$C11 := .0002372316200\, r0^2$$

$$C12 := -.1265349090\, r0^2$$

$$C16 := -.5189169992$$

$$C17 := .0001186158100\, r0^2$$

$$C18 := -.1265759836\, r0^2$$

$$C19 := 1.556750997$$

$$C20 := -.0003558474300\, r0^2$$

$$C21 := -.3797279507\, r0^2$$

```
>wc(r):=((C19*(r^2))/4)+(C20*ln(r/r0))+C21;
```

$$wc(r) :=$$

$$.3891877492\, r^2 - .0003558474300\, r0^2 \ln\!\left(\frac{r}{r0}\right) - .3797279507\, r0^2$$

```
>wc(rh):=eval(wc(r),r=rh);
```

$$wc(.142\, r0) := -.3711857803\, r0^2$$

B.6.2 Scale Factors For Stiffness and Blocked Force

The dimensional analysis for stiffness resulted in the following MAPLE™ output leading to equations

4.26, and 4.27:

JEREMY PALMER
3-26-02
STIFFNESS CALCULATION FOR COMPLETE ANNULAR THUNDER MODEL:
SUBMODEL 3 STANDALONE
HERE, WE SET wc(0+) = 1 AND SOLVE FOR LOAD P, LEADING TO THE SINGLE-
TRANSDUCER STIFFNESS.
REMEMBER, THIS IS AT ZERO POTENTIAL!
RADII ARE ADJUSTED TO REFLECT CONDITIONS IN THE TEST FIXTURE
ADJUSTMENT WAS LATER REMOVED.
STIFFNESS AND ACTUATOR TYPE BLOCKED FORCE ARE EVALUATED FOR THE
EACH SIZE DEVICE (ONE SIZE IS SHOWN HERE).

```
>restart;
```

DATA
```
>pi:= 3.14159;
>ri:=0.865*r0;
>rh:=0.142*r0;
>rs:=r0;
>r:=1E-10*r0;
>nu:=0.27;
```
NOMINAL: 0.27
```
>nuc:=0.3;
>nup:=0.15;
```
GOT THIS FROM ANSYS INPUT FILE
```
>h:=0.5E-03;
>hp:=0.6*h;
>hm:=0.4*h;
>Ep:=6.6E+10;
```
GOT THIS FROM PIEZOSYSTEMS
```
>Em:=190E+09;
```
NOMINAL 190E+09 (STEEL)
```
>V:=0;
```
NOMINAL 480V
```
>d31:=190E-12;
```
GOT THIS FROM PIEZOSYSTEMS
EQUATIONS
```
> zns:=((Ep*hp*((hp/2)+hm))+(Em*hm*(hm/2)))/((Ep*hp)+(Em*hm));
>Ds:=(Em*(hm^3))/(12*(1-(nu^2)));
>Dc:=(((1/3)*(Ep/(1-(nup^2))))*(((hm+hp-zns)^3)-((hm-
zns)^3)))+(((1/3)*(Em/(1-(nu^2))))*(((hm-zns)^3)-((-zns)^3)));
>Mrp:=(Ep*V*d31*(hp-(2*zns)+(2*hm)))/(2*(1-nup));
```
EQUATIONS

$$C13 := .05656727385\, P$$

$$C14 := -.2420166006\, P\, r0^2$$

$$C15 := .3045204985\, P\, r0^2$$

$$C16 := .05609874578\, P$$

$$C17 := .005463085992\, P\, r0^2$$

$$C18 := .04903913290\, P\, r0^2$$

```
>wc(r):=(((P*(r^2))/(8*pi*Dc))*((ln(r/r0))-1))-
((C16*(r^2))/4)-(C17*ln(r/r0))+C18;
```

$$wc(.1\,10^{-9}\, r0) := .1748313366\, P\, r0^2$$

```
>k:=simplify(solve(wc(r)=1,P));
```

$$k := 5.719798404\,\frac{1}{r0^2}$$

Two MAPLE™ files were generated to show the dimensional relationship between the total device thickness, *h*,

and the actuator type blocked force. The following listing justifies Equation 4.31:

JEREMY PALMER
3-26-02
STIFFNESS CALCULATION FOR COMPLETE ANNULAR THUNDER MODEL:
SUBMODEL 3 STANDALONE
HERE, WE SET wc(0+) = 1 AND SOLVE FOR LOAD P, LEADING TO THE SINGLE-
TRANSDUCER STIFFNESS.
REMEMBER, THIS IS AT ZERO POTENTIAL!
> `restart;`
DATA
> `pi:= 3.14159;`
> `r0:=0.022;`
> `ri:=0.865*r0;`
> `rh:=0.142*r0;`
> `rs:=r0;`
> `r:=1E-10*r0;`
> `nu:=0.27;`
NOMINAL: 0.27
> `nuc:=0.3;`
> `nup:=0.15;`
GOT THIS FROM ANSYS INPUT FILE
> `hp:=0.6*h;`
> `hm:=0.4*h;`
> `Ep:=6.6E+10;`
GOT THIS FROM PIEZOSYSTEMS
> `Em:=190E+09;`
NOMINAL 190E+09 (STEEL)
> `V:=0;`
NOMINAL 480V
> `d31:=190E-12;`
GOT THIS FROM PIEZOSYSTEMS
EQUATIONS
> `zns:=((Ep*hp*((hp/2)+hm))+(Em*hm*(hm/2)))/((Ep*hp)+(Em*hm));`
> `Ds:=(Em*(hm^3))/(12*(1-(nu^2)));`
> `Dc:=(((1/3)*(Ep/(1-(nup^2))))*(((hm+hp-zns)^3)-((hm-zns)^3)))+(((1/3)*(Em/(1-(nu^2))))*(((hm-zns)^3)-((-zns)^3)));`
> `Mrp:=(Ep*V*d31*(hp-(2*zns)+(2*hm)))/(2*(1-nup));`
EQUATIONS

$$C13 := .7070909150\,10^{-11}\,\frac{P}{h^3}$$

$$C14 := -.1464200433\ 10^{-13}\ \frac{P}{h^3}$$

$$C15 := .1842349019\ 10^{-13}\ \frac{P}{h^3}$$

$$C16 := .7012343228\ 10^{-11}\ \frac{P}{h^3}$$

$$C17 := .3305167030\ 10^{-15}\ \frac{P}{h^3}$$

$$C18 := .2966867543\ 10^{-14}\ \frac{P}{h^3}$$

```
> wc(r):=(((P*(r^2))/(8*pi*Dc))*((ln(r/r0))-1))-
((C16*(r^2))/4)-(C17*ln(r/r0))+C18;
```

$$wc(.22\ 10^{-11}) := .1057729588\ 10^{-13}\ \frac{P}{h^3}$$

```
> k:=simplify(solve(wc(r)=1,P));
```

$$k := .9454212223\ 10^{14}\ h^3$$

The following listing justifies Equation 4.32:

JEREMY PALMER
ROUND THUNDER DIMENSIONAL ANALYSIS
1-19-02
HERE, WE'RE INTERESTED IN THE RELATIONSHIP BETWEEN DEFLECTION AND THICKNESS
THE 0.700" DIAMETER DEVICE IS CONSIDERED HERE
DATA (METRIC UNITS USED THROUGHOUT, ALL LENGTHS IN METERS)

```
> restart;
> unassign('q','Ds','Dc','nu','nuc','Mrp','ri','rh');
> r0:=8.9e-03;
> q:=0;
> nu:=0.27;
```
NOMINAL: 0.27
```
> nuc:=0.3;
> nup:=0.15;
```

CHANGED FORTESTING 1/13/02
> **Ep:=6.6E+10;**
GOT THIS FROM PIEZOSYSTEMS
> **Em:=190E+09;**
NOMINAL 190E+09 (STEEL)
> **V:=480;**
NOMINAL 480V
> **d31:=190E-12;**
> **hp:=(0.3/0.5)*h;**
> **hm:=(0.2/0.5)*h;**
GOT THIS FROM PIEZOSYSTEMS
EQUATIONS
> **zns:=((Ep*hp*((hp/2)+hm))+(Em*hm*(hm/2)))/((Ep*hp)+(Em*hm));**
> **Ds:=(Em*(hm^3))/(12*(1-(nu^2)));**
> **Dc:=(((1/3)*(Ep/(1-(nup^2))))*(((hm+hp-zns)^3)-((hm-**
zns)^3)))+(((1/3)*(Em/(1-(nu^2))))*(((hm-zns)^3)-((-zns)^3)));
> **Mrp:=(Ep*V*d31*(hp-(2*zns)+(2*hm)))/(2*(1-nup));**
> **ri:=0.865*r0;**
NOMINAL: 0.857r0
> **rh:=0.142*r0;**
NOMINAL: 0.23r0

$$C4 := .1297704983 \ 10^{-6} \frac{1}{h^2}$$

$$C6 := -.2507334294 \ 10^{-11} \frac{1}{h^2}$$

$$C10 := -.1296880015 \ 10^{-6} \frac{1}{h^2}$$

$$C11 := .4697779156 \ 10^{-14} \frac{1}{h^2}$$

$$C12 := -.2505707537 \ 10^{-11} \frac{1}{h^2}$$

$$C16 := -.1297292497 \ 10^{-6} \frac{1}{h^2}$$

$$C17 := .2348889577 \ 10^{-14} \frac{1}{h^2}$$

$$C18 := -.2506520915 \ 10^{-11} \frac{1}{h^2}$$

$$C19 := .3891877495 \ 10^{-6} \frac{1}{h^2}$$

$$C20 := -.7046668733 \ 10^{-14} \frac{1}{h^2}$$

$$C21 := -.7519562746 \ 10^{-11} \frac{1}{h^2}$$

```
> wc(r):=((C19*(r^2))/4)+(C20*ln(r/r0))+C21;
```

$$wc(r) := .9729693738 \ 10^{-7} \frac{r^2}{h^2}$$

$$- \frac{.7046668733 \ 10^{-14} \ln(112.3595506 \ r)}{h^2} - \frac{.7519562746 \ 10^{-11}}{h^2}$$

```
> wc(0):=eval(wc(r),r=1E-20*r0);
```

$$wc(0) := -.7195051658 \ 10^{-11} \frac{1}{h^2}$$

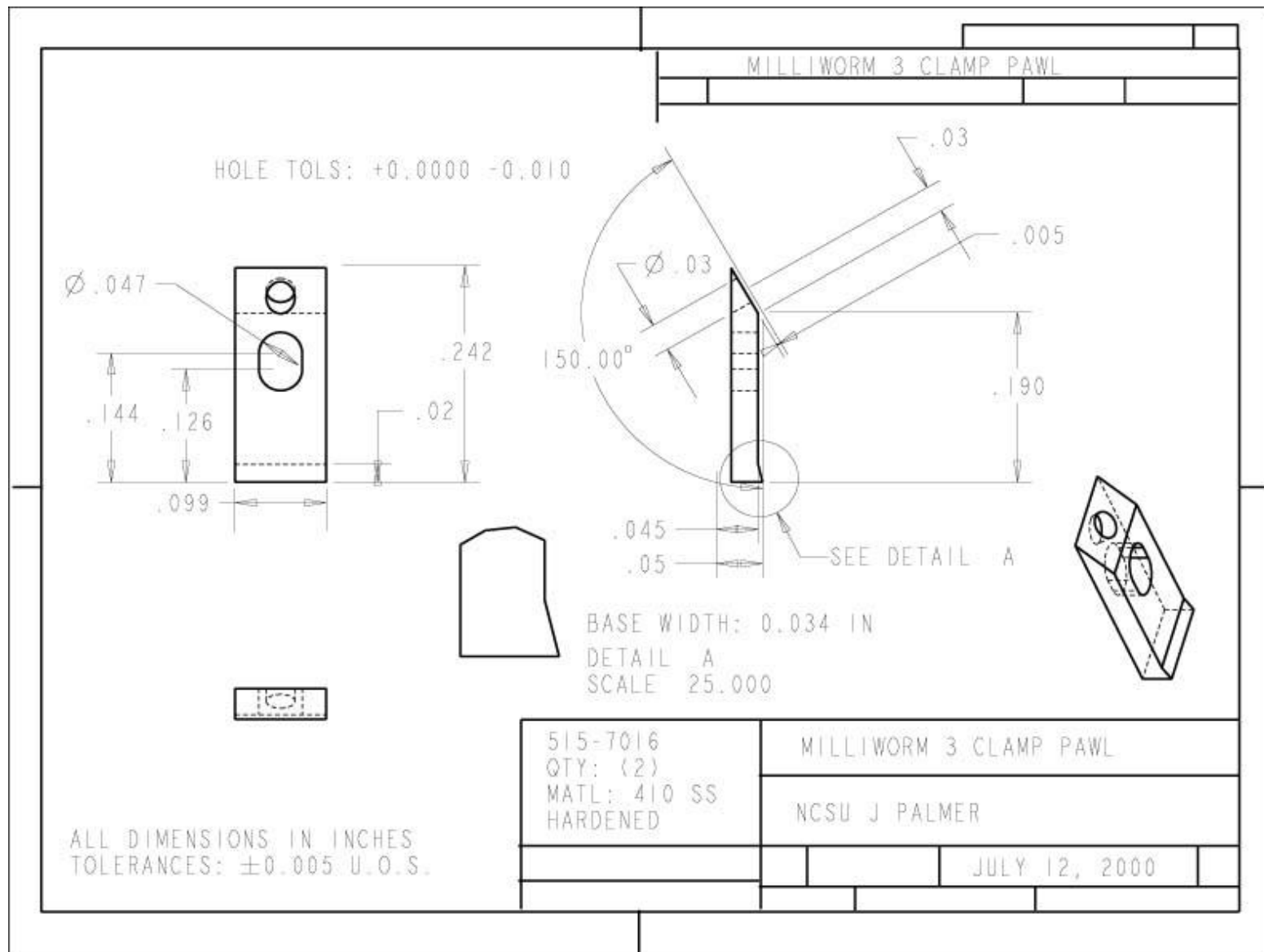## B.7 Milliworm CAD Drawings

Figure B.4. **Milliworm passive latch pawl part drawing**
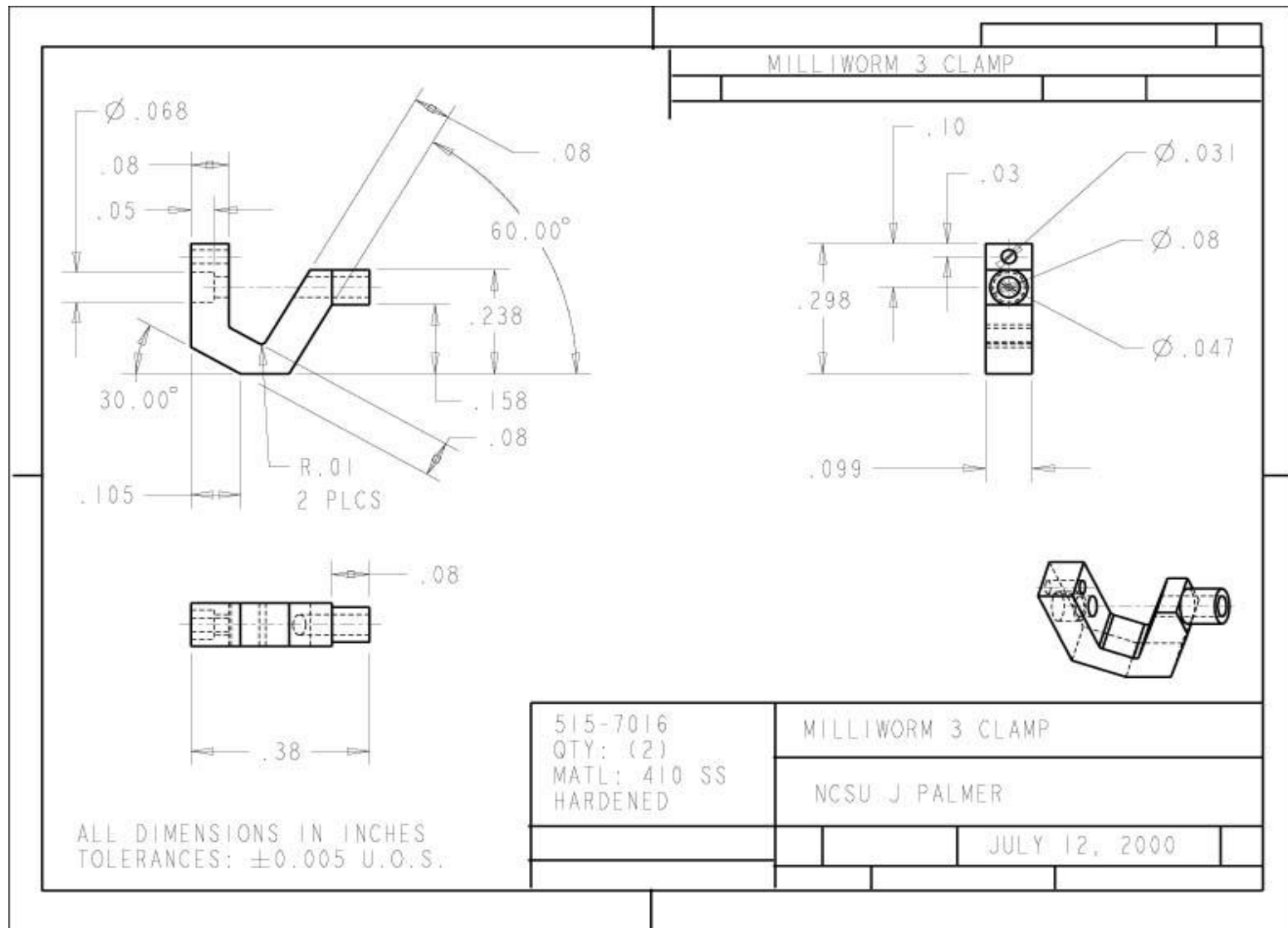
164

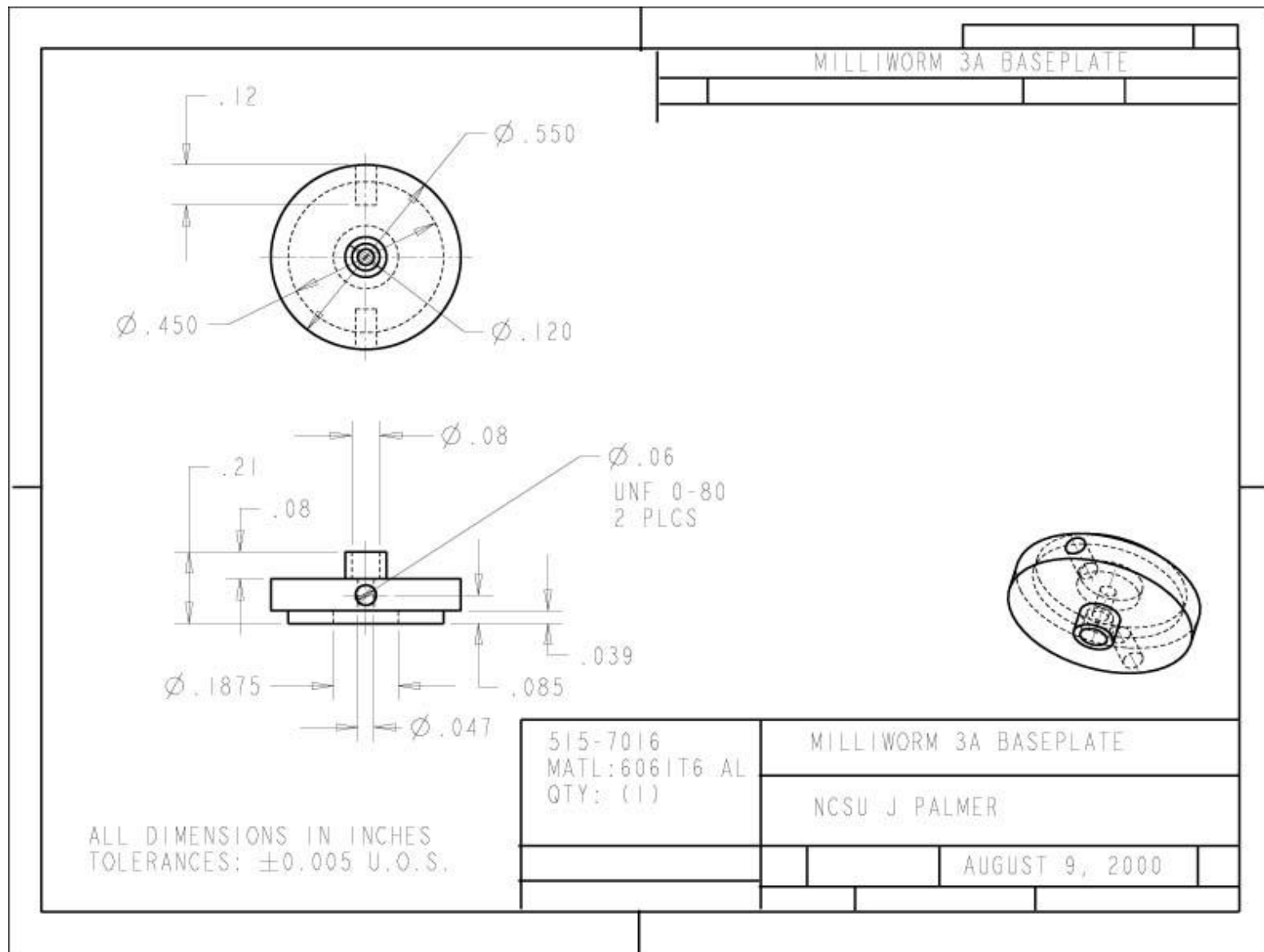Figure B.5. **Milliworm passive latch housing part drawing**

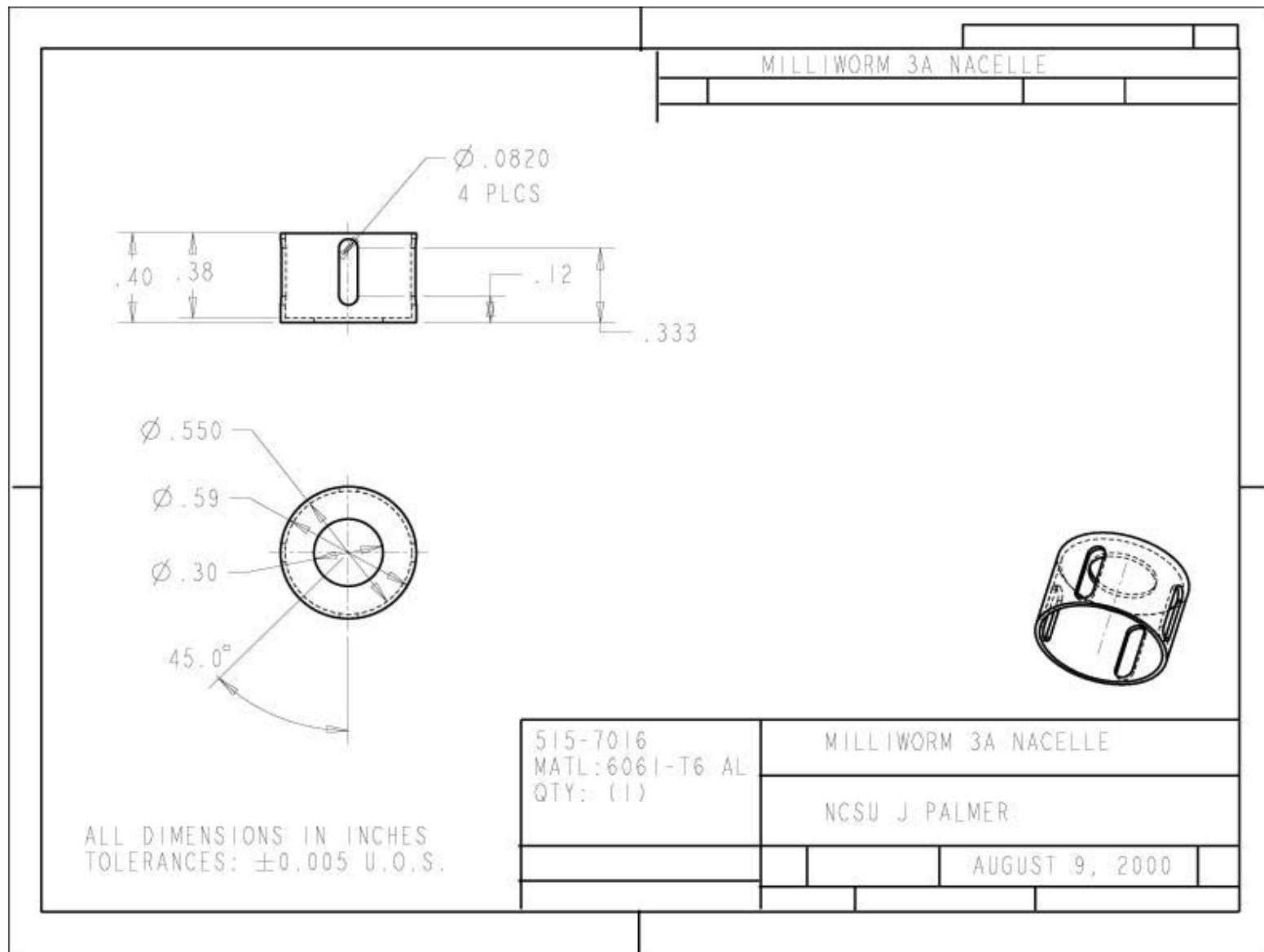Figure B.6. **Milliworm transducer module base plate part drawing**

166

Figure B.7. **Milliworm transducer module housing (nacelle) part drawing**

B.8 Milliworm Characterization Data

Figures B.8 through 10 show blocked force and velocity versus drive frequency data for the Milliworm prototype with three annular THUNDER™ transducers mounted in the Milliworm transducer module. Figure B.10 represents back slip data measured with a single transducer mounted in the module.
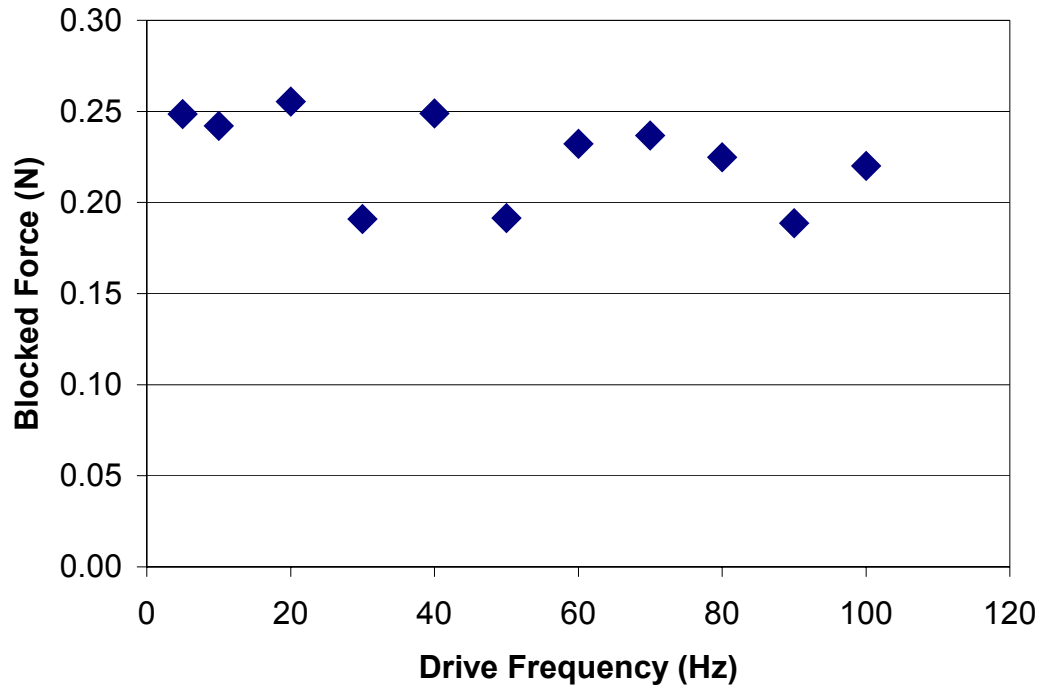
B.8.1 Blocked Force vs. Frequency

Figure B.8. **Blocked force vs. drive frequency for Milliworm prototype with three annular THUNDER™ transducers**

B.8.2 Velocity vs. Frequency
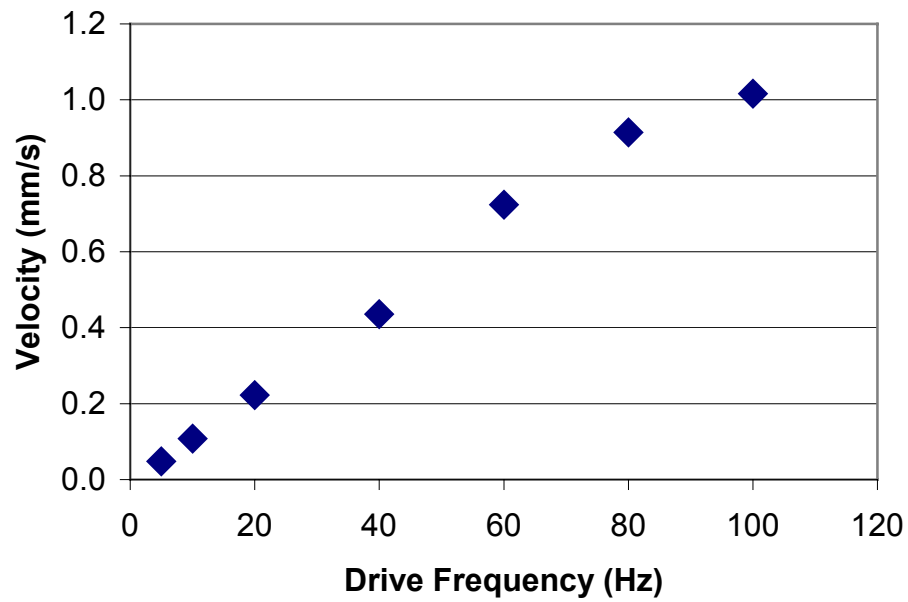
Figure B.9. **Velocity vs. drive frequency for Milliworm with three annular THUNDER™ transducers**

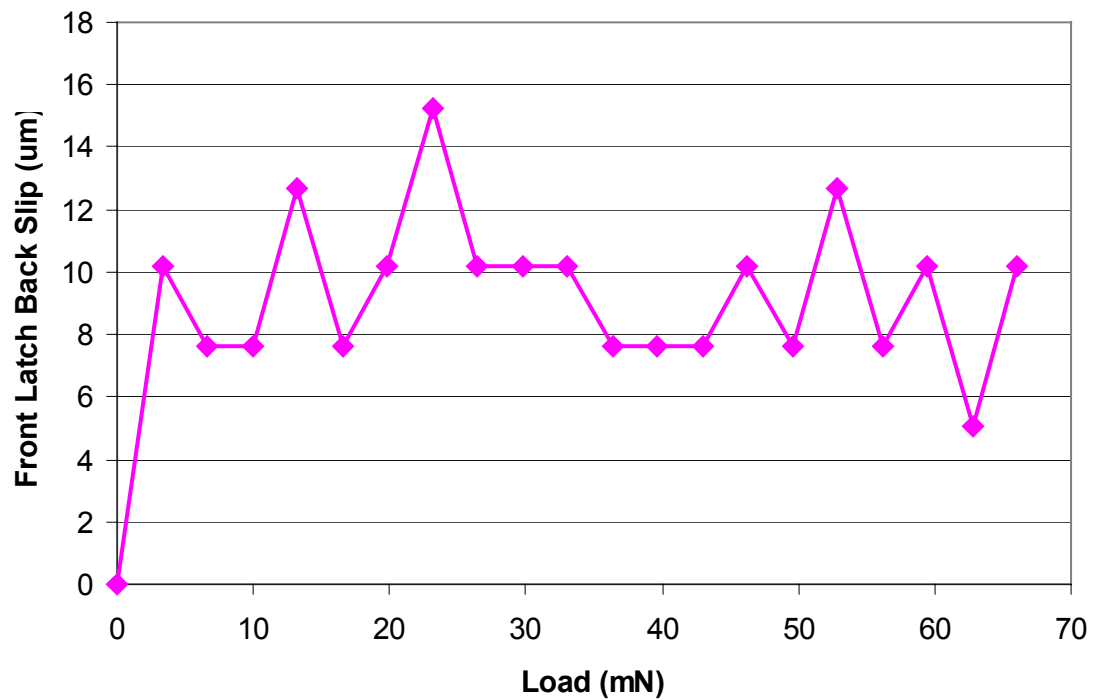## B.8.3 Back Slip vs. Load

Figure B.10. **Velocity vs. drive frequency for Milliworm with three annular THUNDER™ transducers**

B.8.4 Power Density Calculation

The following power density derivation supports the data reported in Table 4.9. Calculating the power density for the Milliworm prototype starts by integrating (with respect to load) the zero-voltage line of the plot of stylus position vs. load (see Figure B.3) to find the total work performed by the THUNDER™ transducer at a load level equal to the actuator type blocked force. In terms of the actuator type blocked force, the total work expression is as follows:

$$W_T = \frac{1}{2}\left(\frac{1}{K_{eq}(0)}\right)F_2^2$$

(B.1)

Equation B.1 assumes the position versus load relationship is linear. As Figure 4.9 illustrates, this is not the case for load characterizations performed on transducers mounted within the module. Thus, Equation B.1 is considered a fair estimate of the total work of the linear piezomotor, and not an exact quantity. Since the power density is used for comparison purposes only, this idealization is acceptable. It follows that power density is expressed as the following:

$$\rho_p = \frac{W_T f}{M_{motor}}$$

(B.2)

where f is the drive frequency in hertz, and M_{motor} denotes the motor mass. Substituting Equation B.1 in Equation B.2 yields:

$$\rho_p = \frac{F_2^2 f}{2K_{eq}(0)M_{motor}}$$

(B.3)

Table B.1 lists the parameters used to calculate the Milliworm power density data.

Table B.1 **Milliworm Power Density Calculation Parameters**

Parameter	Prototype characterization	Module only (3 transducers)	Single transducer, no module
$K_{eq}(0)$ (N/mm)	27.9	26.7	417.6
F_2 (N)	0.23	0.44	6.35
f (Hz)	100	100	100
M_{motor} (kg)	0.01	0.01	0.01

Appendix C

Ultrasonic Motor Dynamic Analysis and Characterization

C.1 USM CAD Drawings

Figures C.1 through C.6 depict the computer aided design (CAD) drawings for major components of the mode conversion ultrasonic motor (USM) prototype.
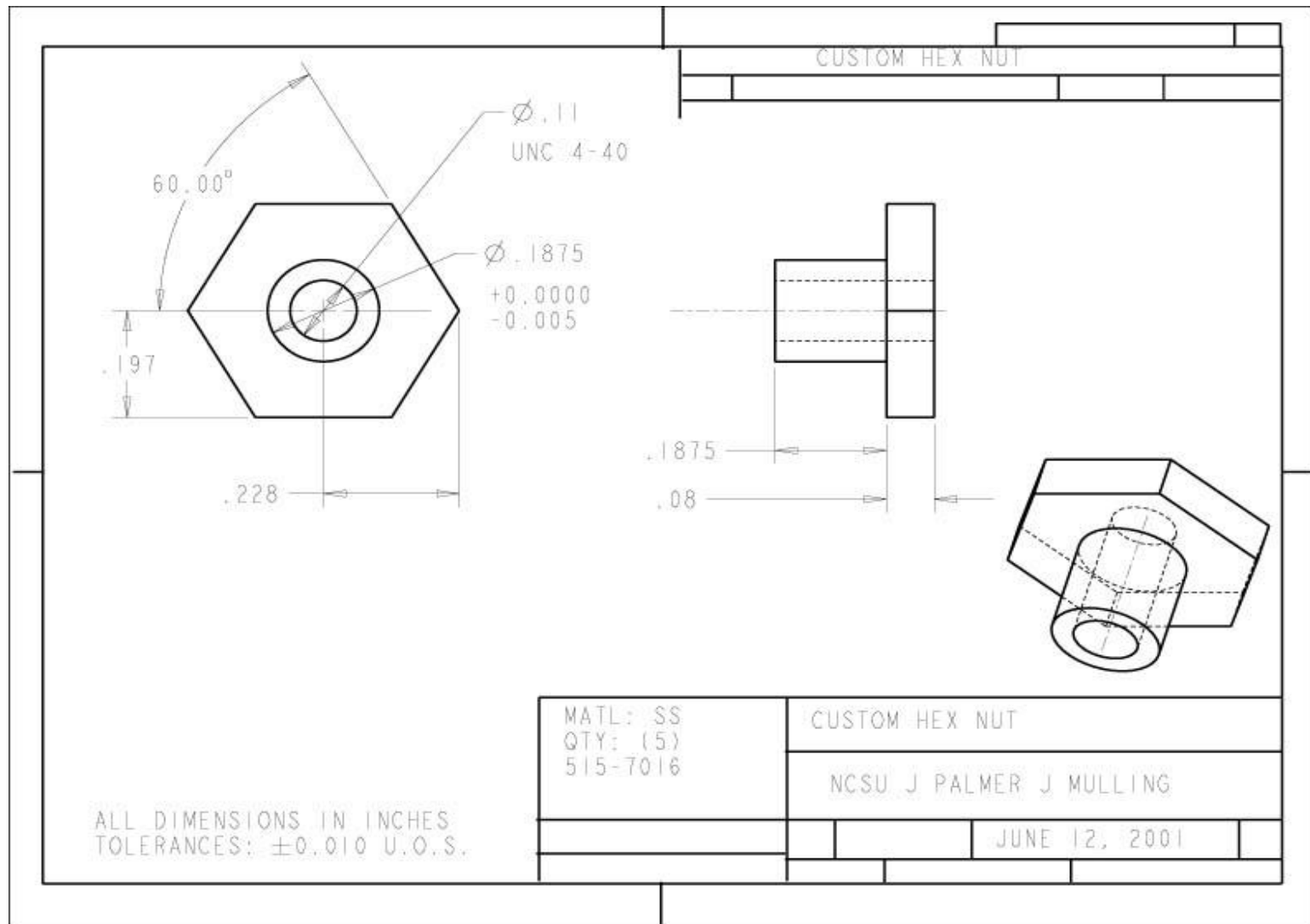
Figure C.1. **Mode conversion USM head/tail mass part drawing**
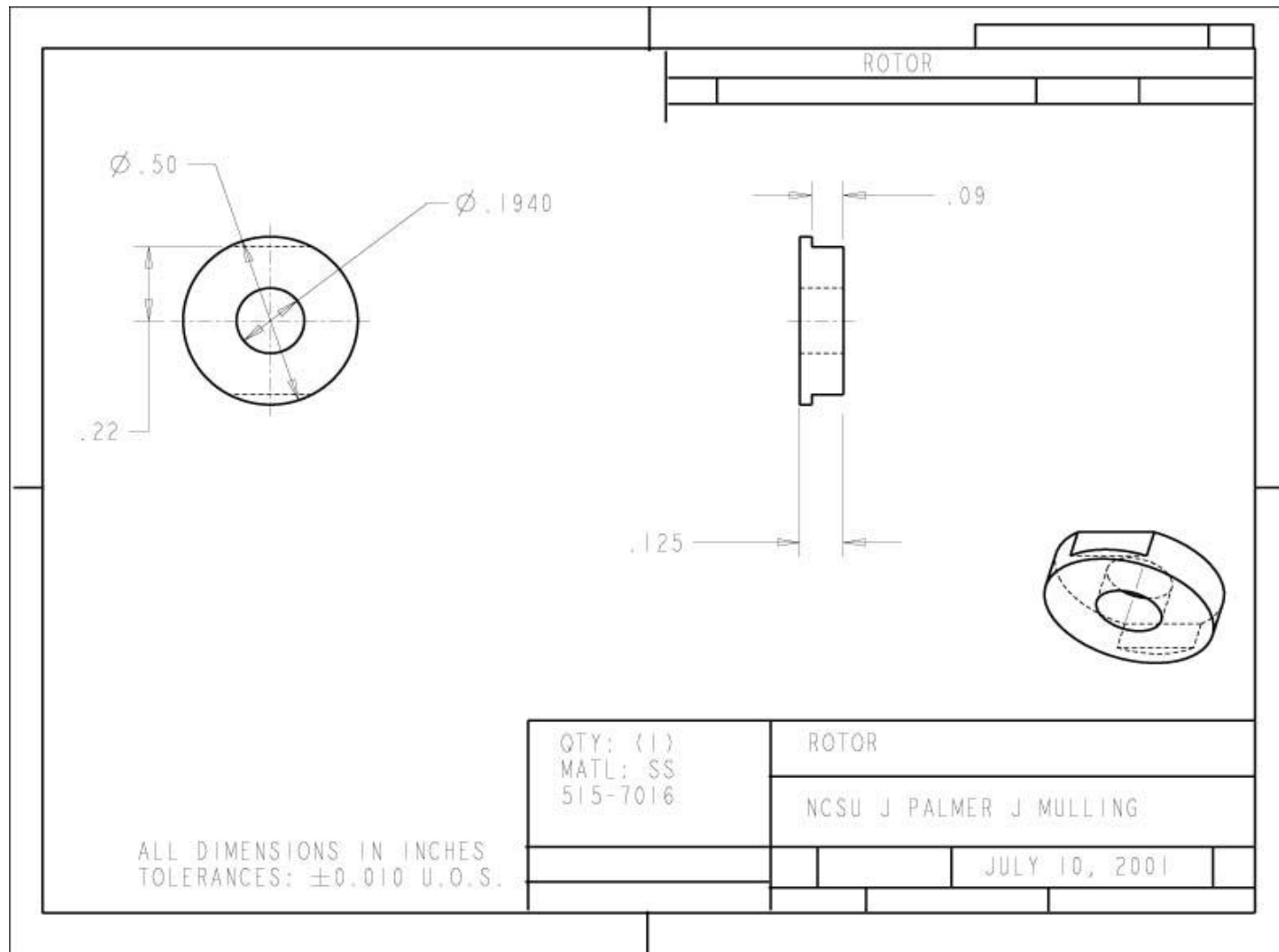
Figure C.2. **Mode conversion USM rotor part drawing***

*Figure C.2 depicts a second-generation version of the rotor that has similar dimensions, but a different edge configuration than the one presented in Chapter 5.
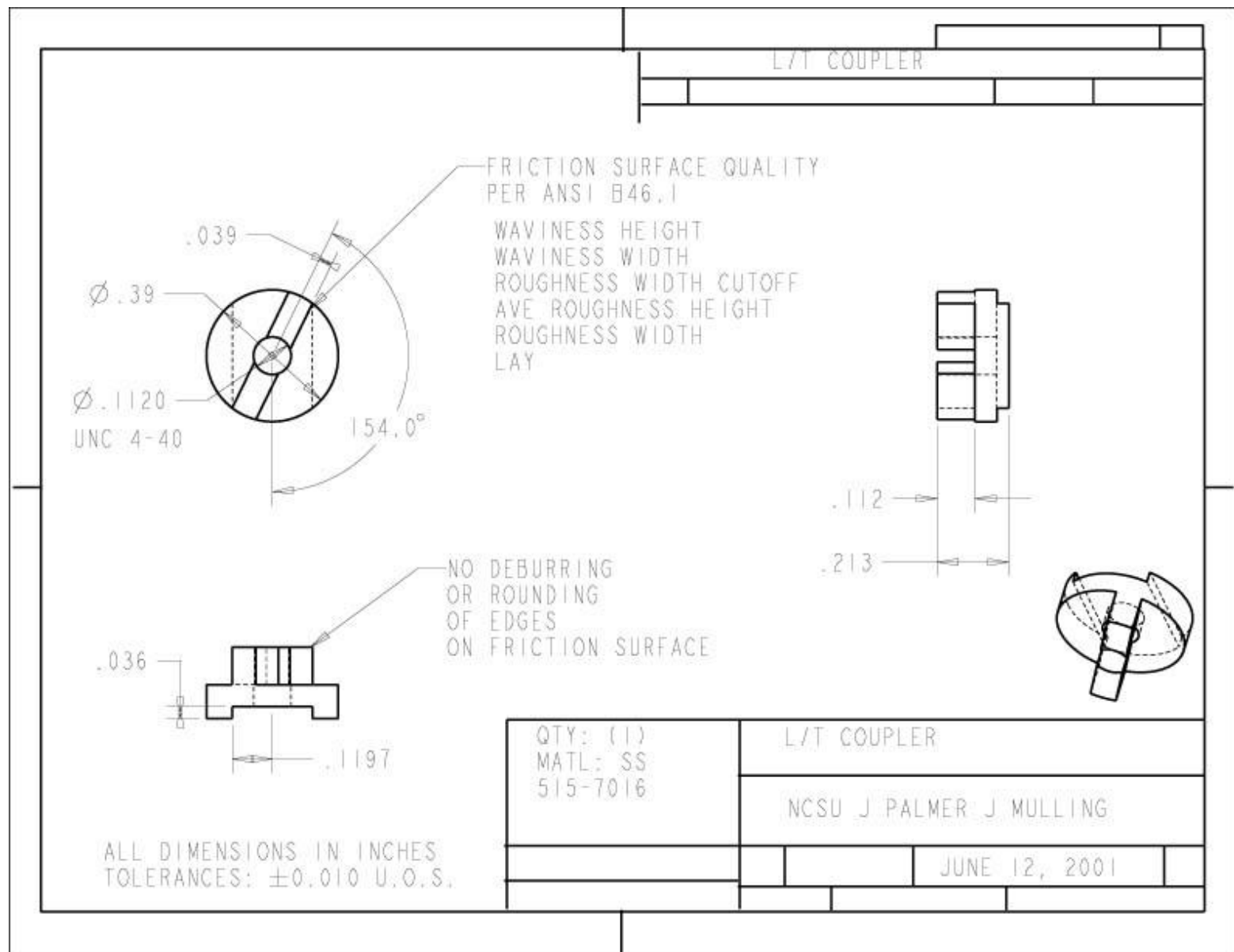
Figure C.3. **Mode conversion USM standard L/T coupler part drawing**
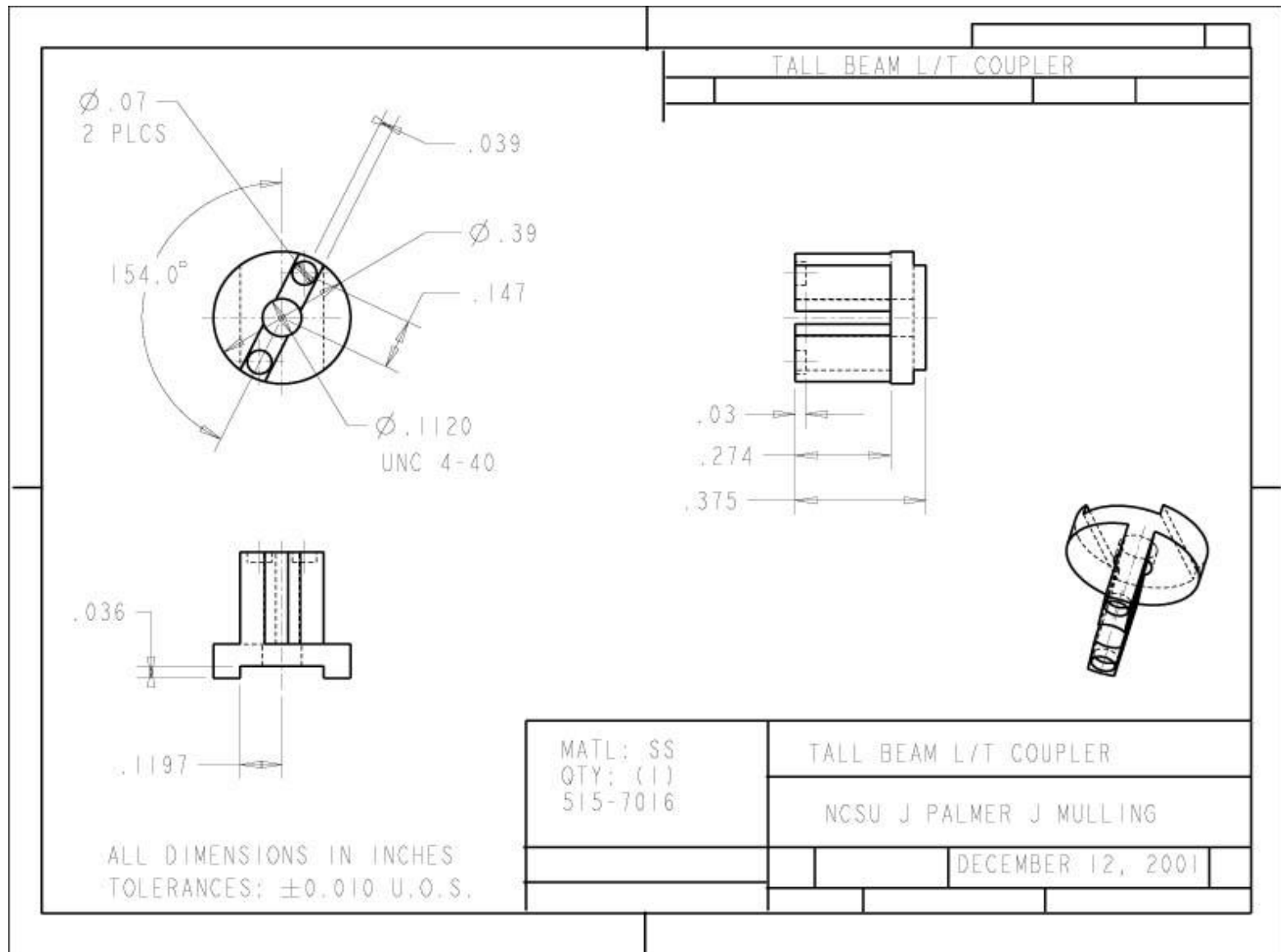
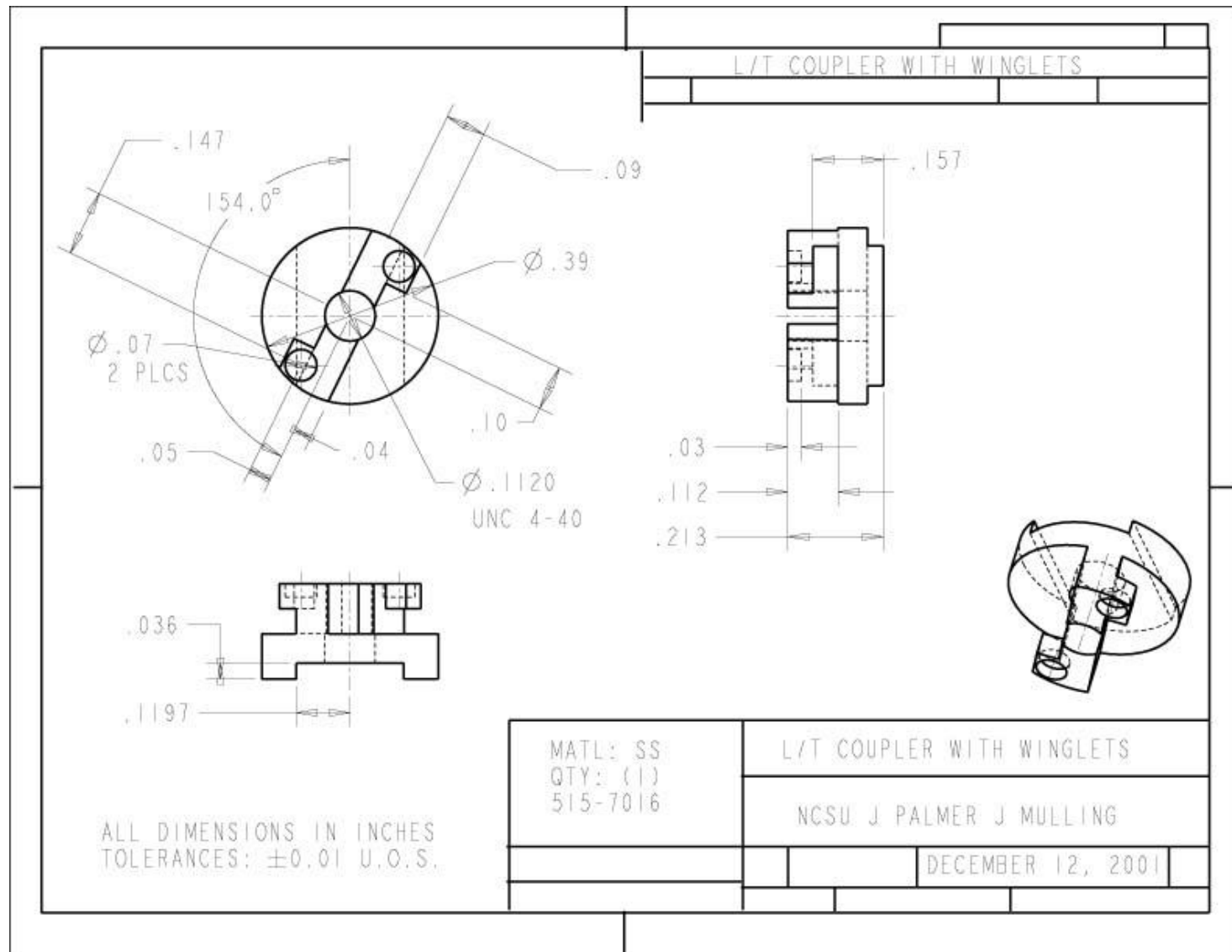Figure C.4. **Mode conversion USM tall beam L/T coupler part drawing**

Figure C.5. **Mode conversion USM winglet L/T coupler part drawing**
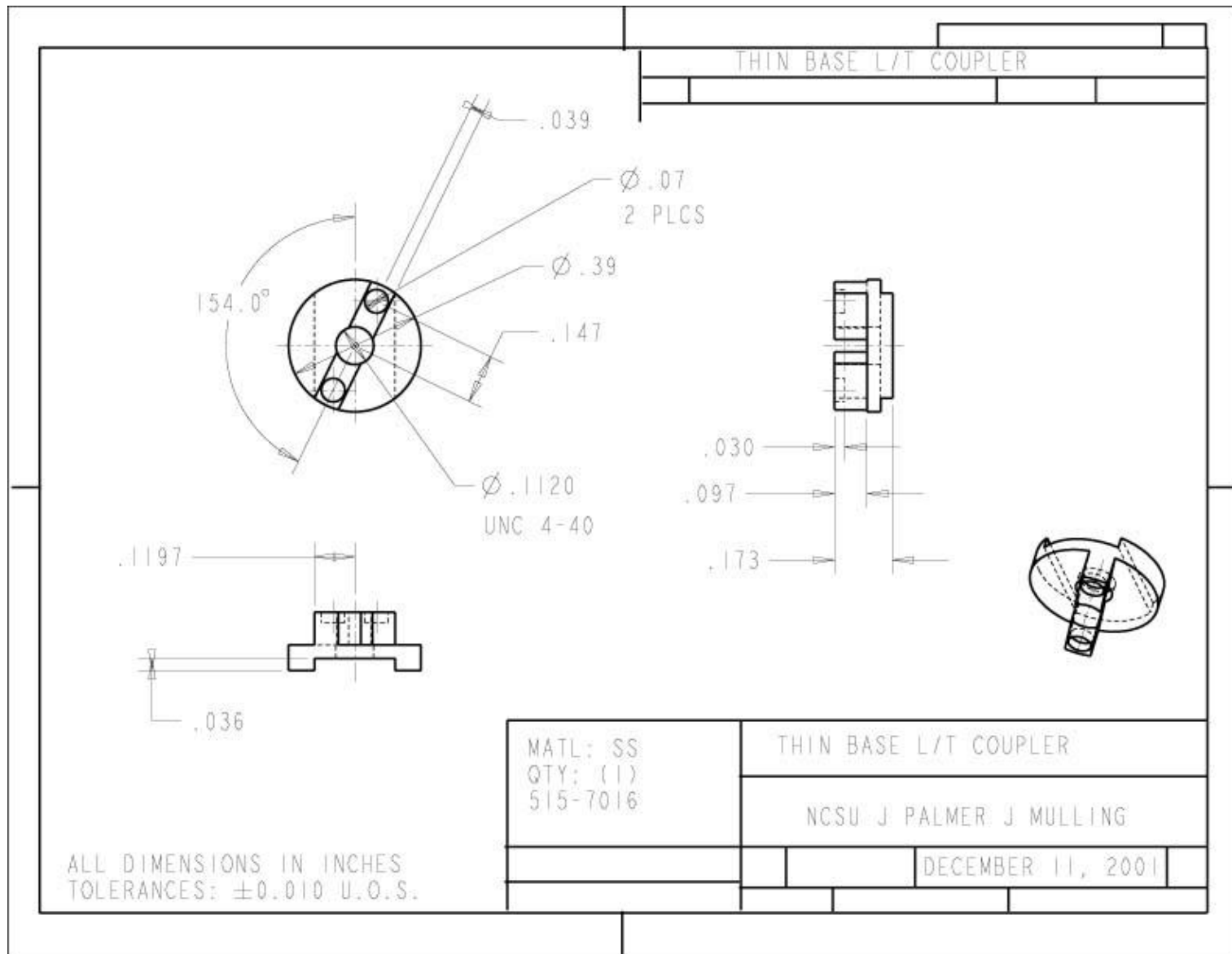
Figure C.6. **Mode conversion USM thin base L/T coupler part drawing**

C.2 Resonator Calculation Parameters

Table C.1 lists the parameters used to calculate the resonator data listed in Table 5.1.

Table C.1 **Resonator Calculation Parameters**

Parameter	Value	Units	Comment
Head mass (horn) density	7860	kg/m^3	AISI type 302 SS (www.matweb.com)
Head mass (horn) area	7.75x10^{-5}	m^2	Output area of head mass (does not account for center hole)
Speed of sound	5130	m/s	Speed of sound in iron (Avallone and Baumeister) [3]

C.3 Numeric Solution Excerpt

C.3.1 Rotor Velocity Verification

Table C.2 lists the parameters used to calculate the theoretical maximum rotor velocity data listed in

Table 5.3. Phase difference inputs to the solution algorithm were determined by examining the resonator

Table C.2 **Theoretical Maximum Rotor Velocity Calculation Parameters**

Parameter	Tall Beam L/TC	Thin Base L/TC	Standard L/TC	Winglet L/TC
Frequency (kHz)	31	56	44	59
L/T phase difference (deg)	50	74	60	40
Static pre-load (N) (arbitrary)	10	5	2	5
Tangential amplitude (um) (peak-to-peak)	6.1	1.6	1.3	2.2

frequency response spectra for each of the L/T coupler designs with the rotor assembled. These plots are shown

in figures C.7 through C.9, and 5.10. The static pre-load values listed in Table C.2 are considered arbitrary

because, as Chapter 5 relates, the numeric solution for rotor velocity shows little sensitivity to this parameter.

Figure C.10 shows the parameter table from the spreadsheet containing the numeric solution calculations.

Figure C.11 is an excerpt of the spreadsheet calculations for the first five time steps. Note that the complete

spreadsheet includes over 59,000 steps. Figure C.12 lists the MATLAB™ solution script.
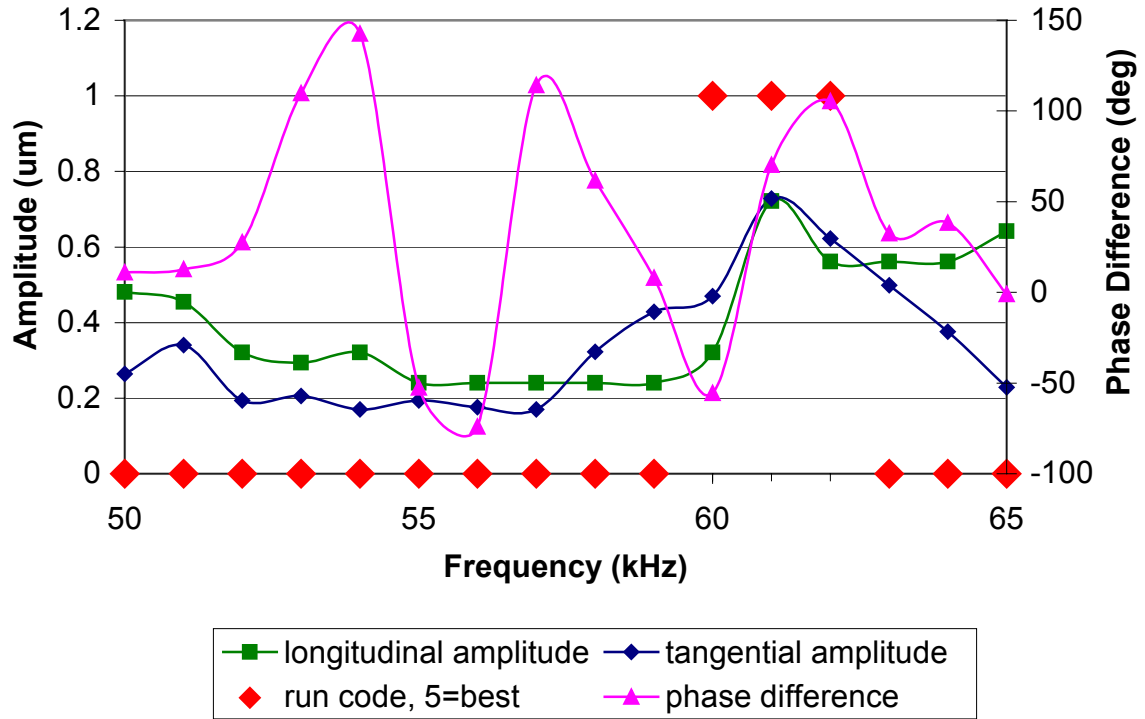
Figure C.7. **Frequency response spectrum for USM prototype with thin base L/T coupler and rotor assembled**
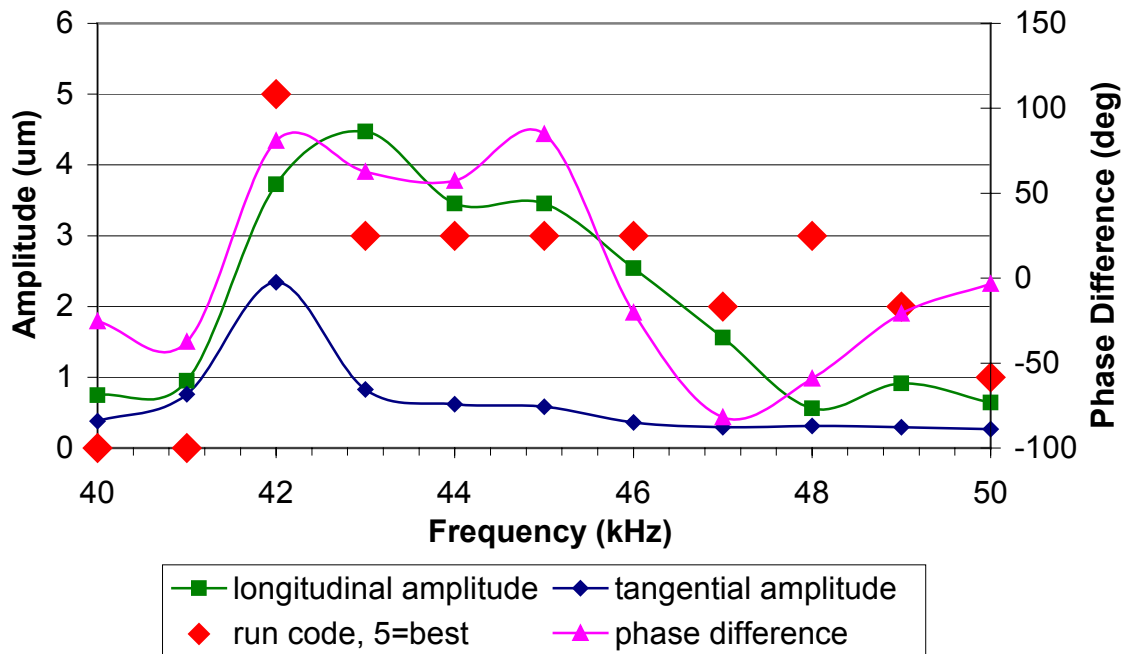
Figure C.8. **Frequency response spectrum for USM prototype with standard L/T coupler and rotor assembled**
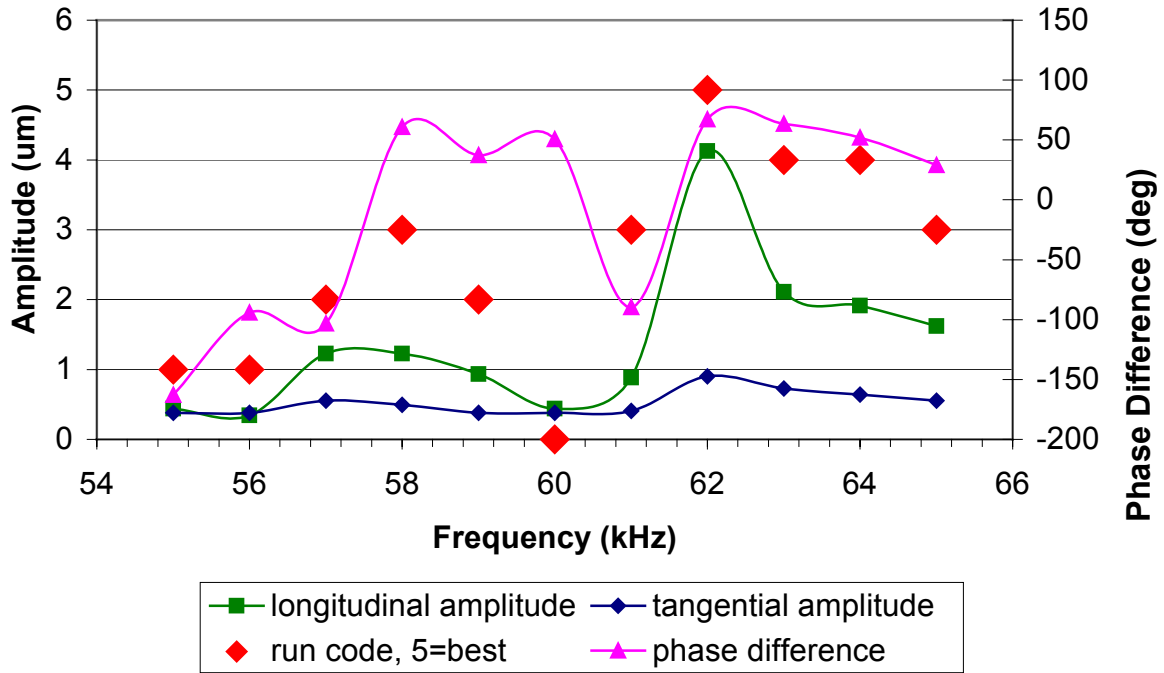
Figure C.9. **Frequency response spectrum for USM prototype with winglet L/T coupler and rotor assembled**

Parameter	Value	Units	Comment
a2	2.36E-06	m	stator tangential amplitude
kpl	2.13E+04	N/m	Pre-load spring stiffness (three black grommets)
N0	5.625	N	Static Pre-load
ω	6.40E+05	rad/sec	Drive frequency
ψ	5.76E+00	rad	long/tang phase diff
reff	1.69E-03	m	effective radius
mR	4.80E-04	kg	rotor mass
ri	9.00E-04	m	rotor hole radius
ro	3.60E-03	m	rotor outside radius
Jo	3.30E-09	kgm^2	Rotor polar mass moment of inertia (Rao, p.116)
μk	0.42		dry hard steel on dry hard steel (Mark's 3-26)

Figure C.10. **USM rotor velocity numeric solution: spreadsheet parameter table**

dt	1.00E-07 sec	Time step	
θRoddot	0.00 rad/sec^2	Rotor initial acceleration	
θRodot	0.00 rad/sec	Rotor initial velocity	
θRo	0.00E+00 rad	Rotor initial position	
θSodot	0.00E+00 rad/sec	Stator initial velocity	
θSodot(i+1/2)	7.89E+02 rad/sec	Stator velocity at t0+dt/2	
nθ(t0+dt/2)	5.81 N		
M	0.5 kg	Load mass	
μkAl	0.47	kinetic friction for dry mild steel on Al	
g	9.81 m/2^2		
rshaft	3.17E-03 m		

Figure C.10. **(Continued)**

TIME, ti, (sec)	ti+dt/2 (sec)	θdotSi (rad/sec)	nθi (N)	θdotS(i+1/2) (rad/sec)	nθ(I+1/2) (N)
1.00E-07	1.50E-07	8.02E+02	5.985	8.15E+02	6.164
2.00E-07	2.50E-07	8.26E+02	6.343	8.37E+02	6.522
3.00E-07	3.50E-07	8.46E+02	6.699	8.55E+02	6.875
4.00E-07	4.50E-07	8.63E+02	7.050	8.71E+02	7.224
5.00E-07	5.50E-07	8.77E+02	7.395	8.82E+02	7.565

K1	K2	K3	K4
0.000E+00	-1.106E-08	1.411E-09	2.823E-09
-1.204E-09	5.936E-10	9.791E-10	3.163E-09
2.906E-09	5.473E-09	5.856E-09	8.807E-09
8.552E-09	1.188E-08	1.226E-08	1.597E-08
1.572E-08	1.980E-08	2.018E-08	2.464E-08

L1	L2	L3	L4
-2.21E-01	2.823E-02	2.823E-02	3.596E-02
3.596E-02	4.367E-02	4.367E-02	3.596E-02
5.136E-02	5.901E-02	5.901E-02	5.136E-02
6.663E-02	7.420E-02	7.420E-02	6.663E-02
8.171E-02	8.916E-02	8.916E-02	8.171E-02

θRddot(i+1) (rad/sec^2)	θRdot(i+1) (rad/sec)	θR(i+1) (rad)
3.60E+05	-1.204E-02	-2.745E-09
5.14E+05	2.906E-02	-1.894E-09
6.66E+05	8.552E-02	3.835E-09
8.17E+05	1.572E-01	1.597E-08
9.65E+05	2.439E-01	3.602E-08

Figure C.11. **USM rotor velocity numeric solution: spreadsheet excerpt**

```
function yp = kumada1(t,y);

%  JEREMY PALMER  3-28-02
%  solver works on the form y'=F(t,y)
%   let 'y' correspond to theta
%  let y(1) = y
%  let y(2) = y'
%  then y(1)'=y(2)

omega=2.64E+05;
phi=0;
no=1;
jo=5.9E-08;
a2=4.2E-06;
psi=3.67;
deff=6.1E-03;
muk=0.42;

yp = zeros(2,1);      %  This is a vector, 2 rows by 1 column!!
yp(1)=y(2);

yp(2)=(sign(y(2)-(((a2*omega)/(deff/2))*cos((omega*t)+psi+phi))))*((-
muk*((no*sin((omega*t)+phi))+no)*deff)/jo);
```

Figure C.12. **USM rotor velocity MATLAB™ solution script**
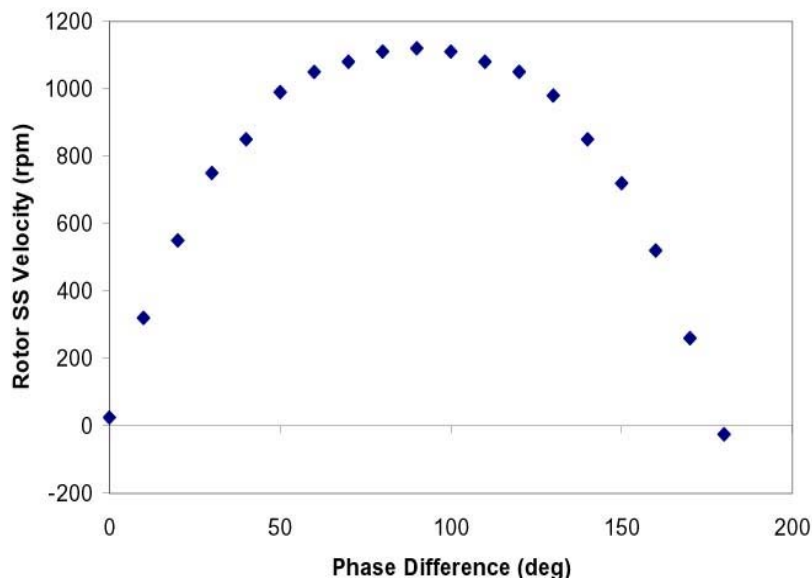
C.3.2 Rotor Velocity Vs. L/T Phase Difference

Figure C.13. **USM theoretical rotor velocity vs. L/T phase difference**

C.4 Ultrasonic Motor Characterization Data

C.4.1 Torque Characterization Data

Figures C.14 through C.17 depict the experimental rotor velocity versus brake force plots that were produced during torque characterization of the mode conversion USM prototype.

stall force = 431.6 / 140.4 = 3.07 N
radius of shaft = 0.00317 m
stall torque = (3.07 N)(0.00317 m) = 0.0097 Nm
torque density = 0.0097 Nm / 0.0305 kg = 0.32 Nm/kg

$$d\theta_R/dt = -140.4F_{brake} + 431.6$$
$$R^2 = 0.8247$$
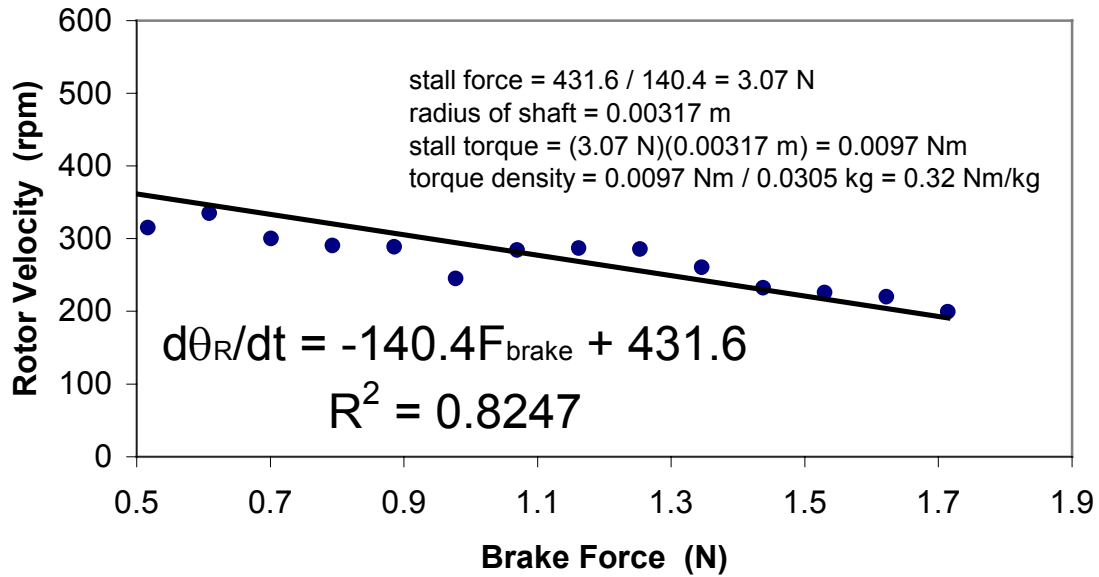
Figure C.14. **Rotor velocity vs. brake force: USM prototype with standard L/T coupler**

$$d\theta_R/dt = -187.8F_{brake} + 672.3$$
$$R^2 = 0.8347$$

stall force = 672.3 / 187.8 = 3.58N
radius of shaft = 0.00317 m
stall torque = (3.58 N)(0.00317 m) = 0.0113 Nm
torque density = 0.0113 Nm / 0.0305 kg = 0.37 Nm/kg
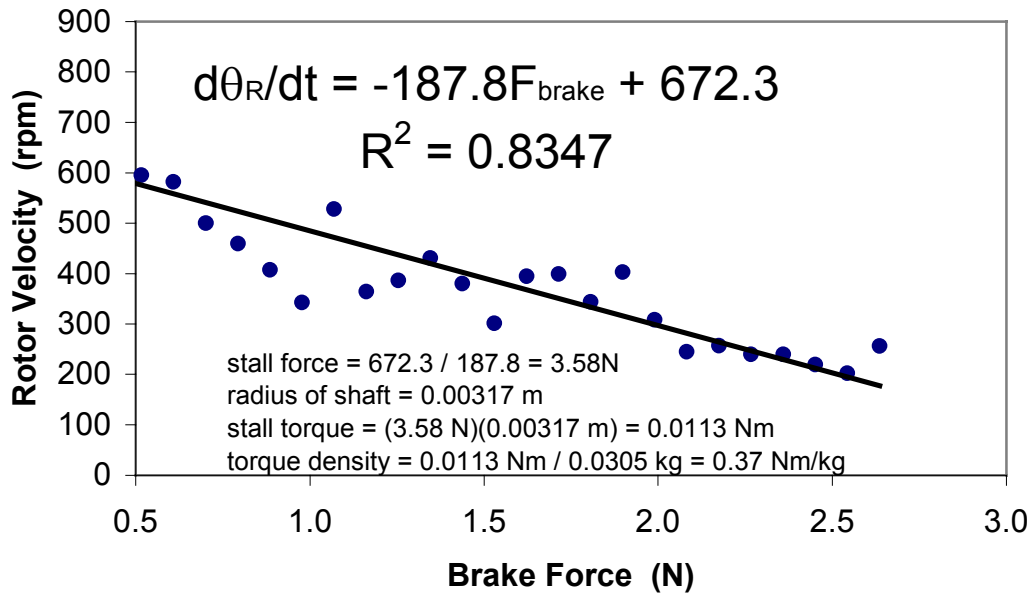
Figure C.15. **Rotor velocity vs. brake force: USM prototype with tall beam L/T coupler**

183

$$d\theta_R/dt = -483.7F_{brake} + 1209.1$$
$$R^2 = 0.8273$$

stall force = 1209.1 / 483.7 = 2.5 N
radius of shaft = 0.00317 m
stall torque = (2.5 N)(0.00317 m) = 0.0079 Nm
torque density = 0.0079 Nm / 0.0305 kg = 0.26 Nm/kg
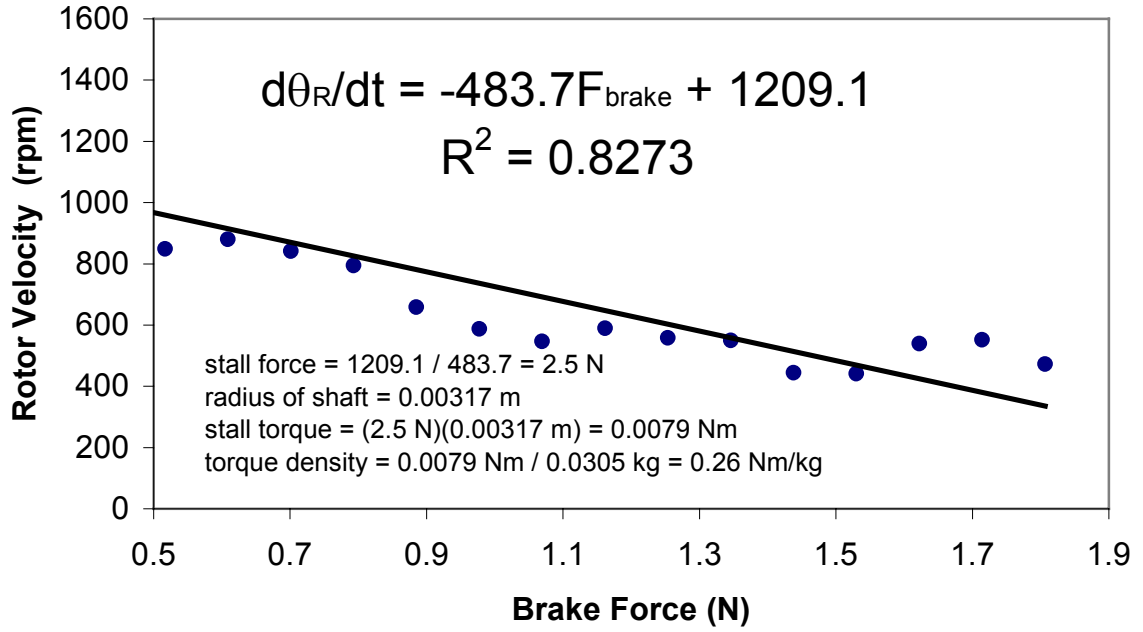
Figure C.16. **Rotor velocity vs. brake force: USM prototype with thin base L/T coupler**

$$d\theta_R/dt = -415.3F_{brake} + 1198.0$$
$$R^2 = 0.9073$$

stall force = 1198.0 / 415.3 = 2.88 N
radius of shaft = 0.00317 m
stall torque = (2.88 N)(0.00317 m) = 0.0091 Nm
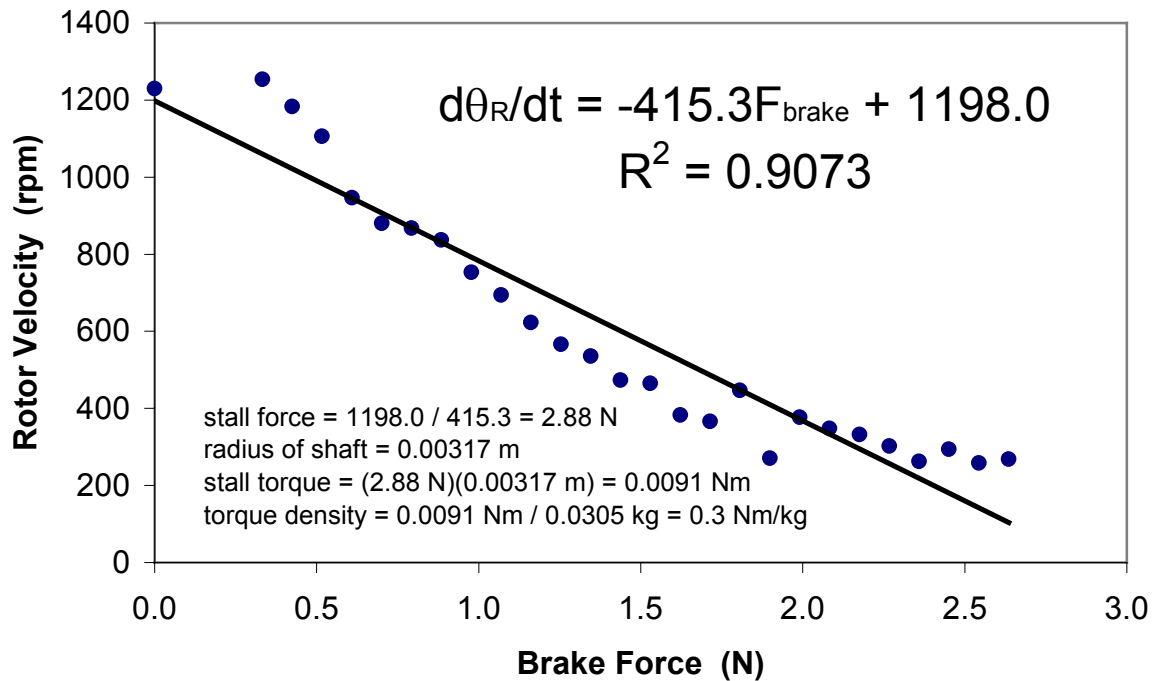torque density = 0.0091 Nm / 0.0305 kg = 0.3 Nm/kg

Figure C.17. **Rotor velocity vs. brake force: USM prototype with winglet L/T coupler**

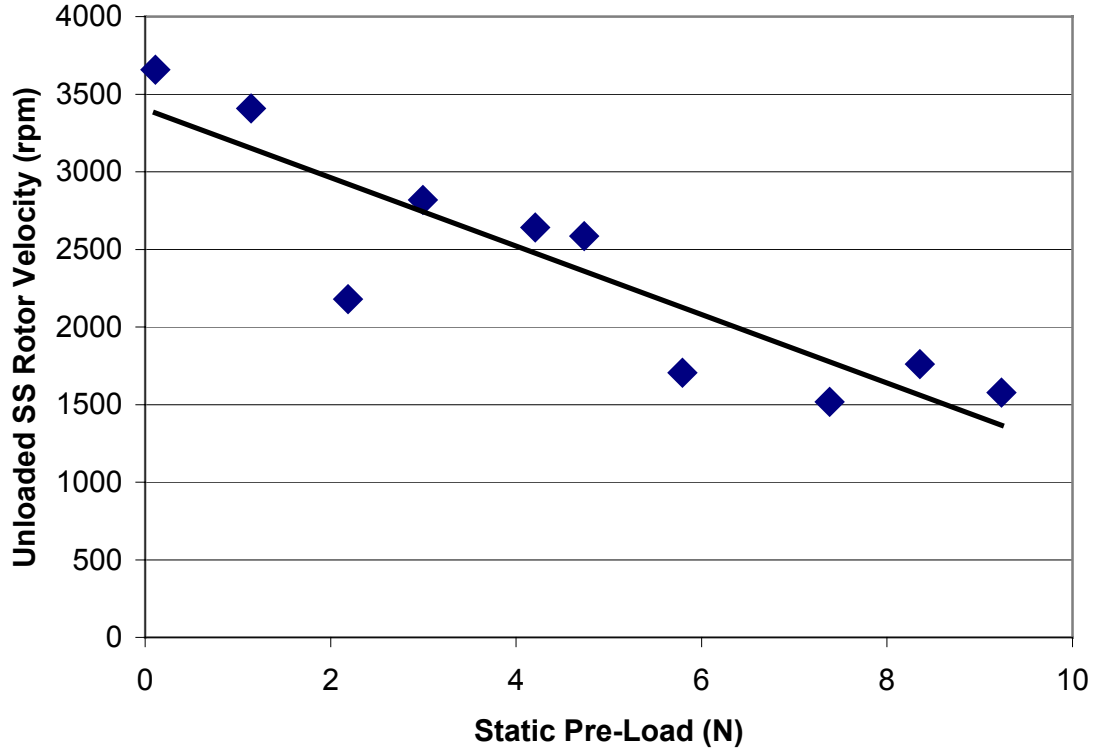## C.4.2 Steady State Rotor Velocity Vs. Static Pre-Load

<u>Figure C.18</u>. **Steady state rotor velocity vs. static pre-load for USM prototype with tall beam L/T coupler**

C.4.3 Motor Constant Derivation

The motor constant is derived from the torque versus armature current relation for a simple DC motor (Boylestad and Nashelsky) [10]. The relation is as follows:

$$\tau_c = K_T I_A \tag{C.1}$$

where τ_c is the continuous output torque in newton meters, I_A is the armature current in amperes, and K_T is the torque constant (Nm/A). The power P (watts) dissipated in the DC motor windings is expressed as:

$$P = I_A^2 R \tag{C.2}$$

where R is the resistance of the windings. Solving for the current and substituting the result in Equation C.1 yields the following:

$$\tau_c = \left(\frac{K_T}{\sqrt{R}}\right)\sqrt{P} \tag{C.3}$$

Solving Equation C.3 for the quantity in parentheses defines the motor constant K_M [10]:

$$K_M = \frac{K_T}{\sqrt{R}} = \frac{\tau_c}{\sqrt{P}} \tag{C.4}$$

Appendix D

Dimensional Analysis

D.1 Ultrasonic Motor Dimensional Analysis Calculations

Figure D.1 is a spreadsheet excerpt listing the dimensions of the simulation that calculates the static

torques and steady state rotor velocities of a set of geometrically similar mode conversion USM's. The

Effective radius, reff, (mm)	Rotor Outer Radius, ro, (mm)	Rotor Inner Radius, ri, (mm)
5.33	11.38	2.84
4.00	8.53	2.13
3.00	6.40	1.60
2.25	4.80	1.20
1.69	3.60	0.90

Rotor Thickness (mm)	Rotor Mass (kg)	Head Mass Thickness (mm)	Head Mass (kg)
5.03	1.52E-02	5.69	1.71E-02
3.77	6.39E-03	4.27	7.23E-03
2.83	2.70E-03	3.20	3.05E-03
2.12	1.14E-03	2.40	1.29E-03
1.59	4.80E-04	1.80	5.43E-04

| Tail Mass Thickness (mm)	Tail Mass (kg)	Primary Op Frequency (kHz)
17.51	5.27E-02	18.14
13.13	2.23E-02	27.93
9.85	9.39E-03	43.00
7.39	3.96E-03	66.20
5.54	1.67E-03	101.92

Figure D.1. **USM dimensional analysis spreadsheet excerpt**

dimensions were calculated assuming a density of steel equal to 7900 kg/m³, and a transducer stiffness of 1.68×10^8 N/m. The prototype with nominal dimensions was simulated with a phase difference of 150 degrees, a tangential displacement amplitude of 4.2 microns peak-to-peak, and a 10-newton static pre-load.

D.2 Milliworm Back Slip Dimensional Analysis Calculations

D.2.1 Pawl Return Rotation

Figure D.2 is a plot of back slip due to pawl return rotation versus transducer outer radius. Figure D.3 is a spreadsheet excerpt of the supporting calculations. All dimensions were scaled by an arbitrary factor of
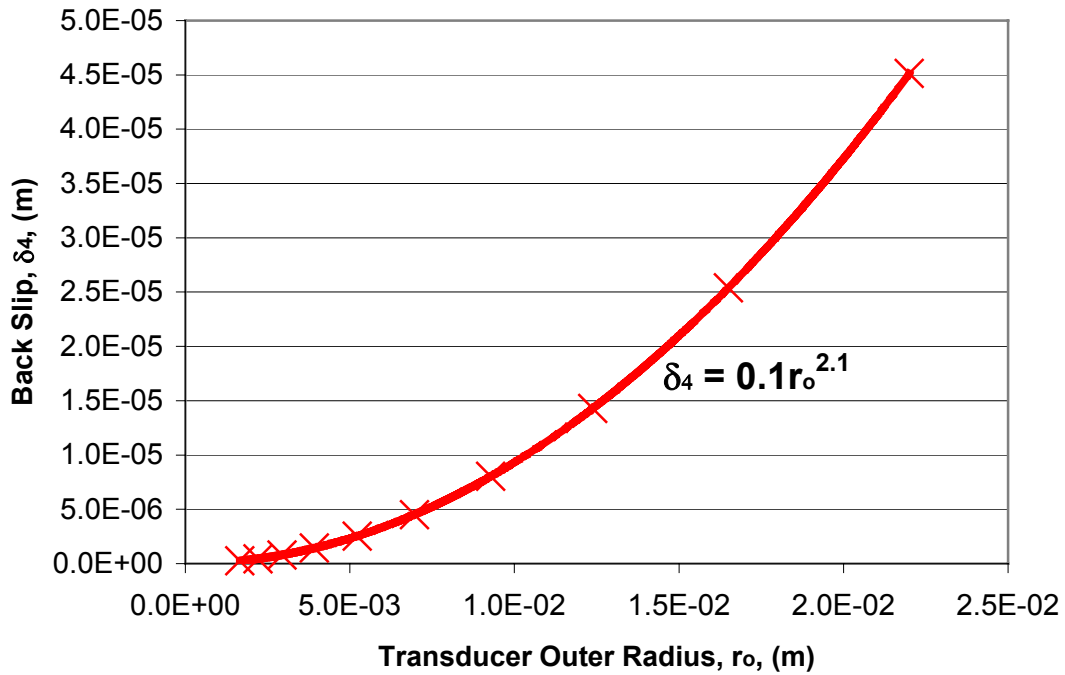
Figure D.2. **Back slip due to pawl return rotation vs. transducer outer radius**

three quarters, while transducer displacement varied with the outer radius according to the following:

$$d_{th} = 0.3712 r_o^2 \qquad \text{(D.1)}$$

This relationship is plotted in Figure 4.6 for the piezoelectric strain coefficient equal to 190×10^{-12} m/V. It was derived assuming unloaded piezoelectric actuation of the annular THUNDER™ transducer at 480 volts. Deflection was calculated at the edge of the hole.

ALL DIMENSIONS IN METERS

Rod Radius, r1	Pawl Hole Diameter, th	Pawl Thickness, tc	L	θ	Pawl Arm, lt	Transducer Outer Radius, ro	Step Displacement, dth
1.588E-03	4.270E-03	1.58E-03	4.553E-03	1.126	7.000E-03	2.200E-02	1.797E-04
1.191E-03	3.203E-03	1.19E-03	3.415E-03	1.126	5.250E-03	1.650E-02	1.011E-04
8.930E-04	2.402E-03	8.89E-04	2.561E-03	1.126	3.938E-03	1.238E-02	5.685E-05
6.697E-04	1.801E-03	6.67E-04	1.921E-03	1.126	2.953E-03	9.281E-03	3.198E-05
5.023E-04	1.351E-03	5.00E-04	1.441E-03	1.126	2.215E-03	6.961E-03	1.799E-05
3.767E-04	1.013E-03	3.75E-04	1.080E-03	1.126	1.661E-03	5.221E-03	1.012E-05
2.825E-04	7.600E-04	2.81E-04	8.103E-04	1.126	1.246E-03	3.916E-03	5.691E-06
2.119E-04	5.700E-04	2.11E-04	6.077E-04	1.126	9.344E-04	2.937E-03	3.201E-06
1.589E-04	4.275E-04	1.58E-04	4.558E-04	1.126	7.008E-04	2.202E-03	1.801E-06
1.192E-04	3.206E-04	1.19E-04	3.419E-04	1.126	5.256E-04	1.652E-03	1.013E-06

s0	st	φ	s1	Back Slip, δ4
1.7585E-03	6.9246E-03	0.0234	1.7396E-03	**4.513E-05**
1.3189E-03	5.2073E-03	0.0175	1.3082E-03	**2.539E-05**
9.8918E-04	3.9134E-03	0.0131	9.8312E-04	**1.428E-05**
7.4188E-04	2.9395E-03	0.0098	7.3846E-04	**8.033E-06**
5.5641E-04	2.2072E-03	0.0074	5.5448E-04	**4.519E-06**
4.1731E-04	1.6568E-03	0.0055	4.1622E-04	**2.542E-06**
3.1298E-04	1.2434E-03	0.0041	3.1237E-04	**1.430E-06**
2.3474E-04	9.3301E-04	0.0031	2.3439E-04	**8.042E-07**
1.7605E-04	7.0002E-04	0.0023	1.7586E-04	**4.524E-07**
1.3204E-04	5.2516E-04	0.0017	1.3193E-04	**2.545E-07**

Figure D.3. **Spreadsheet excerpt for dimensional analysis of back slip due to pawl return rotation**

D.2.2 Pawl Deflection

Back slip due to pawl deflection is calculated from Equation 3.18. The thickness of the pawl determines the moment of inertia I of its cross-section. For a rectangular cross-section, the moment of inertia is expressed as the following (Beer and Johnston) [7]:

$$I = \frac{w_{pawl}t_c^3}{12} \tag{D.2}$$

where w_{pawl} is the pawl width, and t_c is the thickness. Substituting Equation D.2 in Equation 3.18 reveals that pawl deflection (and ultimately back slip due to pawl deflection) varies as the inverse of the thickness cubed.